NASA CONTRACTOR
REPORT

NASA CR-1

d. 1

MATHEMATICAL MODEL FOR
TWO-DIMENSIONAL MULTI-COMPONENT
AIRFOILS IN VISCOUS FLOW

by W. A. Stevens, S. H. Goradia, and J. A. Braden

Prepared by
LOCKHEED-GEORGIA COMPANY
Marietta, Ga.
for Langley Research Center

NATIONAL AERONAUTICS AND SPACE ADMINISTRATION • WASHINGTON, D. C. • JULY 1971

1. Report No. NASA CR-1843	2. Government Accession No.	3. Recipient's Catalog No.
4. Title and Subtitle MATHEMATICAL MODEL FOR TWO-DIMENSIONAL MULTI-COMPONENT AIRFOILS IN VISCOUS FLOW		5. Report Date July 1971
		6. Performing Organization Code
7. Author(s) W. A. Stevens, S. H. Goradia, and J. A. Braden		8. Performing Organization Report No. ER-10896
		10. Work Unit No. 737-54-10-01
9. Performing Organization Name and Address Lockheed-Georgia Company Marietta, Georgia		11. Contract or Grant No. NAS1-9143
		13. Type of Report and Period Covered Contractor Report
12. Sponsoring Agency Name and Address National Aeronautics and Space Administration Washington, D. C. 20546		14. Sponsoring Agency Code

15. Supplementary Notes

16. Abstract

A computer program is described which evaluates the aerodynamic characteristics of multiple-component airfoils in subsonic, viscous flows. The number of components is limited to four elements of arbitrary arrangement. The calculated aerodynamic characteristics include pressure distributions, lift, pitching-moment and skin friction drag up to incipient separation on any element. Within the evaluation procedures, a slot-flow analysis technique is included and both ordinary and confluent boundary layers are represented. Correlation of the program output with experimental results is provided.

17. Key Words (Suggested by Author(s)) Two-dimensional airfoil theory, high-lift airfoil theory, airfoil pressure distributions, aerodynamics, airfoil slot-flow, confluent boundary-layer model, multiple-element airfoil theory	18. Distribution Statement Unclassified - Unlimited	
19. Security Classif. (of this report) Unclassified	20. Security Classif. (of this page) Unclassified	21. No. of Pages 187	22. Price* $3.00

FOREWORD

A computer program is described which evaluates the aerodynamic characteristics of multiple-component airfoils in subsonic, viscous flows. The number of components is limited to four elements of arbitrary arrangement. The calculated aerodynamic characteristics include pressure distributions, lift, pitching-moment and skin friction drag up to incipient separation on any element. Within the evaluation procedures, a slot-flow analysis technique is included and both ordinary and confluent boundary-layers are represented. Correlation of the program output with experimental results is provided.

This program was developed under contract to NASA, Langley Research Center and the designated Langley number for the computer program is A2932.

CONTENTS

MATHEMATICAL MODEL FOR TWO-DIMENSIONAL,

MULTI-COMPONENT AIRFOILS IN VISCOUS FLOW

By W. A. Stevens, S. H. Goradia and J. A. Braden
Lockheed-Georgia Company

SUMMARY

This report describes a computerized method for defining the subsonic, viscid, attached flow about two-dimensional, multi-component airfoils. The methods utilize state-of-the-art technology to evaluate all aspects of the flow, combining boundary-layer solutions with inviscid pressure distributions to obtain a complete viscid characterization of the airfoil. The data obtained defines the viscid pressure distribution on the individual elements of the multi-component section, the total normal force, pitching-moment and skin friction drag. The solution has been programmed for either the UNIVAC 1108 or CDC 6600 computer facilities with required inputs of freestream conditions and airfoil geometry only. Both viscid and inviscid pressure distributions, force and moment data as well as detailed boundary-layer characteristics are provided as output. The computerized model, consisting of a number of self-contained subroutines can be used in the elemental modular form or in combination to analyze, design or correlate various viscous flow phenomena or the performance of single- or multi-element airfoils.

The overall problem solution, represented by the data flow diagram of Figure 1, is seen to be composed of the following primary task areas, each requiring mathematical definition in terms of one or more computer subroutines along with the necessary interfacing logic suitable to digital computations:

° Potential flow solution

° Ordinary boundary layer solution

° Confluent boundary layer solution

° Slot-flow analysis

° Combined solution

The inviscid, potential flow solution makes use of the distributed vortex concept with the vortex singularity comprising the fundamental solution to the Laplace equation. The airfoil surface is approximated as a closed polygon with the elements represented by the distributed singularities. Airfoils, arbitrarily arranged and composed of from one to four segments, are defined in this manner. A typical result of the potential flow solution is compared with the classical, exact solution for a Joukowski airfoil in Figure 2.

Permissible airfoil contours are presently limited to smooth, regular shapes with sharp or pointed trailing-edges. There are indications, however, that irregular or sharply-cornered profiles often encountered in flap or slat cove areas, can be reasonably well represented by modest, local refairings. For computer utilization, the multi-component features of the airfoils being represented demands a highly flexible system for input geometric definition emphasizing relative component orientation. Such a system is described which is limited only by the computer facilities available and has general application to a broad range of multi-component configurations.

The ordinary boundary layer solution is comprised of mathematical models representing state-of-the-art technology for laminar, transition and turbulent boundary layers in subsonic flow. The laminar boundary layer model represents the basic approach of Cohen and Reshotko modified as appropriate to computer utilization techniques evolved during the study. Laminar stall criteria, developed during the study, are presented and discussed. Predictions of short or long bubble formation or bubble burst are shown to be in satisfactory agreement with test results on airfoils exhibiting leading-edge or laminar stall. A typical case is provided in Figure 3. The transition model, evolving from the instability criteria of Schlicting and Ulrich, establishes limiting conditions for accurately defining the position of transition on the airfoil. As presently formulated, the program utilizes two separate mathematical models for ordinary turbulent boundary layer development. The first is an approximate model, developed by Goradia along the lines of the Trukenbrodt boundary-layer equations, which is utilized in the initial iterative calculations. The second and more accurate model, reflecting the methods of Nash, portrays the character of the boundary layer in the final, viscid solution. Each of the boundary layer subroutines are validated as separate programs through correlations with experimental data for a wide variety of test conditions and configurations.

A significant feature of the boundary-layer representation is the incorporation of a confluent boundary-layer model reflecting the merging of the upper surface boundary layer with the slot efflux. This model, developed from the experimental and analytical work of Goradia, accounts for the highly complex viscous phenomena associated with slotted airfoils. It is shown that the confluent boundary layer creates an unusually high rate of boundary layer growth downstream of the slot resulting in a greater "uncambering effect" than would be found in the case of ordinary boundary layers. Associated with the confluent boundary layer, a slot-flow model, available in either isolated subroutine or integral program form, is defined with practical limitations on utilization discussed.

The combined viscous solution utilizes an iterative technique to combine the inviscid solution with the boundary layer calculations. The geometry of an "equivalent airfoil", reflecting local boundary layer displacement thicknesses, is successively defined over a variable number of iterations until a stabilized profile and boundary-layer condition is obtained. Comprehensive comparisons of the combined, viscid solution are provided with appropriate experimental data utilizing both single- and multi-element airfoils. Data are

correlated in terms of pressure distributions, force and moment data and boundary-layer characteristics. As shown in Figure 4, good agreement with experimental results are indicated throughout.

The results of the study indicate that the multiple-airfoil program can provide valuable insight into all areas of multi-element airfoil design. A natural framework is provided in which the existing capabilities can readily be extended into the transonic or separated flow problem areas. Specific areas where such extensions and modifications are within the reach of present technology are noted.

FIGURE 1
MULTIPLE AIRFOIL PROGRAM
DATA FLOW
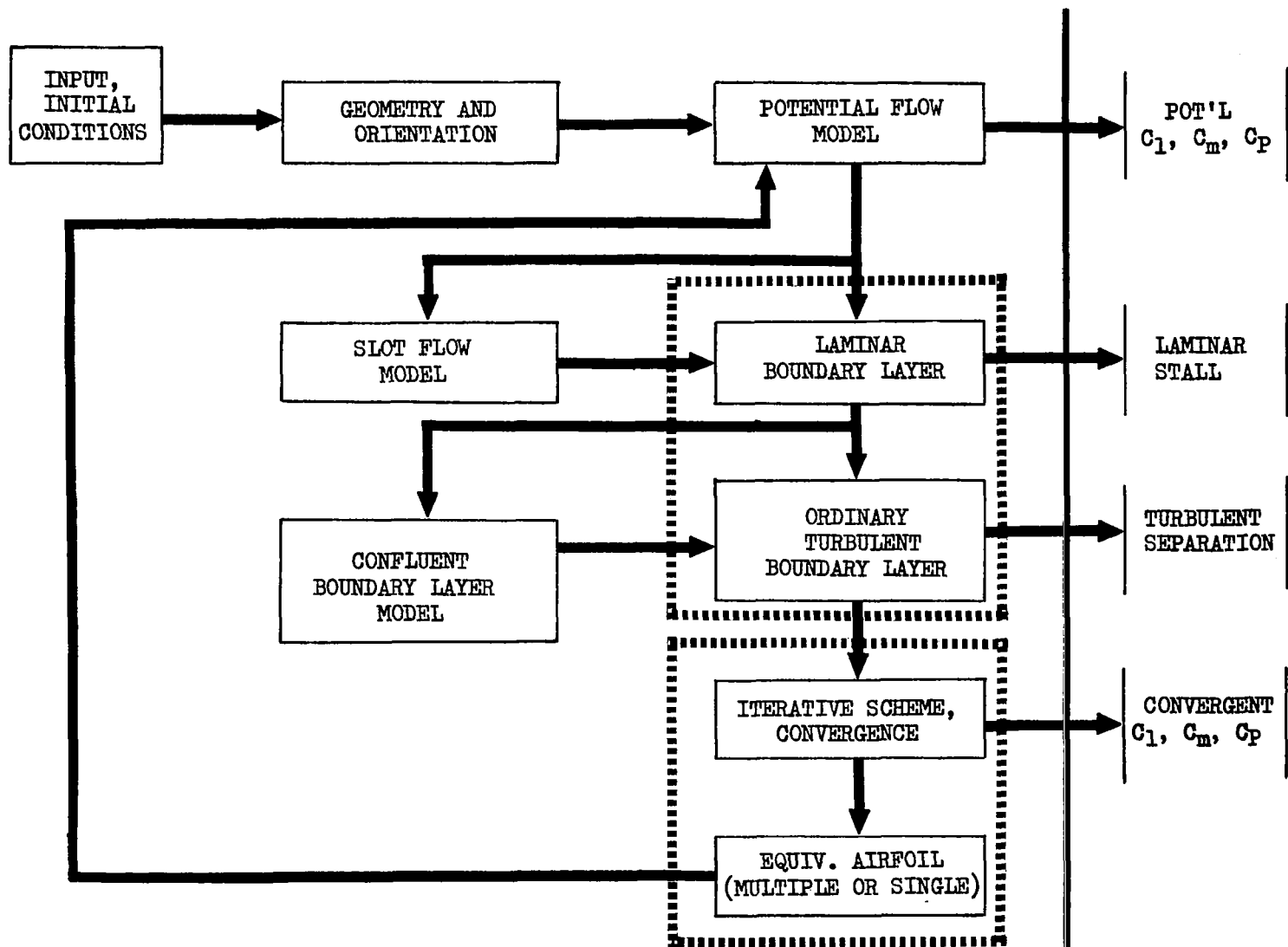
FIGURE 2
COMPARISON OF THEORY AND
EXACT SOLUTION
JOUKOWSKI AIRFOIL
$r = 0.1$
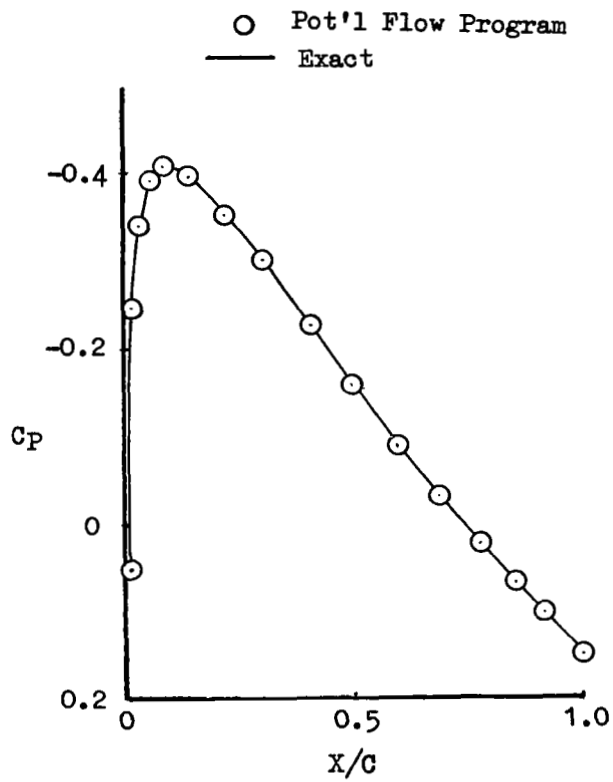
FIGURE 3.-LIFT-CURVE FOR NACA 63_1 - 012 SECTION

$R_N = 5.8 \times 10^6$
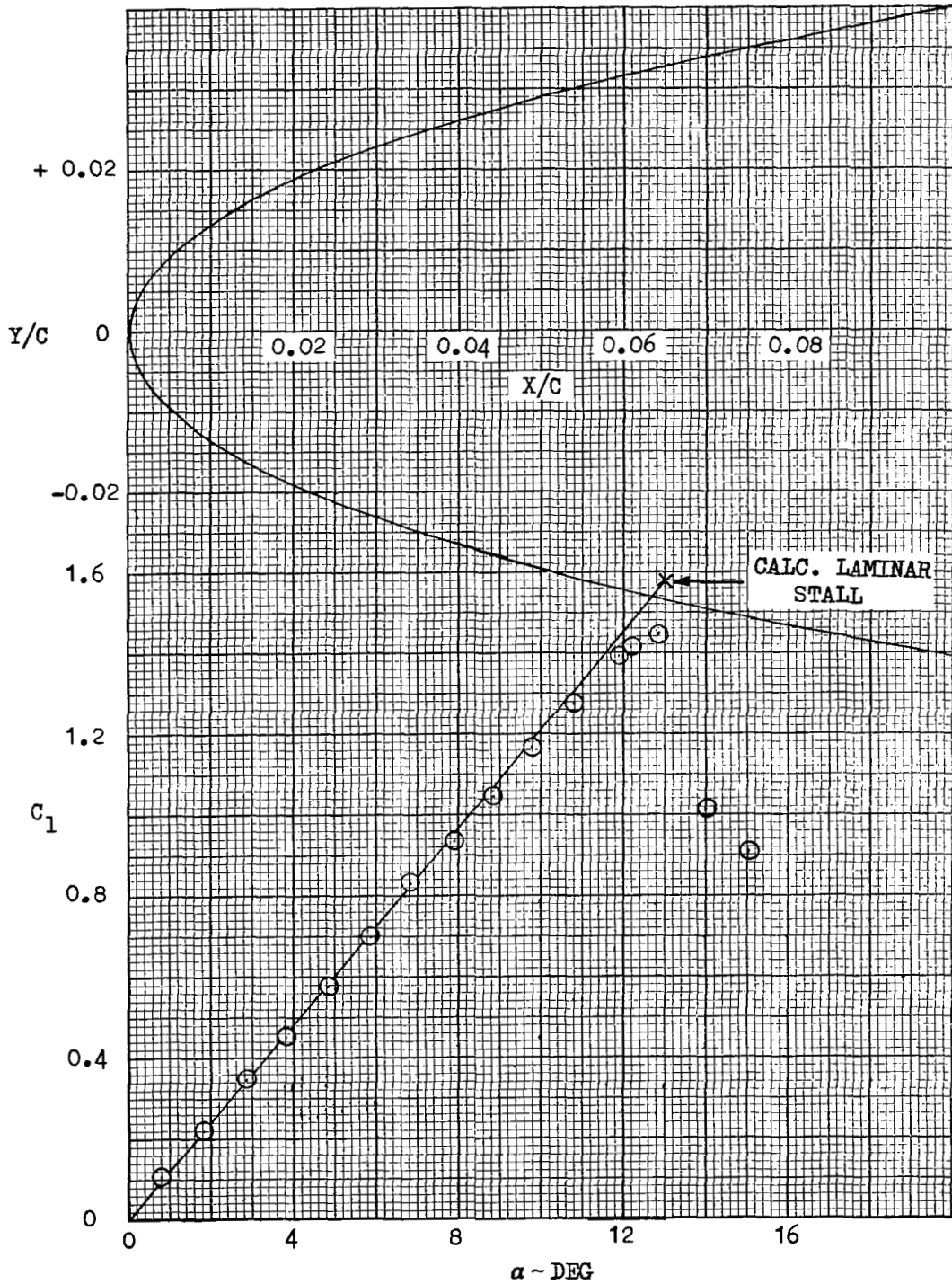
FIGURE 4 — COMPARISON OF EXPERIMENTAL AND PREDICTED PRESSURE DISTRIBUTIONS FOR NACA 4418(MOD.) WITH 35% C.SLOTTED FLAP $M_\infty = 0.19$ $a = 0°$ $\delta_F = 20°$ RN = 2.5 X 10^6
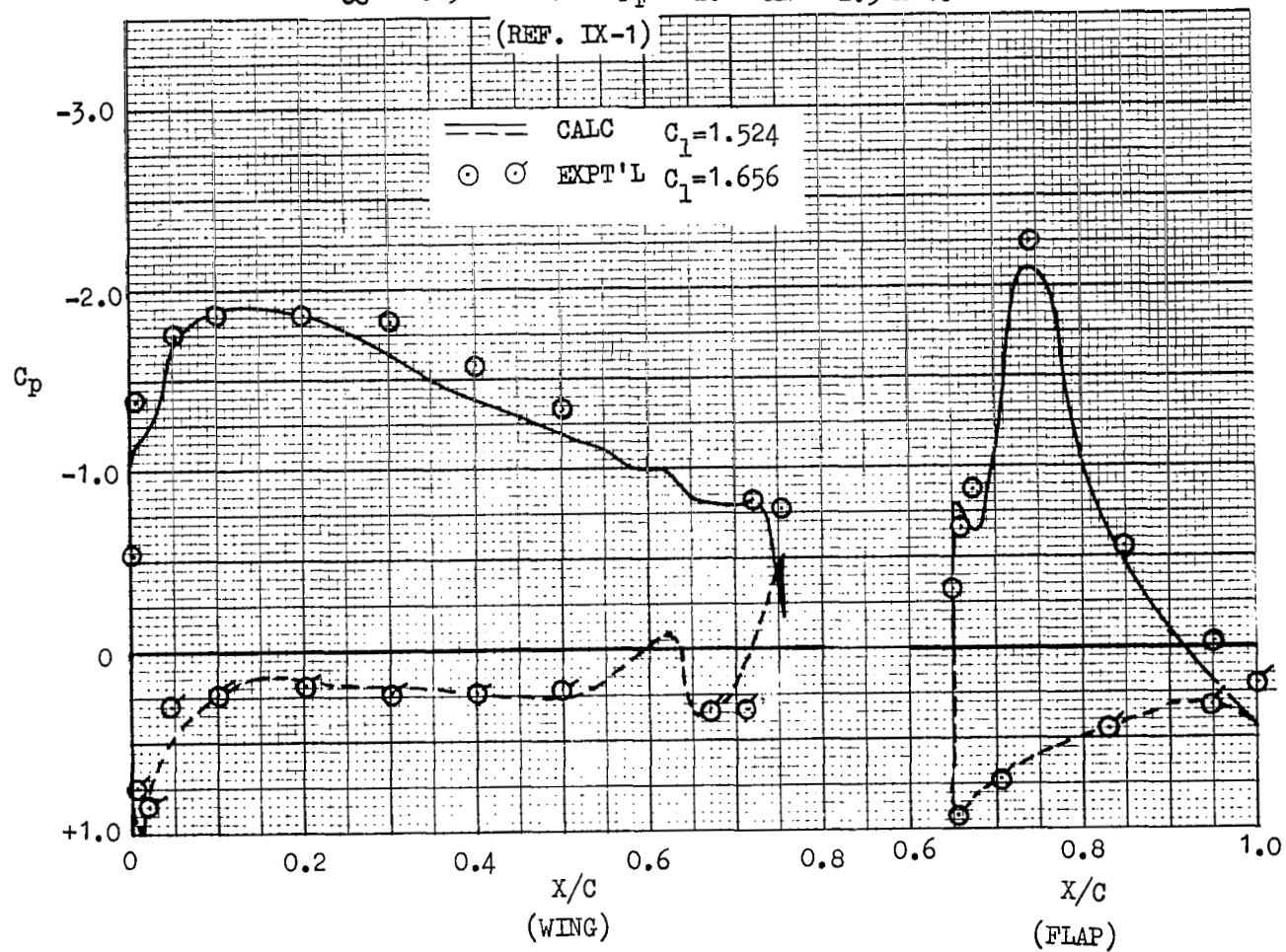
I - INTRODUCTION

Until recently, the design and analysis of high-lift systems for aircraft remained an outstanding example of a "cut and try", empirically-oriented process yielding very reluctantly to a direct analytical attack. Design methods have been based almost entirely on correlation of experimental data which are often questionable, or on the expensive, time-consuming route of wind-tunnel optimizations. Thus, the present-day designer is beset by high expense on one side and high risk on the other.

Present trends toward higher cruise speeds and improved airport performance often produce conflicting cruise and airport requirements which must be addressed at the onset of design activities. Such situations are usually resolved through the incorporation of a highly complex high-lift system. It is a fundamental requirement to three-dimensional high-lift optimization, that the viscous two-dimensional case be amenable to a direct aerodynamic solution; thus, the detailed guidance and fundamental understanding is obtained to knowledgeably approach the finite wing problem. It is to this latter aspect of high-lift design that the work described herein is directed.

Background. - The aerodynamic forces acting on a two-dimensional airfoil are composed of pressure forces normal to the surface and viscous shear forces acting in a tangential direction. Lift and pitching-moment characteristics are, to the first approximation, functions of the pressure forces with drag primarily a function of the viscous forces. While the shear forces are interrelated with the pressure forces through the boundary-layer characteristics, it has been assumed in the past, that these two facets of the flow field can be considered independently. Therefore, airfoil design has relied mainly on potential (inviscid) theory with boundary-layer effects approximated from the theoretical pressures. Hence, the interrelationship between the two has been generally ignored.

No general, mathematically-closed solution presently exists describing the viscid flow-field of an airfoil. Potential flow solutions have long been available to various degrees of sophistication. Additionally, recent advances in boundary layer theory through the work of Nash, Bradshaw, Goradia and others, has provided reasonably accurate models of characteristic behavior. State-of-the-art improvements in these two areas plus the advent of high-speed, high-capacity computers has provided the necessary tools for combining in a practical manner, the potential-flow solution with boundary-layer theory. Use of methods such as the relaxation or iterative schemes have been shown (Reference I-1) to provide significant improvements in prediction accuracies.

The practicality of the iterative method for obtaining combined potential flow and viscous solutions has been demonstrated at Lockheed-Georgia through efforts to improve high-speed airfoil technology. While outstanding high subsonic cruise performance was the principal objective, the techniques developed in this highly successful effort are directly applicable to the single-piece airfoil at low-speeds. A significant portion of this development work was

carried out under contract to the Army Research Organization (Reference I-1) in 1965. An example of the capability developed in this effort is shown in Figure I-1. While not specifically high-lift oriented, it did lay the fundamental ground work, together with the related experience level, necessary to the further extension of the program to the viscous multi-component airfoil case.

In April 1969, in response to a Lockheed-Georgia Company proposal, the National Aeronautics and Space Administration (Langley Field, Virginia), contracted with Lockheed to provide a computer program capable of predicting the viscous aerodynamic characteristics of multi-component airfoils. In accordance with the terms of this contract, the present document is submitted as the Final Technical Report.

Objectives. - The basic objective of the technical effort and the resulting computer program as described herein was to derive a computerized calculation procedure whereby surface pressures would be predicted for viscous, subsonic flows, on airfoils composed of from one to four elements. The scope of the prediction capability is limited to low subsonic ($M_o \leq 0.20$) cases and to those geometries and flow conditions characterizing attached flows. Additionally, force and moment predictions would include normal force, lift and moment coefficients as well as a skin friction drag coefficient. An evaluation of total profile drag is not presently within the scope of the technical effort.

The boundary-layer models utilized for the program encompase the representation of normal laminar, transition and turbulent flow characteristics based upon flat-plate calculation procedures. Thus, roughness and local curvature effects are not represented at the present time.

Included in the overall program objectives is the requirement that the capabilities of the final computer program be demonstrated through correlations of pertinent aerodynamic parameters with available experimental results. The present report includes such correlations with the experimental data selected through mutual agreement with the appropriate NASA personnel. The selection process considered data reliability as well as the scope of the experimental results in providing detailed boundary-layer measurements suitable for correlation. Obviously, data availability in such detail decreases rapidly as the number of airfoil elements increase. In some cases, it has been necessary to select airfoils where the geometries do not completely satisfy the smooth-contouring requirements of the program. In such cases, however, insight is gained as to the effects of minor, local refairing for computer input.

It is believed that the computer program in its present form constitutes a critical first step to the ultimate objective of refined high-lift design. The possibilities for further extending these capabilities along a number of avenues become readily apparent. Section XI of this report considers some of those more significant extensions which can be readily made.

It is believed that the program provides useful and valid information when applied within the scope of the intent.

I - REFERENCES

I-1   Methods for Analysis of Two-Dimensional Airfoils with Subsonic and Transonic Applications, Lockheed-Georgia Report ER-8591, July 21, 1966.

FIGURE I-1

SINGLE AIRFOIL INVISCID SOLUTION IMPROVED BY
INCORPORATION OF VISCOUS EFFECTS
(REFERENCE I-2)

SYMBOL

⊙   EXPERIMENT
⊚   REFERENCE POINT $a = +1.1°$, $C_1 = 0.46$

A —— VISCOUS THEORY   ; $a = +1°$, $C_1 = 0.49$

B - - - - -   { INVISCID THEORY }   APPROX. REF $a = +1°$, $C_1 = 0.75$
C ⊥⊥⊥⊥⊥   APPROX. REF $C_1 = 0.42$, $\iota = -1°$
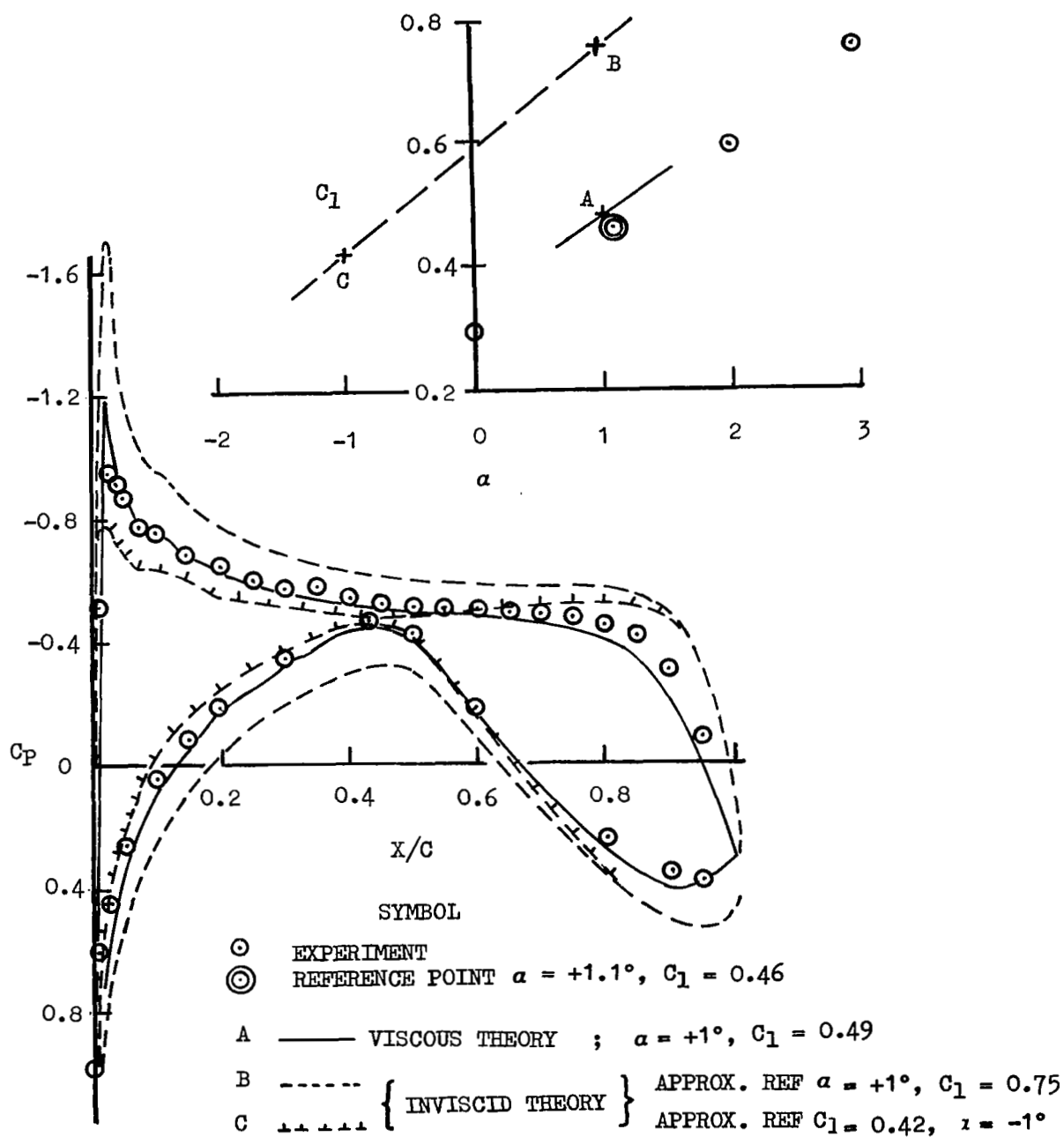
II – PROGRAM FORMULATION

The overall problem of defining the viscous aerodynamic characteristics of two-dimensional airfoils is readily subdivided into the following broad topical areas each requiring precise definition and mathematical formulations for the computer system:

- Geometry definition

- Potential (inviscid) solution

- Boundary-layer characteristics

- Slot-flow characteristics

- Combined (viscid) solution

Figure II-1 shows schematically the calculation sequence by which the final, combined solution is obtained in the present computer program. Also shown on the figure is the breakdown by section in the present report wherein the detailed technical discussions are presented as appropriate to the particular subject noted. In view of the broad range of technical subjects covered in the detailed discussions, reference sources and symbol notations peculiar to each topic are provided in the individual sections. It should be noted that each of these sections comprise separate subroutines in the computer program. These subroutines are each complex analytical models and if used separately can be valuable analysis tools. While the computer program is not formulated to permit this separate usage directly, users should consider such modifications to permit maximum utilization of the complete capabilities of the work described in this report.

The physical or geometric modeling of the complete airfoil, including slats, slots, vanes and flaps obviously requires a highly flexible indexing system ensuring that conventional arrangements of these components are readily adapted to the program. The system for describing these geometric details is presented in Section III. Section IV considers only the potential flow (inviscid) solution for the desired shape through a distributed vortex analysis. Discussions involving boundary-layer characteristics are sub-divided into ordinary turbulent or laminar flow characteristics (Section V) and the special case as a result of a slot, the confluent boundary-layer, (Section VIII). The purely geometric aspects of slot-flow analysis are inherent in the orientation system described in Section III. The aerodynamic considerations for slot-flow are discussed in Section VII.

In defining the "equivalent airfoils" (i.e. actual physical shape as modified by boundary-layer and wake effects), the multi-component case, with the more complex wake pattern, is treated in a somewhat different manner than in the case of the single airfoil. For this reason, separate discussions of the individual approaches are given in Section VI (single-airfoil) and Section IX (multi-component). Section X describes the details of the computer program

in terms of the algorithmic and topographical structural forms of the program. Conclusions drawn and those observations noted during the course of the programming effort, as well as those associated with the correlation analyses, are given in Section XI. This section also provides a summary of the program limitations and discusses those program extensions which can be readily adapted within the existing framework. Customer utilization notes, including input and output format, and program listings are given in a "Supplement to NASA CR-1843", which is available upon request. A request form is included at the back of this paper.

FIGURE II-1
MULTIPLE AIRFOIL PROGRAM
DATA FLOW
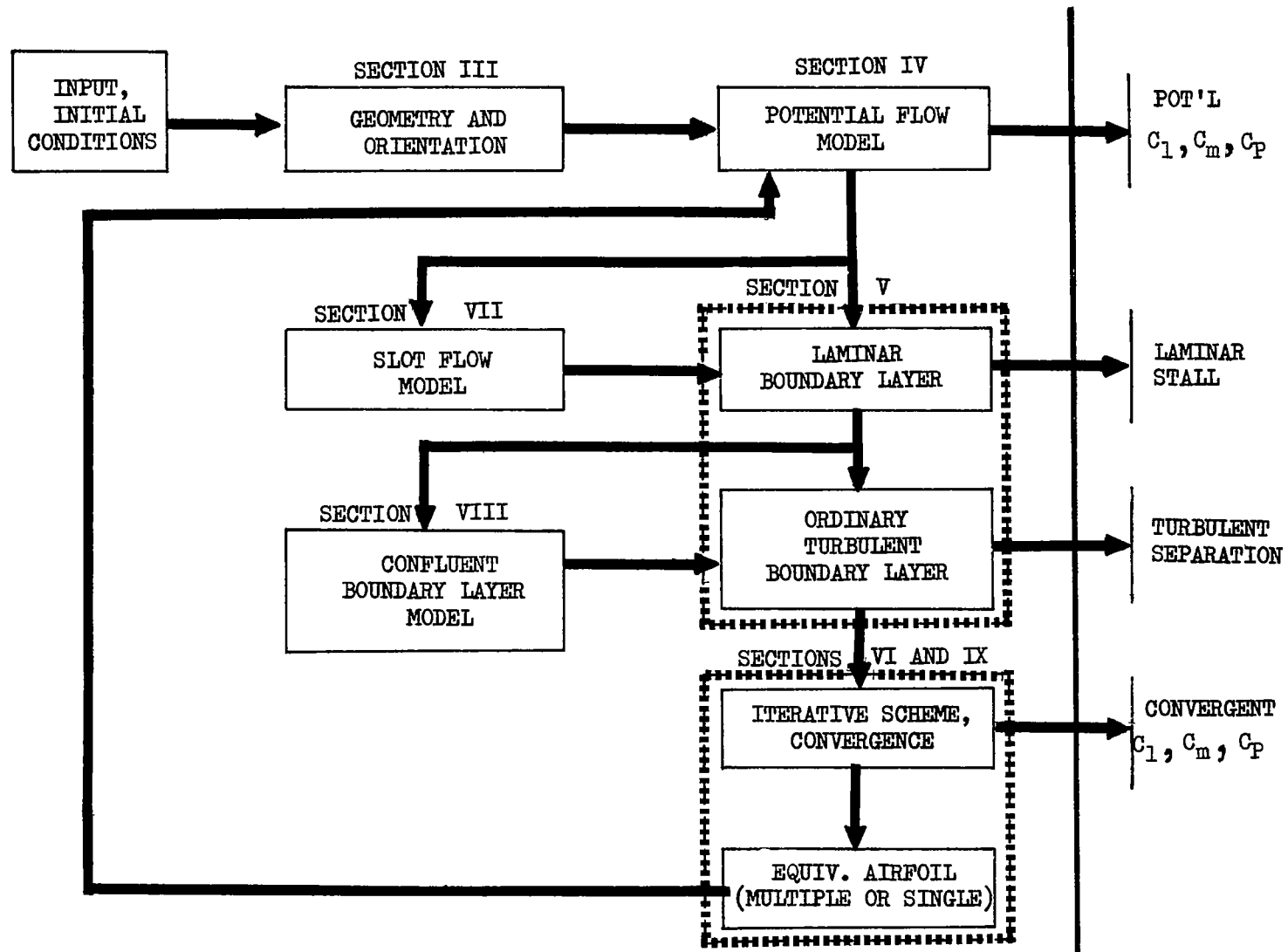
III – GEOMETRY DEFINITION

The basic airfoil geometry is defined by a series of surface coordinates with each component defined in a separate coordinate system. Consider Figure III-1 which illustrates the basic principles of the lofting method. Part (a) illustrates the two components in the separate coordinate systems with a pivot point defined in each system. The first step is to transfer the secondary (flap) system into the primary (main) systems such that the two pivot points become coincident as shown in (b). The secondary component is now rotated through an angle δ_{2-1} about the common pivot point to complete the lofting procedure as in (c).

The pivot point may be defined in several different manners in order to implement different procedures. One example of a convenient definition would be the actual pivot point of the hardware linkage mechanism used to deflect a specific component. Another possible example would be the trailing edge of the fore-component to facilitate the determination of the slot exit area. Other candidates would be the leading edge of the aft-component and the center of curvature for portions of the slot geometry. The primary determining factor in selecting the pivot point is obviously that which most readily adapts to a particular geometric condition requiring an accurate surface definition.

The several features of the lofting procedure of a four-component airfoil are illustrated by Figure III-2. Component 2 is defined as the main or reference component and its coordinate system is the reference coordinate system. Components 1 and 4 are defined as secondary components and are placed in the main system using pivot points A and B respectively. The notations δ_1 and δ_4 are now accomplished in the same manner as δ_{2-1} of Figure III-1. During the translation and rotation of component 4, pivot point C is carried along with the actual surface coordinates. Now the tertiary component (3) can be placed using pivot point C and the appropriate δ_{3-4}. Hence, any component can be placed with respect to any other component as long as one component is defined as the main component and the sequence of placements is defined.

Based on previous experience, a more accurate potential flow solution is generally obtained if the points defining the surface geometry are distributed by

$$\left(\frac{x_i^*}{c_i}\right) = \frac{1}{2}\left[1 + \cos\theta_{i,i}\right]$$

where

$$\theta_{ii} = \frac{i\pi}{N_i}, \quad i = 0, 1, 2 \ldots, 2N_i$$

15

This yields the form of distributions depicted in Figure III-3(a). As shown in this figure, the surface points are grouped near the leading-and trailing-edge of the component which are the regions of rapid change in either geometry or the distribution function for the fundamental solution.

An additional problem is that of determining the proper N_i to allocate the number of available surface points among the components, as seen in Figure III-3(b). The allocation function used herein is

$$N_i = 2\left[\left(\frac{N_{sp} - 21N_c}{4}\right)\frac{c_i}{c_T} + 5\right]$$

where the expression inside the brackets is truncated to the greatest positive integer contained in the result. This function guarantees that each component will be represented by a minimum of 21 surface points and the number of points will be a function of the relative size of the component. Since the bracketed expression is truncated,

$$N_{sp} \geq 2\sum_{i=1}^{N_c} N_i$$

and hence, the additional points are added to the components with the smallest N_i's until

$$N_{sp} = 2\sum_{i=1}^{N_c} N_i$$

The choice of the distribution and allocation functions is rather arbitrary. However, experience gained in using these functions, as formulated, has shown a high degree of success. Therefore, it is recommended that these functions be utilized.

III - SYMBOLS

C_i = Chord of the ith component

$$C_T = \sum_{i=1}^{N_C} C_i$$

N_c = Number of components

N_i = Number of angular increments used in defining a surface of the ith components

N_{SP} = Total number of surface points to be used in defining the airfoil

X_j^* = The distance along the chord, from the nose of the component, to the jth point

δ_{i-J} = The deflection of the ith component with respect to the Jth component.

$\theta_{i,J}$ = The angular distribution function

17

FIGURE III-1.- MULTIPLE AIRFOIL GEOMETRY DEFINITION

(a)

(b)

(c)
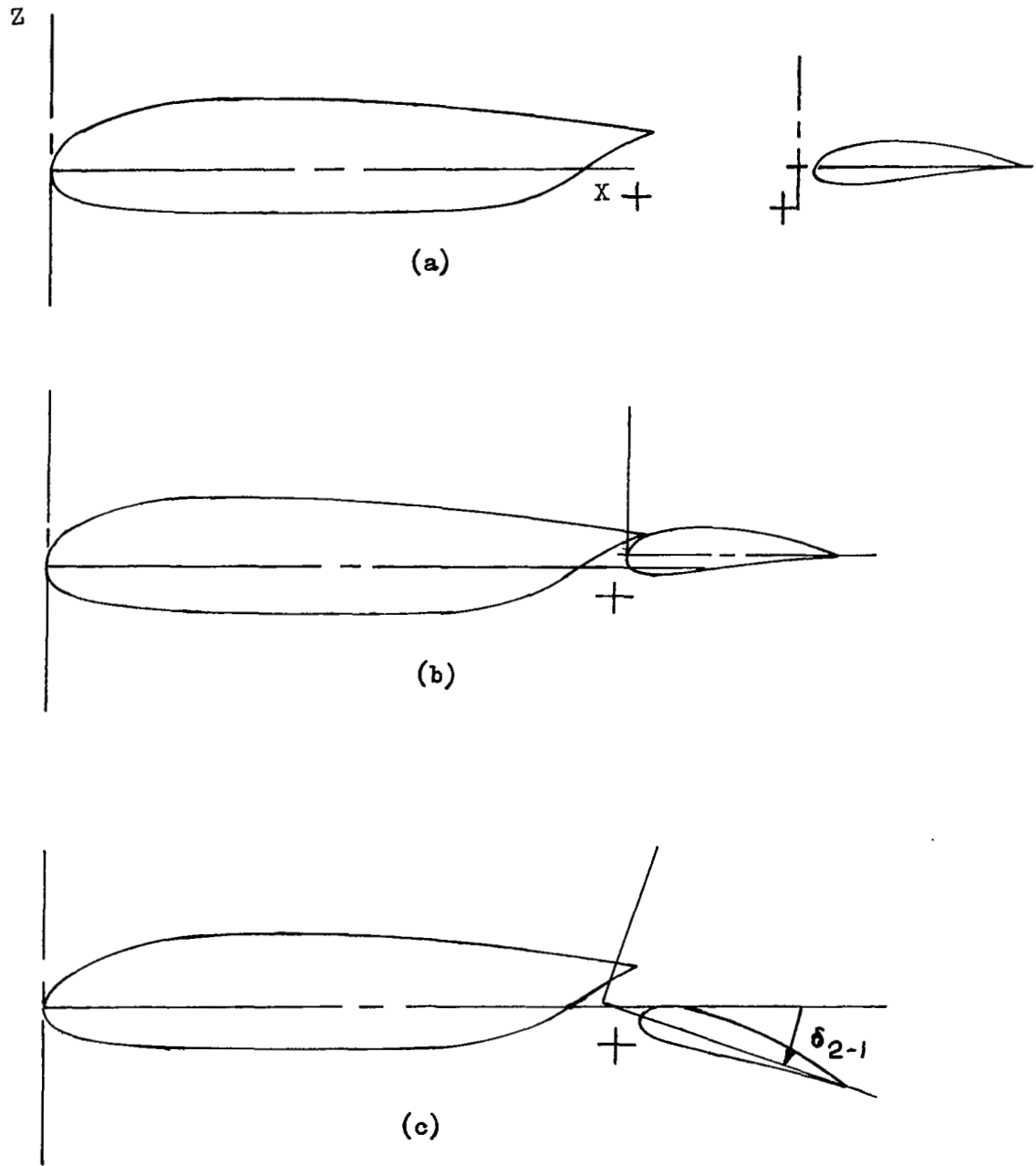
FIGURE III-2 .- LOFTING OF A FOUR-COMPONENT AIRFOIL

COMPONENT 1

COMPONENT 2

COMPONENT 3

COMPONENT 4
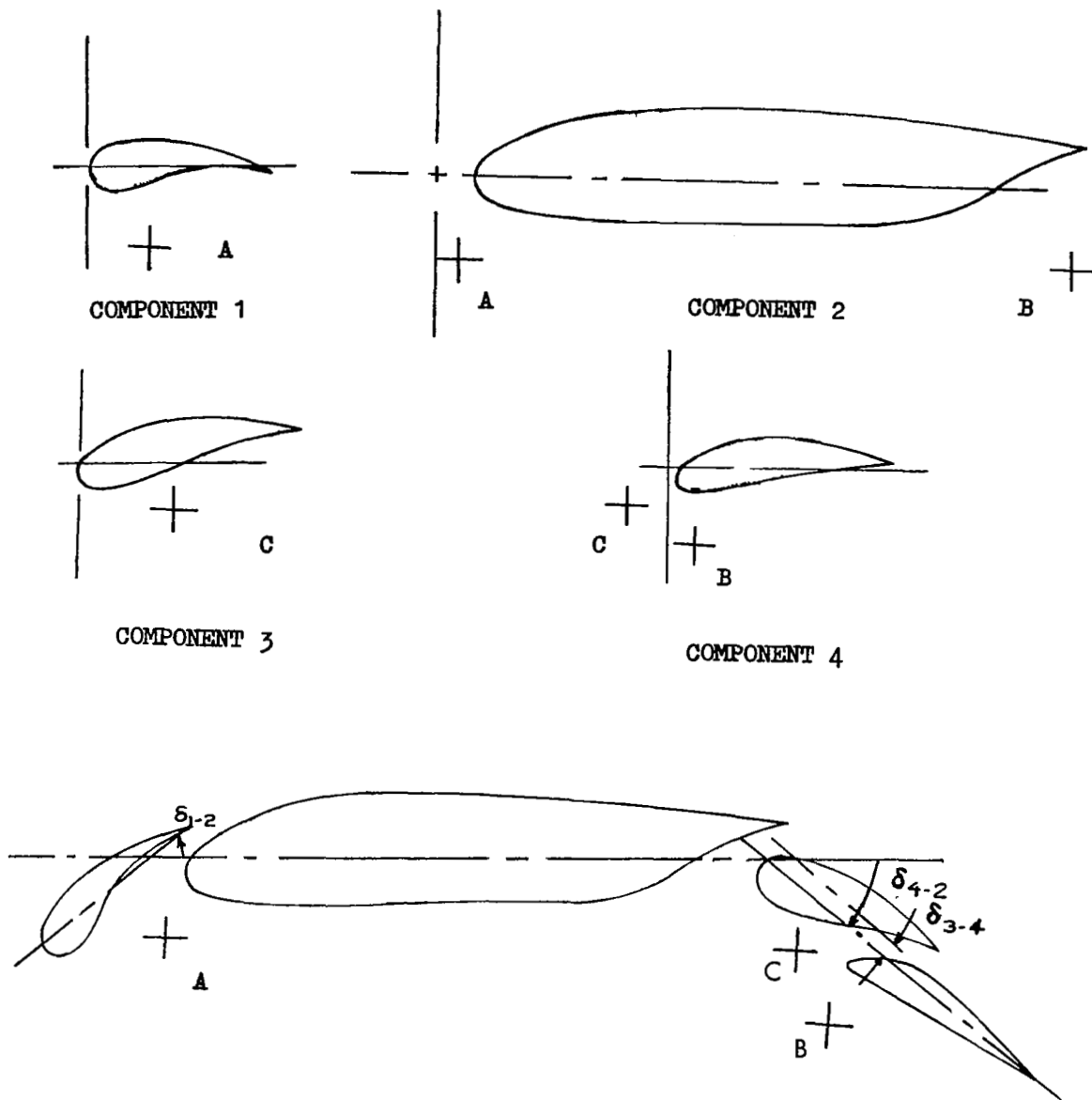
FIGURE III-3.-ILLUSTRATION OF THE DISTRIBUTION AND
ALLOCATION FUNCTIONS

$N_i = 6$

(a)

$N_C = 2$ $N_{S.P.} = 80$

$N_1 = 22$ $N_2 = 18$
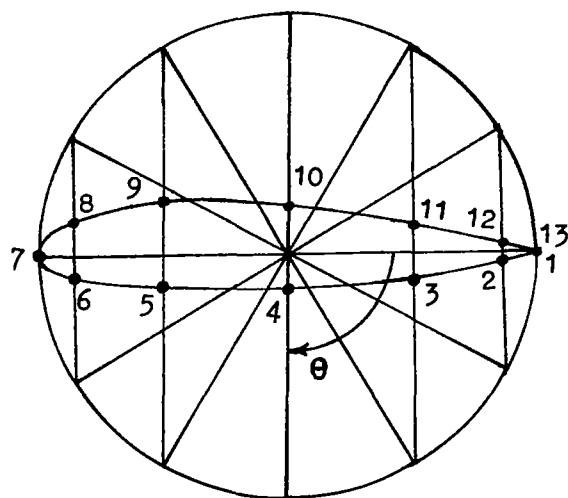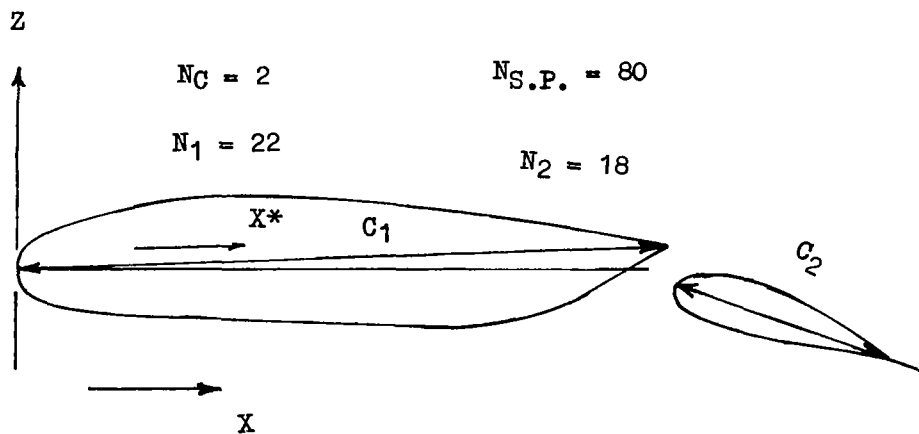
(b)

IV - POTENTIAL FLOW SOLUTION

The potential flow problem is approached by using the vortex singularity as the fundamental solution to the Laplace equation. A slight manipulation of the potential function of a vortex singularity yields the two-dimensional Biot-Savart law:

$$V = \frac{\gamma}{2\pi r} \tag{IV-1}$$

This is modified to a singularity distribution form

$$\vec{V} = \frac{1}{2\pi} \oint_c \frac{\gamma(s)\,\vec{r} \times ds}{r^2} \tag{IV-2}$$

The airfoil is approximated by a closed polygon, as illustrated in Figure IV-1, allowing the Biot-Savart integration to be accomplished. The assumption is made that the surface can be replaced by a distribution of singularities as depicted in Figure IV-2. The form of the singularity distribution is assumed to be linear and continuous at the polygon corners. Thus, the velocity induced at a point is

$$\vec{V} = \frac{1}{2\pi} \sum_{i=1}^{2N} \int_{s_i}^{s_{i+1}} \gamma(s) \frac{\vec{r} \times d\vec{s}}{r^2} \tag{IV-3}$$

which can be integrated to yield an equation of the form:

$$V_{n_i} = \frac{1}{2\pi} \sum_{j=1}^{2N+1} A_{n_{i,j}} \gamma_j \tag{IV-4}$$

The velocity, normal to the surface of the airfoil, induced by the vortex distirbution is:

$$V_n = \vec{V} \cdot \vec{n} = \frac{1}{2\pi} \sum_{j=1}^{2N+1} A_{n_i} \gamma_j \tag{IV-5}$$

or at some point

$$V_{n_i} = \frac{1}{2\pi} \sum_{j=1}^{2N+1} A_{n_{i,j}} \gamma_j \tag{IV-6}$$

Simultaneously, the normal component of the freestream velocity is

$$V_{n_{\infty i}} = V_\infty \left[\cos\alpha\, \vec{i} + \sin\alpha\, \vec{k} \right] \cdot \vec{n}_i \tag{IV-7}$$

21

Combining these two relations in matrix form gives:

$$V_{n_\infty} = \frac{1}{2\pi}\left[A_n\right]\left[\gamma\right] \qquad \text{(IV-8)}$$

which specifies no flow across the surface at the "i" control points. These steps lead to one less control point than end points thus necessitating one additional equation. This equation is the well-known Kutta condition which is written as

$$\gamma_1 = -\gamma_{2N+1} \qquad \text{(IV-9)}$$

Upon the inclusion of this relation, the solution is found to be

$$\left[\frac{\gamma}{V_\infty}\right] = 2\pi\left[A_n\right]^{-1}\left[\frac{V_{n_\infty}}{V_\infty}\right] \qquad \text{(IV-10)}$$

To illustrate the manner in which the influence coefficients, $A_{n_{i,j}}$, are determined, Figure IV-2 shows a typical plate and control point combination; positive directions are as shown. To simplify the expressions, the variables "r" and "s" are defined as follows: The distribution of vortex strength along the surface is assumed to be linear with respect to surface lengths, or,

$$\gamma(s) = \gamma_i + \frac{(\gamma_{i+1} - \gamma_i)s}{l_i} \qquad \text{(IV-11)}$$

Similarly, the surface coordinates are

$$x(s) = x_i + \frac{(x_{i+1} - x_i)s}{l_i}$$

$$z(s) = z_i + \frac{(z_{i+1} - z_i)s}{l_i} \qquad \text{(IV-12)}$$

The distance between the surface and the control point can be written as

$$r^2 = a + bs + cs^2 \qquad \text{(IV-13)}$$

where

$$a_i = (x_{c_i} - x_i)^2 + (z_{c_i} - z_i)^2$$

$$b_i = -\frac{2}{l_i}\left[(x_{c_i} - x_i)(x_{i+1} - x_i) + (z_{c_i} - z_i)(z_{i+1} - z_i)\right] \qquad \text{(IV-14)}$$

and

$$c_i = 1.0$$

Substituting these expressions into Equation (IV-3) results in:

$$\vec{V}_{ij} = \frac{1}{2\pi l_i} \left[\gamma_i (l_{1_{i,i}} \vec{i} - l_{3_{i,i}} \vec{i}) + \gamma_{i+1}(l_{2_{i,i}} \vec{i} - l_{4_{i,i}} \vec{i}) \right] \qquad (IV-15)$$

where

$$l_{1_{i,i}} = \int_0^l \left\{ l_i(z_{c_i} - z_i) - \left[(z_{i+1} - z_i) + (z_{c_i} - z_i) \right] s + \frac{(z_{i+1} - z_i)s^2}{l_i} \right\} \frac{ds}{r^2}$$

$$l_{2_{i,i}} = \int_0^l \frac{\left\{ (z_{c_i} - z_i)s - \left(\frac{z_{i+1} - z_i}{l_i} \right) s^2 \right\}}{a + bs + cs^2} ds$$

$$l_{3_{i,i}} = \int_0^l \left\{ l_i(x_{c_i} - x_i) - \left[(x_{i+1} - x_i) + (x_{c_i} - x_i) \right] s + \left(\frac{x_{i+1} - x_i}{l_i} \right) s^2 \right\} \frac{ds}{r^2} \qquad (IV-16)$$

$$l_{4_{i,i}} = \int_0^l \frac{(x_{c_i} - x_i)s - \left(\frac{x_{i+1} - x_i}{l_i} \right) s^2}{a + bs + cs^2} ds$$

In order to evaluate these four integrals, the following three forms are required:

$$I' = \int_0^l \frac{ds}{a + bs + s^2} = \frac{2}{\sqrt{4a - b^2}} \tan^{-1}\left(\frac{l\sqrt{4a - b^2}}{2a + lb} \right)$$

and

$$I'' = \int_0^l \frac{sds}{a + bs + s^2} = \frac{1}{2} \ln\left(\frac{a + bl + l^2}{a} \right) - \frac{b}{2} I' \qquad (IV-17)$$

$$I''' = \int_0^l \frac{s^2 ds}{a + bs + s^2} = 1 - \frac{b}{2} \ln\left(\frac{a + bl + l^2}{a} \right) + \frac{b^2 - 2a}{2} I'$$

Comparing these results with the form of Equation (IV-4), it can be seen that

$$\vec{A}_{i,j} = l_{2_{i,j-1}} \vec{i} - l_{4_{i,j-1}} \vec{i} + l_{1_{i,i}} \vec{i} - l_{3_{i,i}} \vec{i} \qquad (IV-18)$$

where the first term is zero for j = 1 and the last term is zero for j = 2N + 1.

In utilizing the foregoing procedure, the possibility of computational difficulties under special geometric conditions should be considered. Considering the logarithm term which appears in I'' and I''' and Equation (IV-8), it can be seen that the argument of the logarithm is the ratio of the squares of the radii from the two ends of the plate to the control point in question. Hence the argument is positive definite and can be neither zero nor infinite.

Next, consider the term, q , defined by

$$q = 4a - b^2 \qquad\qquad (IV-19)$$

which appears as a square root in Equation (IV-14). This implies that q must be positive definite in order to avoid imaginary or complex influence coefficients. Substituting Equations (IV-9) and (IV-10) into q to obtain

$$q = \frac{4}{l^2}\left[(x_{c_i} - x_i)(z_{i+1} - z_i) - (z_{c_i} - z_i)(x_{i+1} - x_i)\right]^2 \qquad (IV-20)$$

which implies that q is positive definite. Note that q also appears in the denominator of Equation (IV-14) and hence the limit as q approaches zero must be considered.

$$\lim_{q \to 0} I' = 2 \lim_{q \to 0} \frac{1}{\sqrt{q}} \tan^{-1}\left[\frac{l\sqrt{q}}{2a + lb}\right] \qquad (IV-21)$$

Apply L'Hospital's rule to obtain

$$\lim_{q \to 0} I' = \frac{2l}{2a + lb} \qquad\qquad (IV-22)$$

which is the limit expression for q . The physical implication of q going to zero can be evaluated by examining Equation (IV-22). Setting $q = 0$ yields

$$\frac{z_{c_i} - z_i}{x_{c_i} - x_i} = \frac{z_{i+1} - z_i}{x_{i+1} - x_i} \qquad\qquad (IV-23)$$

which implies that the control point is colinear with the vortex sheet which is inducing the flow. However, the control point does not lie on the surface of the sheet.

Finally, consider the case of the control point lying on the surface of the vortex sheet. In this case, the induced velocity is normal to the sheet itself by the nature of a vortex singularity. Therefore, writing the Biot-Savart law as

$$V = \frac{1}{2\pi} \int_0^l \frac{\gamma ds}{r}$$

where

$$r = s - s_c \qquad (IV\text{-}24)$$

and

$$\gamma = \gamma_i + \frac{1}{l}(\gamma_{i+1} - \gamma_i)s$$

Integrate to obtain

$$V = \frac{1}{2\pi} \ln\left(\frac{l - s_c}{s_c}\right)\left[\frac{\gamma_i(l - s_c) + \gamma_{i+1} s_c}{l}\right] - \frac{\gamma_i - \gamma_{i+1}}{2\pi}$$

where $\qquad\qquad\qquad\qquad\qquad\qquad\qquad\qquad\qquad\qquad\qquad (IV\text{-}25)$

$$s_c = \frac{l}{2}$$

This gives the magnitude of the induced velocity and the direction is given by

$$\overline{e} = \frac{-(z_{i+1} - z_i)\vec{i} + (x_{i+1} - x_i)\vec{i}}{\left[(x_{i+1} - x_i)^2 + (z_{i+1} - z_i)^2\right]^{1/2}} \qquad (IV\text{-}26)$$

which is the unit normal vector to the vortex distribution. However, the influence coefficient is the normal velocity and hence is given by Equation (IV-25).

On additional problem is possible if the influence coefficient matrix is used exactly as presented. When the trailing edge region of the airfoil approaches a cusp, the effects of the first and last vortices tend to become identical. The result of this approach to coincidence is that the matrix tends to become singular. In an effort to avoid this difficulty, consider the Kutta condition for a lifting body. The implication is that the circulation at the trailing edge must be zero. Under these circumstances, it is apparent that the value of the influence coefficients for these vortices can be arbitrarily altered with no significant effect on the proper solution. Hence, the influence coefficients in the upper half of the matrix in the $A_{i,N}$ position are chosen to be $\frac{1}{4\pi}$ and the lower half matrix coefficients in the $A_{i,1}$ position are chosen to be $-\frac{1}{4\pi}$. This arbitrary choice removes the singular nature of the matrix and further can be applied in all cases with no difficulty. However, if an airfoil is cusped and N is chosen large, the 1st and $(N-1)^{th}$ control points tend to experience the same effects causing an approach to singularity in the first and last rows of the influence coefficients. An actual limiting value of N is unknown at the present time. It is recommended that $N \leq 65$.

Considering Equation (IV-21) again, the solution yields a vortex distribution which allows no flow through the surface at the i-control points (x_{c_i}, z_{c_i}). It can easily be shown for a closed surface that the surface velocity distribution is then

$$\frac{V}{V_\infty} = \left|\frac{\gamma}{V_\infty}\right| \qquad \text{(IV-27)}$$

and hence the surface pressure coefficient for incompressible flow is given as

$$c_p = 1 - \left(\frac{\gamma}{V_\infty}\right)^2 \qquad \text{(IV-28)}$$

Results representing this solution are compared with classically exact solutions to four incompressible cases in Figure IV-3. Note that in the case of the Joukowsky airfoil, a non-zero velocity is shown at the trailing edge. This result is obtained by applying the mean value of the upper and lower surface velocities from the point preceding the trailing edge, as the trailing edge velocity.

To represent the effects of compressibility, the Karman-Tsien correction law is employed. From the velocity transformation, the parameter, λ, is defined as

$$\lambda = \frac{M_\infty^2}{\left(1 + \sqrt{1 - M_\infty^2}\right)^2} \qquad \text{(IV-29)}$$

Then, the compressible velocity ratio is given by:

$$\left(\frac{V}{V_\infty}\right)_{comp} = \frac{\left(\frac{V}{V_\infty}\right)_{inc}(1 - \lambda)}{1 - \lambda\left(\frac{V}{V_\infty}\right)^2_{inc}} \qquad \text{(IV-30)}$$

Using the isentropic flow relations, the local Mach number and pressure coefficients are given as

$$M_l = \frac{M_\infty\left(\frac{V}{V_\infty}\right)_{comp}}{\left\{1 + \left(\frac{k-1}{2}\right)M_\infty^2\left[1 - \left(\frac{V}{V_\infty}\right)^2_{comp}\right]\right\}^{1/2}} \qquad \text{(IV-31)}$$

and

$$c_p = \frac{2}{kM_\infty^2}\left\{\left[1 + \frac{(k-1)}{2}M_\infty^2\left(1 - \left[\frac{V}{V_\infty}\right]^2_{comp}\right)\right]^{\frac{k}{k-1}} - 1\right\} \qquad \text{(IV-32)}$$

$A_{i,j}$	Influence coefficient matrix elements
a, b	Coefficients in $r^2 = a + bs + s^2$
C_p	Pressure coefficients
I', I'', I'''	Fundamental integral forms
I_1, I_2, I_3, I_4	Integrals used in the influence coefficient
k	Specific heat ratio (1.4)
l_j	Length of the jth polygon plate
M	Mach number
N	$2N + 1$ polygon points on the surface of the airfoil
n	Unit normal vector
q	$4a - b^2$
r	Radius from the vortex to the control point
S	Surface distance
V	Velocity
(x_j, z_j)	Ordinates of the jth polygon corner
(x_{c_i}, z_{c_i})	Ordinates of the ith control point
α	Angle of attack
γ	Vortex strength
λ	Karman-Tsien compressibility factor,

Subscripts

i, j	plate indices
ℓ	local value

n	Normal component (positive outward)
∞	Freestream conditions
inc	Incompressible value

FIGURE IV-1.- AIRFOIL REPRESENTATION

(a) AIRFOIL APPROXIMATION BY POLYGON
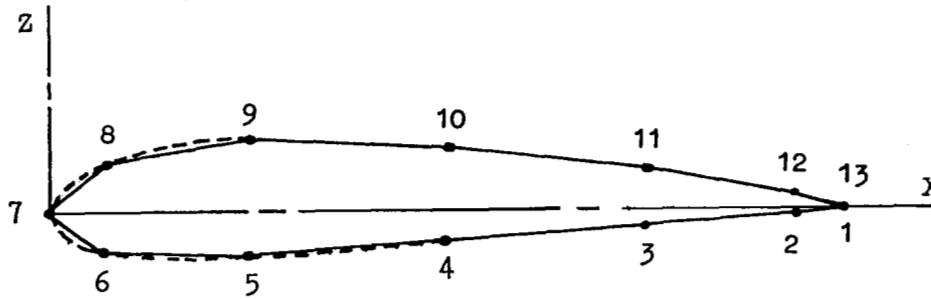
(b) VORTEX REPRESENTATION OF THE AIRFOIL
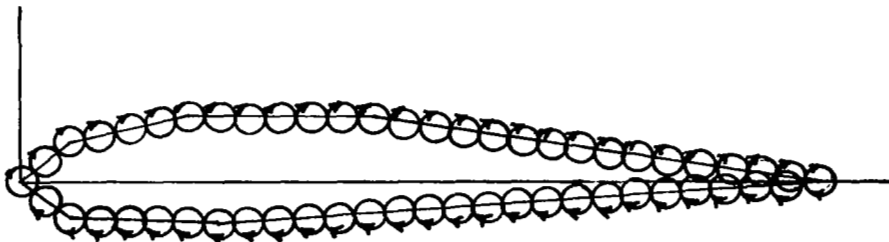
FIGURE IV - 2
DEFINITION OF POSITIVE DIRECTIONS AND
VARIABLES
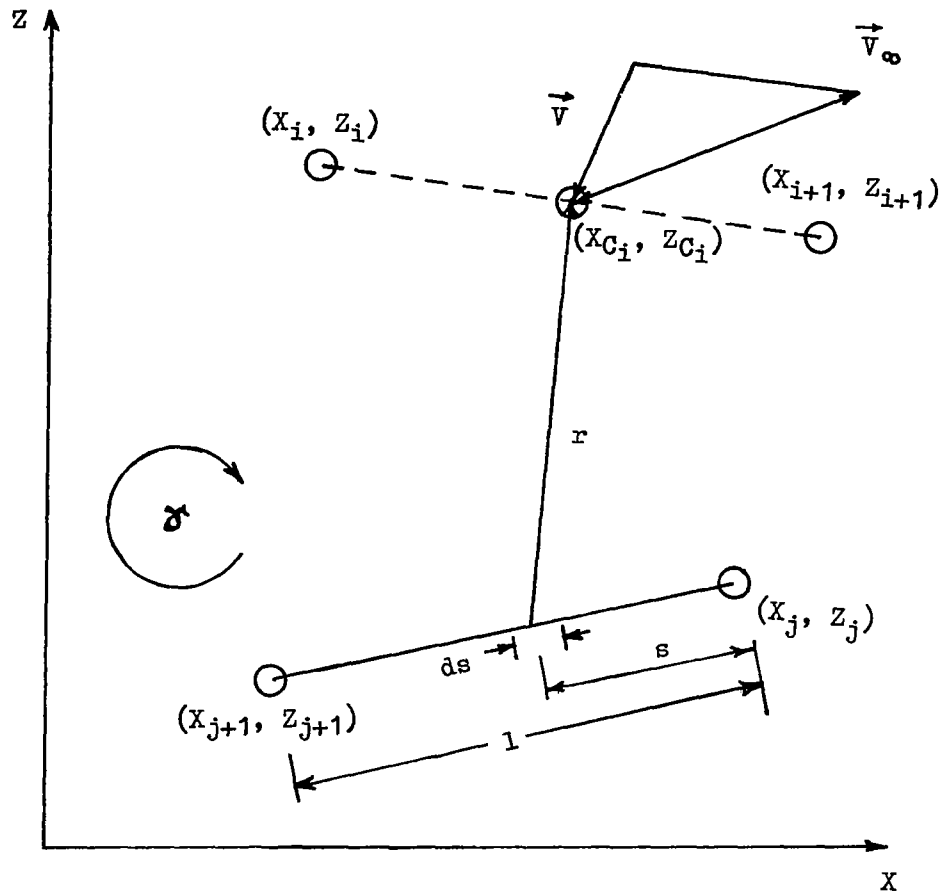
FIGURE IV - 3
COMPARISON OF THEORY AND EXACT SOLUTIONS
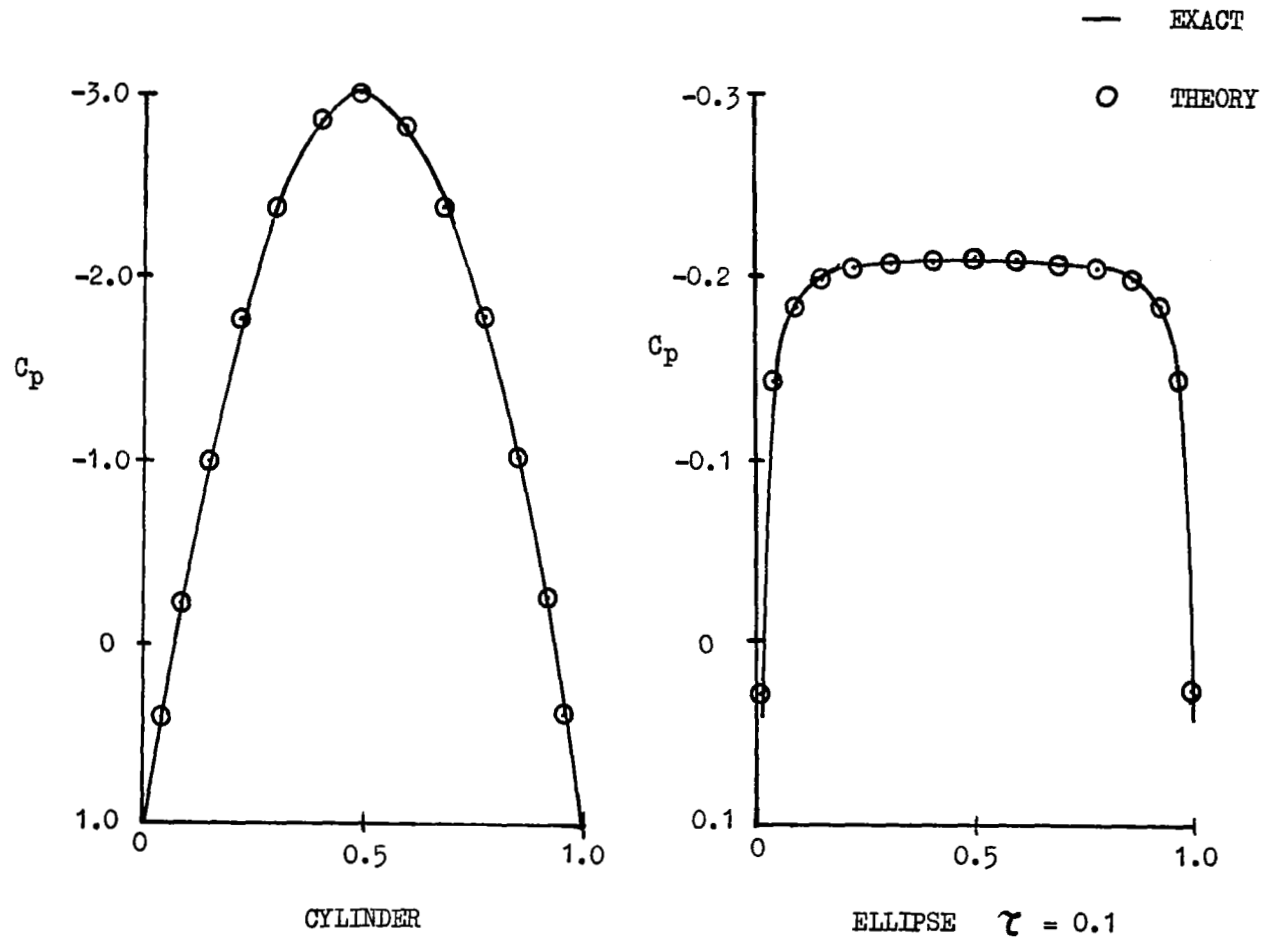
FIGURE IV-3 (CONCLUDED)
COMPARISON OF THEORY AND EXACT SOLUTIONS(CONTINUED)

BICONVEX $\tau = 0.1$ JOUKOWSKI $\tau = 0.1$
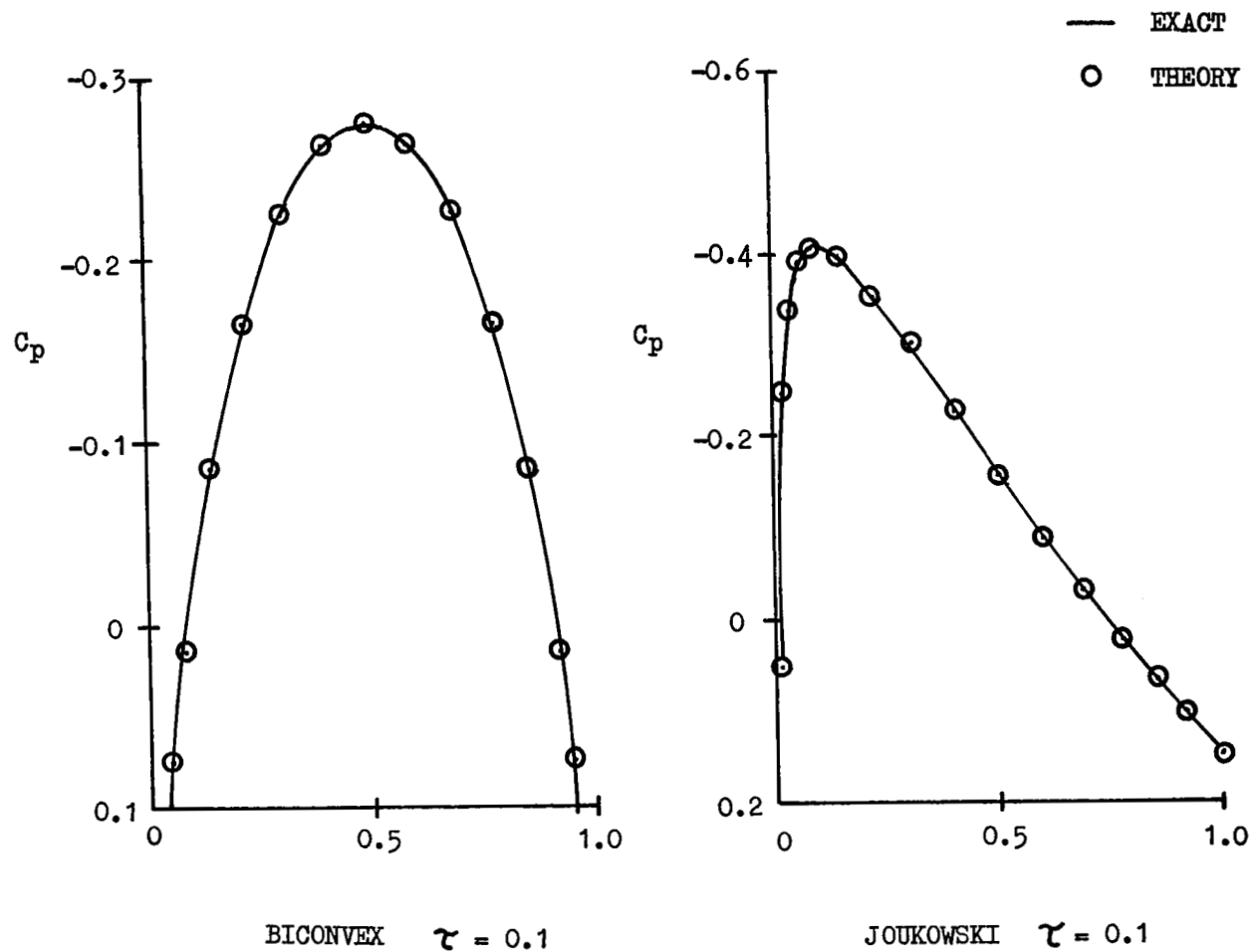
V - ORDINARY BOUNDARY LAYER

The approach selected in accounting for the effects of viscosity is that
of altering the physical geometry of the airfoil to account for the boundary
layer influence. This results in an "equivalent" airfoil upon which the per-
formance of the system is based. It has been found that the displacement thick-
ness, δ^*, is the parameter of prime importance. Therefore, this parameter, the
momentum thickness Θ, form factor H (separation), and C_f (friction drag) are
the parameters to be calculated.

In determining the development of the boundary layer, the basic assump-
tions are made that the influence of viscosity is confined to a relatively thin
fluid layer near the surface of the airfoil, and that the "law-of-the-wall"
applies. The required calculations for the boundary layer for the case of the
single-component airfoil can be divided into three categories:

1. Laminar boundary layer and the formation of short bubbles or long
   bubbles leading to laminar stall.

2. Transition region.

3. Turbulent boundary calculations.

In the paragraphs which follow, the theory for each of the above is
described and the correlation of the calculated parameters with experiments
are presented. For the turbulent boundary layer, two separate math models
are formulated with both a refined and approximate calculation represented.
The derivation and purpose of each are described in the present section. In
the case of multi-component airfoils, calculations must also be performed
for a confluent boundary layer which can be present over the major portion
of the upper surfaces. This is discussed in Section VIII.

Laminar Boundary Layer. - An accurate determination of the laminar
boundary layer from the stagnation point to the beginning of transition is
necessary in order to predict the point of transition and also for the predic-
tion of laminar stall for single component airfoils or for the leading element
of the multi-component section. Further, this determination is needed to
compute the contribution of laminar skin friction drag as well as the determi-
nation of an equivalent airfoil shape up to the beginning of transition. For
the purposes of the present application, the meaningful quantities are the
momentum thickness Θ, displacement thickness δ^*, the form factor H, the skin

friction coefficient C_f and the local Reynold's number based on the momentum thickness Re_θ. These quantities are required for evaluating flow conditions and characteristics consistent with the problem definition - two-dimensional steady-state flow about an airfoil.

The development of theory and equations for the laminar boundary layer calculations used in this report is outlined in detail in Reference V-1. Hence, only the principal equations and theory for laminar boundary layer calculations will be summarized here. Reference V-1 also contains a comprehensive bibliography of theoretical boundary layer development pertinent to the present work.

The Stewartson's transformation is used to convert the ordinates from the physical plane into the compressible plane and vice versa. Thus

$$x = \int_0^\zeta \lambda \frac{a_e\, p_e}{a_o\, p_o}\, d\zeta \quad ; \quad Y = \frac{a_e}{a_o} \int_0^\xi \frac{\rho}{\rho_o}\, d\xi \tag{V-1}$$

The interpolation formula for viscosity is used, based on D. M. Sutherland's theory which is

$$\frac{\mu}{\mu_o} = \left(\frac{T}{T_o}\right)^{3/2} \frac{T_o + K_{su}}{T + K_{su}} \tag{V-2}$$

where μ_o = viscosity at stagnation temperature T_o

and $K_{su} = 198^\circ R$.

The use of Stewartson's transformation gives the following relationship between the quantities in the physical plane and the transformed or compressible plane.

$$U_e = \frac{a_o}{a_e} U_e \qquad \theta_{tr} = \frac{p_e}{p_o} \frac{a_o}{a_e} \theta \qquad H = H_{tr} \left(1 + \sqrt{Pr}\, \frac{\gamma - 1}{2} M_e^2\right) \tag{V-3}$$

The following definitions are introduced.

$$n = -\frac{\partial U_e}{\partial x} \left(\frac{\theta_{tr}^2}{\nu_o}\right) \qquad \ell = \frac{\theta_{tr}}{U_e} \left(\frac{\partial U}{\partial Y}\right)_w \qquad S_w = \frac{T_w}{T_o} - 1 \tag{V-4}$$

where n is defined as the correlation number and ℓ is defined as the shear parameter.

The following momentum integral equation in the transformed plane can be derived in the usual manner:

$$\frac{d\,\theta_{tr}}{dx} + \frac{\partial U_e}{\partial x}\frac{(2\theta_{tr} + \delta^*_{tr})}{U_e} = \frac{\nu_o}{U_e^2}\frac{\partial U_w}{\partial Y} \tag{V-5}$$

After substituting definition (V-4) into (V-5), the following equation can be obtained:

$$-U_e\frac{d}{dx}\left(\frac{n}{\dfrac{\partial U_e}{\partial x}}\right) = 2\left[n(H_{tr} + 2) + \ell\right] \tag{V-6}$$

$$= N(n, S_w)$$

From the results of the similar solutions by Cohen and Reshotko (References V-2 and V-3), the functional relationships between correlation number and momentum parameter, and correlation number and shear parameter are calculated. These relations are shown in Figures V-1 and V-2. The solution for local correlation number, and hence for momentum thickness, from the stagnation point is accomplished by numerical integration of Equation (V-6) along the particular curve in Figure V-1 as corresponding to the average airfoil surface temperature.

The local skin friction is calculated by the use of:

$$\left[C_f\right] = \frac{1}{\sqrt{\dfrac{u_e\,s}{\nu_w}}}\left[2\ell\left\{\frac{s}{c}\left(-\frac{dM_e}{d(s/c)}\frac{1}{\eta}\right)\frac{1}{M_e}\right\}^{1/2}\right] \tag{V-7}$$

The local form factor, H, is obtained by the use of the following expression which is derived from the numerical solution results of Chapman and Rubesin (Reference V-4) and Crocco's relation for temperature distribution in the boundary layer:

$$H = H_m\left[1 + C_1\left(\frac{T_w}{T_e} - 1\right) + C_2\left(\frac{T_{aw}}{T_e} - 1\right)\right] \tag{V-8}$$

where

$$C_1 = \frac{7.31 - 4.65(Pr)^{1/2}}{2.62} \quad , \quad C_2 = \left[4.65(Pr)^{1/3} - 3.65(Pr)^{1/2}\right]$$

$$T_{aw} = T_e\left[1 + (Pr)^{1/2}\frac{\gamma - 1}{2}M_e^2\right] \quad , \quad H_m = 1.1138(n) + 2.384$$

Quantities such as $\theta, H, \dfrac{\theta^2}{\nu}\dfrac{du_e}{dS}, \dfrac{u_e\theta}{\nu},$, calculated by the above method at discrete points can then be used to determine the location of transition as well as provide a method for short bubble or long bubble prediction.

Transition Prediction. - The process of transition from laminar to turbulent boundary-layer flow on the airfoil is a very complex phenomena dependent upon pressure gradient, wall roughness, free stream turbulence, local Mach number, Reynold's number and body forces (i.e. centrifugal forces due to convex or concave walls).

Figure V-3 shows the development of the boundary layer on a flat plate with zero pressure gradient in the axial direction. The three regions shown ((1), (2) and (3)) are the laminar region, the transition region, and the turbulent region, respectively. Figure V-3 also shows schematically the stability curve of $a\delta^*$ versus Reynolds' number, based on displacement thickness. This curve is computed from the stability theory for the Blausius velocity profile. The laminar region, from "0" to "a", is completely stable to any disturbances. Point "a" is determined from the stability curve, and thus it is a function of the freestream Reynold's number. Point "a" represents the position at which any disturbance - such as free stream turbulence, wall roughness, oscillations of the plate, etc. - will cause fluctuations in the velocity, temperature, etc. within the boundary layer. The region from "a" to "b" thus represents the time or distance required to start these fluctuations. The length of the region from "a" to "b" depends on the type and extent of the disturbances and heat transfer. Still, the flow from "a" to "b" is laminar boundary layer flow. At point "b", sharp increases in boundary layer thickness and changes in skin friction begin to take place. The length of the transition region, b-c, depends on the same factors as the region a-b. The location of point "b", for the flat plate is thus given by

$$3 \text{ X } 10^5 \leqq (\text{Reynold's number})_{\text{beginning of transition}} \leqq 4 \text{ X } 10^6$$

This relationship depends upon: free stream turbulence, wall roughness, heat transfer, free stream Mach number, etc. The location of point "a", length of region a-b, and length of region b-c would also depend very strongly on the pressure gradient, if present.

Figure V-4 shows the velocity profile, form factor, boundary layer thickness, and skin friction in the different regions mentioned above.

The theory and equations for transition prediction are outlined in detail in Reference V-1. Only the principal equations will be summarized here.

Figure V-5 shows the curve of the critical local momentum thickness Reynold's number versus the local shape factor $K = (\theta^2/\nu)(dU_e/ds)$. This curve was derived from the curves of neutral stability calculated by Schlicting and Ulrich for various pressure gradients. The region between this curve and the X-axis is the stable region and the region above and including the curve represents a condition of instability in the boundary layer corresponding to the one described between points "a" and "b" in Figure V-3. Thus, when the local quantities such as θ, U_e, and dU_e/ds at the discrete points evaluated as a

laminar boundary layer, are such that the point corresponding to local values

of $\left(R_e\theta,\ \frac{\theta^2}{\nu}\ du_e/ds\right)$ fall above or on the curve shown in Figure V-5, then

the boundary layer has become unstable to external disturbances. Calculations are then performed downstream of this instability point to determine the location of the point of transition to the turbulent boundary layer.

Figure V-6 shows the curve of $\left[\left(\frac{U_e\theta}{\nu}\right)_{transition} - \left(\frac{U_e\theta}{\nu}\right)_{instability}\right]$

versus $\overline{K}$. Here, $\overline{K}$ is defined as the mean value of the pressure gradient parameter calculated from the instability point to the downstream point on the airfoil, i.e.:

$$\overline{K} = \frac{1}{s/c - (s/c)_{\substack{instability \\ point}}} \int_{s/c_{instability}}^{s/c} \frac{\theta^2}{\nu}\frac{d\,u_e}{d\,s/c}\ d(s/c) \tag{V-9}$$

and,

$\left(\frac{U_e\theta}{\nu}\right)_{instability}$ = Momentum thickness Reynold's number at instability point on the airfoil which is determined by the previous calculation.

$\left(\frac{U_e\theta}{\nu}\right)_{transition}$ = Momentum thickness Reynold's number at the point of transition to be determined.

The values of θ, $\frac{d\,u_e}{d\,s/c}$ and $\frac{\theta^2}{\nu}\frac{d\,u_e}{d\,s/c}$ calculated at discrete points, downstream of point of instability, are then used to locate the point;

$\left[\frac{U_e\theta}{\nu} - \left(\frac{U_e\theta}{\nu}\right)_{instability},\ \overline{K}\right]$ in Figure V-6.

If the point falls below the curve in Figure V-6 then the calculations of laminar boundary layer are continued to the next point on the airfoil surface. This process is continued until values calculated fall on or above the curve at which point transition from laminar to turbulent boundary layer is assumed to have taken place.

Laminar Stall Prediction. - Study of the evolution of wing lift as a function of incidence has shown in many instances the presence of bubble separation at the airfoil leading-edge resulting in laminar section stall. Experimental data on two-dimensional "peaky" airfoil sections indicate that $C_{l_{max}}$, as limited by laminar stall, is strongly dependent on leading-edge shape and, freestream Reynold's number. The laminar boundary layer, which develops on the upper surface of the airfoil, at high angles-of-attack, is subjected to a very high adverse pressure gradient after traveling only a short distance downstream. As a result, the local momentum-thickness Reynold's number, just aft of the pressure peak, has not reached a level sufficiently high to cause transition to a turbulent boundary layer. On the other hand, the laminar layer, because of a low kinetic energy level has insufficient

energy to surmount the "pressure hill" of the adverse gradient near the leading edge. The result is that the laminar boundary layer separates from the surface of the airfoil. The separated shear-layer which is formed, may curve back onto the surface within a very short distance; this is defined as short bubble formation. In certain cases, the separated viscous layer near the pressure peak may not reattach to the surface at all or, may reattach within 0.2-0.3 chord lengths downstream. In either case, the flow over the airfoil is unsteady because of the extensive separation and hence is of little practical interest. This extended separated region is defined as long bubble separation.

Figure V-7 shows typical pressure distributions for single-piece airfoils exhibiting both laminar and trailing-edge (or turbulent) stall. Figure V-8 shows characteristic lift curves for laminar short-bubble, laminar long-bubble and turbulent trailing-edge stall for the single-component airfoil. When the short bubble, which is formed near the pressure peak, bursts, and the flow remains unattached, the lift coefficient decreases sharply with further increases in angles-of-attack, as shown in the Figure V-8. When the short bubble bursting is followed by downstream reattachment (long bubble formation), the lift curve exhibits a characteristic discontinuity as denoted by point C_1 in Figure V-8. Because extensive and increasingly larger regions of separated flow are occurring after point C_1, the flow over the airfoil, in the range of α between α C_1 and α D_1 is unsteady and is therefore not representative of the steady-state conditions which are considered here.

Apart from the observation of Sir Melvill Jones (References V-5 and V-6) over 30 years ago, little work was carried out on the bubble problem until fresh interest was aroused through the use of thin airfoil sections for improving drag divergence Mach numbers. Von Doenhoff (Reference V-7) suggested certain reattachment criteria based on simple geometrical arguments. His subsequent method for predicting bubble bursting did not appear to be applicable to the general case. McGregor (Reference V-8) experimentally investigated leading-edge bubbles and hypothesized that the change in kinetic energy in going from the shear layer to the bubble must balance the losses due to viscous dissipation. Bubble expansion appeared to be a likely mechanism for maintaining this equilibrium. Owen and Klafner (Reference V-9) analyzing experimental pressures on several airfoils found that leading-edge bubbles could be typified as either "long" or "short" depending upon whether the separation boundary-layer Reynolds number ($Re \delta *$) was larger than or less than about 450. Crabtree (Reference V-10 and V-11), correlating a large amount of experimental data by plotting log $\ell/\delta *$ against $Re \delta *$, confirmed the existence of a critical Reynold's number of about 450-500 separating the two bubble regimes. Experimental cases have been found, however, which show much larger bursting Reynold's numbers (1200 for a blunt-nosed model) and some attempt has been made to explain these differences through consideration of the pressure rise over the bubble (Reference V-10).

From the foregoing discussion, it is apparent that the presently available analytical techniques for predicting short or long bubble formation, as well as laminar stall, are useful for data correlation only; this is due in part to the many simplying assumptions in the calculation of laminar boundary layer

parameters. An attempt was made within the present program framework, to correlate criteria for laminar stall prediction as suggested by Reference V-12, with erratic results. Consequently, Goradia-Lyman criteria for the prediction of laminar stall on single-piece airfoils were developed for the multiple-airfoil computer application. In this development, certain dimensionless parameters, comprising the laminar stall criteria, were derived by dimensional analysis. The actual relationship existing between the selected parameters was subsequently determined through correlation with experimental data. In the paragraphs which follow, the derivation of the laminar stall criteria through the dimensional analysis technique is outlined.

The momentum integral equation for a laminar boundary layer under the influence of a pressure gradient is given as:

$$\frac{\tau_o}{\rho} = U_e^2 \frac{d\theta}{ds} + (2\theta + \delta^*)U_e \frac{d\,U_e}{ds} \tag{V-10}$$

A fourth order velocity profile assumption (after K. Pohlhausen) takes into account the no-slip conditions at the wall as well as those separated velocity profiles having a point of inflection, thus:

$$\frac{u}{U_e} = f(\eta) = a\eta + b\eta^2 + c\eta^3 + d\eta^4 \tag{V-11}$$

where: $\eta = y/\delta$ and $0 \le \eta \le 1$ and $\frac{u}{U_e} = 1.0$ for $\eta \ge 1$

Four free constants (a, b, c, d) are determined when the following boundary conditions are prescribed:

$$y = 0, \ u = 0, \ \nu \frac{\partial^2 u}{\partial y^2} = \frac{1}{\rho} \frac{dP}{dx} = -U_e \frac{d\,u_e}{dx} \tag{V-12}$$

$$y = \delta, \ u = U_e, \ \frac{\partial u}{\partial y} = 0, \ \frac{\partial^2 u}{\partial y^2} = 0$$

The non-dimensional quantities may be defined as:

$$\Lambda = \frac{\delta^2}{\nu} \frac{dU_e}{ds} \quad ; \quad K = \frac{\theta^2}{\nu} \frac{dU_e}{ds} \tag{V-13}$$

By making use of Equation (V-11) and the boundary conditions, the following relations can be derived:

$$\frac{\delta^*}{\delta} = \frac{3}{10} - \frac{\Lambda}{120}$$

$$\frac{\theta}{\delta} = \frac{37}{315} - \frac{\Lambda}{945} - \frac{\Lambda^2}{9072}$$

$$\frac{\tau_o \delta}{\mu U_e} = 2 + \frac{\Lambda}{6}$$

(V-14)

$$K = \left(\frac{37}{315} - \frac{\Lambda}{945} - \frac{\Lambda^2}{9072}\right)^2 \Lambda$$

(V-15)

$$H = \frac{\delta^*}{\theta} = \frac{\frac{3}{10} - \frac{\Lambda}{120}}{\frac{37}{315} - \frac{\Lambda}{945} - \frac{\Lambda^2}{9072}} = f_1(K)$$

(V-16)

$$\frac{\tau_o \theta}{\mu U_e} = \left(2 + \frac{\Lambda}{6}\right)\left(\frac{37}{315} - \frac{\Lambda}{945} - \frac{\Lambda^2}{9072}\right) = f_2(K)$$

By further definition:

$$z = \frac{\theta^2}{\nu}, \text{ then } K = z\frac{dU_e}{dx}$$

(V-17)

By substituting Equations (V-5) through (V-7) into the momentum integral equation (V-1), and, after simplification, the following is obtained:

$$\frac{dz}{ds} = \frac{F(K)}{U_e} \quad , \quad K = z\frac{dU_e}{ds}$$

(V-18)

In order to establish an empirical criteria for the presence of a short or long bubble (i.e. for the prediction of laminar stall) various pairs of physical parameters which are shown in Equations (V-15) through (V-18) may be selected. For example, the pair, H (or $\frac{\delta^*}{\theta}$) and the pressure gradient parameter, K (or $\frac{\theta^2}{\nu}\frac{dU_e}{dx}$), as seen in Equation (V-16), could be chosen. The form factor, H, is used extensively in predicting separation for the turbulent boundary layer or trailing-edge stall on single-component airfoils. This criteria, however, cannot be used in the case of laminar stall prediction because the measurement of velocity profiles downstream of the pressure peak in the adverse pressure gradient show an inconsistent variation of H as associated with transition phenomena. On the other hand, by considering the combination

($\frac{\tau_o \theta}{\mu U_e}$) and (K) from Equation (V-17), a source-pair is obtained which, after the following simplification, provides the desired correlation parameters:

$$\frac{\tau_o \theta}{\mu U_e} \sim \frac{\theta^2}{\nu} \frac{dU_e}{dx}$$

$$\tau_o = \mu \left. \frac{\partial u}{\partial y} \right|_{y=0} \qquad\qquad\qquad (V-19)$$

$$\left(\left. \frac{\partial u}{\partial y} \right|_{y=0} \right) \frac{\theta}{u_e} \sim \frac{\theta^2}{\nu} \frac{dU_e}{dx}$$

Measured velocity profiles downstream of the pressure peak indicate that there is little change in the value of the slope of the profile until the flow leaves the surface. Hence the $\left. \frac{\partial u}{\partial y} \right|_{y=0}$ downstream of the pressure peak can be regarded approximately constant.

Thus, after dividing both sides of Equation (V-9) by $\frac{\theta^2}{\nu}$ the following is obtained:

$$\frac{\nu}{U_e \theta} \sim \frac{dU_e}{dx} \sim \frac{dM_e}{d(s/c)} \qquad\qquad\qquad (V-20)$$

where, C, is the airfoil chord. Also, the freestream Mach number and local Mach number are both assumed to be sufficiently small that the compressibility effects are likewise small.

Equation (V-20), derived by a dimensional analysis of laminar boundary layer behavior, suggests that a pair of parameters, such as local Mach number gradient $\frac{dM_e}{dx/c}$ and local momentum thickness Reynold's number Re_θ, can provide correlation for the prediction of laminar stall. The least square straight line shown in Figure V-9, comprising the desired criteria curve, was derived on this basis using experimental velocity profiles in the vicinity of the bubble region along with pressure distributions. These stall criteria are used in the present program for predicting laminar stall on the single-component airfoil.

Figure V-10 illustrates schematically the sequence of steps used in the program in going from the laminar boundary layer calculations to obtain initial conditions for the ordinary turbulent or the confluent boundary layers. When the airfoil is at the stall criteria, the program logic stops further calculations. Other boundary layer calculation sequences are shown in this figure.

Turbulent Boundary Layer. - Ordinary turbulent boundary layer is usually present on the upper surface and lower surface of the single-component airfoil and on the upper surface of the most forward element of the multi-component

section. The main quantities normally desired from turbulent boundary layer calculations are the momentum thickness and displacement thickness, the point of separation if any, and skin friction drag.

Most recently developed ordinary turbulent boundary layer theories consider only the time-averaged turbulent motion, thus yielding only "mean" or "time-averaged" results. If the time-averaging process is performed on the Prandtl's boundary layer equations for continuity, momentum and thermal energy, the resulting equations would contain terms consisting of the time-averaged product of the fluctuation quantities. The expressions for these quantities are approximated by various semi-empirical theories. As an example of the above approach, consider the momentum equation for the incompressible laminar boundary layer flow which is given by;

$$\rho\left(u\frac{\partial u}{\partial x} + v\frac{\partial u}{\partial y}\right) = -\frac{\partial P}{\partial x} + \mu\frac{\partial}{\partial y}\left(\frac{\partial u}{\partial y}\right) \tag{V-21}$$

If one makes the following substitution in Equation (V-11)

$$P = \overline{P} + P' \quad ; \quad u = \overline{u} + u' \quad ; \quad \overline{v} = v + v' \tag{V-22}$$

then after time-averaging the resulting equation, the following equation is obtained:

$$\rho\left(\overline{u}\frac{\partial\overline{u}}{\partial x} + v\frac{\partial\overline{u}}{\partial y}\right) = -\frac{\partial P}{\partial x} + \mu\frac{\partial}{\partial y}\left(\frac{\partial\overline{u}}{\partial y}\right) - \frac{\partial}{\partial y}\left(\overline{\rho u'v'}\right) \tag{V-23}$$

The resulting Equation (V-23) contains an additional term, the product of the fluctuation quantities $\rho\,u'\,v'$ which is defined as shearing stress due to turbulent fluctuations. Different semi-empirical expressions have been advanced for this turbulent shearing stress by Prandtl, Boussinesa, Deissler, Ludwieg-Tillmann, and Von Karman, as examples.

As will be shown in the correlation section of this report, the majority of the multiple airfoil configurations considered exhibit some degree of localized separation throughout the angle-of-attack range. In contrast, the turbulent boundary-layer model, just described, is structured around the assumption of completely attached flow conditions over the entire airfoil. Under this format, the attainment of specified separated flow criteria would therefore represent a sufficient condition for terminating further calculations. This procedure could lead to obvious difficulties when approaching the final, viscous solution through an iterative procedure which starts with a potential flow pressure distribution generally unfavorable for maintaining completely attached flow. Additionally, running multiple-case loads through the program could become a time-consuming process when the number of separated

42

flow cases is high. It therefore became desirable and convenient to formulate a separate turbulent boundary-layer model which would remain stable under the influence of extreme gradients, both favorable and adverse, and which would simultaneously provide reasonable magnitudes of momentum and displacement thicknesses downstream of the separation point. Under this scheme, a refined Nash boundary-layer model would be used to accurately describe the attached-flow character of the turbulent boundary-layer during the last several program iterations where potential pressure gradients are substantially reduced. Additionally, when flow separation is apparent in the viscous solution, the refined model would be used to accurately define the point of separation. Goradia's approximate model would be used in the initial iterations thereby successively reducing the gradients toward more realistic levels or, when separation is present, provide the means of continuing the calculations to the next case. The formulation of both of the turbulent boundary-layer models is described in the following paragraphs.

(A) Nash's Ordinary Turbulent Boundary Layer Method. - The method is applicable for both low Mach number and high transonic Mach number flow over the airfoil surface. A detailed description of the method is available in Reference V-13 and so only a brief description of the method is presented here.

The momentum-integral equation and the kinetic-energy integral equation for the mean motion in a compressible turbulent boundary layer in two-dimensional or axisymmetric flow can be written as

$$\frac{1}{r} \frac{d}{dx} (\rho_e U_e^2 r \theta) = \tau_w - \rho_e U_e \frac{dU_e}{dx} \delta^* \qquad (V-24)$$

$$\frac{1}{2r} \frac{d}{dx} (\rho_e U_e^3 r \delta^{**}) = \int_0^\infty \tau \frac{\partial u}{\partial y} - \rho_e U_e^2 \frac{dU_e}{dx} \theta^* \qquad (V-25)$$

where r is a constant for a two-dimensional flow and is the transverse radius of the body for an axisymmetric flow.

The mean velocity profile assumption is as given by a modified Coles' relation, or:

$$U = \frac{U_\tau}{K} \ln \frac{y}{\delta} + U_e - U_B \left\{ 1 + \cos \left(\frac{\pi y}{\delta} \right) \right\} \qquad (V-26)$$

where U_τ = friction velocity = $\sqrt{\frac{\tau_w}{\rho}}$

The relation between H and $\bar{H}$, as used for low Mach numbers, is given by the following curve-fit expression:

$$H = 1.0 + 1.333(2 - \widetilde{H}) + 12.0(2 - \widetilde{H})^4 \qquad (V-27)$$

43

where $H = \dfrac{\delta^*}{\theta}$, $\tilde{H} = \dfrac{\delta^{**}}{\theta}$

The skin friction expression for the low Mach number is given by a modified Ludwieg-Tillman expression:

$$c_f = \frac{\frac{1}{H} - 0.4}{\left[3.18 \log_{10}\left(\frac{U_e \theta}{2}\right) - 1.0\right]^2} \qquad \text{(V-28)}$$

The dimensionless shear stress is defined by

$$I = \int_0^\infty \frac{\tau}{\frac{1}{2}\rho_e U_e^3} \frac{\partial u}{\partial y} dy + \frac{1}{2} c_f \qquad \text{(V-29)}$$

The differential equation for I is given by,

$$\frac{dI}{dx} = \frac{\lambda}{8} I (\hat{I}^{1/2} - I^{1/2}) \qquad \text{(V-30)}$$

Where $\hat{I}$ is the corresponding value of I for an equilibrium boundary layer. $\hat{I}$ is a function of H and is expressed as a 4$^{\text{th}}$-order polynomial in H.

The unknowns to be calculated are θ , H and the shear integral. The equations used to calculate the above are Equations (V-24), (V-25) and V-26). These equations are solved by using a predictor-corrector numerical technique at each step.

(B) Goradia's Ordinary Turbulent Boundary Layer Method. - For incompressible two-dimensional boundary-layer flow, the dissipation energy integral equation and the momentum integral can be respectively written in the following forms:

$$\frac{1}{2} \frac{d}{dx}\left\{U_e^3 \delta^{**}\right\} = \frac{1}{\rho} \int_0^\delta \tau \frac{\partial u}{\partial y} dy \qquad \text{(V-31)}$$

$$\frac{d\theta}{dx} + \frac{\theta}{U_e} \frac{dU_e}{dx}(H + 2) = \frac{\tau_w}{\frac{1}{2}\rho U_e^2} \qquad \text{(V-32)}$$

44

From the experimental data of Reference V-14, the expression for the shear integral, $\int_0^\delta \tau \frac{\partial u}{\partial y}\, dy$, as deduced by Truckenbrodt (V-15) is shown to be independent of the form factor H. The expression for the shear integral can be written to good approximation as,

$$\int_0^\delta \frac{\tau}{\rho U_e^2} \frac{\partial}{\partial y} \frac{U}{U_e}\, dy = \frac{0.56 \times 10^{-2}}{\left(\dfrac{U_e \theta}{\nu}\right)^{1/6}} \qquad (V\text{-}33)$$

The experimental values of turbulent skin friction at the wall can be written as follows, Reference V-16:

$$\frac{\tau_w}{\rho U_e^2} = 0.123 \times 10^{-0.678H} \left(\frac{U_e \theta}{\nu}\right)^{-0.268} \qquad (V\text{-}34)$$

By substituting the expression of the shear integral (V-33) in Equation (V-31) and simplifying, the following analytical expression for momentum thickness, θ, is obtained:

$$\theta = \left[(\theta_i)^{1.17} \left(\frac{U_{e_i}}{U_e}\right)^{3.51} \left(\frac{\nu}{\nu_i}\right)^{0.167} + 0.00792 \frac{(\nu)^{0.17}}{(U_e)^{3.51}} \int_{x_i}^{x} (U_e)^{3.332}\, dx \right]^{1/1.17} \qquad (V\text{-}35)$$

Subscript i refers to the condition at the point of transition from laminar to ordinary turbulent boundary layer.

The equation for the incompressible form factor, H, can be obtained through the algebraic simplification of Equations (V-32) and (V-33):

$$\frac{d\widetilde{H}}{dx} = \left[\frac{0.0123}{(U_e \theta/\nu)^{0.17}} - \widetilde{H}\left(\frac{\tau_w}{\rho U_e^2}\right) + (H - 1.1) \frac{\widetilde{H}\theta}{U_e} \frac{dU_e}{dx} \right] \Big/ \theta \qquad (V\text{-}36)$$

The form factor, H, based on dissipation energy thickness, and appearing in the above equation is related to the usual form factor H by:

$$\widetilde{H} = \frac{1.269H}{H - 0.379} \qquad (V\text{-}37)$$

The above expression is deduced from the experimental results of Reference V-20. The incompressible momentum thickness and form factor may be calculated numerically by a single step iterative method. The local value of skin friction is obtained through the use of Equation (V-35).

Equations (V-34) through (V-38) represent the de-sensitized turbulent boundary-layer equations programmed for the computer. Further discussions of

the programmed interplay between Goradia's model and the previously-discussed Nash model is provided in the description of the iterative procedure, Section VI.

Boundary-Layer Correlation. - To validate the foregoing applications of boundary-layer theory to the realistic development of ordinary boundary-layers on airfoils, a number of correlation studies were performed. These analyses encompassed laminar, transition, laminar stall, and turbulent boundary-layer correlated to varying depths dependent upon the quantity or quality of the experimental data available. In each instance, a computer subroutine, developed according to the foregoing formats, was used as an isolated or modular program to obtain the desired correlation. Thus, subroutine check-out and program verification could be performed simultaneously.

(a) Laminar. - Comparisons of predicted and experimental laminar boundary-layer characteristics are presented in Figures V-11 through V-13 for several single-element airfoils, NACA 0012 and NACA 0025. In each case, the predicted boundary-layer data reflects the experimentally-determined pressure distributions of Reference V-17. Several unpublished input parameters required for the calculation of these data were the position of the stagnation point and the wall temperature. The former could be readily determined from the experimental pressures and the latter parameter could be obtained by the logical assumption of a wall-to-free stream temperature ratio of unity inasmuch as the tests were conducted at low Mach number $(M_\infty = 0.3)$. The comparisons are provided in terms of momentum thickness $\left(\frac{\theta}{c}\right)$, form factor (H) and displacement thickness $\left(\frac{\delta^*}{c}\right)$ up to the point of transition. Approximate transition points are shown on the figures. It is seen in these comparisons that the computer subroutine calculations are in very good agreement with the experimental results.

(b) Transition. - Comparisons of predicted and experimental transition points are presented in Figure V-14 for a number of airfoils with variations in both airfoil geometry and test conditions. The calculated data were obtained from the computer subroutine operated in its modular form. In each case, the experimental pressure distribution was utilized as input data.

The majority of the data provided in Figure V-14 are shown to fall within a ± 10 percent accuracy band. These airfoils represent tests conducted under relatively ideal conditions of low freestream turbulence and smooth model surfaces. The computer program, in its present form, does not account for surface roughness nor the intensity of freestream turbulence. Consequently, a few of the comparative cases, where these conditions were not rigidly controlled, fall beyond the ± 10 percent band.

(c) Laminar Stall. - Figures V-15 through V-17 show the results of a correlation study performed to determine the validity of the laminar stall criteria as programmed. Three NACA airfoils were used to conduct the correlation: 63A009, 631012 and 64A010, References V-18, V-19 and V-20, respectively.

The laminar stall point is highly sensitive to the level of leading-edge peak pressure as well as the pressure gradient immediately downstream. In

many instances, the maximum peak pressure location on experimental airfoils may not be coincident with the pressure pick-ups such that the actual pressure peak may be lost. For this reason, as well as the need for a refined definition of the local pressure gradient (i.e. close point spacing), the potential-flow subroutine was used to generate the pressure distributions required for the study. With the pressure data introduced into the laminar stall subroutine, the existence of short bubble or bubble burst was determined through the use of the criteria of Figure V-9. As can be seen from the figures, the laminar stall subroutine, as well as the criteria contained therein, provides an excellent technique for predicting laminar stall.

(d) Turbulent. – Comparison of predicted and experimental turbulent boundary-layer characteristics are presented in Figures V-18 through V-20. The comparisons presented in these figures reflect the use of experimental pressure data obtained on the indicated airfoils as correlated against the Nash turbulent boundary-layer model.

The initial conditions required for the starting of the turbulent boundary layer calculations were obtained from the laminar boundary layer subroutine at the predicted transition point. Early correlations indicated the calculations to be relatively insensitive to the initial value of form factor, as long as the value for momentum thickness is needed in that an error in the initial value results in considerable magnification of the initial error in the downstream calculations. Furthermore, relatively small errors in the initial momentum thickness can effect to a significant extent the predicted point of separation on the airfoil, where such exists.

The flow conditions, Mach number, total pressure, and total temperature required as input were not specified in the test data. Therefore, where necessary, logical assumptions were made in estimating these conditions.

Figure V-21 summarizes both laminar and turbulent boundary layer correlations, based on several airfoils. For those cases where the flow remained attached, use of experimental pressure distribution in predicting the boundary layer quantities, resulted in the majority of the parameters calculated falling within 10% of the experimental results. While the prediction of the boundary-layer characteristics under the influence of extensive separated flow conditions is not an objective of the present study, it will constitute a future prerequisite to a refined Cl_{max} prediction. For the present purposes, however, it is concluded that the turbulent boundary-layer model is capable of predicting turbulent separation accurately under the conditions that such separation occurs within the last 5 percent of the airfoil chord.

For validating Goradia's approximate or desensitized turbulent boundary-layer model, discussed in Section V, comparisons were made between results from this math model to that of the more accurate Nash model. Such comparisons performed on the program sub-routine, utilized the same initial conditions and several representative pressure distributions. Results from this comparison, given in Figure V-22 and V-23, show that both momentum thickness (θ) and form factor (H) are represented to good accuracy by the approximate model in both favorable and adverse gradients. The significant and characteristic feature

of the approximate model is shown in those regions where the more accurate model can go to either negative values of Θ (highly favorable gradient) or unrealistically large values of Θ following turbulent separation. In such regions, the approximate model can neither separate nor go to negative values but does establish realistic trends in the indicated boundary layer parameters. Thus, the approximate turbulent model offers an ideal means of calculating boundary-layer parameters in the initial stages of the iteration process where the extremes on pressure gradient are normally encountered.

Laminar Boundary Layer:

H_{eq} = equivalent incompressible form factor

H_{tr} = transformed form factor, $H_{tr} = \dfrac{\delta^*_{tr}}{\theta_{tr}}$

k = thermal conductivity

K_{su} = Sutherland's constant, = 198°R

h = enthalpy

ℓ = dimensionless wall shear parameter $\ell = \dfrac{\theta_{tr}}{U_e}\left(\dfrac{\partial u}{\partial y}\right)_w$

M = Mach number

N = momentum parameter = $2\left[n(H_{tr} + 2)\ell\right]$

m = exponent from Falkner-Skan external velocity distribution $U_e = C_1 X^m$

n = correlation number, $n = -\dfrac{\left(dU_e/dX\right)\theta^2_{tr}}{\nu_o}$

h_{ew} = local Reynold's number based on conditions at wall, $R_{ew} = \dfrac{\rho_w U_e s}{\mu_w}$

Re_θ = local momentum thickness Reynold's number = $\dfrac{U_e \theta}{\nu}$

$\bar{r}$ = recovery factor at the wall, = $\sqrt{P_r}$

S_w = $\dfrac{T_w}{T_o} - 1$

T_{aw} = adiabatic wall temperature

U = transformed longitudinal velocity = $\dfrac{a_o}{a_e}u$

V = transformed normal velocity

X = transformed coordinate along surface = $\displaystyle\int_0^s \lambda\, \dfrac{a_e}{a_o}\, \dfrac{p_e}{p_o}\, ds$

Y = transformed normal coordinate = $\dfrac{a_e}{a_o}\displaystyle\int_0^\xi \dfrac{\rho}{\rho_o}\, dg$

τ = shear stress,

ζ, ξ = curvilinear coordinates

Transition:

k = second shape factor = $\dfrac{\theta^2}{\nu} \dfrac{d\,U_e}{d\,s}$

$\bar{k}$ = mean Pohlhausen shape factor = $\dfrac{1}{S/C - (S/C)_{instability}} \displaystyle\int_{S/C_{ins}}^{S/C} K\,d\,(S/C)$

$R_{e_{\delta^*}}$ = Reynold's number based on displacement thickness = $\dfrac{U_e \delta^*}{\nu}$

R_{e_θ} = Reynold's number based on momentum thickness = $\dfrac{U_e \theta}{\nu}$

$a\,\delta^*$ = Wave length displacement thickness parameter

η = dimensionless distance normal to airfoil surface = $\left(\dfrac{\xi}{\delta}\right)$

ν_m = mean kinematic viscosity = $\dfrac{1}{\delta} \displaystyle\int_o^\delta \nu\,d\xi$

Laminar Stall:

a, b, c, d = free constants appearing in Equation (V-2)

c = airfoil chord

K = second shape factor = $\dfrac{\theta^2}{\nu} \dfrac{d\,U_e}{ds}$

s = distance along airfoil surface

U_e = velocity at the edge of boundary layer

z = $\dfrac{\theta^2}{\nu}$

$f_1(K), f_2(K)$ defined by Equation (V-6)

τ_o = wall shear stress

Λ = first shape factor = $\dfrac{\delta^2}{\nu} \dfrac{d\,U_e}{ds}$

50

Ordinary Turbulent Boundary Layer:

C_π = dimensionless turbulent production integral

$$= \int_0^\infty \frac{\tau}{\frac{1}{2}\rho_e U_e} \frac{\partial u}{\partial y} \, dy$$

H_u = incompressible form factor = $\dfrac{\displaystyle\int_0^\infty 1 - \frac{u}{U_e} \, dy}{\displaystyle\int_0^\infty \frac{u}{U_e} \left(1 - \frac{u}{U_e}\right) dy}$

$\widetilde{H}$ = $\dfrac{\delta^{**}}{\theta}$

x, y = orthogonal coordinates, x being measured along the surface and y normal to the surface.

δ^{**} = kinetic energy thickness

$$= \int_0^\infty \frac{\rho u}{\rho_e U_e} \left(1 - \frac{u^2}{U_e^2}\right) dy$$

π = dimensionless pressure gradient = $\dfrac{\delta^*}{\tau_w} \dfrac{d\rho}{dx}$

Common Symbols:

a = speed of sound, ft./sec.

c = airfoil chord, ft.

cf = local skin friction coefficient, $cf = \dfrac{\tau_w}{\frac{1}{2}\rho_w U_e^2}$

$\overline{cf}$ = $\dfrac{\displaystyle\int_0^s \tau_w \, ds}{\frac{1}{2}\rho_\infty U_\infty^2 s}$

C_p = constant pressure specific heat

Cv = constant value specific heat

H = form factor = $\dfrac{\delta^*}{\theta}$

M_e = local Mach number at the outer edge of boundary layer

Pr = Prandtl number, $Pr = \dfrac{\mu C_p}{k}$

P	=	static pressure
s	=	coordinate along airfoil surface
T	=	surface temperature °R
U	=	longitudinal velocity component
V	=	normal velocity component
μ	=	dynamic viscosity
ν	=	kinematic viscosity, $\dfrac{\mu}{\rho}$
ρ	=	mass density
δ	=	overall boundary layer thickness
δ^*	=	boundary layer displacement thickness
λ	=	constant for viscosity $= \left(\dfrac{T}{T_o}\right)^{1/2} \dfrac{T_o + K_{su}}{T + K_{su}}$
θ	=	$\displaystyle\int_0^\delta \dfrac{\rho u}{\rho_e u_e}\left(1 - \dfrac{u}{U_e}\right) d\xi$

Superscripts:

	=	fluctuating quantity

Subscripts:

e	=	external edge of boundary layer
o, w	=	conditions at wall
tr	=	transformed quantity

V - REFERENCES

V-1 Goradia, S. H., and Bennett, J. A., Methods for Analysis of Two-Dimensional Airfoils, Lockheed-Georgia Report ER-8591, July 1966

V-2 Cohen, C. B., and Reshotko E., Similar Solutions for the Compressible Laminar Boundary Layer with Heat Transfer and Pressure Gradient, NACA Report 1293, 1956

V-3 Cohen, C. B., and Reshotko E., The Compressible Laminar Boundary Layer with Heat Transfer and Arbitrary Pressure Gradient, NACA Report 1294, 1956

V-4 Chapman, D. R., and Rubesin, M. W., Temperature and Velocity Profiles in the Compressible Laminar Boundary Layer with Arbitrary Distribution of Surface Temperature, Jour. Aero. Sci., Vol. 16, no. 9, Sept. 1949, pp. 547-565

V-5 Jones, B. M., An Experimental Study of the Stalling of Wings, A.R.C. R & M 1588, Dec. 1933

V-6 Jones, B. M., and Stalling, J., Aero. Soc. 38, pp. 753-770, Sept. 1934

V-7 von Doenhoff, A. E., A Preliminary Investigation of Boundary-Layer Transition Along a Flat Plate with Adverse Pressure Gradient, NACA TN 639, March 1938

V-8 McGregor, I., Leading Edge Bubble on Sharp and Blunt Hosed Aerofoils, Ph.D Thesis, Queen Mary College, London, 1954

V-9 Owen, P. R., and Klanfer, L., On the Laminar Boundary Layer Separation from the Leading Edge of a Thin Aerofoil, A.R.C. CP 220, 1955

V-10 Crabtree, L. F., The Formation of Regions of Separated Flow on Wing Surfaces, Part II, Laminar-Separation Bubbles and the Mechanism of the Leading-Edge Stall, A.R.C. R & M 3122, 1959

V-11 Crabtree, F. F., The Formation of Regions of Separated Flow on Wing Surfaces, Part I, Low Speed Tests on a Two-Dimensional Unswept Wing with a 10-Percent Thick RAE 101 Section, R.A.E. Report Aero 2528 (Nov. 1953); reissued as Part I of A.R.C. R & M 3122, 1959

V-12 Gaster, M., The Structure and Behavior of Laminar Separation Bubbles, N.P.L. Aero Report 1181, August 1966

V-13 Nash, J. F., A Practical Calculation Method for Compressible Turbulent Boundary-Layers in Two-Dimensional and Axisymmetric Flows, Lockheed-Georgia Research Memorandum, ER-9428, August 1967

V-14   Rotta, J., Schubspannungsverteilung und Energiedissipation bei turbulenten Grenzschichten, Ing. Arch., Vol. 20, 1952, pp. 195-207

V-15   Truckenbrodt, E., Ein Quadraturverfahren zur Berechnung der laminaren und turbulenten Reibungsschicht bei ebener und rotationssymmetrischer Stromung, Ing. Arch., Vol. 20, 1952, pp. 211-228

V-16   Ludwieg, H., und Tillmann, W., Untersuchungen uber die Wandschubspannung in turbulenten Reibungsschichten, Ing. Arch., Vol. 17, 1949, pp. 288-299 (English translation in NACA TM 1285, 1950)

V-17   Baker, J. V., Boundary Layer Transition on the NACA 0012 and 23012 Airfoils in the 8-Foot High-Speed Wind Tunnel, NACA-WR-L 682, 1940

V-18   Gault, D. E., Boundary-Layer and Stalling Characteristics of the NACA 63-009 Airfoil Section, NACA TN 1894

V-19   McCullough, G. B., and Gault, D. E., An Experimental Investigation of an NACA 63-012 Airfoil Section with Leading Edge Suction Slots, NACA TN 1683, 1948

V-20   Peterson, R. F., The Boundary-Layer and Stalling Characteristics of the NACA 64A010 Airfoil Section, NACA TN 2235, Nov. 1950

V-21   Altman, J. M., and Hayter, N. L. F., A Comparison of the Turbulent Boundary-Layer Growth on an Unswept and a Swept Wing, NACA TN 2500, Ames Aeronautical Laboratory, Moffett Field, Calif. - NACA, Washington, September 1951

V-22   Bullivan, W. K., Tests of the NACA 0025 and 0035 Airfoils in the Full-Scale Wind Tunnel, NACA Rep. No. 708, 1941

FIGURE V-1

CORRELATION NUMBER VERSUS MOMENTUM PARAMETER
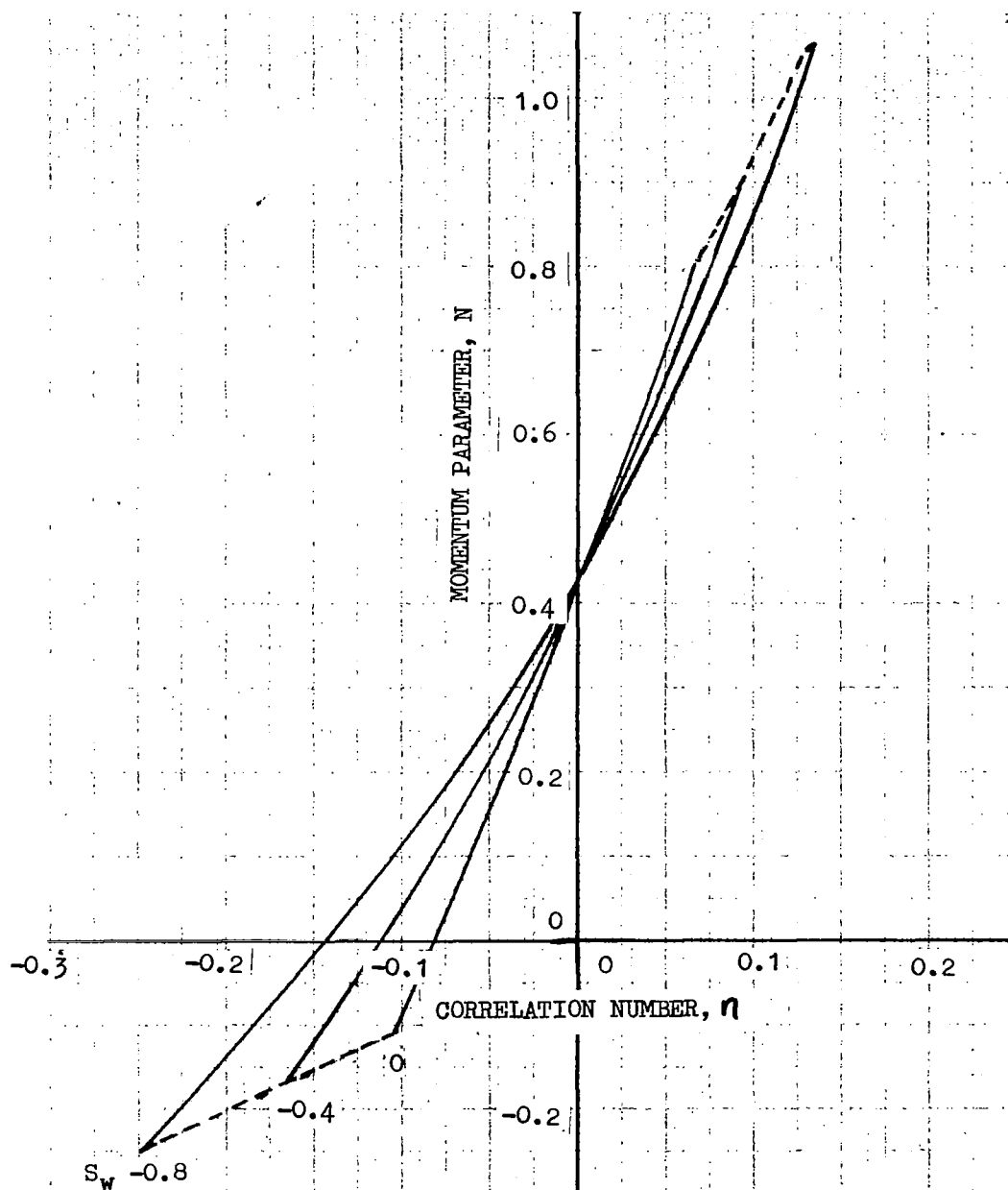
FIGURE V-2

CORRELATION NUMBER VERSUS SHEAR PARAMETER

CORRELATION NUMBER, η
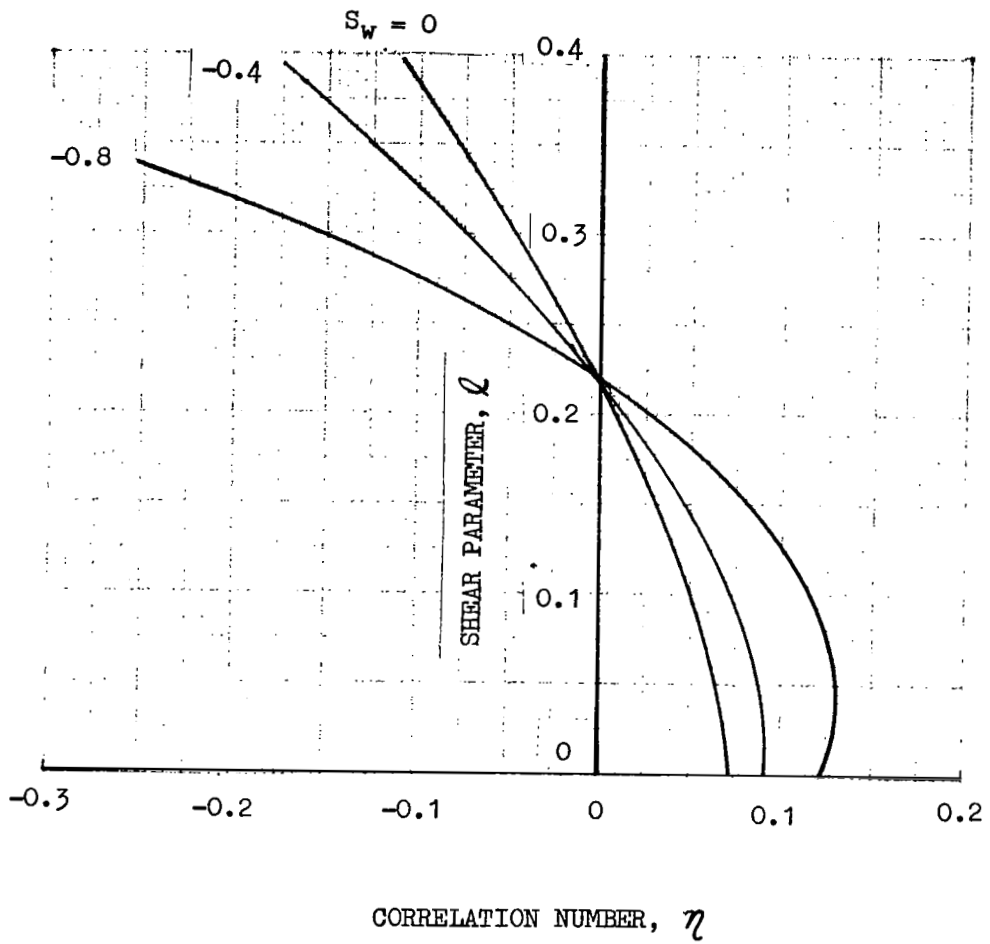
FIGURE V-3.—BOUNDARY LAYER CHARACTERISTICS
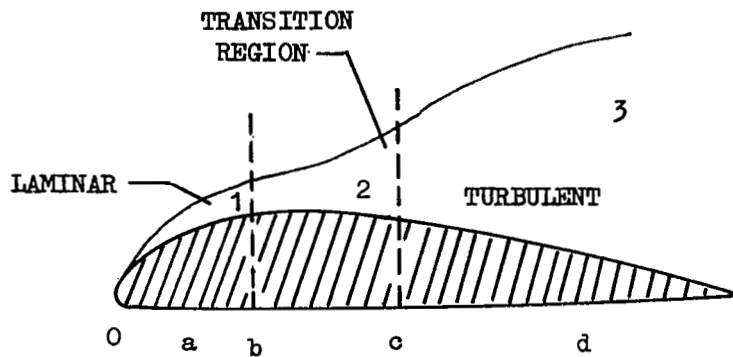
(a) BOUNDARY LAYER COMPOSITION
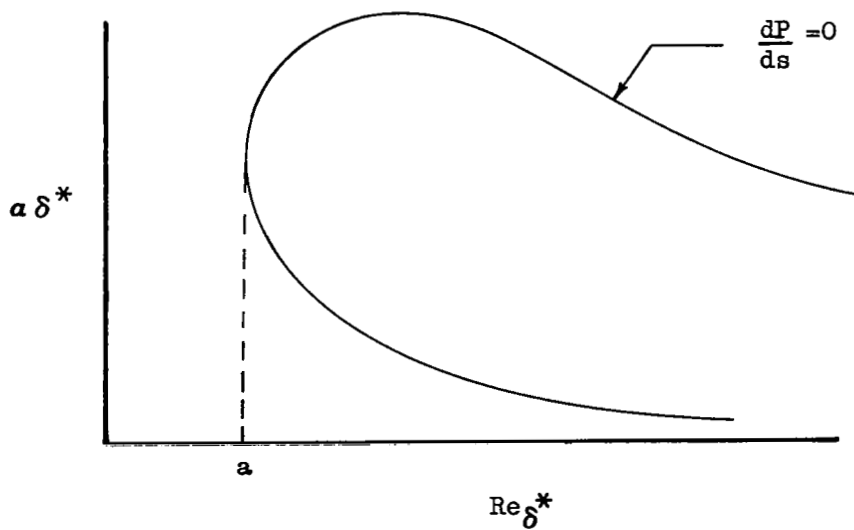
(b) STABILITY CURVE FOR A FLAT PLATE

FIGURE V-4:
QUALITATIVE COMPARISON OF BOUNDARY LAYER PARAMETERS
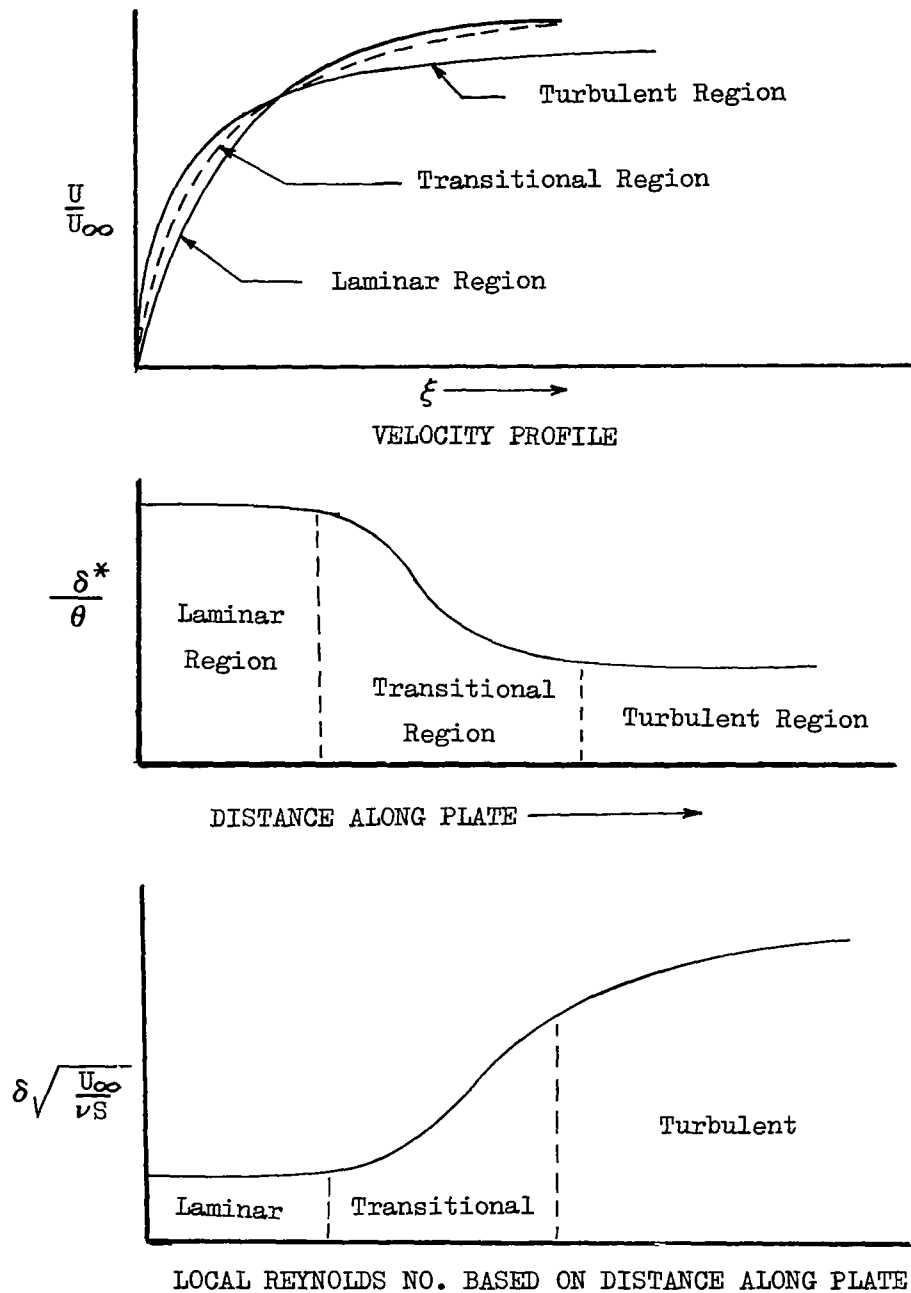
FIGURE V-5
CRITICAL MOMENTUM THICKNESS REYNOLD'S NUMBER
VERSUS
SECOND SHAPE FACTOR
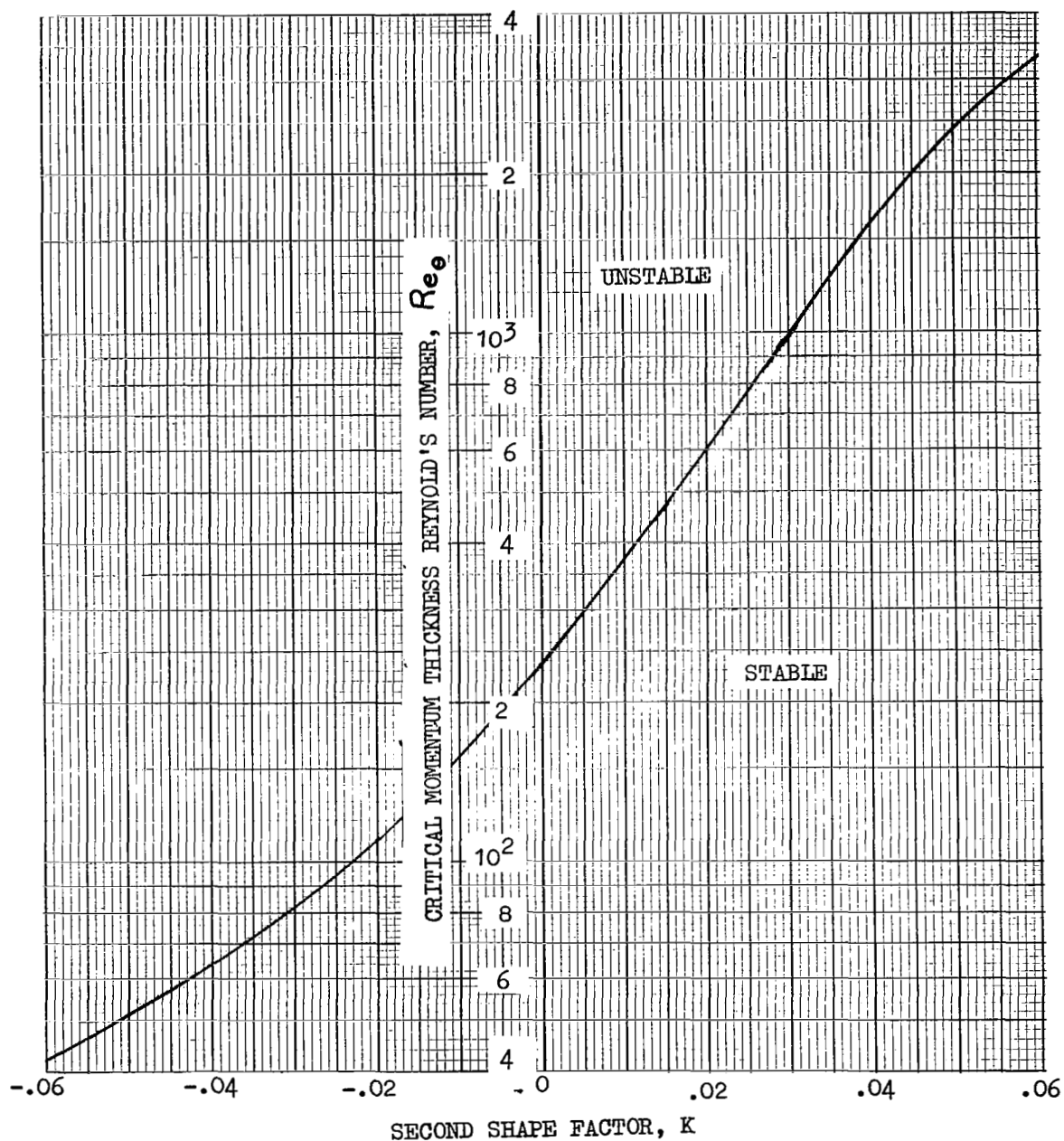
FIGURE V-6

TRANSITION MINUS INSTABILITY MOMENTUM THICKNESS
REYNOLD'S NUMBER VERSUS MEAN SECOND SHAPE FACTOR

TRANSITION MINUS INSTABILITY MOMENTUM
THICKNESS REYNOLD'S NUMBER, M

TRANSITION TO TURBULENT
BOUNDARY LAYER

LAMINAR B.L.

UNSTABLE BUT NO

TRANSITION

MEAN SECOND SHAPE FACTOR, $\bar{K}$
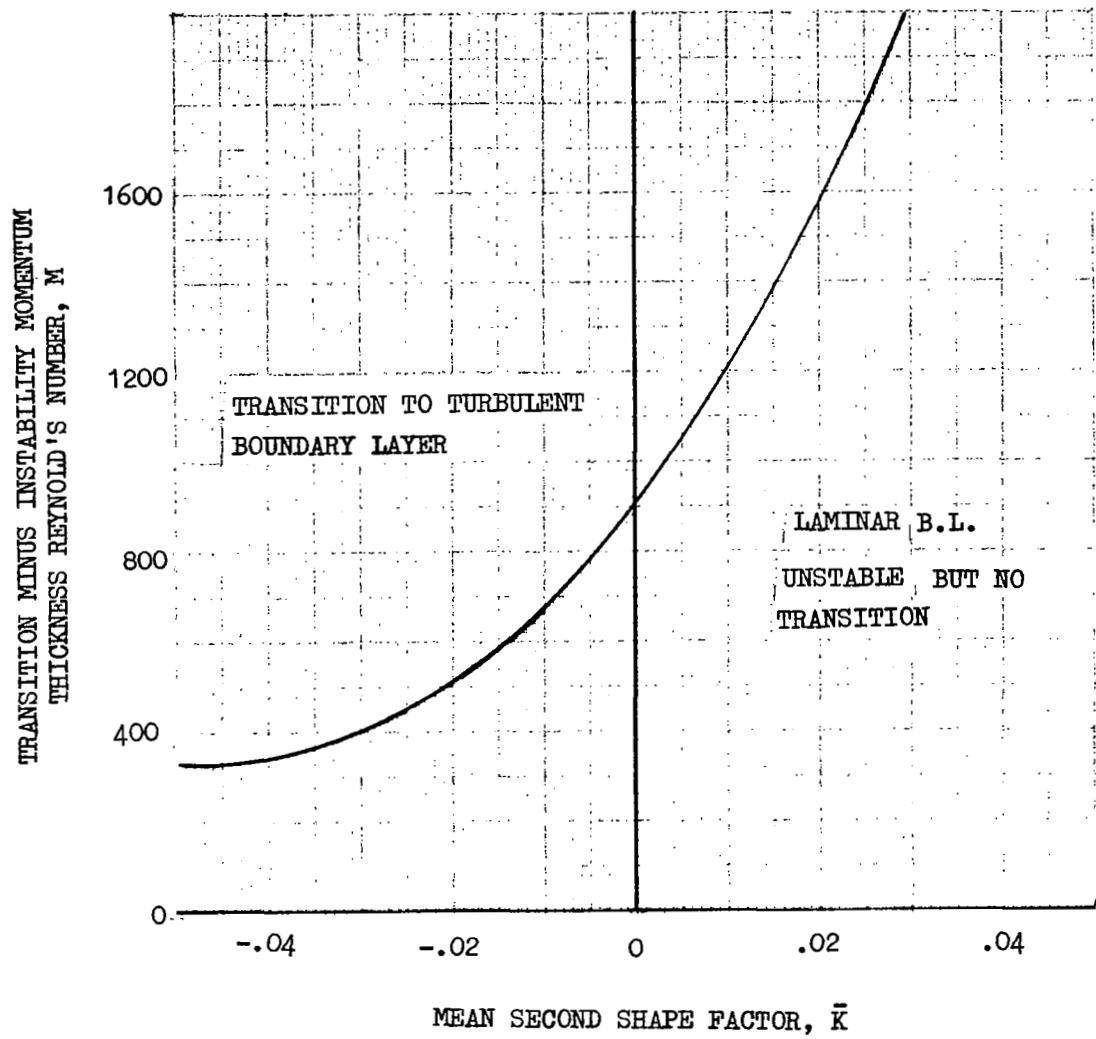
FIGURE V-7 —SHAPE OF THE PRESSURE
DISTRIBUTION NEAR STALL
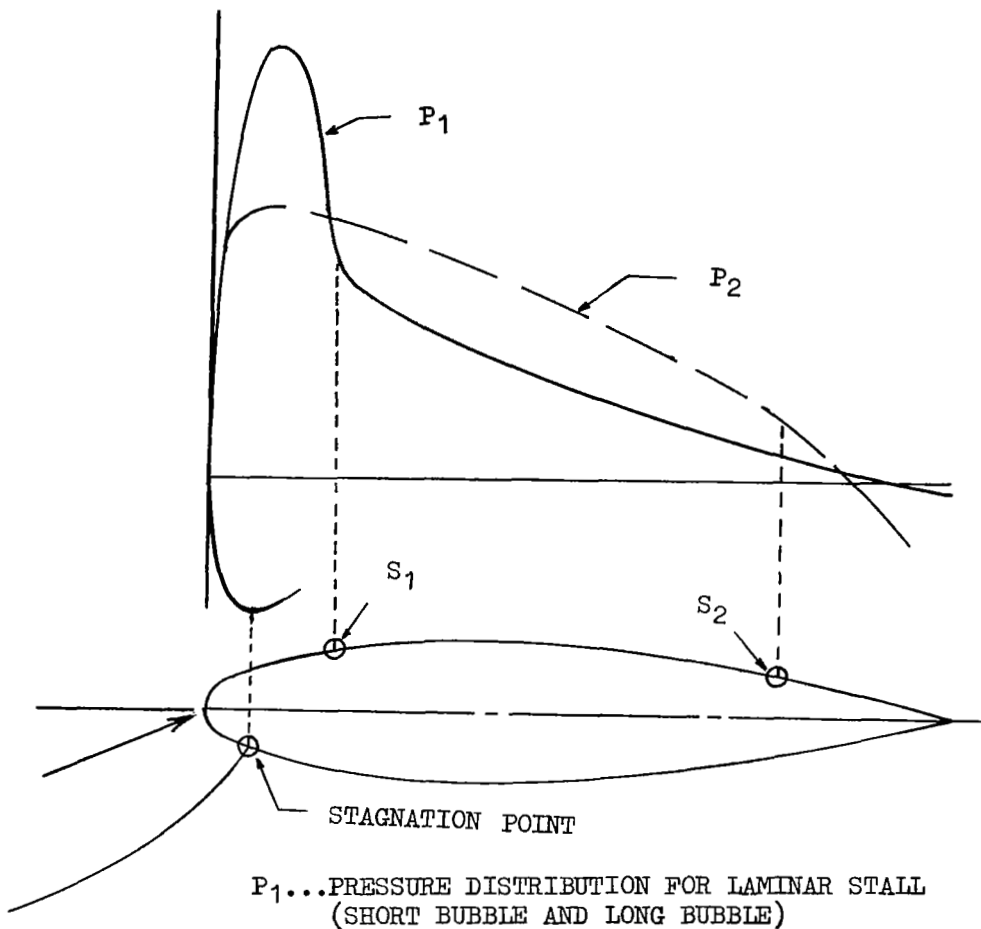
P_1...PRESSURE DISTRIBUTION FOR LAMINAR STALL
(SHORT BUBBLE AND LONG BUBBLE)

P_2...PRESSURE DISTRIBUTION FOR TURBULENT STALL
(TRAILING EDGE STALL)

S_1...POINT OF LAMINAR SEPARATION AND REATTACH-
MENT OR LAMINAR SEPARATION ONLY

S_2...POINT OF TURBULENT SEPARATION

FIGURE V-8.- TYPICAL AIRFOIL STALL PATTERNS
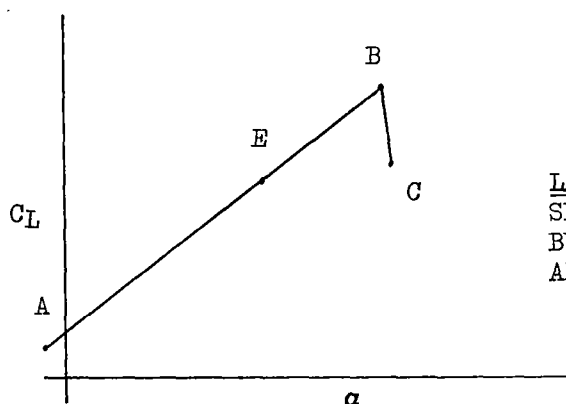
LAMINAR SHORT BUBBLE
SHORT BUBBLE AT S1
BURSTS AND C_L DROPS
ABRUPTLY FROM B TO C.
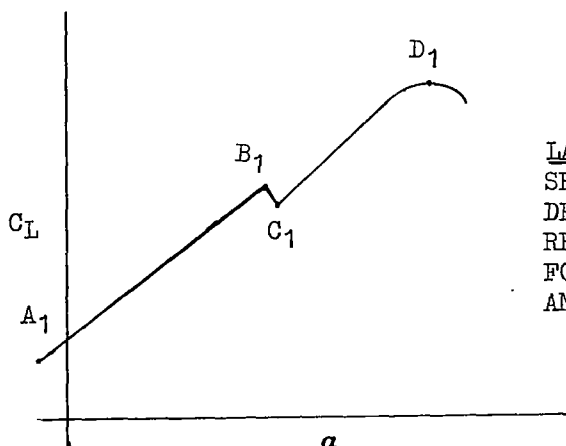
LAMINAR LONG BUBBLE
SHORT BUBBLE AT S1
DEVELOPS INTO EXTENDED
REGION OF SEPARATION
FOR C_L'S BETWEEN C_1
AND D_1, FLOW IS UNSTABLE
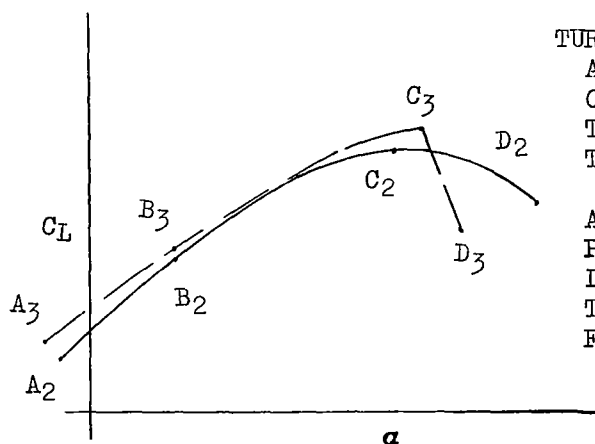
TURBULENT TRAILING EDGE STALL
$A_2B_2C_2D_2$ BOUNDARY LAYER
CHANGES FROM LAMINAR TO
TRANSITION TO TURBULENT AND
THEN SEPARATES AT C_2.

$A_3B_3C_3D_3$ BOUNDARY LAYER
PROGRESSES FROM LAMINAR TO
LOCAL SEPARATION THEN TO
TURBULENT REATTACHMENT AND
FINALLY TO TURBULENT SEPARATION.

FIGURE V-9
GORADIA-LYMAN CRITERIA FOR LAMINAR
STALL PREDICTION

The figure is a graph with the y-axis labeled $\frac{d\,M_e}{d(S/C)}$ and the x-axis labeled $\frac{U_e\theta}{\nu}$.

DATA SOURCE: REF V-18 THROUGH V-20

BUBBLE BURST AND LAMINAR STALL

SHORT BUBBLE AND REATTACHMENT
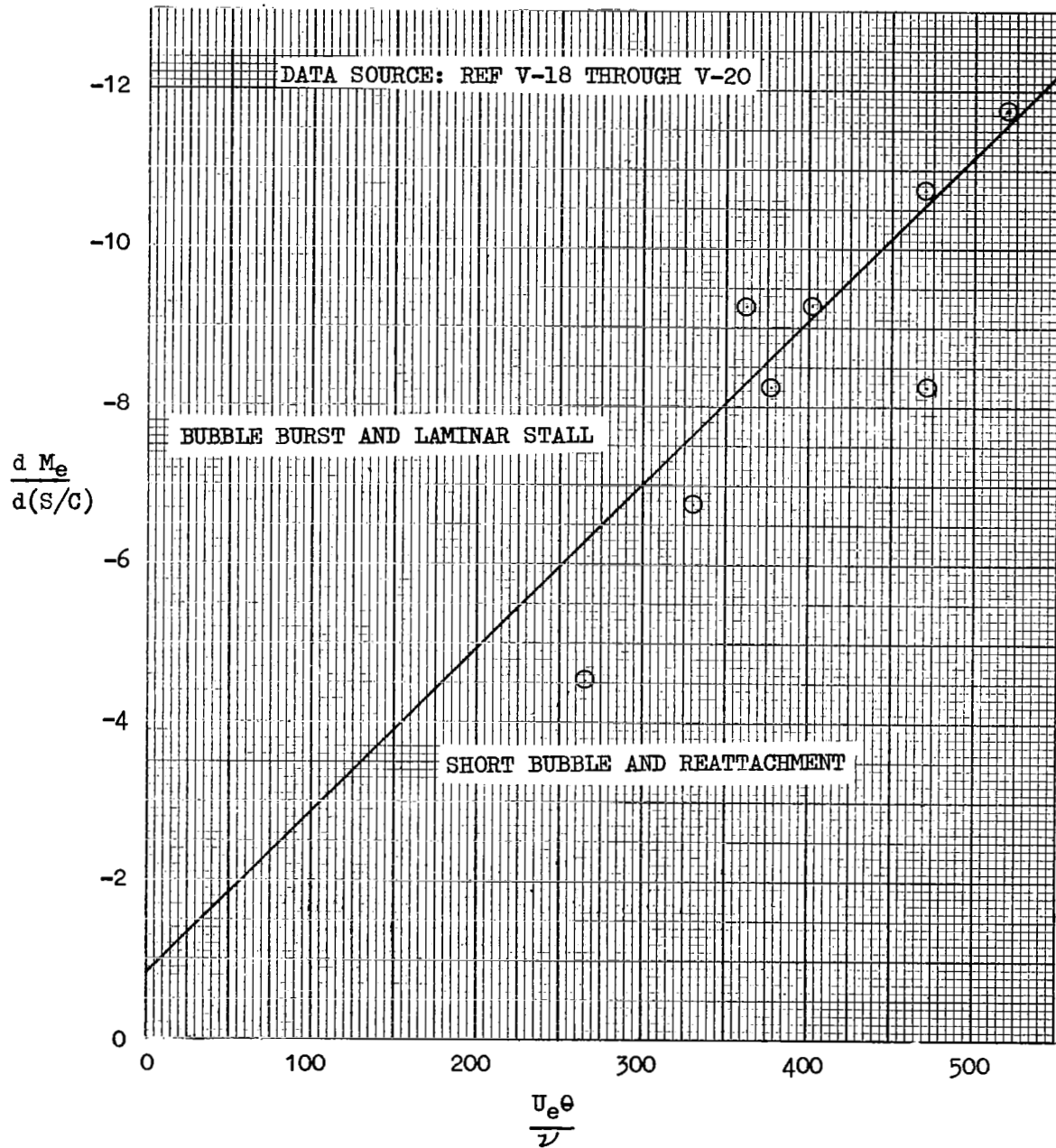
FIGURE V-10 — BOUNDARY-LAYER STABILITY/SEPARATION
CALCULATION SEQUENCE

Forward Stagnation Point
on Each Airfoil Component

Laminar Boundary Calcula-
tions to Compute

Check for Laminar Instabil-
ity Point from Theoretical
Schlicting-Ulrich Instabil-
ity Curve. FIG. V-5.

If Laminar Boundary Layer
Unstable Then Check for
Transition to TBL by Cri-
teria of   FIG. V-6

If Transition to
Turbulent B.L.
Indicated, Go to
Turbulent B.L. Comp.

If No Transition Indicated,
Check for Theoretical Laminar
Separation When $\frac{\theta^2}{\nu}\frac{du_e}{ds} = -.07$
& Check for Laminar Stall by
FIG. V-9.

If Short Bubble & Reattach-
ment Then Go to Ordinary Tur-
bulent B.L. Comp. If Stall In-
dicated by FIG. V-9 Then Stop
Cal.

STABILITY CURVE

$\left(\frac{U_e \theta}{\nu}\right)$ INSTABILITY

UNSTABLE

THEORETICAL
SCHLICTING-
ULRICH CURVE

STABLE

$\frac{\theta^2}{\nu}\frac{dU_e}{dS}$

$\left(\frac{U_e \theta}{\nu}\right)_{TRAN.} - \left(\frac{U_e \theta}{\nu}\right)_{INST.}$

TRANSITION TO
TURBULENT
B.L.

TRANSITION
CURVE

LAMINAR B.L. UNSTABLE
BUT NO TRANSITION

$$\frac{1}{(S/C) - (S/C)_{INST.}} \int_{S/C_{INS.}}^{S/C} \frac{\theta^2}{\nu}\frac{dU_e}{dS} dS$$

GORADIA-LYMAN CRITERIA FOR
LAMINAR STALL PREDICTION

$\frac{d M_e}{d S/C}$

BUBBLE BURST &
LAMINAR STALL

SHORT BUBBLE AND REATTACHMENT

$\left(\frac{U_e \theta}{\nu}\right)$ AT THEORETICAL
LAMINAR SEPARATION

FIGURE V-11.--LAMINAR BOUNDARY LAYER CORRELATION
NACA 0025 (REFERENCE V-22)

$C_l = 0.0$ $\quad\quad\quad\quad\quad\quad\quad\quad \alpha = 0^\circ$
$R_N = 3.2 \times 10^6$ $\quad M_\infty = 0.079$
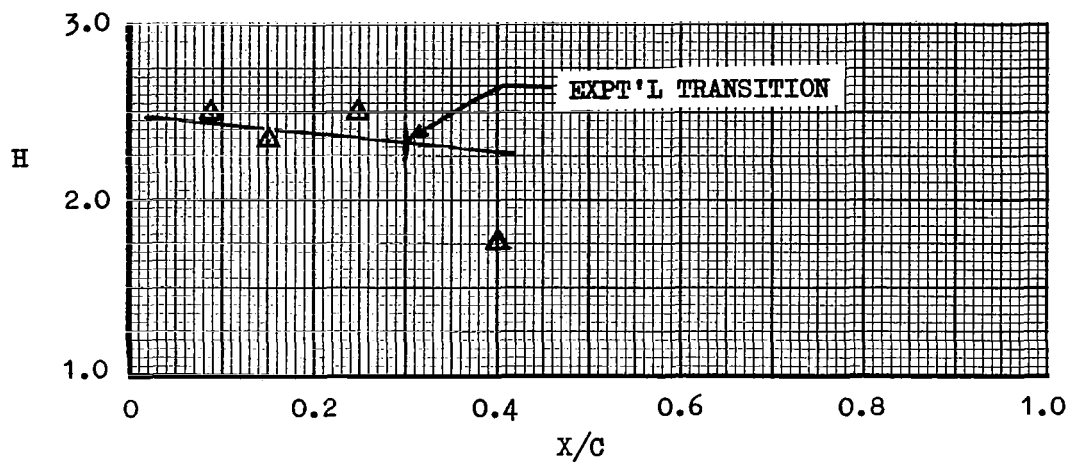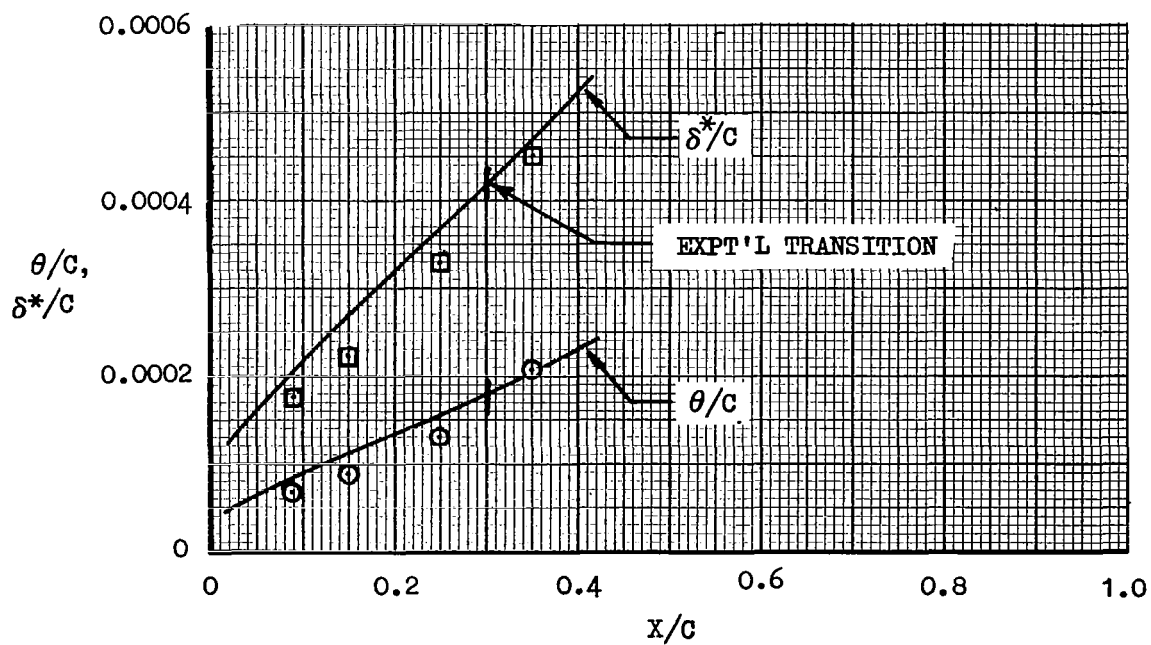
FIGURE V-12.- LAMINAR BOUNDARY LAYER CORRELATION
NACA 0012 (REFERENCE V-17)
$C_1 = -0.57$ $a = -5.2°$
$R_N = 3.35 \times 10^6$
$M_\infty = 0.079$
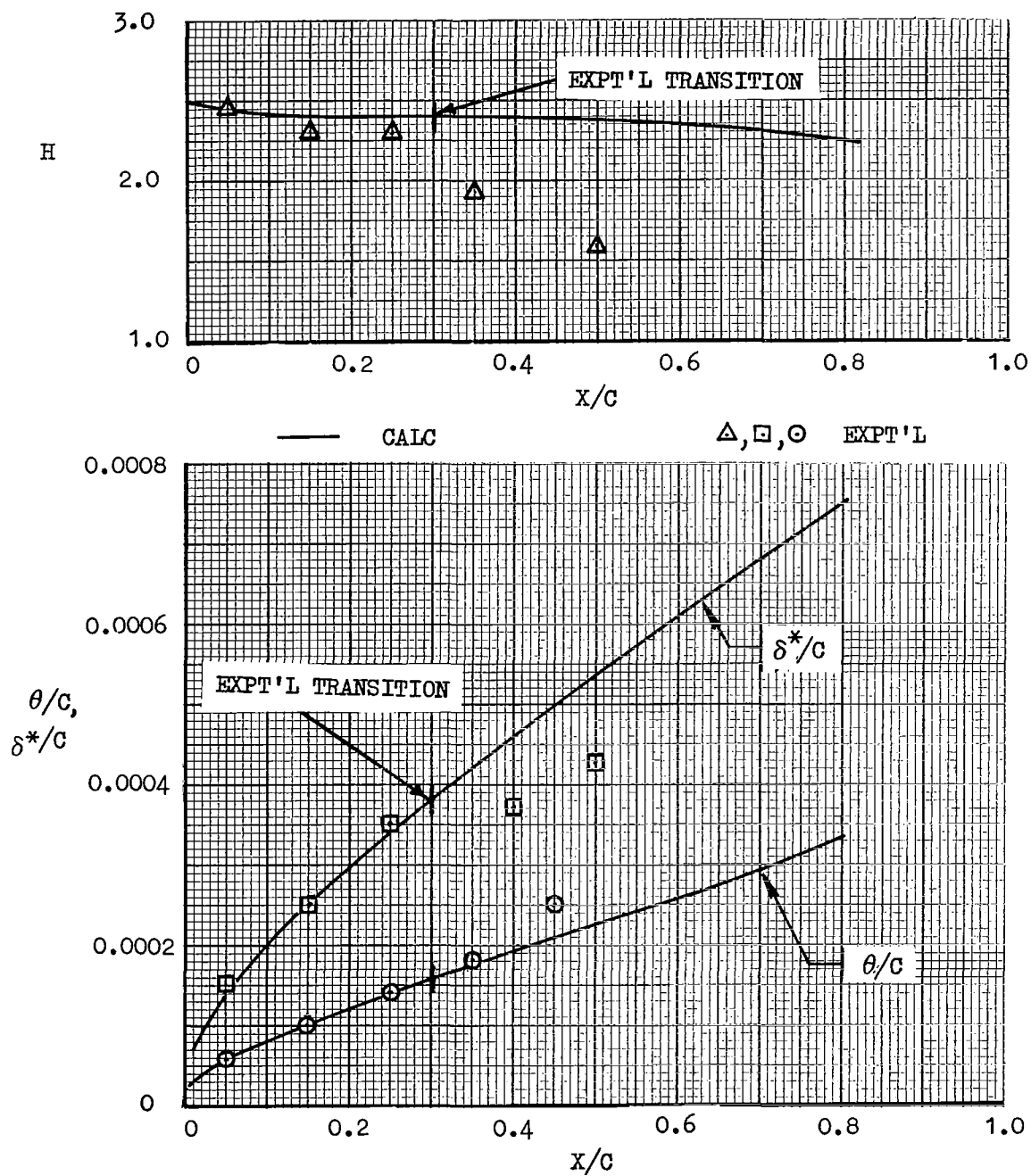
FIGURE V-13--LAMINAR BOUNDARY LAYER CORRELATION
NACA 0012 (REFERENCE V-17)
$C_l = 0.0 \quad \alpha = 0°$
$R_N = 10.25 \times 10^6$
$M_\infty = 0.284$
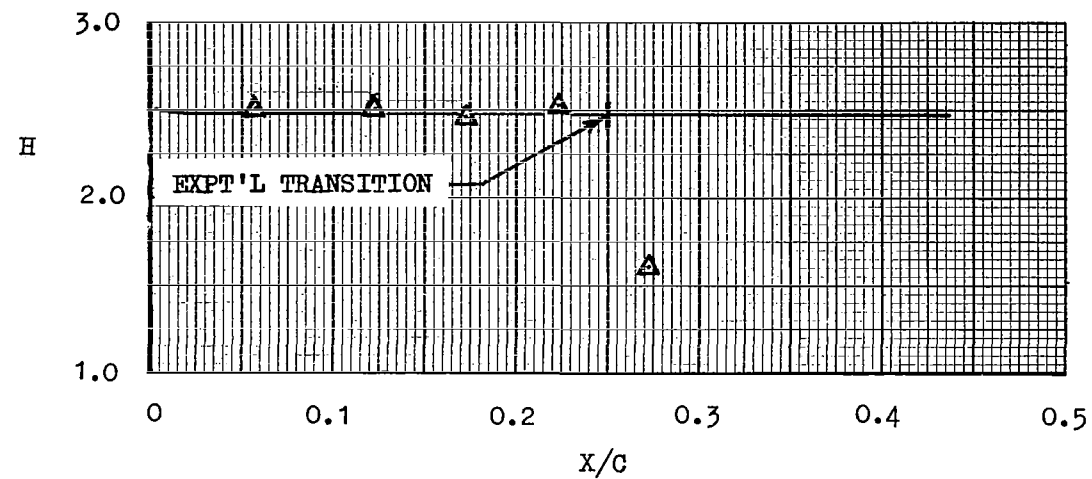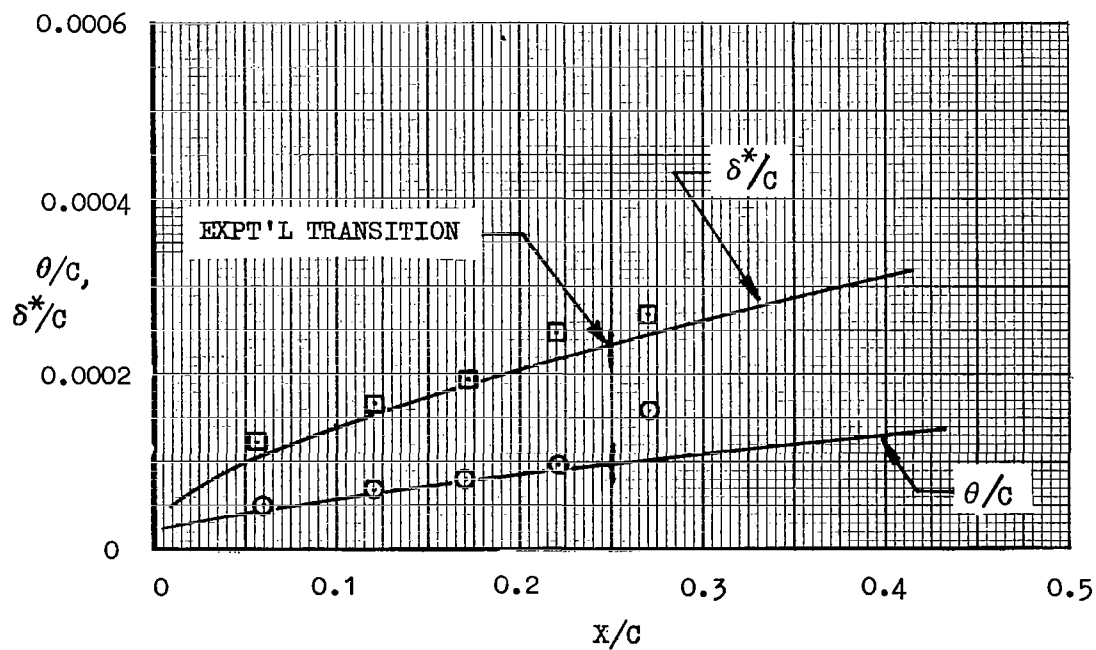
FIGURE V-14.- TRANSITION CORRELATION

SYM	AIRFOIL	R_N RANGE, $X10^{-6}$
⊙	NACA 0035	3.2
⊡	NACA 0025	3.2
△	NACA 0018	3.35
◇	NACA 0012	3.35 & 10.25
⬠	NACA 64A015	4.0 - 21.0
◁	NACA $65_2$15114	25 - 50
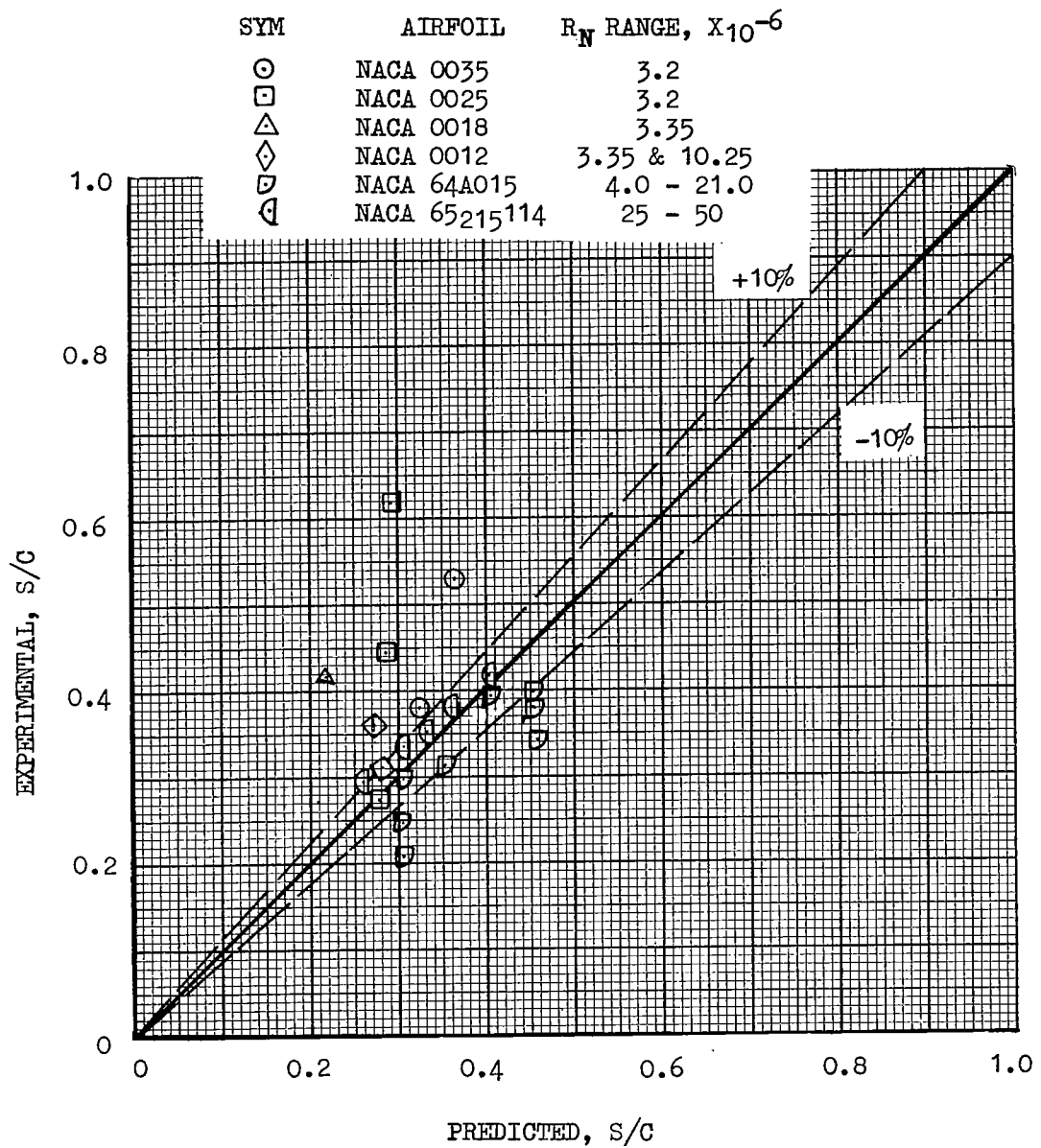
FIGURE V-15

COMPARISON OF PREDICTED AND EXPERIMENTAL LEADING-EDGE STALL

NACA 63A009 SECTION
$R_N = 5.8 \times 10^6$
(REF. V-18)
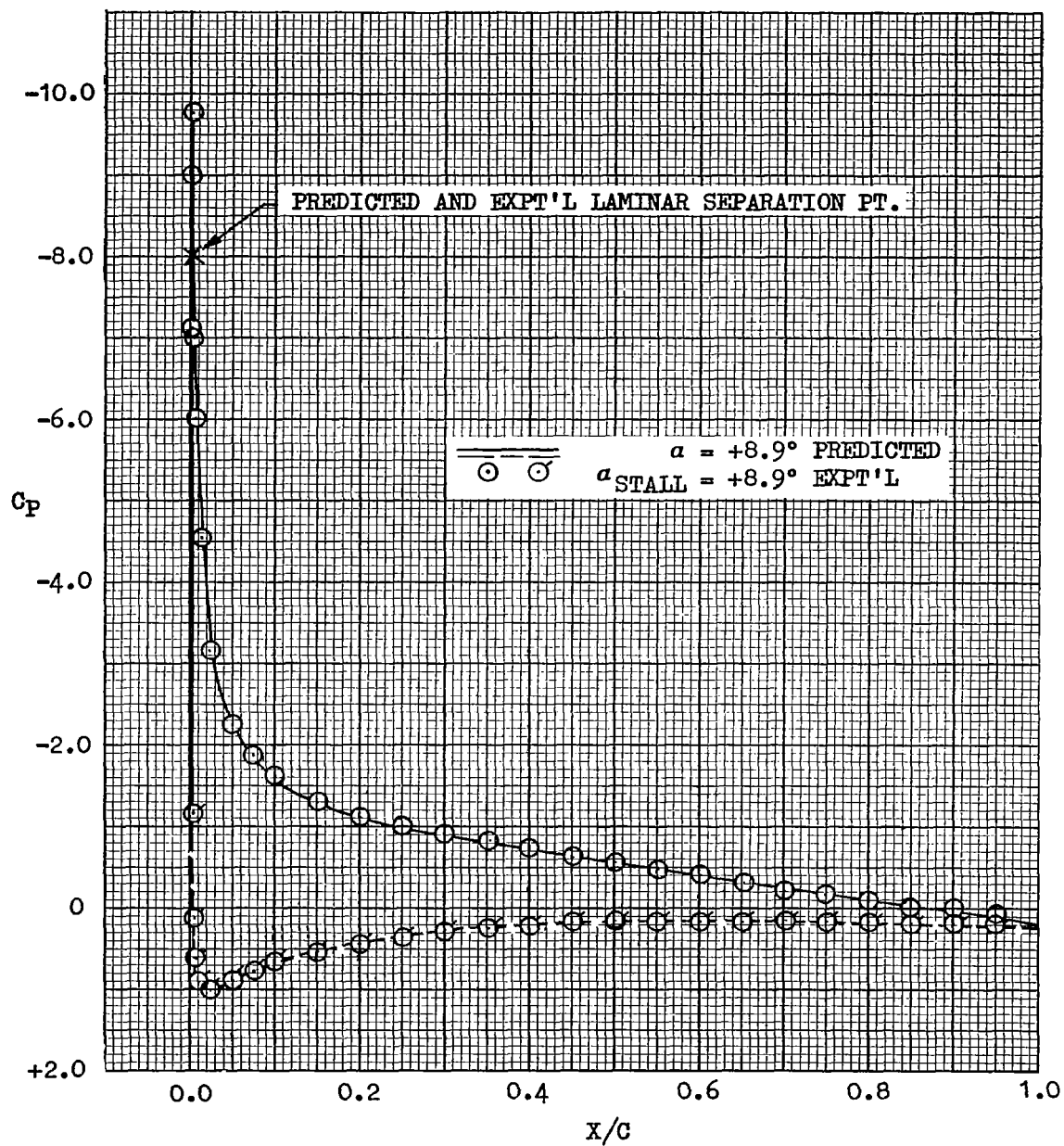
FIGURE V-16 ←LIFT-CURVE FOR NACA 63_1 - 012 SECTION

R_N = 5.8 X 10^6
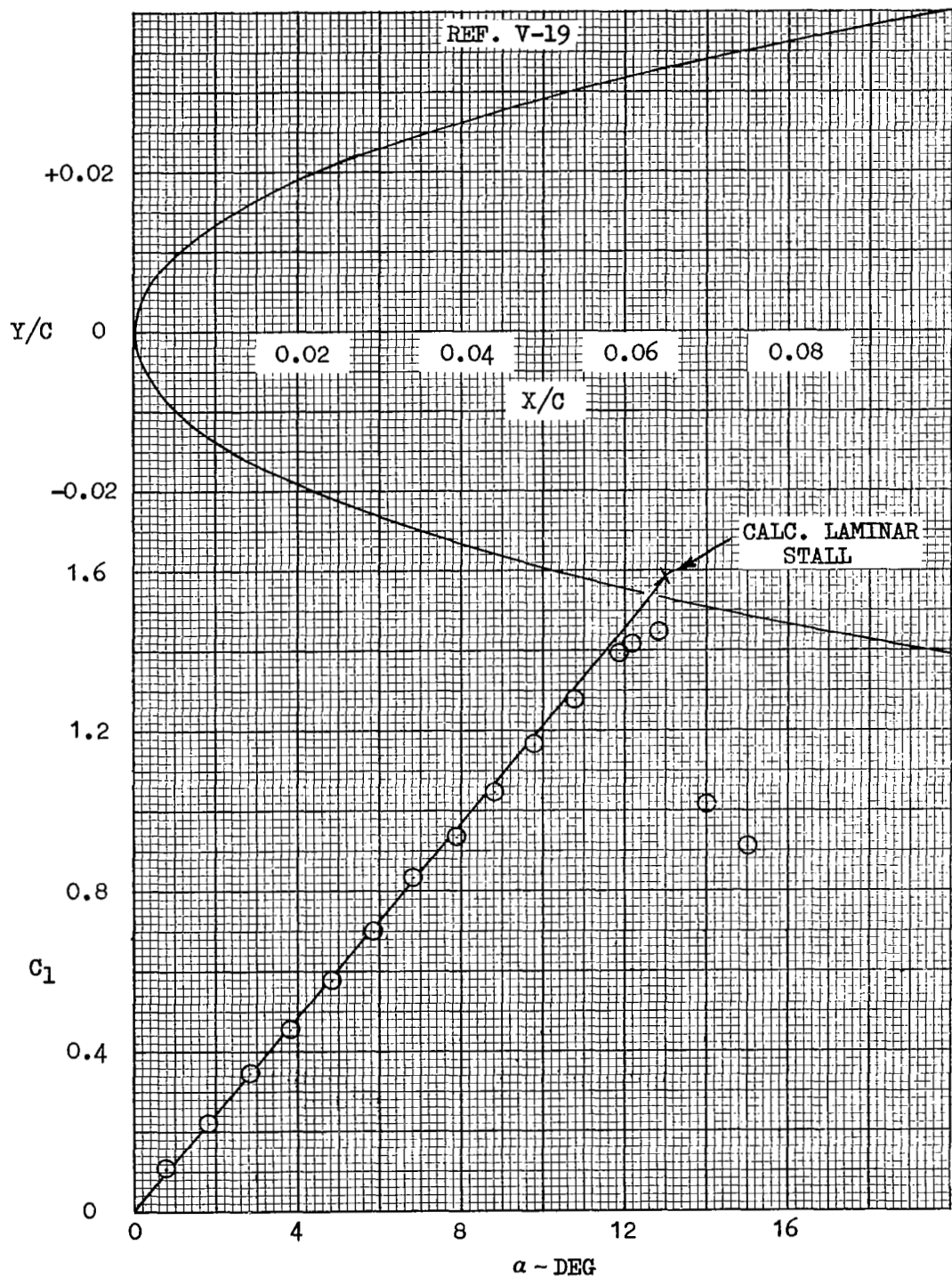
FIGURE V-17.-LIFT-CURVE FOR NACA 64A010 SECTION
$R_N = 4.0 \times 10^6$
(REF. V-20)
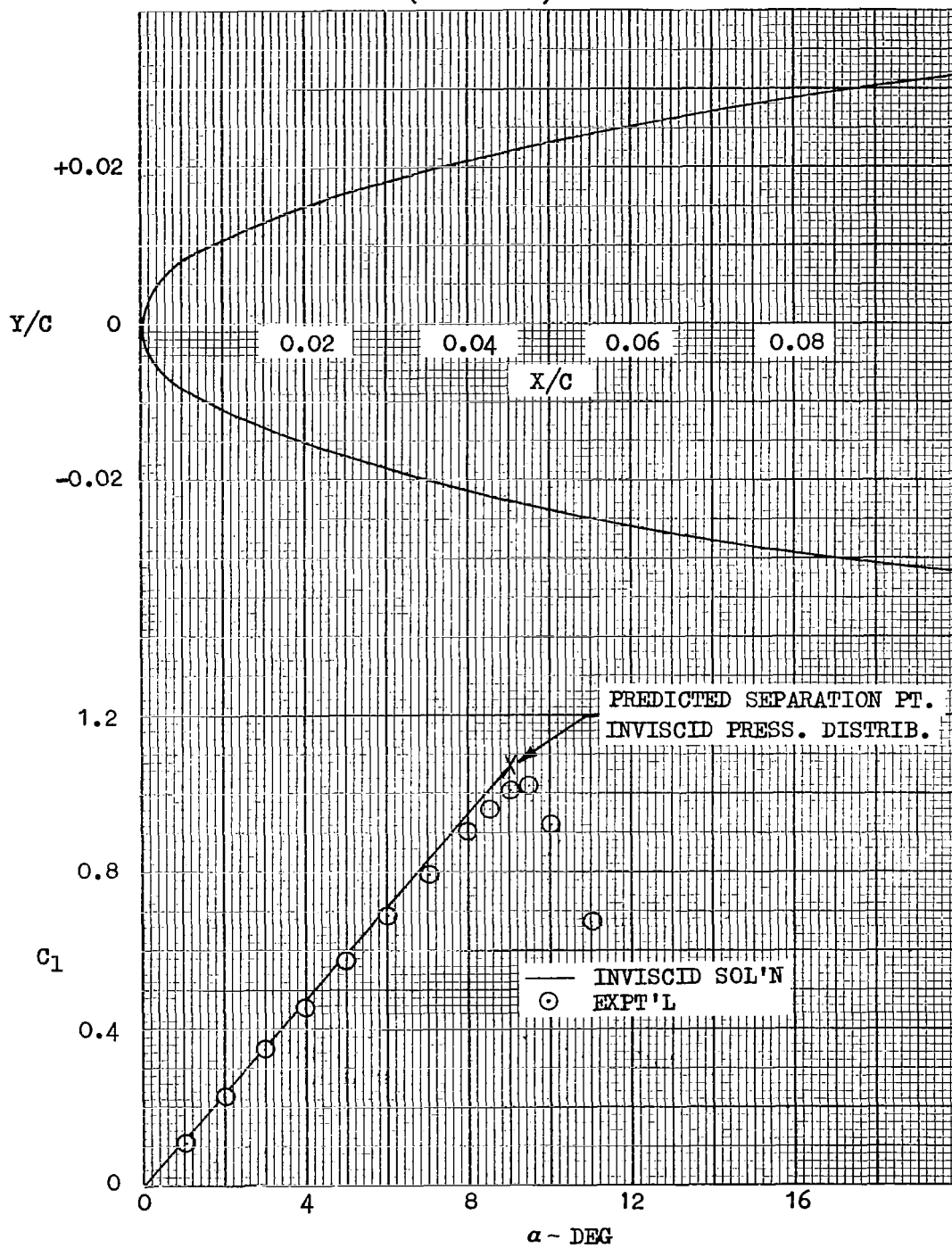
FIGURE V-18.—TURBULENT BOUNDARY LAYER
CORRELATION   NACA
$63_3 - 018$ (REFERENCE V-18)
$C_l = 0.74$ $a = +6°$
$R_N = 5.8 \times 10^6$ $M_\infty = 0.167$

——— CALC.   △,□,⊙   EXPT'L
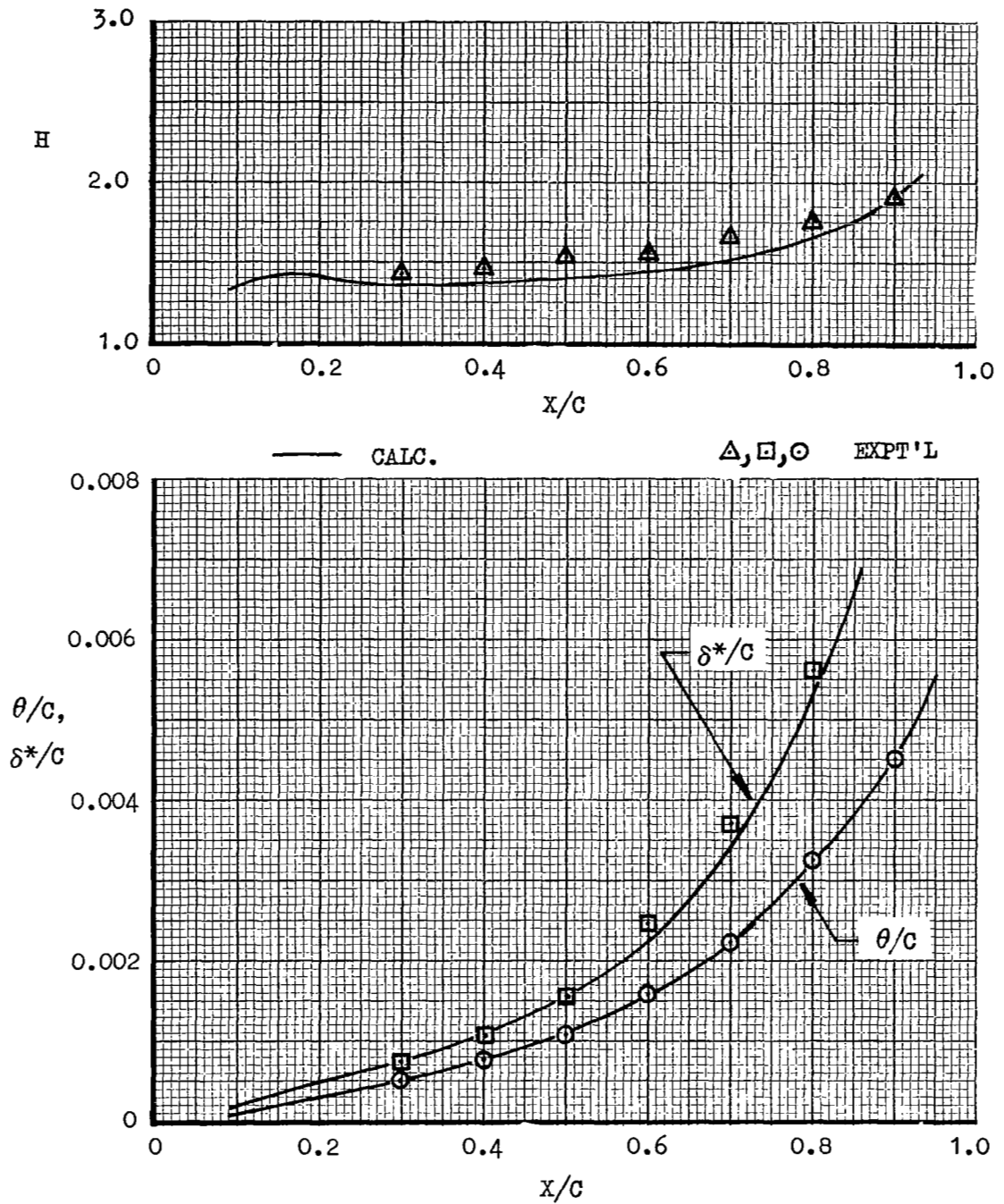
FIGURE V-19 — TURBULENT BOUNDARY LAYER CORRELATION
NACA 63_1 - 012 (REFERENCE V-19)
$C_l = 0.47$ $a = 3.8°$
$R_N = 5.8 \times 10^6$ $M_\infty = 0.167$
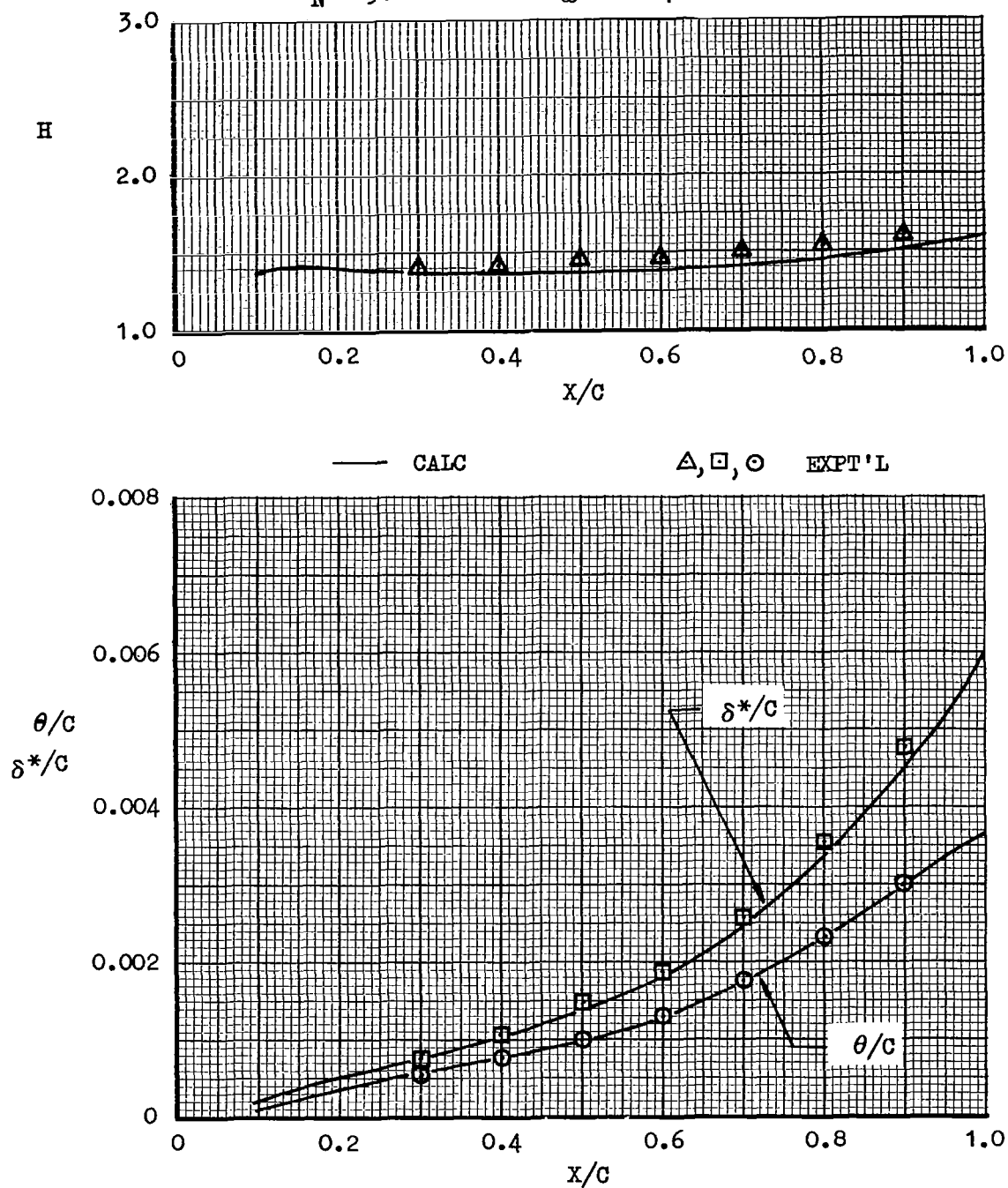
FIGURE V-20- TURBULENT BOUNDARY LAYER CORRELATION
NACA 63-009 (REFERENCE V-18)

$C_l = 0.48$ $\qquad a = 4.0°$
$R_N = 5.8 \times 10^6$ $\quad M_\infty = 0.167$
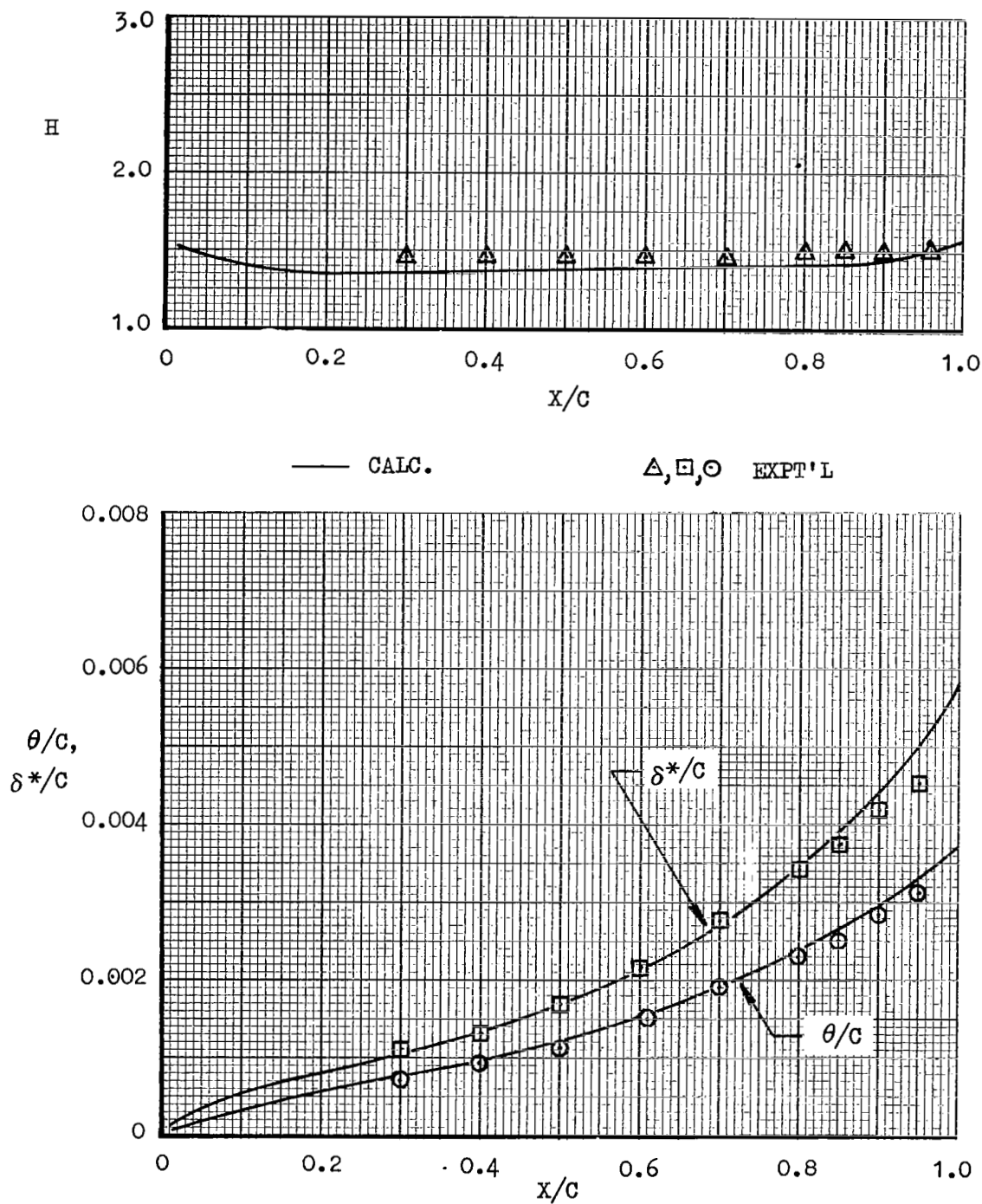
FIGURE V-21.- LAMINAR BOUNDARY LAYER PREDICTION EVALUATION

(REFERENCE V-1)
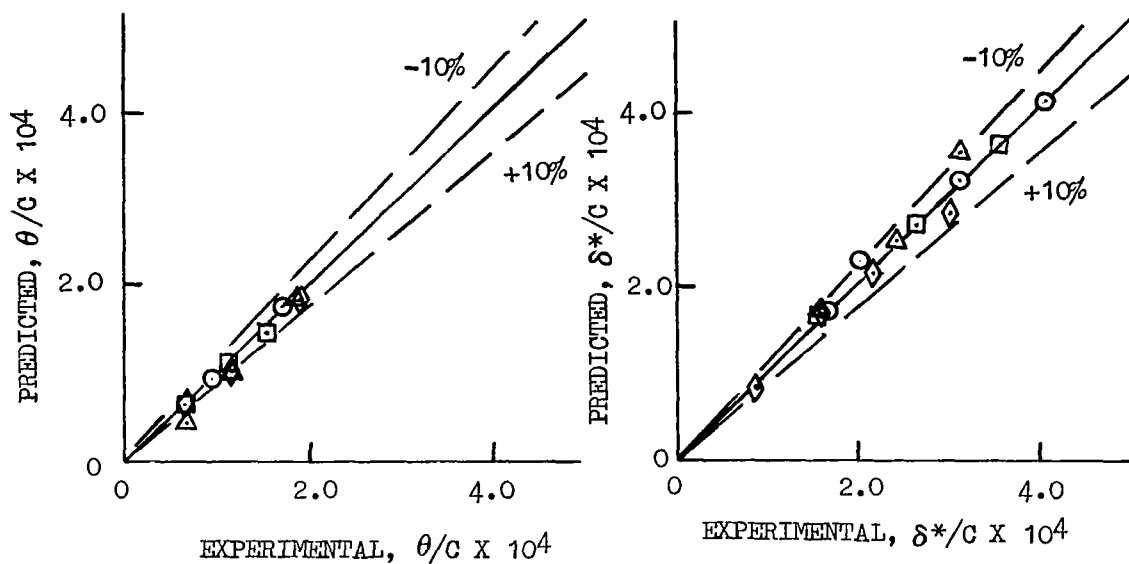
TURBULENT BOUNDARY LAYER
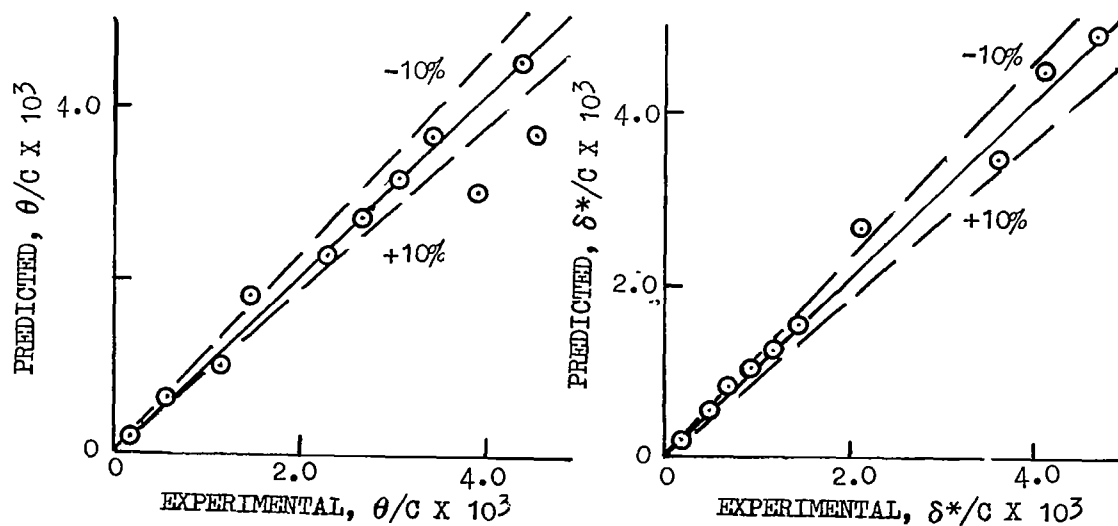
FIGURE V-22 - COMPARISON OF TURBULENT BOUNDARY LAYER MOMENTUM THICKNESS AS CALCULATED BY TWO METHODS

FAVORABLE PRESSURE GRADIENT

NASH BL MODEL
⊙ ⊘ GORADIA'S APPROX. BL MODEL

θ/c

s/c

ADVERSE PRESS. GRADIENT

HIGH ADVERSE PRESSURE GRADIENT

MILD ADVERSE PRESSURE GRADIENT

θ/c

x/c

76
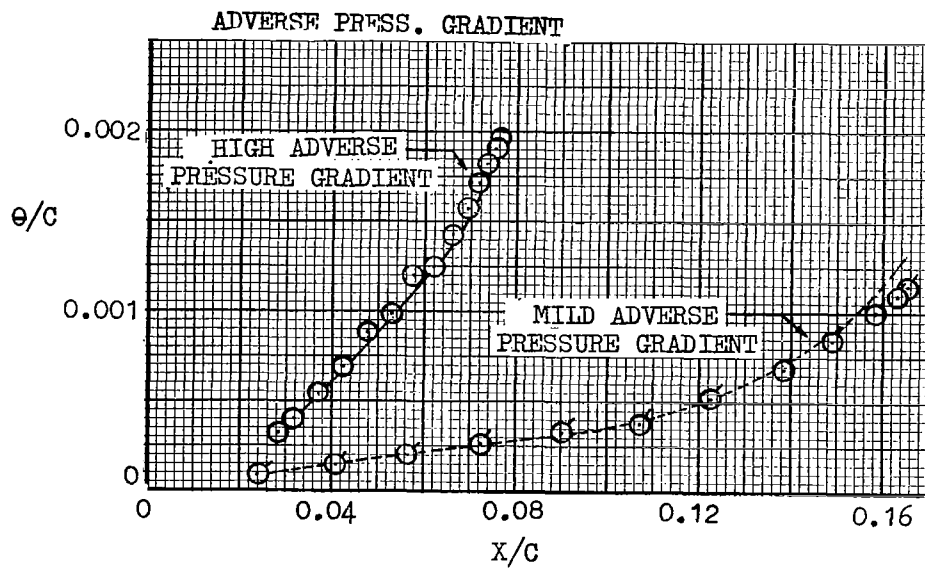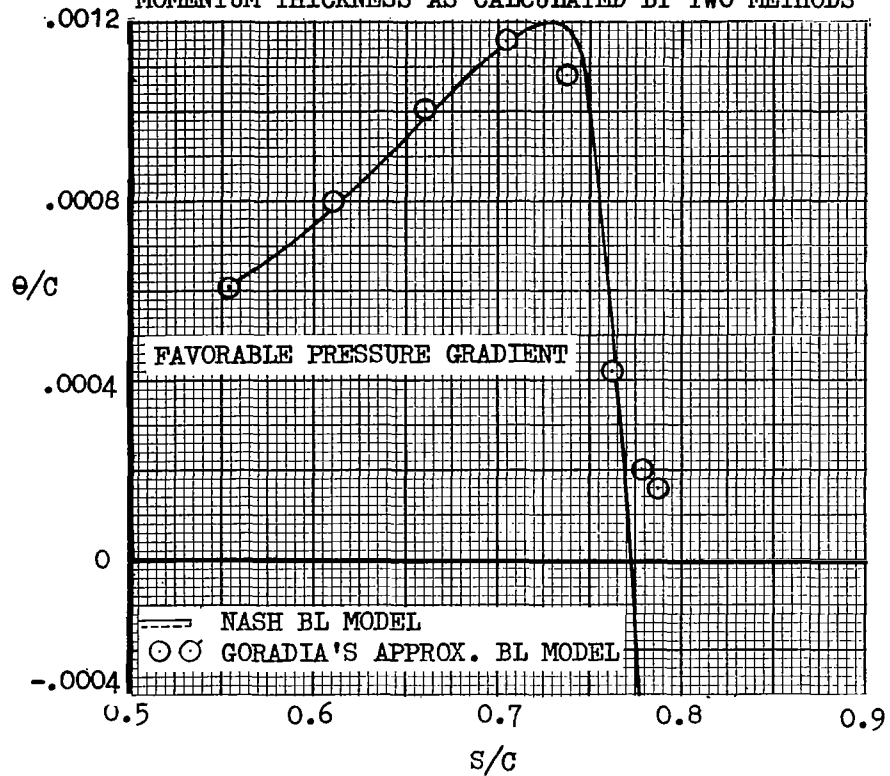
FIGURE V-23 - CORRELATION OF TURBULENT BOUNDARY LAYER FORM FACTOR AS CALCULATED BY TWO METHODS
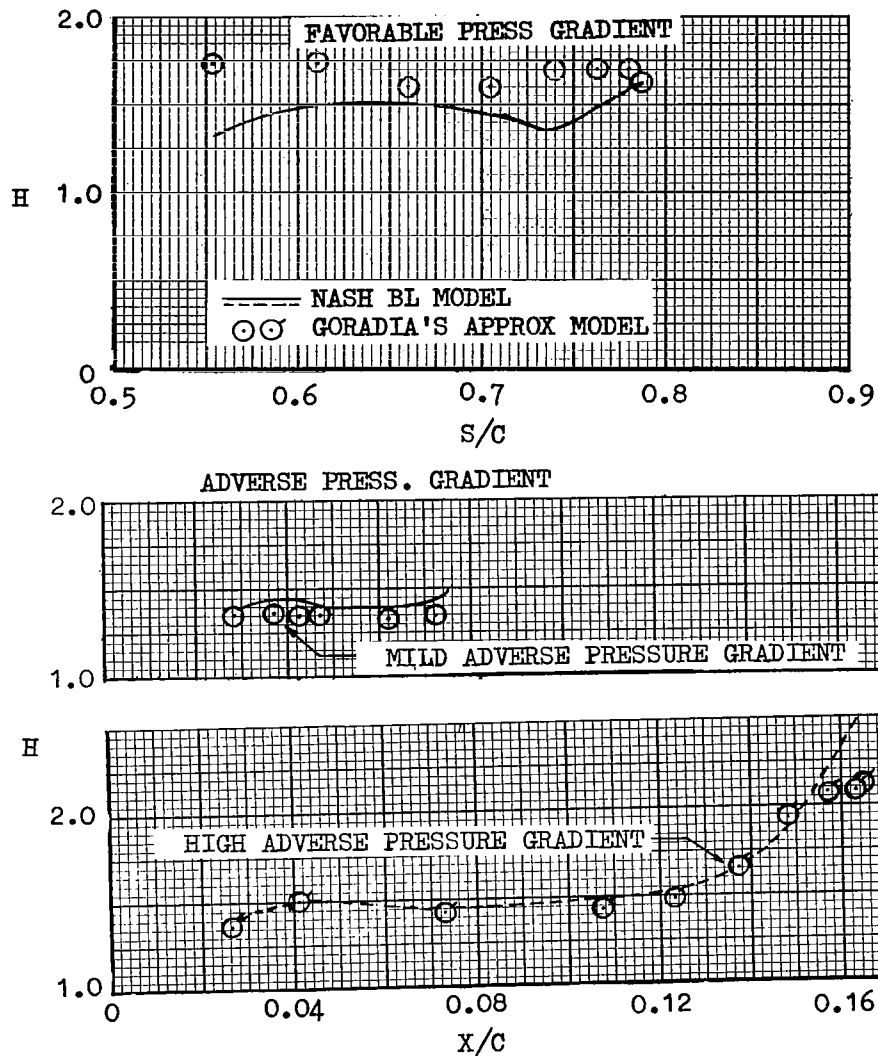
VI - EQUIVALENT AIRFOIL (SINGLE ELEMENT)

Airfoil Representation. - The boundary layer is assumed to have two basic effects on the pressure distribution obtained on a single-component airfoil. The major effect is depicted in Figure VI-1(a). This effect is treated as a modification of the camber line and represents an effective decrease in the angle-of-attack. The change in camber is found by using the upper and lower surface displacement thicknesses and halving the sum as shown. Since the potential flow computation is very sensitive to surface fluctuations, the entire displacement thickness array for any given component is smoothed three times. A standard least squares smoothing technique is applied in such a manner as to keep $\delta^*_{T.E.}$ fixed. The primary consequence of this modification is to reduce the airfoil loading.

The pressure distribution still tends to a stagnation condition at the trailing edge which artificially over-thickens the boundary layer in that region. In the actual case, the thickness effects due to the existence of the boundary layer tend to relieve the stagnation condition in the trailing-edge region. This effect is somewhat less pronounced than the effective camber shift. Hence, it is assumed that this effect can be computed by linear superposition as illustrated in Figure VI-1(b). First the actual airfoil is uncambered to produce a symmetrical case for $\left(\frac{V}{V_\infty}\right)_{BT}$. The displacement thickness from the boundary layer is added symmetrically to yield a $\left(\frac{V}{V_\infty}\right)_{BT+BL}$. This computation is accomplished by decreasing the wake thickness exponentially behind the airfoil to a sharp trailing edge. Now,

$$\Delta\left(\frac{V}{V_\infty}\right) = \left(\frac{V}{V_\infty}\right)_{BT+BL} - \left(\frac{V}{V_\infty}\right)_{BT} \qquad (VI-1)$$

which gives an approximation to the thickness relief effect and is added to the camber modification solution. This modified pressure distribution is then used to compute a new boundary layer.

The iteration procedure is basically to compute a local Mach number distribution over the airfoil and a boundary layer based on this distribution. The computed boundary layer is then used to modify the effective airfoil geometry based on the displacement thickness and the procedure is repeated until the normal force coefficient stops changing more than some predetermined amount. If this procedure is followed exactly, the solution will converge with some tendency to over-correct the solution on each iteration. Therefore, the effective airfoil is found by using two-thirds of the current solution and one-third of the previous solution.

It is found through use of the program that by retaining the trailing-edge pressure as computed by the potential-flow solution fluctuations can be introduced into the iterative process through the influence of local Mach gradients on boundary layer build-up. Additionally, highly localized but rapid changes in Mach gradient can create undesirable "kinks" in the equivalent airfoil camber line. To avoid these possible difficulties, are extrapolation and smoothing

process is utilized over the last few trailing-edge control points of the single airfoil.

In the Mach number extrapolation process, the last two computed Mach numbers on the trailing-edge upper surface are discarded and a least-squares, linear curve fit is applied to the five points immediately upstream. The linear fit is then moved so as to provide a quantitative match at the most forward point (i.e. the seventh computed Mach number upstream of the trailing edge). The extrapolation of the linear fit to the trailing-edge provides the upper surface trailing-edge Mach number. On the lower surface trailing-edge, the last three computed Mach numbers are deleted and the last point replaced by the extrapolated upper-surface value. A second-order Mach number variation is then applied between the trailing-edge Mach number and the fourth and fifth computed points upstream of the trailing-edge. These modified values of local Mach number are used only in the calculation of the local boundary layer characteristics. The actual computed values are printed out in the pressure coefficient listing.

In addition to the trailing-edge Mach number, the values of trailing-edge δ^* on both upper and lower surfaces are obtained similarly by the extrapolation of a least-squares linear fit over the last seven computed points.

Finally, to assure a highly stable convergence to the final viscous solution, the function, δ^* vs. θ_{ij}, is smoothed three times by a least-squares process to remove local discontinuities in the equivalent camber line. This smoothing process is applied to both upper and lower surfaces.

In utilizing the iterative technique to obtain a viscous solution, the initial boundary layer calculation is performed on the basis of the potential-flow pressures. Generally speaking, in successive iterations, the equivalent airfoil loading, and thus local pressure gradients, are gradually reduced as the upper-surface boundary layer tends to uncamber the "original" airfoil. In cases where the viscous solution tends to exhibit marginally-critical pressure gradients, program shutdown can be encountered in the first iteration as a result of the more adverse pressure gradients exhibited in the potential distribution. This effect constitutes more of a problem area to the multiple airfoil calculations than in the single-element case since highly adverse gradients can exist with the former, even at low angles-of-attack. To circumvent program shutdown during the iteration process, the modified boundary layer model is used throughout. Thus, as the final viscous solution is approached, the extreme gradients characterizing the potential-flow solution are relieved by the uncambering effect of the equivalent airfoil. During the third, fourth and fifth iterations, the boundary layer characteristics as defined by the accurate Nash turbulent boundary-layer model are also calculated and printed. This is done to afford a quantitative parameter comparison for the two models and to properly identify possible separation points by the more refined model in the last few iterations. Incorporating both boundary layer models within the program adds significantly to the flexibility of the iterative scheme. With only a slight program modification the iteration can be continued on the basis of the more accurate Nash model only or this model can be brought into the equivalent airfoil calculations at an earlier stage. For the correlations considered herein, however, such refinements did not appear to significantly alter the final viscous solution.

Correlation. - Three single-element airfoils were chosen as representative for correlation purposes for this report. All of these airfoils have experimental results which are readily available in the literature. The NACA 63-009 is a typical, symmetrical-cusped thickness distribution. The correlation of pressure distribution and boundary layer parameters is shown in Figures VI-3 and VI-4, respectively. Force and moment comparisons for the NACA 63-009 airfoil are given in Figure VI-5.

The theoretical results were obtained by viscous iteration in the computer at the same angle-of-attack as the experimental data rather than the same C_1 as is the common practice. The reason for this approach is that program results would normally be used to predict variations with angle-of-attack. Constant C_1 is commonly used due to the difficulty in evaluating the true aerodynamic angle-of-attack of the airfoil under test conditions which may be peculiar to the test facility. For instance, the C_{1_a} - curve of Figure VI-5 would compare even more favorably if the experimental data were taken from Reference VI-1. In this case, the experimental results were taken from Reference VI-2 since the pressure and boundary layer data are from the same reference.

The second and third airfoils, NACA 23012 and NACA 64A010, were chosen for correlation examples since these are the basic airfoils used in deriving the multiple-component cases. Data similar to those presented for the 63-009 airfoil are provided in Figures VI-6 through VI-8 for the NACA 23012. Figures VI-9 and VI-10 compare pressure distributions and force data, respectively, for the NACA 64A010 airfoil. A source of experimental boundary layer parameters is lacking in the latter case.

In all three cases, the moment coefficient is presented as C_m about the nose of the airfoil since this is the manner it is computed for the individual components in the basic program. Thus, an airfoil with zero moment about the quarter chord would generate a straight line with a (dC_m/dC_1) of 0.25 on these plots.

In all of these correlation cases, the number of iterations used in the program varied from four to six, with the lower number corresponding to the lower a -ranges. These three correlation cases indicate that, in the case of the single-element airfoil, the computer program output provides reasonable agreement with experiment in terms of pressure distribution, force characteristics and boundary-layer parameters. Additional correlation should be performed to more clearly establish any significant trends in the slight differences between experiment and calculations, particularly on the pitching moment which appears to be the more sensitive parameter.

VI - SYMBOLS

C   Airfoil chord

C_l Section lift coefficient

C_m Section moment coefficient about the nose of the airfoil

C_{l_α} $\dfrac{d\,C_l}{d\,\alpha}$

H   Boundary layer form factor,

i   Iteration number

M_{TE} Local Mach number at the trailing edge

M_{TE_0} Local Mach number at the trailing edge from basic potential flow solution

S   Distance along surface

U_e Velocity at edge of boundary layer

$\left(\dfrac{\Delta v}{V_\infty}\right)$ Increment due to boundary layer thickness

$\left(\dfrac{v}{V_\infty}\right)$ Local velocity ratio

δ^* Boundary layer displacement thickness

θ Boundary layer momentum thickness

ρ Density

τ_0 Wall shear stress

Subscripts:

BL   Boundary layer

BT   Basic thickness

BL + BT   Boundary layer plus basic thickness

VI - REFERENCES

1. Abbott, Ira H. and Doenhoff, Albert E.: Theory of Wing Sections, 1949

2. Gault, Donald E.: Boundary-Layer and Stalling Characteristics of the NACA 63-009 Airfoil Section, NACA TN 1894

3. Wenzinger, Carl J: Pressure Distribution Over an NACA 23012 Airfoil with an NACA 23012 External-Airfoil Flap, NACA Report No. 614, 1937

4. Peterson, Robert F: The Boundary-Layer and Stalling Characteristics of the NACA 64A010 Airfoil Section, NACA TN 2235, 1950

FIGURE VI-1 — AIRFOIL GEOMETRY MODIFICATION
DUE TO BOUNDARY LAYER

(a)
CAMBER MODIFICATION

(b)
THICKNESS RELIEF
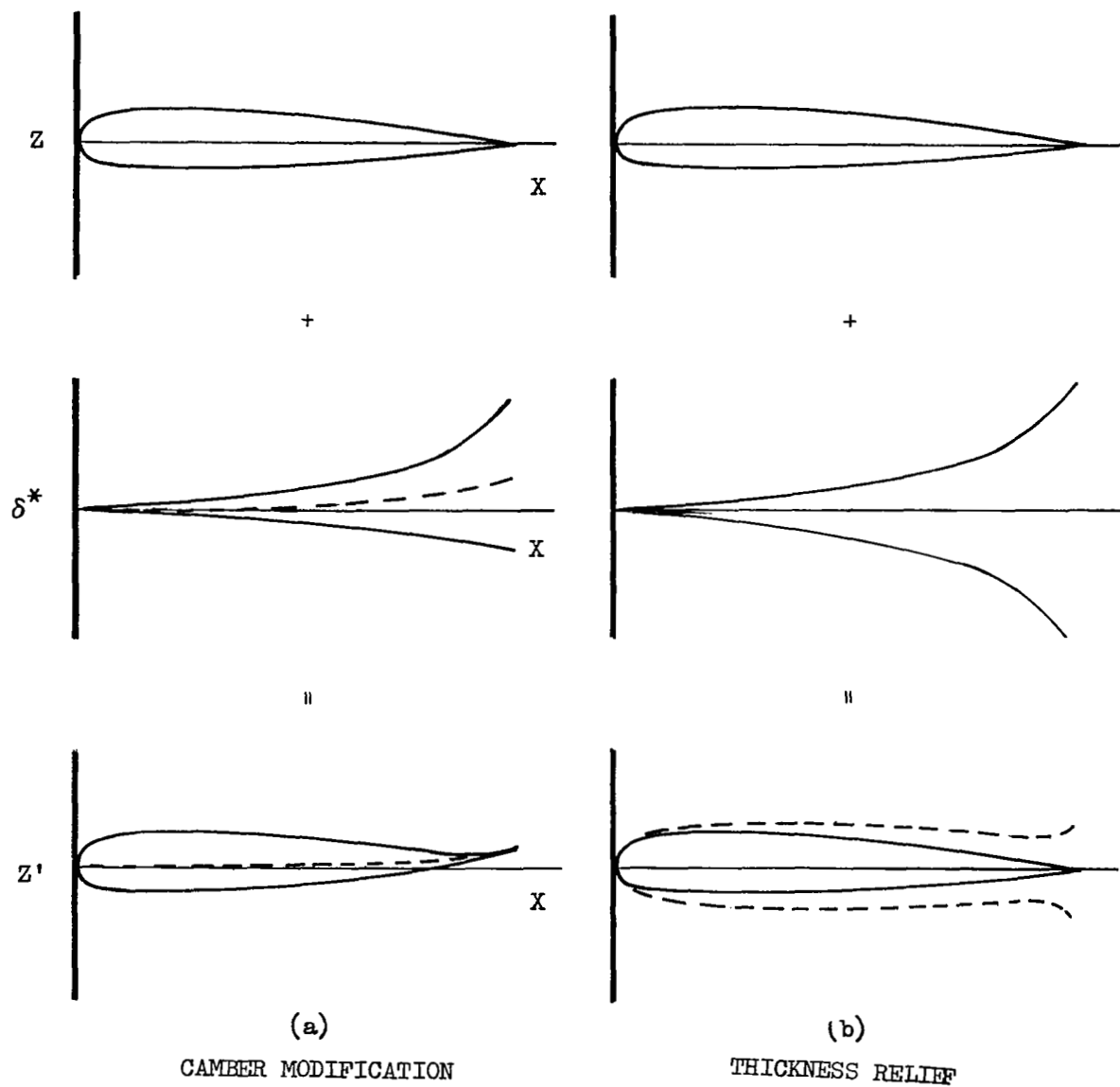
FIGURE VI-2—COMPARISON OF PREDICTED AND
EXPERIMENTAL PRESSURE DISTRIBUTION
FOR NACA 63-009 AIRFOIL
$M_\infty = 0.167$ $a = 8.5°$ $R_N = 5.8 \times 10^6$
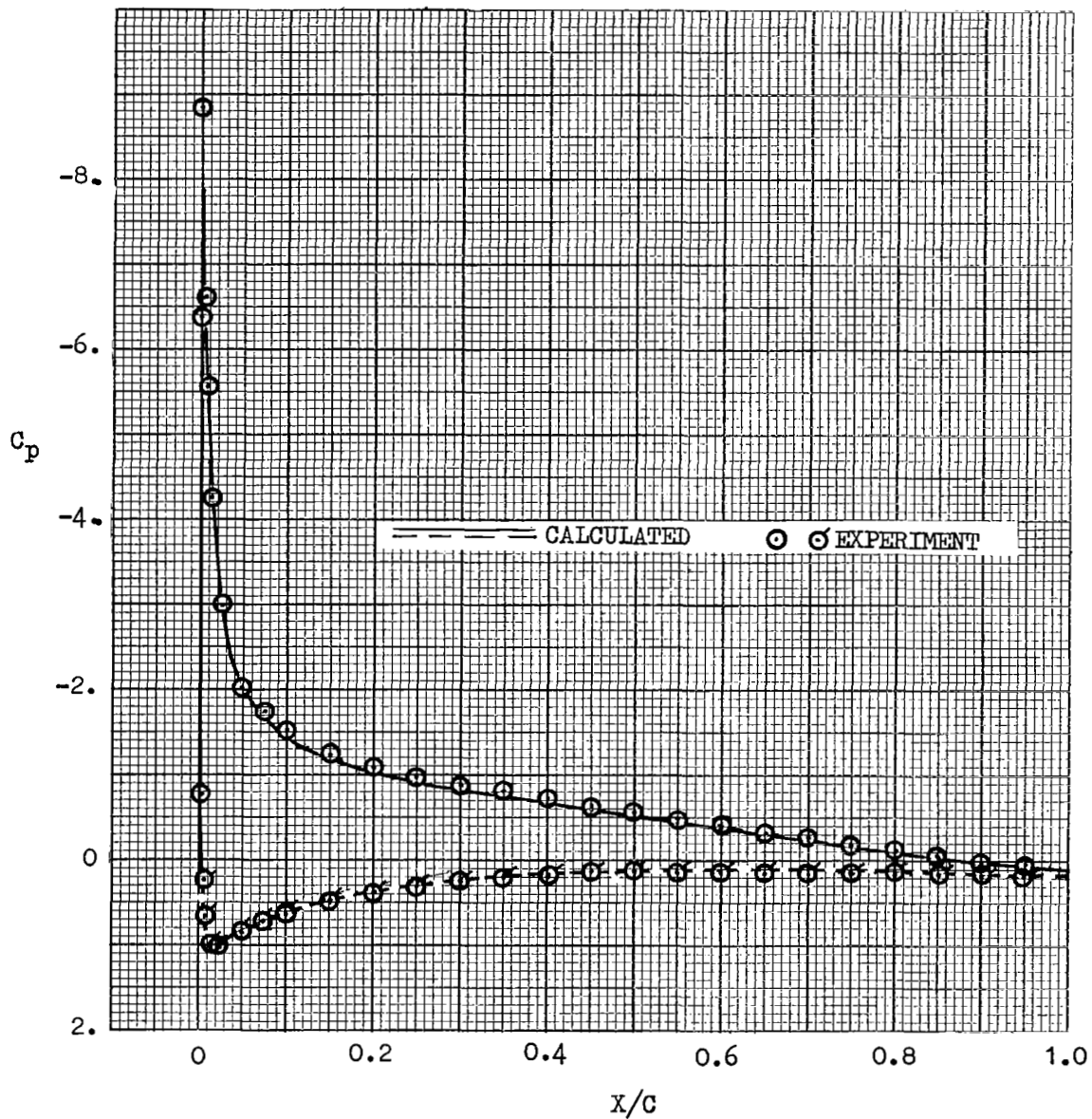
(REF. VI-2)

FIGURE VI-3 – COMPARISON OF PREDICTED AND
EXPERIMENTAL BOUNDARY LAYER
PARAMETERS FOR NACA 63-009 AIRFOIL
$M_\infty = 0.167$ $a = 8.5°$ $R_N = 5.8 \times 10^6$
(REF. VI-2)
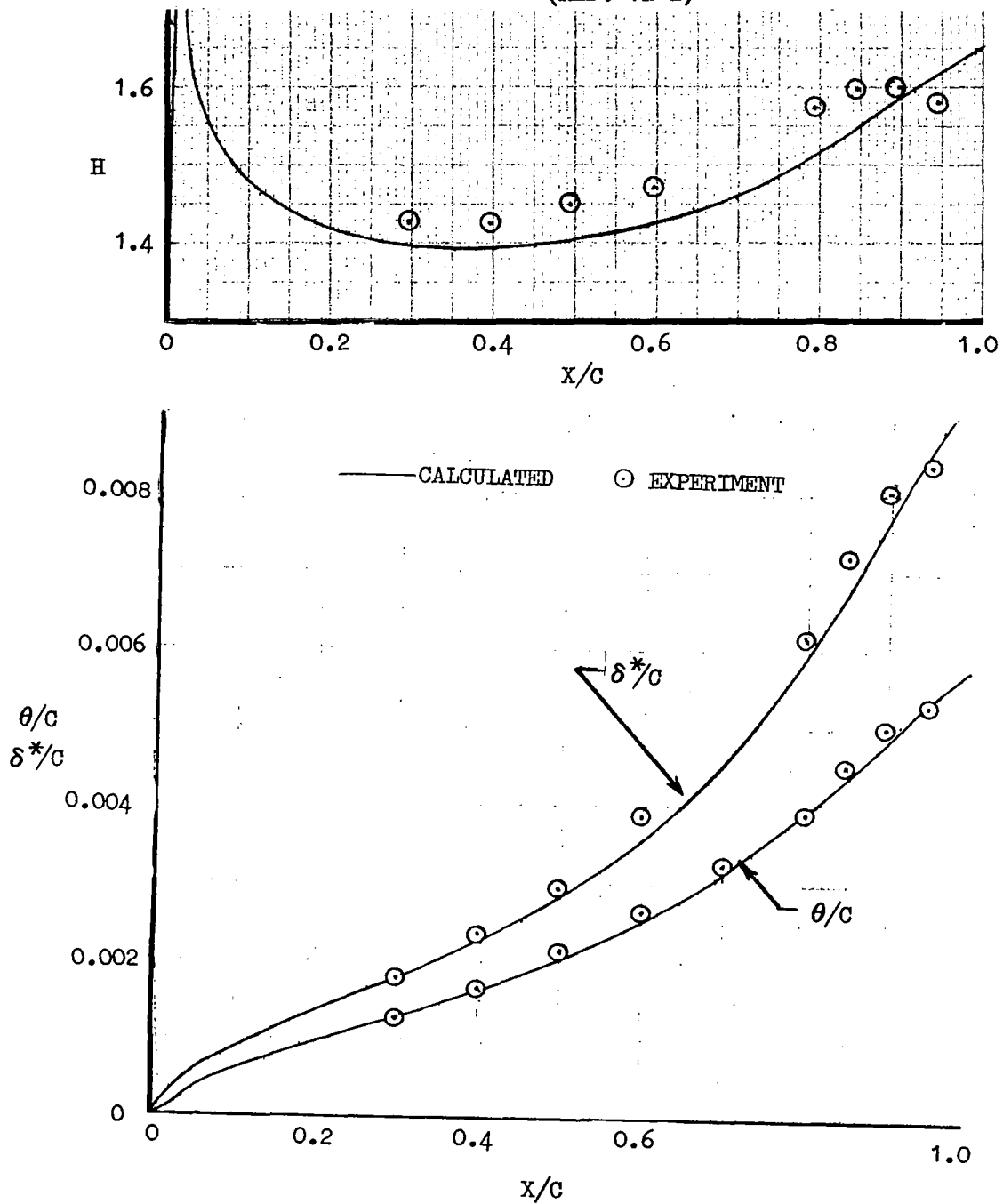
FIGURE VI-4-COMPARISON OF LIFT AND MOMENT
COEFFICIENTS PREDICTED AND
EXPERIMENTAL FOR NACA 63-009
$M_\infty = 0.167 \quad R_N = 5.8 \times 10^6$
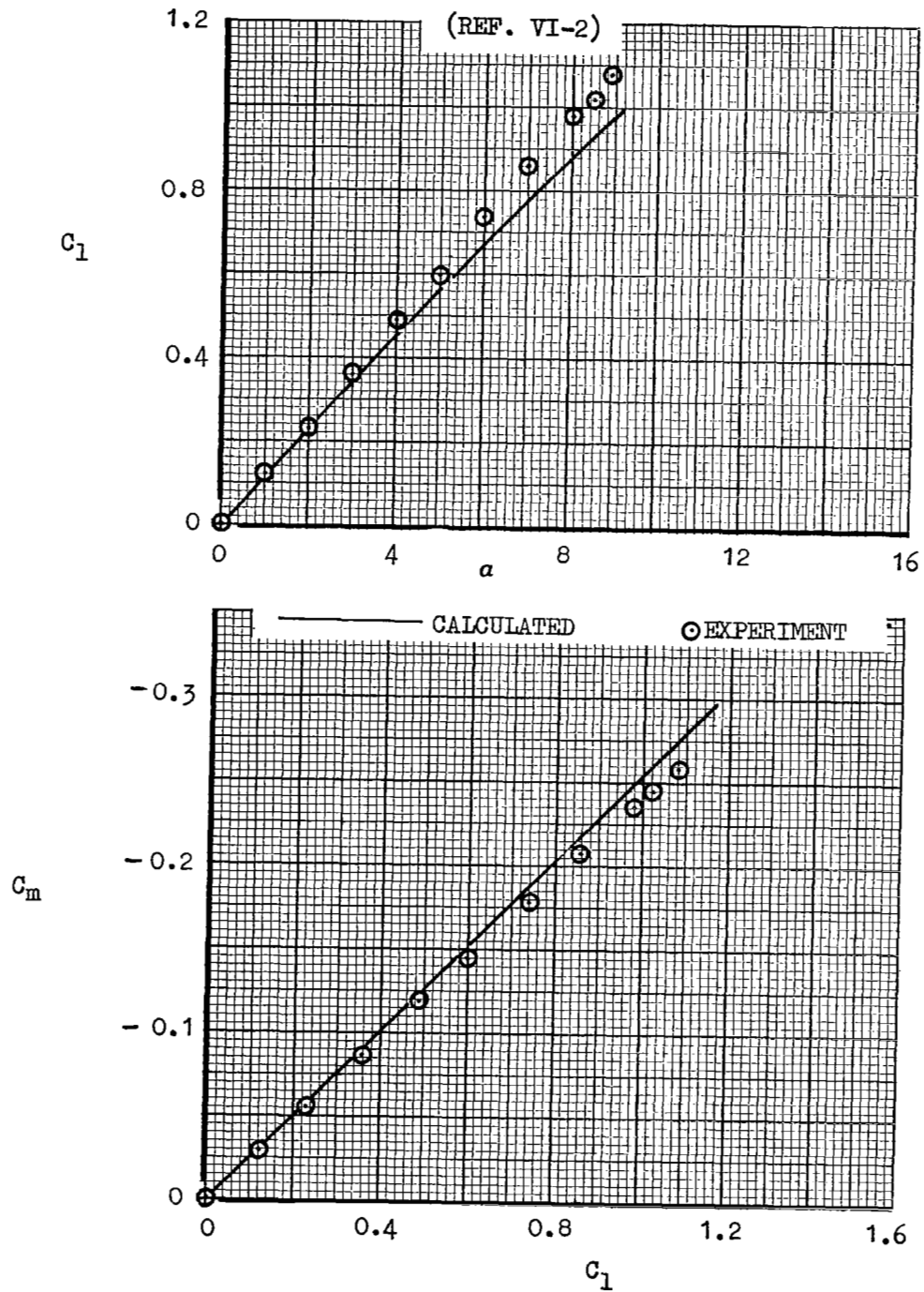
FIGURE VI-5—COMPARISON OF PREDICTED AND
EXPERIMENTAL PRESSURE DISTRIBUTION
FOR NACA 23012 AIRFOIL
M_∞= 0.105 a = 5.74° R_N = 1.7 x 10^6
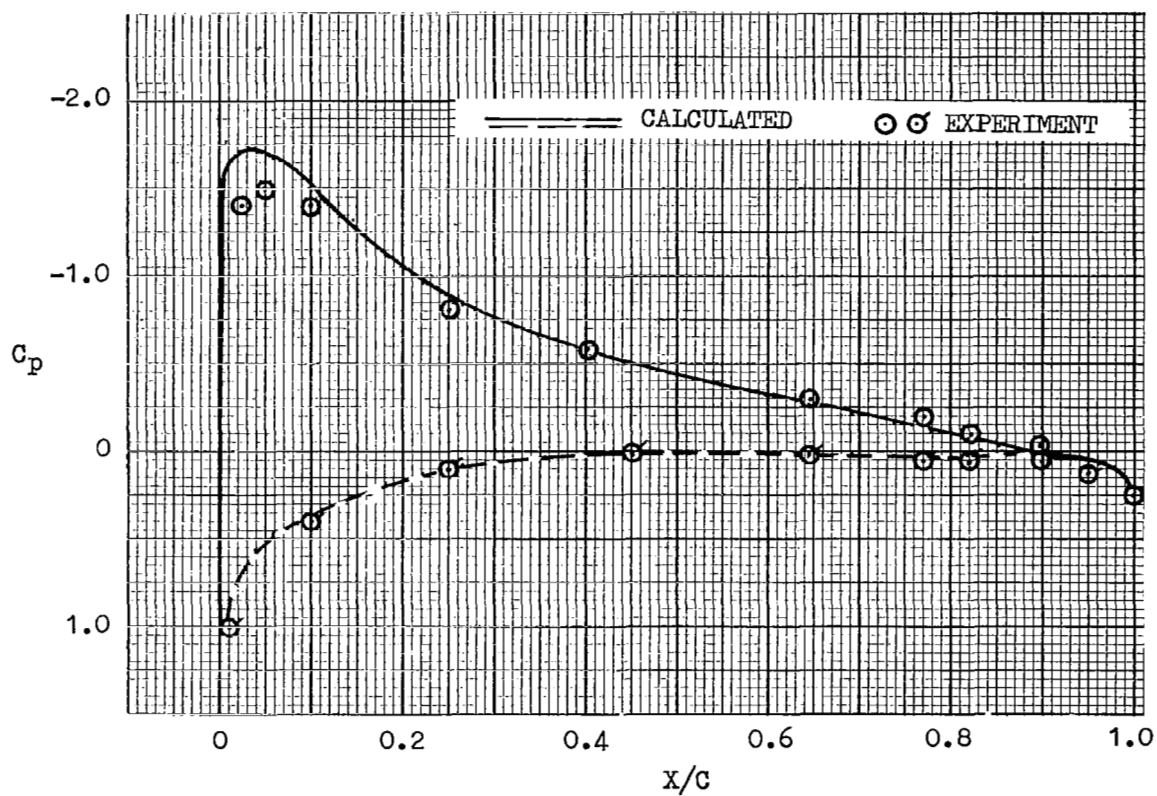
(REF. VI-3)

FIGURE VI-6
BOUNDARY LAYER PARAMETERS FOR
NACA 23012 AIRFOIL
$M_\infty = 0.105$ $a = 5.75°$ $R_N = 1.7 \times 10^6$
(REF. VI-3)
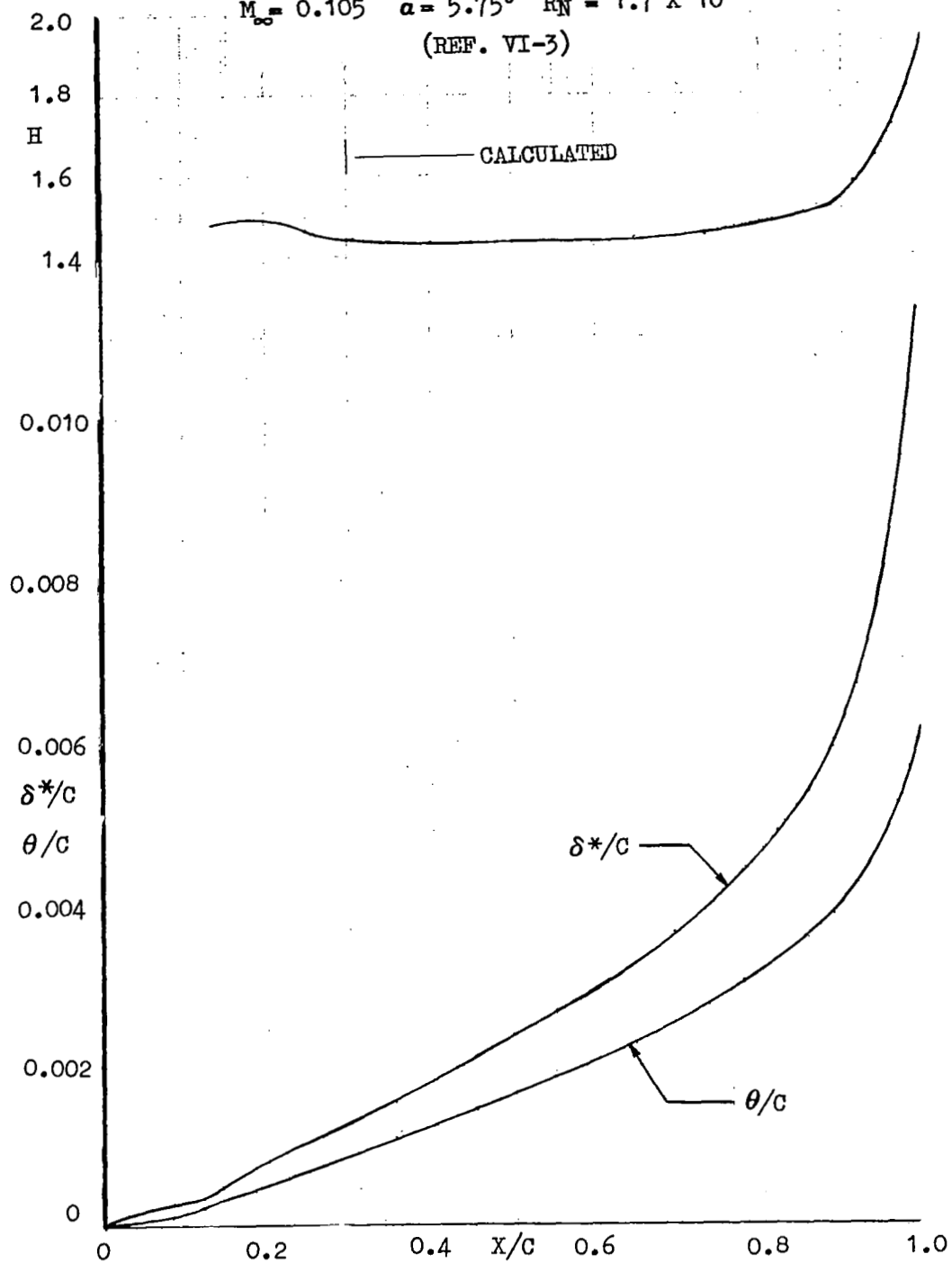
FIGURE VI-7
COMPARISON OF PREDICTED AND EXPERIMENTAL
NORMAL FORCE AND MOMENT COEFFICIENTS FOR
NACA 23012 AIRFOIL
$M = 0.105$ $R_N = 1.7 \times 10^6$
(REF. VI-3)
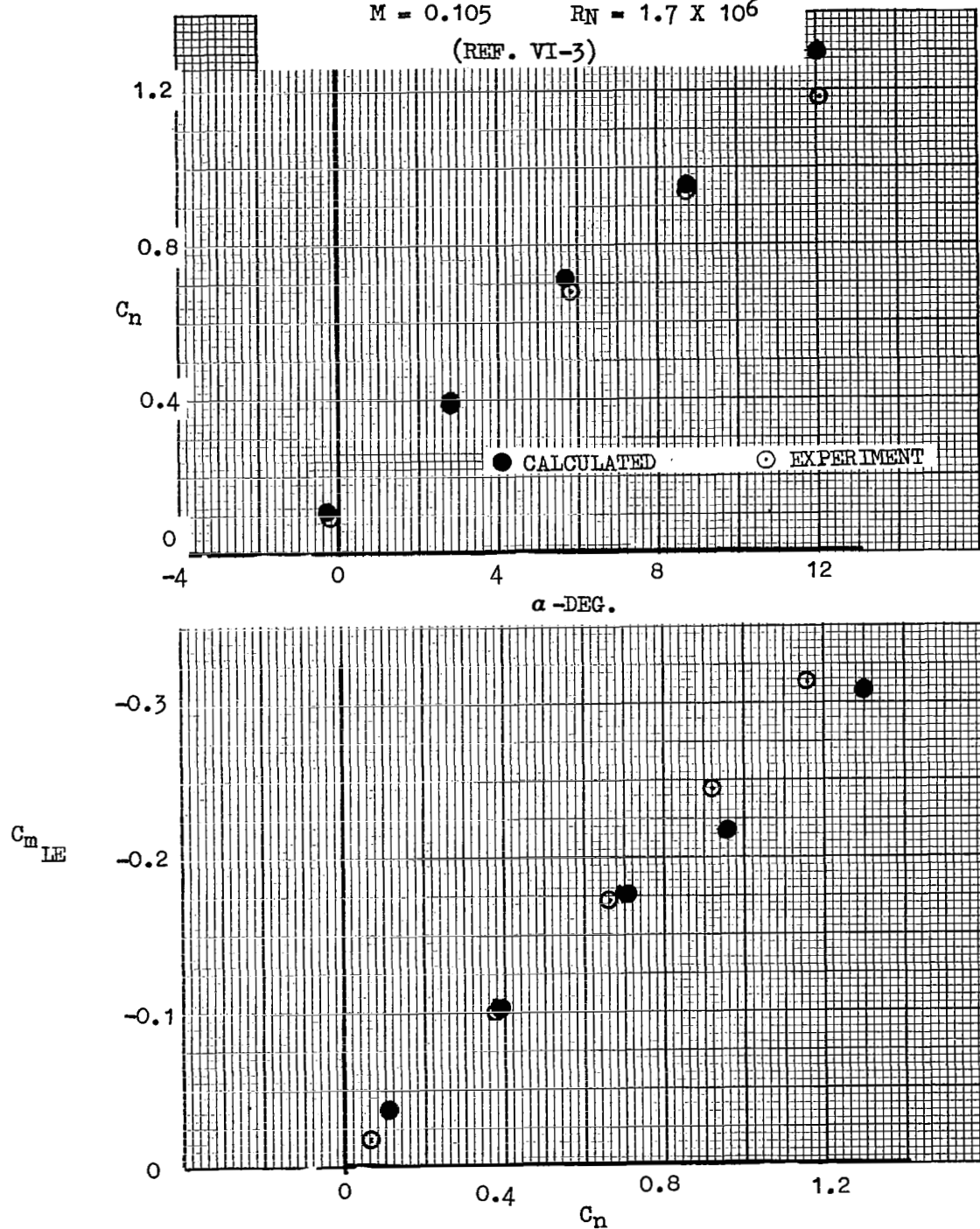
FIGURE VI-8 — COMPARISON OF PREDICTED AND
EXPERIMENTAL PRESSURE DISTRIBUTION
FOR NACA 64A010 AIRFOIL
M_{∞}= 0.167 a= 8° R_N = 4.1 X 10^6
(REF. VI-4)
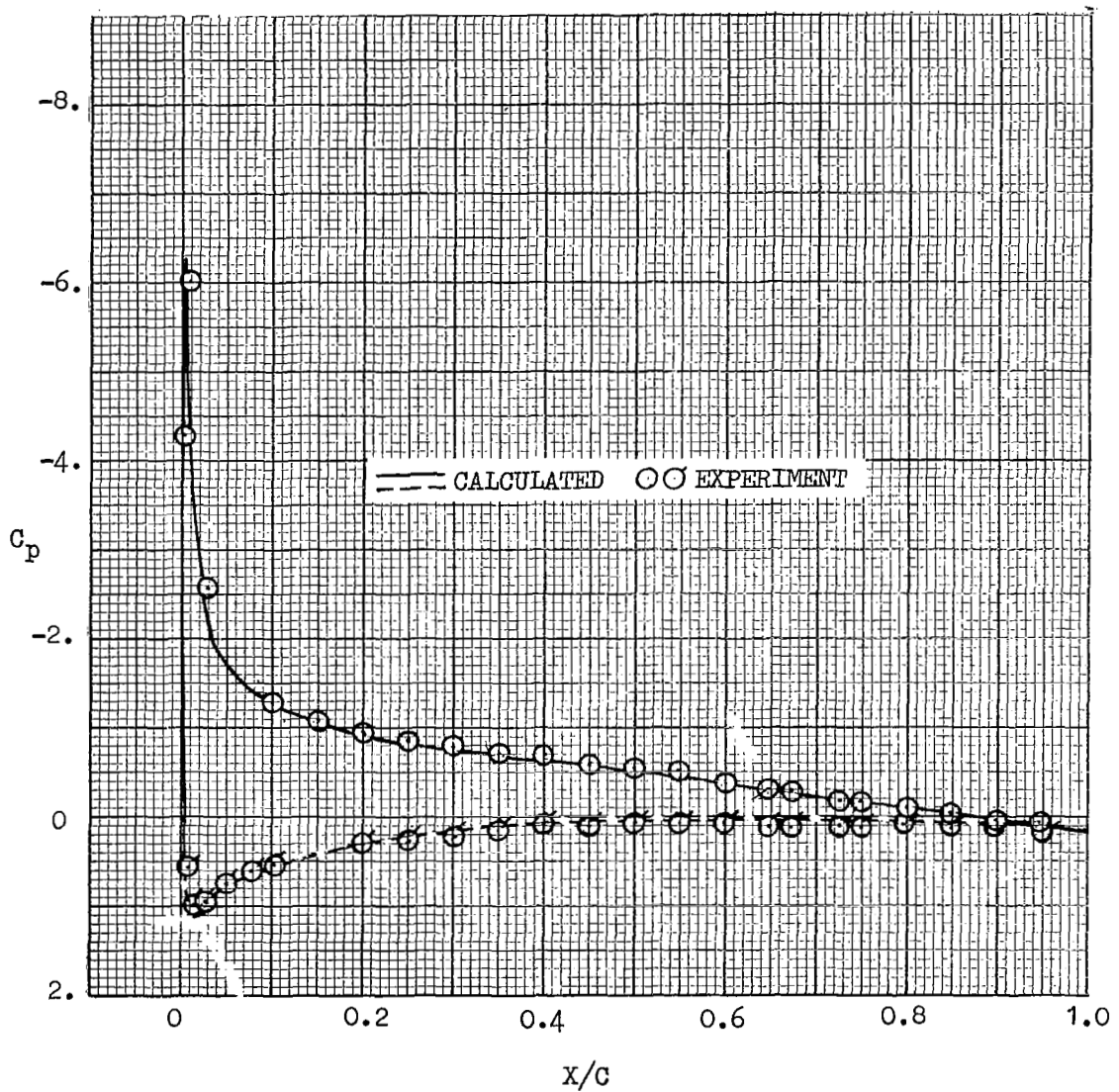
FIGURE VI-9 - COMPARISON OF LIFT AND MOMENT COEFFICIENTS PREDICTED AND EXPERIMENTAL FOR NACA 64A010 AIRFOIL $M_\infty = 0.167$ $R_N = 4.1 \times 10^6$ (REF. VI-4)
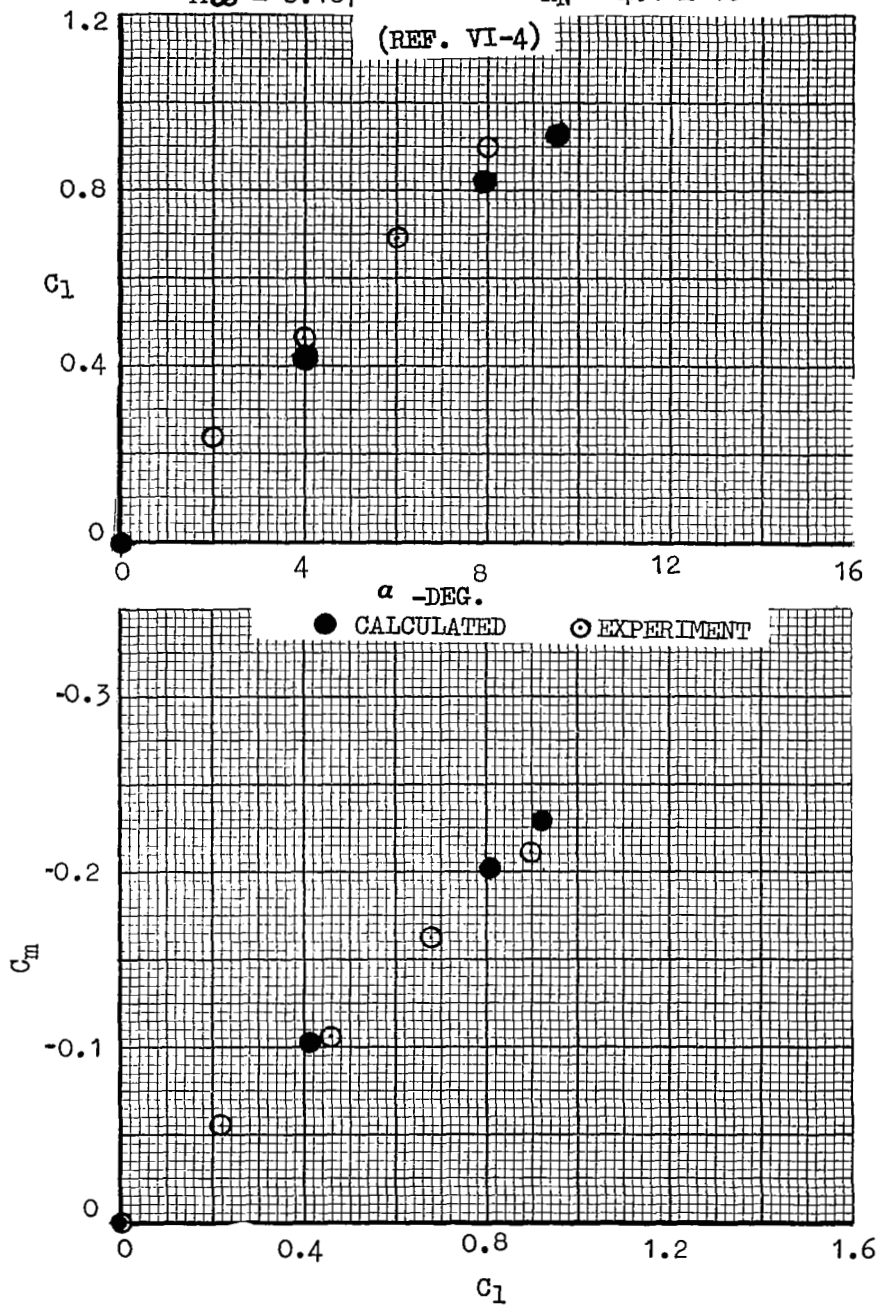
As used herein, the airfoil slot is defined as that region which is formed between two adjacent components of the airfoil. Some of the more conventional arrangements of slots, utilized primarily for high-lift generation, are typified in Figure VII-1. It is well recognized that the usual function of the slot is that of a boundary-layer control device permitting highly adverse upper surface pressure gradients to be sustained without incurring severe separation. This stabilizing influence results from the injection of the high-energy slot-flow into the upper-surface boundary layer.

The benefits of slotting in high-lift generation has long been recognized and, more recently, slotted airfoils have become of interest in transonic airfoil design work. It was in this latter application, where fairly long, narrow slots were typical (see Figure VII-1, (h)), that the Lockheed-Georgia Company recognized the need for an accurate slot-flow analysis technique to represent the high frictional and body curvature effects influencing the pressures in the slot region. In the initial planning for the multiple-airfoil program, it was felt that, while slot geometries normally encountered in low-speed, high-lift applications would be less critical to a need for a detailed slot-flow representation, this capability would add significant flexibility for program correlation and would be highly desirable from an applications standpoint. For this reason, the slot-flow model as derived herein is programmed as a part of the present computer calculations. It will be shown, however, that with the relatively short slots characterizing the airfoils used in the present correlations, (Figures VII-1 (b)-(d) are typical) slot pressures are governed primarily by the potential pressures (modified somewhat by viscous effects) and that these pressures are further modified only slightly by the introduction of the detailed slot-flow analysis. It is therefore suggested that in such normal applications, the slot-flow analysis be bypassed in the calculation sequence except where warranted by the more unique slot configurations such as (h) in Figure VII-1.

In the present computer program, the slot-flow exit conditions partially form the initial conditions for the calculation of the upper surface confluent boundary layer. In the marching-type calculation procedure utilized, it becomes highly important that these initial conditions are accurately established. Inasmuch as the slot-flow evaluation is a function of gap-height distribution and slot-inlet Mach number, accurate exit conditions are contingent upon an equally-accurate evaluation of the true aerodynamic entry conditions. Therefore, to provide a valid representation of the function of the slot, the computerized problem resolves into:

° An accurate definition of the slot geometry in terms of position and local slot contours.

° A generalized mathematical model for flow in the slot region, exit velocities and boundary-layer parameters.

92

° A method of general applicability for establishing the entry point and entry conditions.

Geometric Limitations. – Configurations (a) through (d), shown in Figure VII-1, all employ slots characterized by a smooth, continuous area distribution from the entry to the exit. Maintaining this feature is usually a basic design goal in most slot layouts. However, in many practical applications of slotted flaps, (configuration (e) in Figure VII-1) the cove area does not necessarily conform to a smooth contour due to considerations of objectionable structural or system complexities. Slots with abrupt changes in contour can create localized "corner flow" or "standing eddy flow patterns which are not readily amenable to a theoretical representation. Therefore, for the present, the mathematical model of the flow within the slot area is assumed to be confined only to those cases exhibiting smooth continuous area distributions. For slots exhibiting discontinuities in profile, a simple smoothing process would appear adequate for a reasonable representation of the airfoil characteristics. Additional correlative work needs to be performed to establish the details and limits of such techniques, however.

Slot Geometry. – The procedures for computing the "slot area" is presented in the following discussion. The geometry of the slot is depicted in Figure VII-2. Beginning at the point (X_1, Z_1) on the fore-component, the slope and therefore the normal, may be found as

$$Z = Z_1 - \left(\frac{dX}{dZ}\right)_1 (X - X_1) \qquad \text{(VII-1)}$$

The normal will strike the line representing the aft-component surface between the kth and $(k + 1)^{th}$ points at (X_2, Z_2).

$$X_2 = \frac{(Z_1 - Z_K) + \dfrac{X_1}{\left(\dfrac{dZ}{dX}\right)_1} + X_K m_K}{\left[m_K + \dfrac{1}{\left(\dfrac{dZ}{dX}\right)_1} \right]} \qquad \text{(VII-2)}$$

$$Z_2 = Z_K + m_K (X_2 - X_K)$$

where

$$m_K = \frac{Z_{K+1} - Z_K}{X_{K+1} - X_K}$$

The point (X^*, Z^*) can now be found by projecting a normal to the chordline of the aft-component from (X_2, Z_2).

$$X^* = \frac{(Z_2 - Z_{TE}) + \dfrac{X_2}{m_A} + X_{TE} m_A}{\left(m_A + \dfrac{1}{m_A}\right)} \qquad \text{(VII-3)}$$

X* can then be used to find the (x/c) of X* on the aft-component. This (x/c)-value is converted to a θ by:

$$\frac{x}{c} = \frac{1}{2}(1 + \cos\theta) \tag{VII-4}$$

which can be used as an interpolant to find (X_s', Z_s'). This latter point is assumed to be the same as (X_s, Z_s) and the slot area (gap) is found as:

$$g = \sqrt{(X_1 - X_s')^2 + (Z_1 - Z_s')^2} \tag{VII-5}$$

In the actual calculation procedure as utilized in the computer program, the initial calculation is performed at the slot exit and the gap or slot height determined. Subsequent calculations are performed moving upstream through the slot. The calculation is terminated, and the slot entrance thus defined, when the normal from the fore-component surface strikes the most forward point on the aft-component (see Figure VII-2).

This procedure implies that for a defineable slot to exist, a prerequisite is that the nose of the aft-element must lie on or forward of the normal from the lower trailing-edge surface. To provide a reasonable number of control points within the slot-area for which slot-flow calculations can be made, an additional constraint is imposed for program useage. The normals from the forward component to the flap surface must number at least five and the base of these normals must encompass a longitudinal distance of at least one percent of the fore-component chord (i.e. flap over lap must be at least one percent chord). There are obvious cases of slotting, in a strict sense, that do not meet this requirement. An example would be an external airfoil flap such as shown in Figure VII-1(f). In these cases, the slot is of such short length that pressures in the slot region and therefore the boundary-layer, are governed primarily by the potential flow characteristics. Therefore, the foregoing definition of the slot region has been formulated to emphasize those slotted configurations for which the slot friction and curvature effects become of considerable significance to the pressure distribution prediction.

Basic Equations. - Figure VII-3 shows an enlarged view of a typical slot design and includes the parameter nomenclature used in the slot-flow analysis. Also included are typical pressure variations along the contours comprising the slot boundaries. The known parameters are assumed to be the local pressures at points (A) and (B), the inlet gap (h_{inlet}) and the downstream area (or gap) distribution.

The primary parameters which most influence the boundary-layer development aft of the slot are (from Figure VII-3):

° The velocities, U_e and U_s

° The upper surface (trailing-edge of fore-component) displacement and momentum thickness, δ_U^* and θ_U, respectively

° The slot boundary-layer thicknesses δ_2 and δ_3

° The Reynolds number based on exit conditions, $\dfrac{U_s h_{out}}{\nu}$

By considering the control volumes shown in cylindrical coordinates in Figure VII-4, the following equations of continuity and momentum can be derived:

$$\frac{\partial \rho \theta}{\partial \theta} + \rho\, V_r + \gamma\, \frac{\partial \rho V_r}{\partial r} = 0 \qquad \text{(VII-6)}$$

$$\cdot \rho \left[r\, V_r\, \frac{\partial V_r}{\partial r} + V\theta\, \frac{\partial V_r}{\partial \theta} - V\theta^2 \right] = \rho V^2 \theta - P - \gamma\, \frac{\partial P}{\partial r} \qquad \text{(VII-7)}$$

$$\rho \left[\gamma\, V_r\, \frac{\partial V\theta}{\partial r} + V\theta\, \frac{\partial V\theta}{\partial \theta} + V_r\, V\theta \right] = \frac{\partial P}{\partial \theta} - \tau_\theta \qquad \text{(VII-8)}$$

By neglecting the low-order terms (i.e. $V_r \ll V_\theta$, $\tau_r = 0$, etc.) and using the ideal gas relations the foregoing equations become:

$$\left(\frac{1 - M^2}{2} \right) \frac{\partial M^2}{\partial \theta} = - \frac{\tau_\theta}{P_o K \left(1 + \frac{K - 1}{2} M^2 \right)^{\frac{1 - 2K}{K - 1}}} \qquad \text{(VII-9)}$$

$$\frac{\partial M^2}{\partial r} = \frac{2}{rK} \left[1 - \frac{3K + 1}{2} M^2 - K(K - 11)M^4 \right] \qquad \text{(VII-10)}$$

These partial differential equations, being difficult to resolve, can be reduced to ordinary differential equations if the shape of the velocity profile across the slot is known. However, experimental data is completely lacking whereby a generalization of the exit profile can be formulated. Therefore, the more rigorous slot-flow model as represented by Equations (VII-9) and (VII-10) has been replaced by a somewhat semi-empirical method for defining the pressure distribution throughout the slot region.

The following equation, obtained from Reference VII-1, is applicable to one-dimensional flow with area changes and friction and body (curvature) forces represented:

$$\frac{dM^2}{M^2} = -2\, \frac{1 + \frac{K - 1}{2} M^2}{1 - M^2} \frac{dh}{h} + \frac{KM^2 \left(1 + \frac{K - 1}{2} M^2 \right)}{1 - M^2} \left[4F\, \frac{dx}{D} + \frac{xdx}{\frac{1}{2} KPhM^2} \right] \qquad \text{(VII-11)}$$

where:

$$\frac{dh}{h} = \text{area change term}$$

$$4F\, \frac{dx}{D} = \text{friction term}$$

$$\frac{xdx}{\frac{1}{2} KPhM^2} = \text{body force term}$$

Combining friction and body-force effects under a common term, F, and simplifying gives:

$$\frac{dY}{dX} = -2\frac{Y(1 + 0.2Y)}{1 - Y}\frac{dh}{dX}\frac{1}{h} + \frac{1.4Y^2}{1 - Y}(1 + 0.2Y)\frac{2F}{h_{(x)}}$$

(VII-12)

where:
$$Y = M^2$$

Also:

$$Y\big|_{x+\Delta x} = Y\big|_x + \frac{dY}{dX}\bigg|_x \Delta x + \frac{d^2Y}{dX^2}\bigg|_x \frac{\Delta X^2}{2!}$$

(VII-13)

and

$$\frac{d^2Y}{dX^2} = \frac{1}{h(1 - Y)}\left[-\frac{d^2h}{dX^2}(2Y + 0.4Y^2) - \frac{dh}{dX}\frac{dY}{dX}(3 - 0.2Y)\right.$$

$$\left. + h\left(\frac{dY}{dX}\right)^2 + 5.6F\frac{dY}{dX} + 1.68FY^2\frac{dY}{dX}\right]$$

(VII-14)

Therefore, with Y (or M^2) known at X and $\frac{dY}{dX}$ and $\frac{d^2Y}{dX^2}$ given from Equations (VII-12) and (VII-14), Y at $(X + \Delta X)$ can be determined from Equation (VII-13). The factor F is evaluated through correlation with experimental data. The local Mach Number distribution through the slot can therefore be determined from the given slot-height distribution and the inlet Mach numbers. The local C_p may be calculated from:

$$c_{p_{(x)}} = \frac{2}{KM_\infty^2}\left[\frac{h_{in}}{h_{(x)}}\frac{M_\infty}{M_{(x)}}\sqrt{\frac{1 + \frac{K-1}{2}M_{in}^2}{1 + \frac{K-1}{2}M_\infty^2}}\left(\frac{c_{p_{in}}}{2}KM_\infty^2 + 1\right) - 1\right]$$

(VII-15)

This expression can be reduced at low Mach numbers to:

$$c_{p_{(x)}} = \frac{2}{KM_\infty^2}\left[\left(\frac{1 + 0.2M_\infty^2}{1 + 0.2M_{(x)}^2}\right) - 1.0\right]$$

(VII-16)

Correlation. - In the present application, Equations (VII-12) through (VII-14) are applied along each of the surfaces of the slot boundary with the factor, F, representing the correlation parameter for establishing trends compatible with experimental results. It would be anticipated that the magnitude of F would vary with the particular surface (fore- or aft-slot surface) as well as slot location. Experimental slot-surface pressures have been obtained from the data of References VII-2 and VII-3. Figures VII-5 through VII-8 show the correlation obtained between the foregoing method and the test results for various values of the factor, F. It is seen in Figure VII-6 that the pressure

distribution along the slot surface is relatively insensitive to the magnitude of F when the surface considered is that formed by the lower surface of the forward component.

A greater sensitivity to F is shown when considering the upper surface of the aft component (Figure VII-5). It is also noted that the value of F providing the better agreement with experiment varies with the surface considered as well as with slot location. In each instance, the values of the parameter, F, best approximating the test trends have been introduced into the computer program slot-flow subroutine. Since these values are based on one set of experimental data, additional data and further correlation are required to validate their generalized application.

In the correlation analysis for the factor, F, it has also been noted that at high-subsonic Mach numbers, the pressure distribution in the slot region is very sensitive to the magnitude of F. This fact should be recognized when applying the program under marginally-high free-stream Mach conditions (i.e. $M_\infty > 0.25$).

Slot Entry and Exit Conditions. - Characteristic pressure variations in the region of the slot are shown schematically for both component surfaces in Figure VII-3. Typically, on the forward surface, the pressure reaches a maximum positive C_p level of about +0.4 - +0.6 (point A on the C_p vs X sketch) just prior to establishing a highly-favorable negative gradient through the slot. It is logical that this maximum pressure point would approximately represent the slot entry condition on the forward surface. From consideration of both calculated and experimental results, it would appear that the geometric forward-surface entry point, as previously defined, consistently approximates the chordwise position of the desired pressure level. In the correlation of the slot-flow analysis technique, Figures VII-5 through VII-8, comparison with experimental slot measurements indicated that the calculated entry pressure level would provide more representative slot-exit conditions if a slight modification to the entry pressure were made. The requirement for this modification reflects the high sensitivity of the boundary-layer calculations in the slot to small variations in slot pressure gradient (for example, potential vs viscous distributions). Accordingly, the entry pressure on the forward surface is modified to:

$$C_p = 1.432 \ (C_p)_{calc} - 0.53$$

where $C_{p_{calc}}$ is from the calculated potential flow pressures.

As previously described, the entry point on the aft-component surface is predetermined by the location of the entry point on the forward surface. As seen in the sketch of Figure VII-3, the aft-surface entry point (B) will lie in a region of extremely high negative pressure gradient as the flow expands around the flap upper surface. Because of this, the calculated level of entry pressure at B is very sensitive to small variations in slot contour (i.e. slight variations in point A and thereby, point B) or to aft-component relative positioning. Unless the flap is very carefully positioned, this sensitiv-

ity can cause the aft-surface slot calculations to be initiated at a C_p-level that is too positive with a corresponding reduction in exit velocity and a less than desirable flap load at the leading-edge. Additional work is required in this area of the slot-flow calculations. Refinements to the definition of the slot entry point, particularly on the aft-component surface, are needed to reduce the extreme sensitivity encountered in the correlation analysis.

The velocity at the slot exit is an element of the initial conditions required for the confluent boundary-layer calculations. A simple numerical average of the computed velocities at points E and G, Figure VII-3, is used to quantify this parameter.

As will be noted in the multiple-airfoil correlation (Section IX), cases have been encountered where the combined boundary layer thicknesses of the main element lower surface and the flap upper surface exceed the slot exit height. This obviously creates a difficulty in defining the confluent boundary layer initial conditions. Where this situation occurs, the boundary-layer thickness on the main element lower surface at the slot exit is set to a value of one-half of the slot-exit height. The magnitude of the momentum thickness, θ, is correspondingly reduced by the ratio of the calculated to fixed boundary layer thickness. The presence of these circumstances within the calculations is flagged by a statement in the program output.

VII - SYMBOLS

C_p = pressure coefficient = $(P - P_\infty)/\frac{1}{2}\rho U_\infty^2$

F = slot flow correlation factor to take into account friction and centrifugal forces on fluid in slot

h_{out} = slot height at the exit

h_{in} = slot height at the inlet

P = pressure in the slot region

K = ratio of specific heats for air

M = local Mach number in the slot

U_e = velocity at the fore component Ⓜ trailing edge on the upper surface

U_s = average velocity at the exit of slot

V_r = radial component of velocity

V_θ = tangential component of velocity

δ^2 = boundary layer thickness at slot exit on lower surface of main component M

δ^3 = boundary layer thickness

δ^*_u = displacement thickness on the upper surface of component M

θ_u = Momentum thickness on the upper surface of component M

ρ = density of air in the slot

ν = kinematic viscosity of air

VII - REFERENCES

VII - 1   Shapiro, A. H.: The Dynamics and Thermodynamics of Compressible
               Fluid Flow. Vol. I. Ronald Press Co., N.Y., 1953

VII - 2   Seebohm, T.: Boundary Layer, Transition, and Wake Measurements
               at Low Mach Number for an Aerofoil with Single-Slotted Flap.
               Report 69-1, Mechanical Engineering Research Laboratories,
               McGill University, Montreal, 1969

VII - 3   Giesing, J. P., Potential Flow About Two - Dimensional Airfoils,
               Part I: A Summary of Two Dimensional Airfoil Methods, Part II;
               Solution of the Flow Field About One or More Airfoils of Arbitrary
               Shape in Uniform or Non-Uniform Flows by the Douglas Neumann
               Method; Douglas Aircraft Company, Report No. LB31946, Dec. 1965

FIGURE VII-1   TYPICAL SLOTTED CONFIGURATIONS

(a)
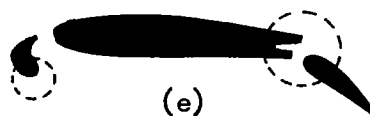
(e)

(b)
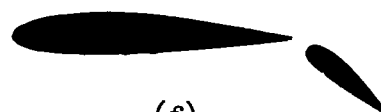
(f)

(c)

(g)

(d)

(h)

FIGURE VII-2   SLOT-AREA CALCULATION PROCEDURE
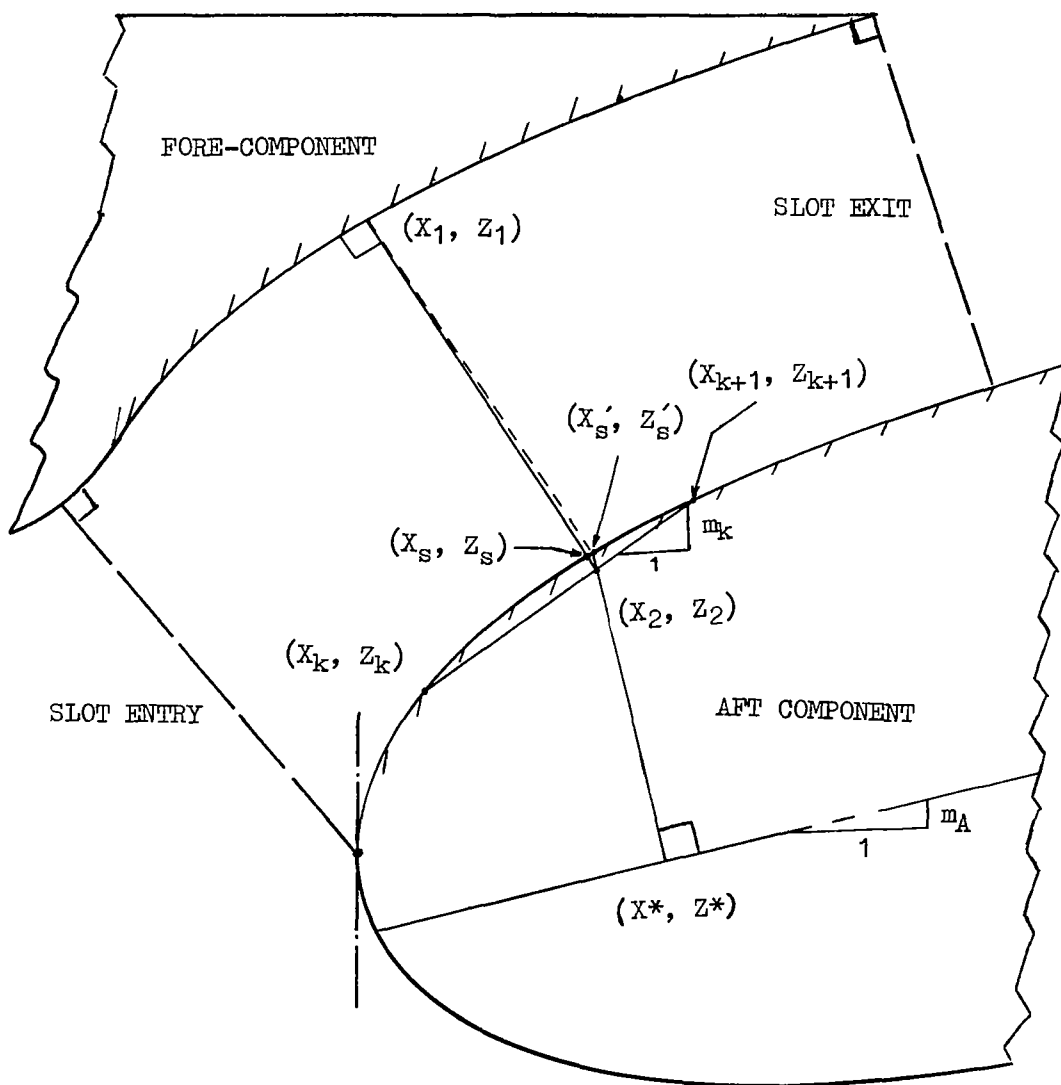
FIGURE VII-3   SLOT-FLOW PARAMETERS
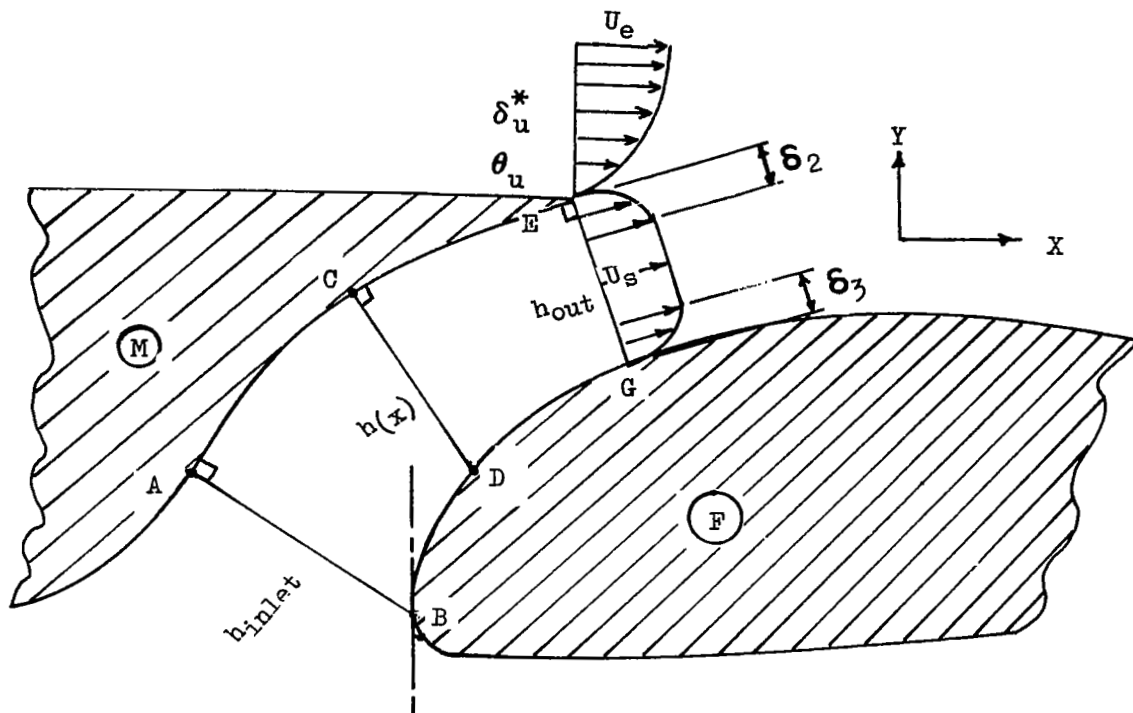
CURVE A-C-E   PRESSURE DISTRIBUTION
               ON LOWER SURFACE OF
               COMPONENT Ⓜ

CURVE B-D-G   PRESSURE DISTRIBUTION ON
               UPPER SURFACE OF
               COMPONENT Ⓕ

h_{inlet} AND $h_{(x)}$ INPUT

C_p AT A & B INPUT FROM POT'L
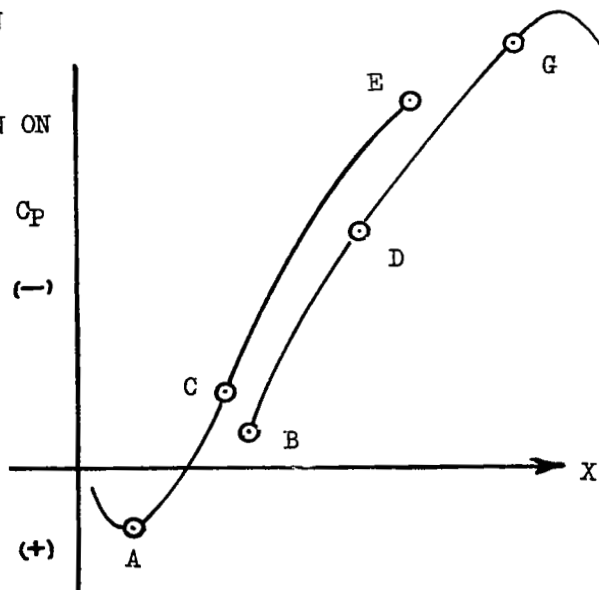
FLOW CALCS.

(a)   CONTINUITY CONTROL VOLUME
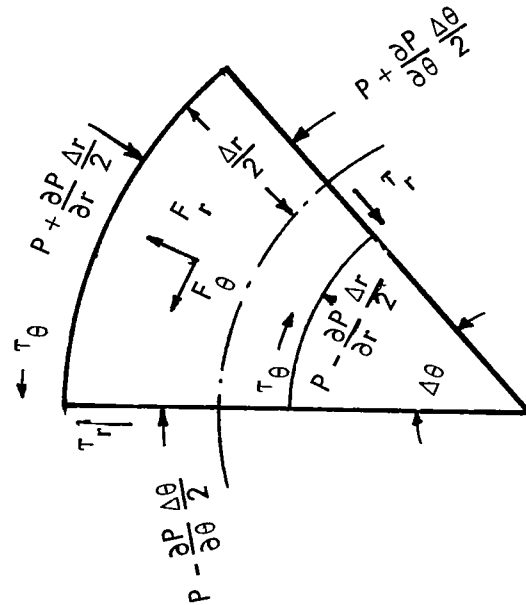
FIGURE VII-4. - CONCLUDED

(b) MOMENTUM CONTROL VOLUME
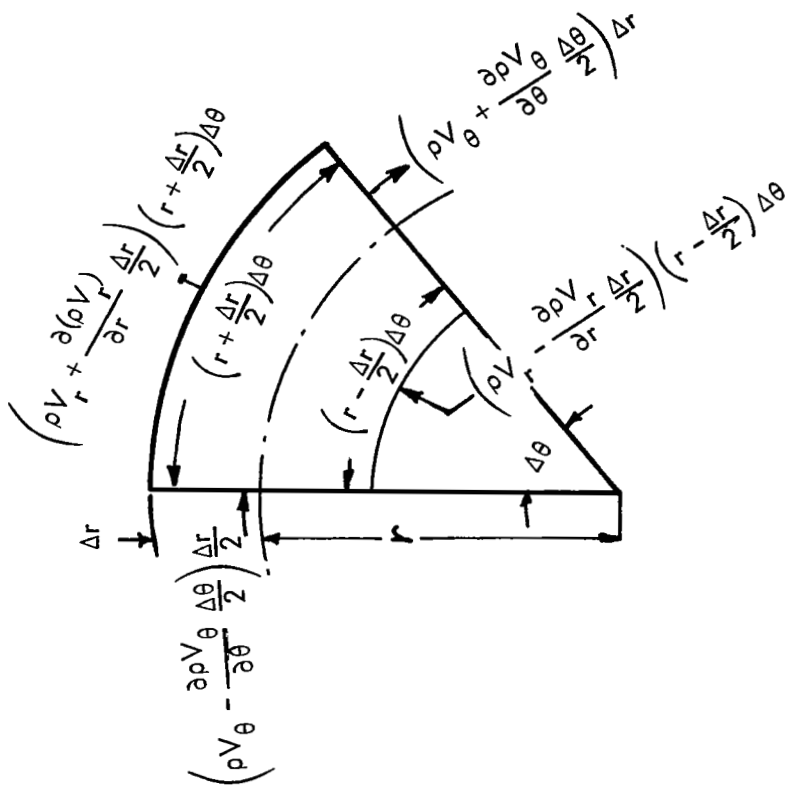
FIGURE VII-5   COMPARISON OF EXPERIMENTAL AND CALCULATED
PRESSURES IN SLOT REGION
NACA 4418(MOD) AIRFOIL (REF. VII-2)
$a = 0°$ $\delta_F = 10°$ $M_\infty = 0.19$
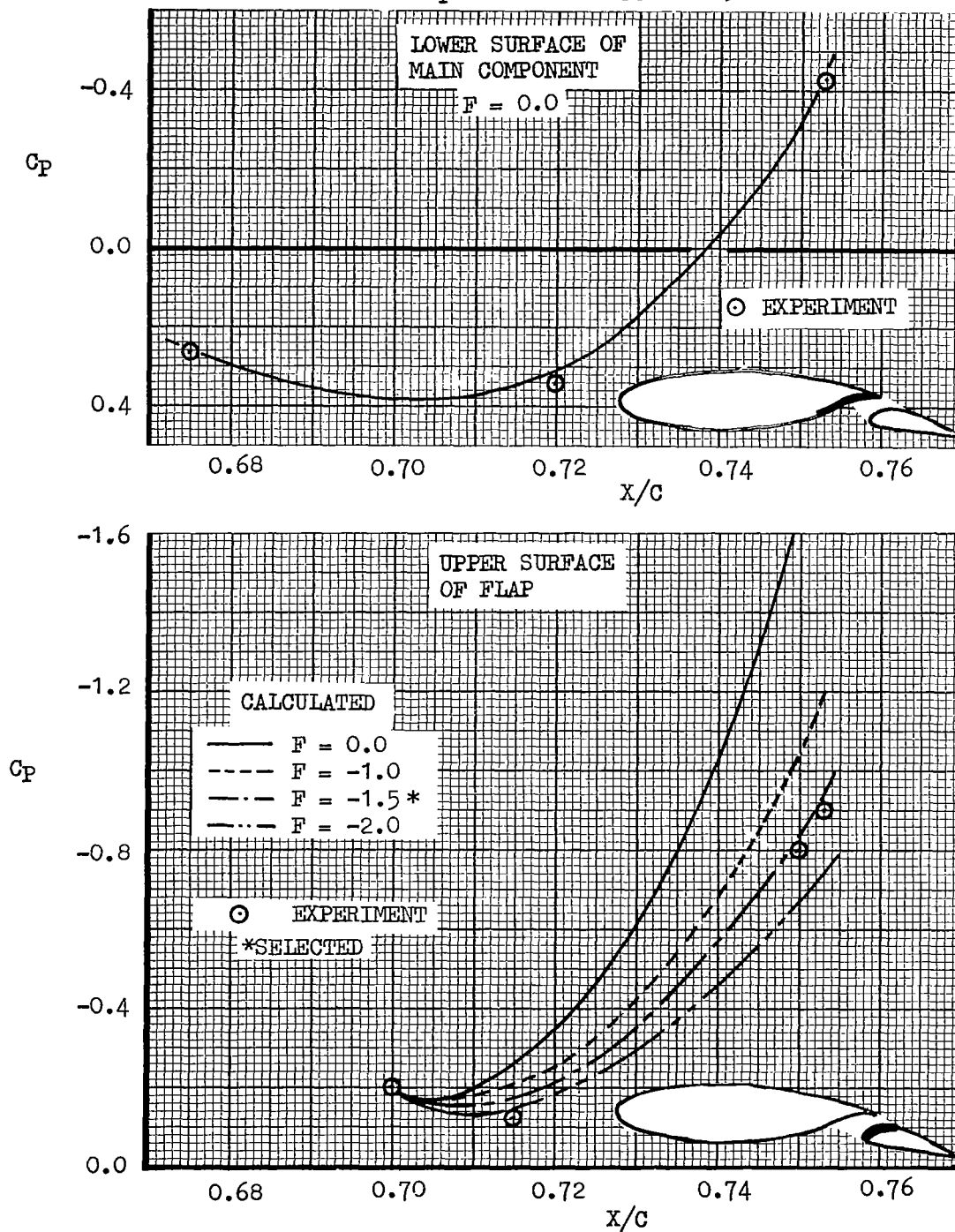
FIGURE VII-6   COMPARISON OF EXPERIMENTAL
AND CALCULATED PRESSURES IN SLOT REGION
NACA 4418(MOD) AIRFOIL (REF. VII-2)
$a = 0°$ $\delta_F = 20°$ $M_\infty = 0.19$
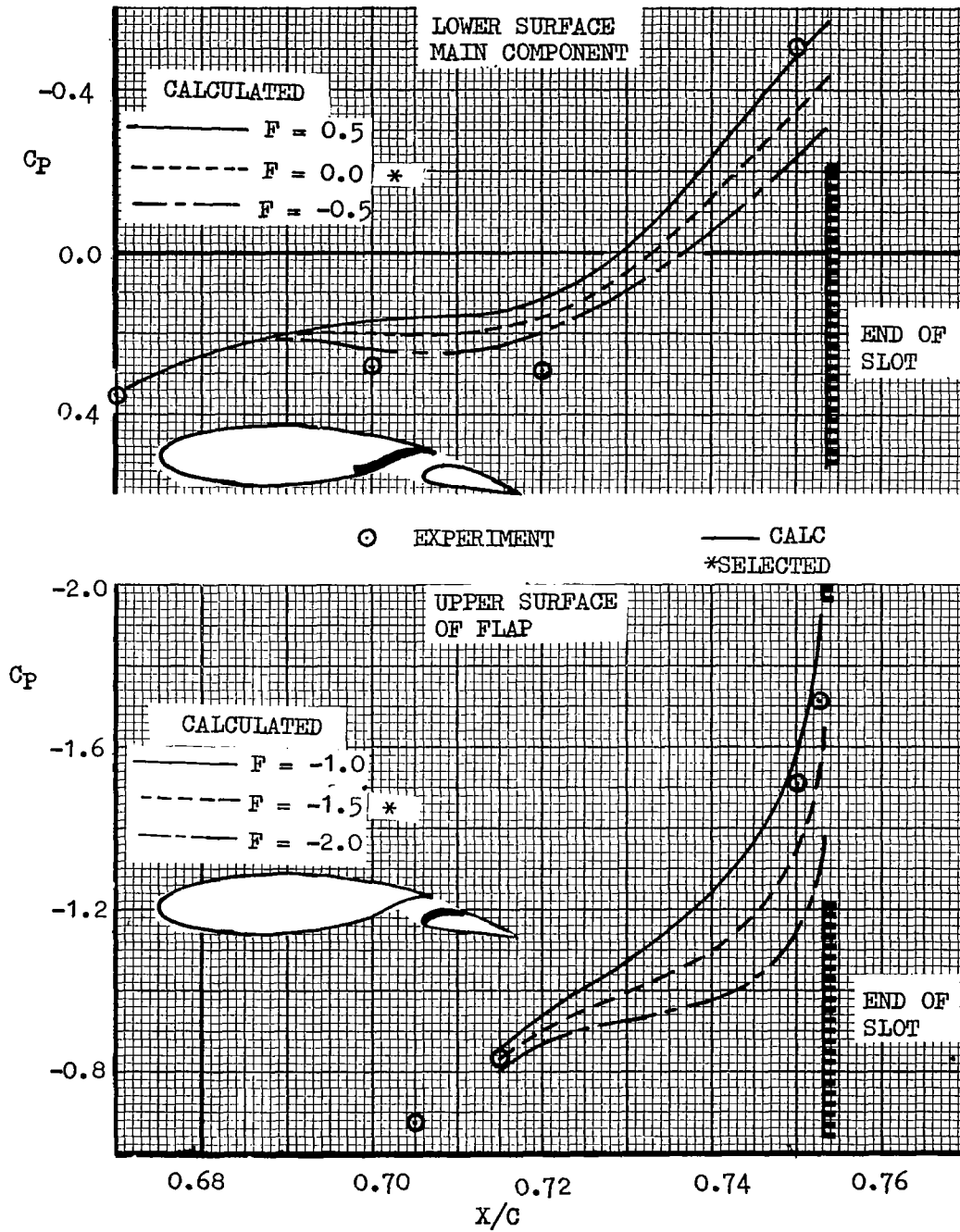
FIGURE VII-7   COMPARISON OF EXPERIMENTAL AND CALCULATED
PRESSURES IN FORWARD SLOT REGION
NACA 23012   3 COMPONENT AIRFOIL
$a = 8°$ $\delta_F = 20°$ $M_\infty = 0.105$
(REF. VII-2)
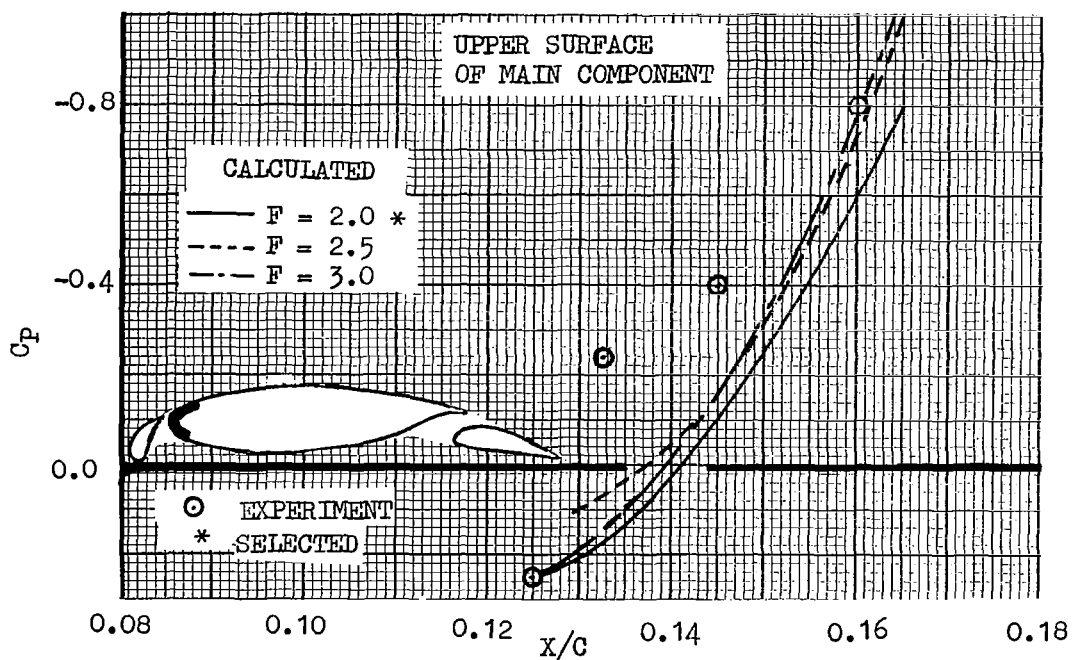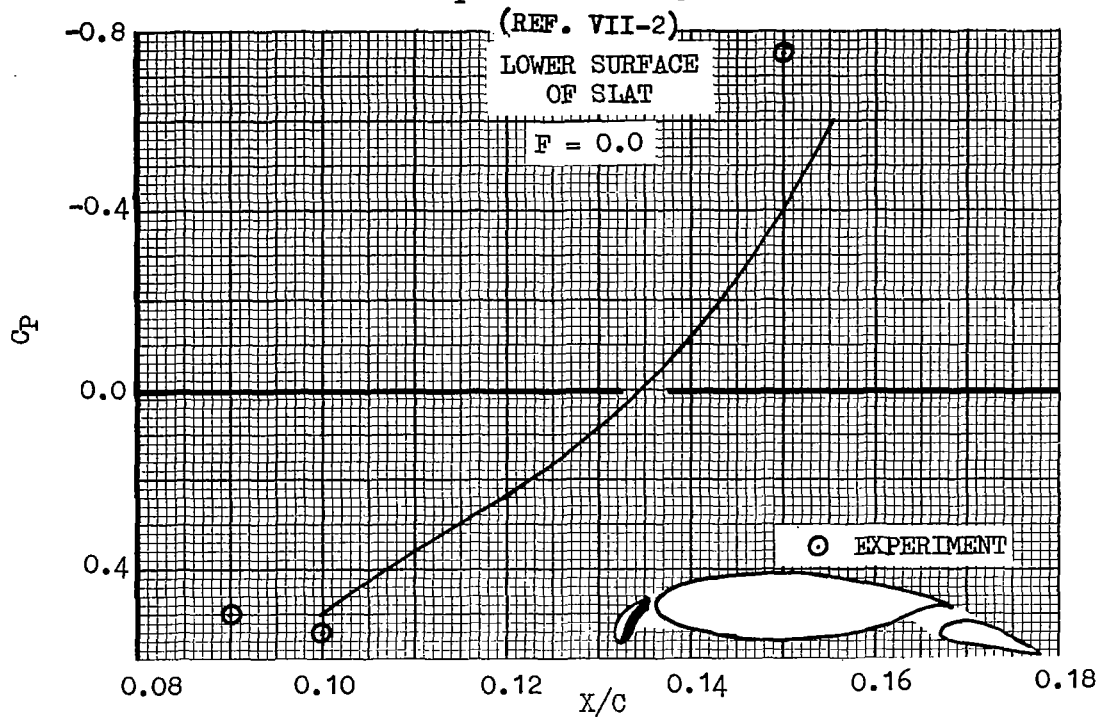
FIGURE VII-8   COMPARISON OF EXPERIMENTAL AND CALCULATED
PRESSURES IN AFT SLOT REGION
NACA 23012   3 COMPONENT AIRFOIL
$a = 8°$ $\delta_F = 20°$ $M_\infty = 0.105$
(REF. VII-3)
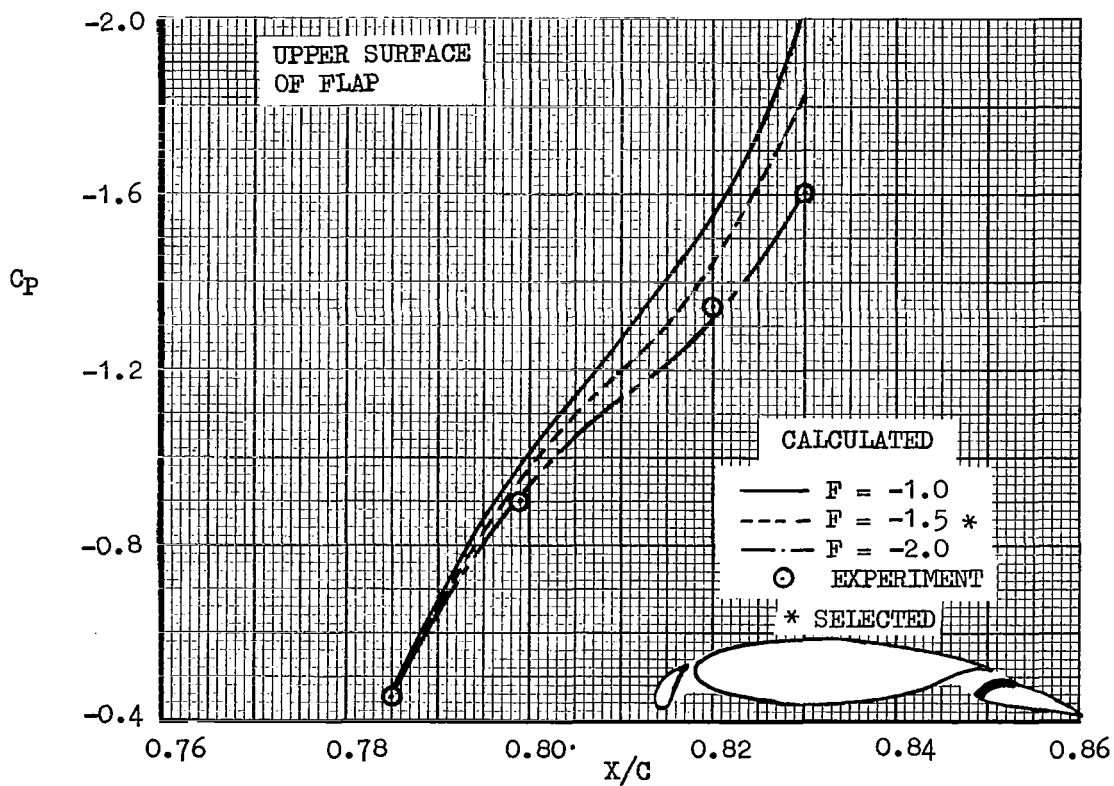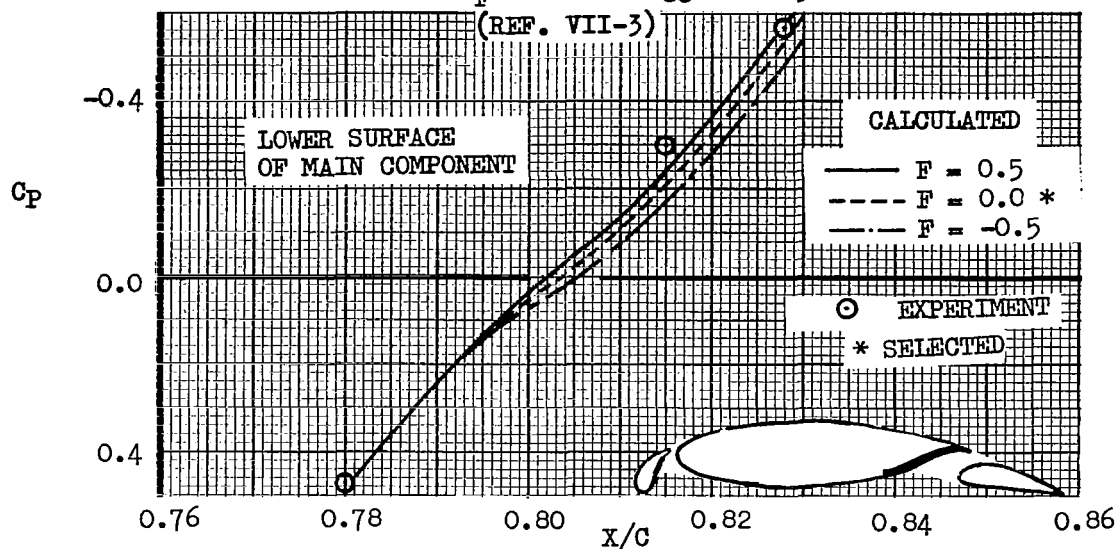
VIII - CONFLUENT BOUNDARY LAYER

Experimental velocity profiles on two-piece airfoils as measured by Seebohm (VIII-1) and Bradshaw and Gee (VIII-2), indicate that aft of the slot, the upper surface of the airfoil exhibits the presence of a confluent boundary layer as typified in Figure VIII-1. The confluent boundary layer is developed as a result of the stream through the slot mixing with the boundary layer developed on the upper surface of the forward component. On the upper surface of the aft component, in the more general situation, the existence of both the confluent boundary layer and the ordinary turbulent boundary layer is possible depending upon the initial conditions at the slot exit and the pressure distribution. The upper surfaces of single, double or triple-slotted flaps invariably have the confluent boundary layers up to the trailing edges. Because of the existence of the confluent boundary layer on a major portion of the upper surfaces of a multi-component airfoil, it is imperative that a realistic and accurate means of calculating the various parameters for this very complex viscous phenomena be available. Goradia's computational method for confluent boundary layers was developed in partial fulfillment of the requirement of the degree of Ph.D.

Description of Model. - Figure VIII-2 shows a sketch of a mathematical model which was derived from preliminary experimental data. This model is used as a basis for derivation of the differential equations necessary for the solution of the various physical quantities involved.

As seen in Figure VIII-2, the flap is represented by a flat plate thus ignoring curvature effects, but the viscous region is assumed to be subjected to the external arbitrary pressure distribution. The boundary layer emerging from the slot is assumed to have a constant-velocity core, as indicated in Figure VIII-2 at station 0. This boundary layer mixes with the second boundary layer developed up to the trailing edge of the fore-component. It is assumed that the required initial conditions, for example δ_F, slot exit velocity $U_c(o)$, velocity at the trailing edge, $U_e(o)$, δ_{s1} and δ_{s2} are known.

The region between stations 0 and 1 is defined at the Initial Region. The region between stations 1 and 2 is defined as the Main Region I and between stations 2 and 3 as Main Region II. The region downstream of station 3 and up to the point of separation, is similar to the ordinary turbulent boundary layer flow.

A typical velocity profile in the Initial Region between stations 0 and 1 is as shown at station 0. The layer from $y = 0$ to $y = \delta_1$ is called the wall layer. If the velocity in this layer is non-dimensionalized with respect to U_c and distance y is non-dimensionalized with respect to δ_1, this non-dimensional velocity plot looks similar to the ordinary boundary layer velocity profile. From $y = \delta_1$ to $y = \delta_2$, the velocity is constant and this layer is called the "potential core." Due to differences in the velocities at the slot exit and the fore-component trailing-edge, and also due to finite trailing-edge thickness as well as trailing-edge boundary layer, there is a depression in

the velocity at $y = \delta_3$. The layer from $y = \delta_2$ to $y = \delta_3$ is defined as the jet layer, because "similar velocity profiles" are obtained when the velocity and distances for the points in this layer are non-dimensionalized in a way analogous to that for free-jet flow. The layer from $y = \delta_3$ to $y = \delta_4$ is defined as the wake layer for this same reason.

The Initial Region terminates at station 1 which forms the starting point for calculations for the Main Region. A typical velocity profile in the Main Region between stations 1 and 2 is shown in Figure VIII-2 at station 1. The velocity $U_{m(x)}$ at the edge of wall layer ($y = \delta_5$) must be determined from a viscous solution in contrast to $U_{c(x)}$ which is determined from potential flow. The wake layer from $y = \delta_3$ to $y = \delta_4$ is shown to terminate at station 2. Actually, this wake layer may terminate in either the Initial Region between station 0 and 1 or in the Main Region I between station 1 and 2 depending upon the initial conditions at station 0 and the pressure distribution.

At station 3, the jet layer terminates and the viscous flow becomes qualitatively similar to ordinary turbulent boundary layer flow. The initial conditions at station 3, necessary for the solution of pertinent quantities downstream, are obtained from the solution of the equations in the Main Region up to station 3.

Theoretical Derivations. - In the succeeding paragraphs, a summary of the equations comprising the theoretical development of the confluent boundary, and as utilized in the multiple-airfoil program, is provided. A more detailed description of the analytical development is given in References VIII-3 and VIII-4. As will be seen in the theoretical summary contained herein, the flow downstream of the slot is categorized into the various regions and layers described earlier. This permits the transformation of the boundary-layer-type of partial differential equations into ordinary differential equations suitable to high-speed digital computations. Inasmuch as analytical work on the confluent boundary-layer has only recently been emphasized, a bibliography of pertinent reference material is included at the end of this section.

(A) Relation between velocity in the core in the Initial Region and static pressure coefficient for the Flow Model, Figure VIII-2. - In order to derive two equations for the two unknowns, $U_{c(x)}$ and $U_{e(x)}$ in terms of the U_0, $C_{P(0)}$, $C_{P(x)}$ and $U_{e(0)}$, the following assumptions are made:

○ $\dfrac{\partial P}{\partial y} = 0$ i.e., static pressure remains constant in y direction

○ Density is independent of pressure but depends upon temperature. Specifically, ρ_0 and ρ_e are based on some mean temperature which is a function of wall temperature, temperature of slot stream at exit and free stream temperature.

○ Bernoulli equation, $\displaystyle\int \dfrac{dP}{\rho} + \dfrac{q}{2}$ = constant, is assumed to be valid in the core as well as at the external edge of viscous layer; q is the velocity vector.

111

When use is made of the above assumptions the following equations can be derived for the two unknowns $U_{C(x)}$ and $U_{e(x)}$:

$$\left(R_{1(x)}\right)^2 = \left(\frac{U_{e(x)}}{U_{c(x)}}\right)^2 = \frac{\rho_o}{\rho_e}\left[1 - \frac{\left\{1 - \frac{\rho_e}{\rho_o}R_o^2\right\}}{\left\{1 + \frac{\rho_\infty U_\infty^2}{\rho_o U_o^2}(c_{P_o} - c_{P_{(x)}})\right\}}\right] \qquad \text{(VIII-1)}$$

$$\frac{U_{c(x)}^2}{U_{o(x)}^2} = \frac{1 - \frac{\rho_e}{\rho_o}R_o^2}{1 - \frac{\rho_e}{\rho_o}R_1^2} \qquad \text{(VIII-2)}$$

(B) _Derivation of pertinent equations for the Wall Layer in the Initial Region._ - In order to solve for the unknowns, θ_1 and H_1, we require two equations. $U_{C(x)}$ can be calculated from Equation (VIII-2). The following approach is taken to derive the desired equations:

For incompressible flow, the governing partial differential equations for viscous flow with usual two-dimensional boundary layer assumptions are as follows:

Continuity Equation. -

$$\frac{\partial u}{\partial x} + \frac{\partial v}{\partial y} = 0 \qquad \text{(VIII-3)}$$

X - Momentum Equation. -

$$u\frac{\partial u}{\partial x} + v\frac{\partial u}{\partial y} = -\frac{1}{\rho_o}\frac{dp}{dx} + \frac{1}{\rho_o}\frac{\partial \tau}{\partial y} \qquad \text{(VIII-4)}$$

Y - Momentum Equation with the usual boundary layer assumptions for attached flow can be written as:

$$\frac{\partial P}{\partial y} = 0 \qquad \text{(VIII-5)}$$

Following Truckenbrott, we assume that wall layer velocity profile form a one parameter family of curves and can be represented as,

$$\frac{u}{U_c} = \left(\frac{y}{\delta_1}\right)^{1/n} \qquad \text{(VIII-6)}$$

112

Where n is dependent on the previous upstream history and is primarily a function of pressure gradient.

By making use of Equation (VIII-6) in the definitions for θ_1, δ_1^*, δ_1^{**}, etc. the following relations can be derived:

$$\frac{\theta_1}{\delta_1} = \frac{n}{(n+2)(n+1)} \quad ; \quad \frac{\delta_1^*}{\delta_1} = \frac{1}{n+1}$$

$$\frac{\delta^{**}}{\delta_1} = \frac{2n}{(n+1)(n+3)} \quad ; \quad H_1 = \frac{n+2}{n}$$

$$\widetilde{H} = \frac{2(n+2)}{n+3} = \frac{4H_1}{3H_1 - 1} \tag{VIII-7}$$

$$n = \frac{2}{(H_1 - 1)} \quad ; \quad \frac{\theta_1}{\delta_1} = \frac{H_1 - 1}{H_1(H_1 + 1)}$$

The Euler equation, valid at external edge $A_1A_2A_3$ in Figure (VIII-1) can be written as:

$$\frac{dP}{dx} = -\rho_e U_{e_{(x)}} \frac{dU_e}{dx} \tag{VIII-8}$$

By making use of Equation (VIII-5) in Equations (VIII-1) and (VIII-2), we can write,

$$\frac{dP}{dx} = -\rho_o U_{c_{(x)}} \frac{dU_e}{dx} \tag{VIII-9}$$

From the continuity Equation (VIII-3) we have,

$$V = -\int_0^y \frac{\partial U}{\partial x} \, dy \tag{VIII-10}$$

Boundary conditions applicable to the wall layer under consideration are:

$$\text{At} \quad y = 0 \; : \; u = 0 \; , \; v = 0 \; , \; \tau = \tau_w$$

$$\text{At} \quad y = \delta_1 \; : \; u = U_c \; , \; \tau = \tau_{(\delta_1)} \; , \; -\frac{1}{\rho_o}\frac{dP}{dx} = U_c \frac{dU_c}{dx} \tag{VIII-11}$$

Integrating Equation (VIII-4) from $y = 0$ to $y = \delta_1$ and making use of Equations (VIII-5) through (VIII-11), the following <u>Momentum Integral Equation for Wall Layer in the Initial Region</u> is derived:

$$\frac{d\theta_1}{dx} + \frac{\theta_1}{U_c}\frac{dU_c}{dx}(2 + H_1) = \frac{\tau_w}{\rho_o U_c^2}\left(1 - \frac{\tau_{(\delta_1)}}{\tau_w}\right) \tag{VIII-12}$$

A second equation is derived by first multiplying Equation (VIII-4) by u and then integrating from $Y = 0$ to $Y = \delta_1$. Use is also made of Equations (VIII-5) through (VIII-10) to obtain the following equation:

$$\frac{dH_1}{dx} = \frac{H_1}{\theta_1}(3H_1 - 1)\frac{\tau_w}{\rho_o U_c^2} + \frac{(H_1 - 1)(3H_1 - 1)}{2\theta_1}\frac{\tau_w}{\rho_o U_c^2}\frac{\tau_{(\delta_1)}}{\tau_w}$$

$$- H_1(3H_1 - 1)(H_1 - 1)\left(\frac{1}{U_c}\frac{dU_c}{dx}\right) - \frac{(3H_1 - 1)}{2\theta_1}\int_0^{\delta_1}\frac{\tau}{\rho_o U_c^2}\frac{\partial}{\partial y}\left(\frac{u}{U_c}\right)dy \tag{VIII-13}$$

The above equation is the <u>dissipation energy integral equation</u> or the <u>form factor equation</u> for the wall layer in the initial region.

(C) <u>Derivation of Pertinent Equations for Jet Layer (i.e. Region between</u> $\delta_2 - \delta_3$ <u>in Figure VIII-2 in the Initial Region).</u> - From experimental data of the velocity profiles, it is found that velocity profiles in the jet layer in the Initial Region are similar for various pressure distributions as well as for different ratios of slot exit to the initial free stream velocities if the similarity parameters and similarity function are defined in the following manner:

$$\eta_1 = \frac{\delta_3 - y}{\delta_3 - \delta_2} \qquad f(\eta_1) = \frac{U_c - u}{U_c - U_w} \tag{VIII-14}$$

where

u = velocity in $\delta_2 - \delta_3$ layer at any distance Y above wall (see Figure VIII-2)

$U_W = U_{W(X)}$ = velocity at $Y = \delta_3$

U_C = velocity in the core

Boundary conditions for the layer $\delta_2 - \delta_3$ are as follows:

$$\text{At} \quad y = \delta_2 \ : \ \eta_1 = 1 \ , \ f(\eta_1) = 0 \ , \ \tau = \tau_{(\delta_2)}$$

$$\text{At} \quad y = \delta_3 \ : \ \eta_1 = 0 \ , \ f(\eta_1) = 1 \ , \ \tau = \tau_{(\delta_2)} \tag{VIII-15}$$

Integrate Equation (VIII-4) from $Y = \delta_2$ to $Y = \delta_3$, make use of Equation VIII-14), boundary conditions (VIII-15) and also Equations (VIII-12) and (VIII-13) to obtain the following momentum integral equation for the jet layer, $\delta_2 - \delta_3$, in the initial region:

$$\left\{\int_0^1 (1-f(\eta_1))d\eta_1\right\}\left[\frac{d}{dx}\left\{(\delta_3 - \delta_2)U_c(U_c - U_w)\right\}\right] - \left\{\int_0^1 f(\eta_1)d\eta_1\right\}\left[\frac{d}{dx}\left\{(\delta_3 - \delta_2)(U_c - U_w)^2\right\}\right]$$

$$+ \left\{\int_0^1 f^2(\eta_1)d\eta_1\right\}\left[\frac{d}{dx}\left\{(\delta_3 - \delta_2)(U_c - U_w)^2\right\}\right] + U_c \frac{dU_w}{dx}(\delta_3 - \delta_2)$$

$$- (U_c - U_w)(\delta_3 - \delta_2)\left(\frac{dU_w}{dx}\right)\int_0^1 f(\eta_1)d\eta_1 + U_c(U_c - U_w)\frac{d\delta_2}{dx}$$

$$\text{(VIII-16)}$$

$$- (U_c - U_w) U_c H_1 \left\{\frac{\tau_w}{\rho_o U_c^2}\left(1 - \frac{^{\tau}(\delta_1)}{\tau_w}\right) - \frac{\theta_1}{U_c}\frac{dU_c}{dx}(H_1 + 2)\right\}$$

$$- (U_c - U_w) U_c \left\{H_1(3H_1 - 1)\frac{\tau_w}{\rho_o U_c^2} + \frac{(H_1 - 1)(3H_1 - 1)}{2}\left(\frac{\tau_w}{\rho_o U_c^2}\right)\left(\frac{^{\tau}(\delta_1)}{\tau_w}\right)\right.$$

$$\left. - H_1(3H - 1)(H_1 - 1)\left(\frac{1}{U_c}\frac{dU_c}{dx}\right)\theta_1 - \frac{(3H_1 - 1)^2}{2}\int_0^{\delta_1}\frac{\tau}{\rho_o U_c^2}\frac{\partial}{\partial y}\left(\frac{u}{U_c}\right)dy\right\}$$

$$- (U_c - U_w) H_1 \theta_1 \frac{dU_c}{dx} + (U_c - U_w)\delta_2\frac{dU_c}{dx} - U_c\frac{dU_c}{dx}(\delta_3 - \delta_2)$$

$$= \frac{\tau_w}{\rho_o}\left\{\frac{^{\tau}(\delta_3)}{\tau_w} - \frac{^{\tau}(\delta_2)}{\tau_w}\right\}$$

In analogy with free jet flow, the rate of growth of boundaries of jet layer $\delta_2 - \delta_3$ can be expressed as:

$$\frac{d(\delta_3 - \delta_2)}{dx} = C_1 \frac{U_c - U_w}{U_c + U_w} \qquad \text{(VIII-17)}$$

C_1 = constant determined experimentally (≈ 0.4)

(D) <u>Derivation of equations for the wake layer (i.e. region between</u> $\delta_3 - \delta_4$ <u>in Figure VIII-2 in the Initial Region</u>). - From experimental data of the velocity profiles, it is observed that velocity profiles in the wake layer become "similar" if the similarity variable and similarity function is defined in the following manner:

$$\eta_2 = \frac{y - \delta_3}{y_{1_c} - \delta_3} \quad ; \quad f(\eta_2) = \frac{U_e - u}{U_e - U_w} \qquad \text{(VIII-18)}$$

where, (see Figure VIII-2)

δ_3 = distance above surface at the common boundary of jet and wake layers

u = velocity at any distance y above wall in the wake layer

U_e = velocity at $y = \delta_4$ where the flow can be considered inviscid

y_{1c} = distance y where $u = \dfrac{U_e + U_w}{2}$

The "similarity curve" of $f(\eta_2)$ vs η_2 can reasonably well be approximated by a third order least square polynomial.

The third order is chosen for the reason that this curve has a point of inflection. Thus,

$$f(\eta_2) = A_1 + A_2(\eta_2) + A_3(\eta_2)^2 + A_4(\eta_2)^3 \qquad (VIII-19)$$

where A_1, A_2, A_3, and A_4 are coefficients for least square 3rd order polynomials.

The boundary conditions for the wake layer $\delta_3 - \delta_4$ are as follows:

$$\text{At } y = \delta_3 \; : \; \eta_2 = 0 \;,\; f(\eta_2) = 1 \;,\; \tau = \tau_{(\delta_3)}$$

$$\text{At } y = y_{1c} \; : \; \eta_2 = 1 \;,\; f(\eta_2) = 0.5 \;,\; u = \frac{U_e + U_w}{2} \qquad (VIII-20)$$

$$\text{At } y = \delta_4 \; : \; f(\eta_2) = 0 \;,\; u = U_e \;,\; \tau = 0 \;,\; \eta_2 = K_1$$

$$\text{where } K_1 = \eta_2\big|_{y=\delta_4}$$

Integrating Equation (VIII-4) from $y = \delta_3$ to $y = \delta_4$ and making use of the Equations (VIII-10), (VIII-12), (VIII-13), and (VIII-18) and also boundary conditions given by (VIII-20), the following equation is obtained:

116

$$- \left\{ \int_0^{K_1} f(\eta_2)d\eta_2 \right\} \left[\frac{d}{dx} \left\{ (y_{1c} - \delta_3)(U_e)(U_e - U_w) \right\} \right]$$

$$+ \left\{ \int_0^{K_1} f^2(\eta_2)d\eta_2 \right\} \left[\frac{d}{dx} \left\{ (y_{1c} - \delta_3)(U_e - U_w)^2 \right\} \right] - \frac{d\delta_3}{dx} U_w (U_e - U_w)$$

$$- \left\{ \int_0^{K_1} f(\eta_2)d\eta_2 \right\} \left[\frac{dU_e}{dx} (U_e - U_w)(y_{1c} - \delta_3) \right] + (U_e - U_w) U_c H_1 (3H_1 - 1) \frac{\tau_w}{\rho_o U_c^2}$$

$$+ \frac{(U_e - U_w)}{2} U_c (H_1 - 1)(3H_1 - 1) \frac{\tau_w}{\rho_o U_c^2} \frac{\tau_{(\delta_1)}}{\tau_w} - (U_e - U_w) \theta_1 H_1 (3H_1 - 1)(H_1 - 1) \frac{dU_c}{dx}$$

$$- \frac{U_e - U_w}{2} U_c (3H_1 - 1)^2 \int_0^{\delta_1} \frac{\tau}{\rho_o U_c^2} \frac{\partial}{\partial y} \left(\frac{u}{U_c} \right) dy + (U_e - U_w) U_c H_1 \frac{\tau_w}{\rho_o U_c^2} \qquad \text{(VIII-21)}$$

$$- (U_e - U_w) U_c H_1 \frac{\tau_w}{\rho_o U_c^2} \frac{\tau_{\delta_1}}{\tau_w} - 2(U_e - U_w) H_1 \theta_1 \frac{dU_c}{dx} - (U_e - U_w) H_1^2 \theta_1 \frac{dU_c}{dx}$$

$$+ (U_e - U_w) \theta_1 H_1 \frac{dU_c}{dx} - (U_e - U_w) \delta_2 \frac{dU_c}{dx} - (U_e - U_w)(\delta_3 - \delta_2) \frac{dU_c}{dx}$$

$$- (U_e - U_w) \frac{d\delta_3}{dx} (U_c - U_w) + (U_e - U_w) \left\{ \int_0^1 f(\eta_1)d\eta_1 \right\} \frac{d}{dx} \left\{ (\delta_3 - \delta_2)(U_c - U_w) \right\}$$

$$= - \frac{\tau}{\rho_e} \frac{\tau_{(\delta_3)}}{\tau_w}$$

The above equation is the momentum integral equation for wake layer in the Initial Region.

The rate of growth of wake layer $\delta_3 - \delta_4$ is expressed in an analogous manner to the jet layer $\delta_2 - \delta_3$ as follows:

$$\frac{d}{dx}(y_{1c} - \delta_3) = C_2 \frac{U_e - U_w}{U_e + U_w} \qquad \text{(VIII-22)}$$

$$C_2 = \text{constant determined empirically } (\approx 0.18)$$

The unknowns which are to be determined in the Initial Regions are (1) velocity in the core, $U_{c(x)}$, (2) wall layer momentum thickness, $\Theta_{(x)}$, (3) wall layer form factor, $H_{(x)}$, (4) outer edge of core layer, $\delta_{2(x)}$, (5) outer edge of jet layer $\delta_{3(x)}$, (6) velocity at the junction of jet layer and wake layer, $U_{w(x)}$, (7) outer edge of wake layer, δ_4. The seven equations used to solve for the seven unknowns are Equations (VIII-2), (VIII-12), (VIII-13), (VIII-16), (VIII-17), (VIII-21), and (VIII-22).

The initial conditions required for the solution of the above equations are the conditions at the exit of the slot. Those shown in Figure VIII-2 are (1) boundary layer thickness on the upper surface of main component at the trailing edge, (2) momentum thickness on the upper surface of the main component at the trailing edge, (3) boundary layer thickness δ_{s1} on the under-surface of the main component at trailing edge, (4) momentum thickness on the under-surface at the trailing edge, θ_{s1}, (5) velocity at the trailing edge, $U_{e(o)}$, (6) slot velocity at the exit $U_{c(o)}$, (7) boundary layer momentum thickness on the flap upper surface at slot exit, θ_{s2}, (8) boundary layer thickness on the flap upper surface at slot exit, δ_{s2}.

(E) <u>Derivation of pertinent equations in Main Region I between Stations 1 and 2. (Referring to Figure VIII-2, the Main Region is defined as extending from station 1 to station 3)</u>. - Solution of the equations derived in the previous section for the Initial Region would yield the values of H_1, θ_1, δ_1 ($=\delta_2$), δ_3, δ_4 and U_W at station 1 in Figure VIII-2. These values then become the initial conditions for the solution of equations which are developed in this section.

Because of the existence of a potential core, velocity at the edge of wall layer in the Initial Region was given by the use of Bernoulli equation and the condition of constancy of pressure in the y direction. In the Main Region where flow is viscous from the wall to the external edge of viscous layer, the velocity U_M at the edge of wall layer has to be determined from a viscous solution.

In the Main Region between stations 1 and 2, Main Region I, there are six unknowns, namely, θ_5, H_5, U_M, U_W, δ_3, and δ_4. Therefore, six equations are needed which have to be solved simultaneously.

(F) <u>Wall-Layer (between stations 1 and 2 in Main Region)</u>. - Assume that velocity profiles in the Main Region can be represented as one parameter family of profiles defined as follows:

$$\left(\frac{u}{U_m}\right) = \left(\frac{y}{\delta_5}\right)^{1/n_2} \tag{VIII-23}$$

Making use of Equation (VIII-23) in the definitions for δ_5^*, θ_5, H_5, $\widetilde{H}_5$ and δ_5^{**}, the following relations can be derived:

$$\delta_5^* = \int_0^{\delta_5} \left(1 - \frac{u}{U_m}\right) dy \qquad \theta_5 = \int_0^{\delta_5} \frac{u}{U_m}\left(1 - \frac{u}{U_m}\right) dy$$

$$H_5 = \frac{\delta_5^*}{\theta_5} \qquad \delta_5^{**} = \int_0^{\delta_5} \frac{u}{U_m}\left\{1 - \left(\frac{u}{U_m}\right)^2\right\} dy \qquad \widetilde{H}_5 = \frac{\delta_5^{**}}{\theta_5} = \frac{4H_5}{3H_5 - 1}$$

$$\frac{u}{U_m} = \left(\frac{y}{\delta_5}\right)^{1/n_2} \qquad \frac{\theta_5}{\delta_5} = \frac{H_5 - 1}{H_5(H_5 + 1)} = \frac{n_2}{(n_2 + 1)(n_2 + 2)} \qquad \text{(VIII-24)}$$

$$\tilde{H}_5 = \frac{4H_5}{3H_5 - 1} \qquad\qquad n_2 = \frac{2}{H_5 - 1} \qquad\qquad \frac{n_2}{n_2 + 1} = \frac{2}{H_5 + 1}$$

$$\delta_5 \frac{n_2}{n_2 + 1} = 2\theta_5 \frac{H_5}{H_5 - 1} \qquad\qquad \delta_5^* = \frac{\delta_5}{n_2 + 1} \qquad\qquad H_5 = \frac{n_2 + 2}{n_2}$$

Boundary conditions for the wall layer are:

$$\text{At} \qquad y = 0 \;:\; u = 0 \;,\; v = 0 \;,\; \tau = \tau_w \qquad\qquad \text{(VIII-25)}$$

$$\text{At} \qquad y = \delta_5 \;:\; u = U_m \;,\; \tau = \tau_{\delta_5}$$

The Euler equation, valid at the external edge of the viscous layer, is:

$$-\frac{1}{\rho}\frac{dP}{dx} = U_e \frac{dU_e}{dx} \qquad\qquad \text{(VIII-26)}$$

Integrate Equation (VIII-4) with respect to y from $y = 0$ to $y = \delta_5$, and make use of Equations (VIII-16), (VIII-26), (VIII-24) and boundary conditions (VIII-25) to obtain the following momentum integral for the wall layer in the Main Region between stations 1 and 2:

$$\frac{d\theta_5}{dx} - 2\frac{\theta_5}{H_5 - 1}\frac{1}{U_m}\frac{dU_m}{dx} + \frac{U_e}{U_m^2}\frac{dU_e}{dx}\frac{\theta_5 H_5(H_5 + 1)}{H_5 - 1} = \frac{\tau_w}{\rho U_m^2}\left\{1 - \frac{\tau(\delta_5)}{\tau_w}\right\} \qquad \text{(VIII-27)}$$

Multiply both sides of Equation (VIII-4) by u, integrate from $y = 0$ to $y = \delta_5$ and make use of Equations (VIII-10), (VIII-24), (VIII-26) and boundary conditions (VIII-25) to obtain the following equation:

$$\frac{dH_5}{dx} = \frac{H_5}{\theta_5}(3H_5 - 1)\frac{\tau_w}{\rho U_m^2} + \frac{H_5 - 1}{2\theta_5}(3H_5 - 1)\left(\frac{\tau_w}{\rho U_m^2}\right)\left(\frac{\tau(\delta_5)}{\tau_w}\right)$$

$$-\frac{U_e}{U_m^2}\frac{dU_e}{dx}(H_5)(3H_5 - 1)(H_5 - 1) - \frac{(3H_5 - 1)^2}{2\theta_5}\int_0^{\delta_5}\frac{\tau}{\rho U_m^2}\frac{\partial}{\partial y}\left(\frac{u}{U_m}\right)dy \qquad \text{(VIII-28)}$$

Equation (VIII-28) is the form factor equation for wall layer in Main Region between stations 1 and 2.

(G) Jet Layer $\delta_5 - \delta_3$, between stations 1 - 2. - Experimental data for velocity profiles in the Main Region indicate that the "similarity of velocity

profiles for jet layer" is obtained when the similarity parameter and similarity function are defined as follows:

$$\eta_3 = \frac{\delta_3 - y}{\delta_3 - \delta_5} \quad ; \quad \xi(\eta_3) = \frac{U_m - u}{U_m - U_w}$$

(VIII-29)

Applicable boundary conditions for this layer are:

$$\text{At} \quad y = \delta_5 \; : \; u = U_m \; , \; \eta_3 = 1 \; , \; \xi(\eta_3) = 0 \; , \; \tau = \tau_{(\delta_5)}$$

$$\text{At} \quad y = \delta_3 \; : \; u = U_w \; , \; \eta_3 = 0 \; , \; \xi(\eta_3) = 1$$

(VIII-30)

Integrate Equation (VIII-4) with respect to y from $y = \delta_5$ to $y = \delta_3$, make use of Equations (VIII-24), (VIII-10), (VIII-26), (VIII-27) and (VIII-28) and also the boundary conditions (VIII-30) to obtain the following momentum integral equation for the jet layer in the Main Region between stations 1 and 2:

$$\left\{ \int_0^1 \left(1 - f(\eta_3) \right) d\eta_3 \right\} \left[\frac{d}{dx} \left\{ U_m (U_m - U_w)(\delta_3 - \delta_5) \right\} \right]$$

$$- \left\{ \int_0^1 f(\eta_3) d\eta_3 \right\} \left[\frac{d}{dx} \left\{ (U_m - U_w)^2 (\delta_3 - \delta_5) \right\} \right]$$

(VIII-31)

$$+ \left\{ \int_0^1 f^2(\eta_3) d\eta_3 \right\} \left[\frac{d}{dx} \left\{ (U_m - U_w)^2 (\delta_3 - \delta_5) \right\} \right] + U_m (\delta_3 - \delta_5) \left(\frac{dU_w}{dx} \right)$$

$$- \left(\frac{dU_w}{dx} \right) (\delta_3 - \delta_5)(U_m - U_w) \int_0^1 f(\eta_3) d\eta_3 + 2(U_m - U_w)\theta_5 \frac{H_5(H_5 + 1)}{(H_5 + 1)^2} \left(\frac{dU_m}{dx} \right)$$

$$- 4U_m(U_m - U_w) \frac{H_5^2}{(H_5 - 1)^2} \left(\frac{\tau_w}{\rho U_m^2} \right) - U_m(U_m - U_w) \frac{\tau_w}{\rho U_m^2} \frac{\tau_{(\delta_5)}}{\tau_w} \frac{5H_5 - 1}{H_5 - 1}$$

$$+ 2(U_m - U_w) \frac{H_5}{(H_5 - 1)^2} (2H_5^2 - 5H_5 + 1)\theta_3 \frac{U_e}{U_m} \frac{dU_e}{dx}$$

$$+ U_m(U_m - U_w) \frac{(3H_5 - 1)^2}{(H_5 - 1)^2} \int_0^{\delta_5} \frac{\tau}{\rho U_m^2} \frac{\partial}{\partial y} \left(\frac{u}{U_m} \right) dy - U_e \frac{dU_e}{dx} (\delta_3 - \delta_5)$$

$$= \frac{\tau_w}{\rho} \frac{\tau_{(\delta_3)}}{\tau_w} - \frac{\tau_w}{\rho} \frac{\tau_{(\delta_5)}}{\tau_w}$$

The rate of growth of the jet layer $\delta_5 - \delta_3$ between stations 1 and 2 can be expressed as follows:

$$\frac{d}{dx}(\delta_3 - \delta_5) = C_3 \frac{U_m - U_w}{U_m + U_w} \qquad (VIII\text{-}32)$$

where C_3 is an empirical constant (≈ 0.17).

(H) <u>Wake Layer $\delta_3 - \delta_4$, between stations 1 and 2.</u> – Experimental data for the velocity profiles in Main Region for different pressure distributions indicate that the velocity profiles in the wake layer become "similar" for the following similarity parameters:

$$\eta_4 = \frac{y - \delta_3}{y_{2c} - \delta_3} \qquad\qquad f(\eta_4) = \frac{U_e - u}{U_e - U_w} \qquad (VIII\text{-}33)$$

where, (see Figure VIII-2)

  u = velocity at any point y above wall in the wake layer

  U_e = velocity at $y = \delta_4$ where the flow is considered inviscid

  y_{2c} = distance y above surface where $U = \dfrac{U_e + U_W}{2}$

$f(\eta_4)$ can be approximated reasonably well by the third order least square polynomial as follows:

$$f(\eta_4) = B_1 + B_2(\eta_4) + B_3(\eta_4)^2 + B_4(\eta_4)^3 \qquad (VIII\text{-}34)$$

where B_1, B_2, B_3, and B_4 are coefficients of least square polynomial.

Applicable boundary conditions are as follows:

$$
\begin{aligned}
&\text{At} \quad y = \delta_3 \quad : \quad \eta_4 = 0 \;,\; f(\eta_4) = 1 \;,\; \tau = \tau_{(\delta_4)} \;,\; u = U_{w(1)} \\[4pt]
&\text{At} \quad y = y_{2c} \quad : \quad \eta_4 = 1 \;,\; f(\eta_4) = 0.5 \;,\; u + \frac{U_e + U_w}{2} \qquad\qquad (VIII\text{-}35) \\[4pt]
&\text{At} \quad y = \delta_4 \quad : \quad f(\eta_4) = 0 \;,\; u = U_e \;,\; \tau = 0 \;,\; \eta_4' = K_2 = \text{constant}
\end{aligned}
$$

By making use of the above boundary conditions and following the procedure previously described, the following momentum integral equation for the wake layer in the Main Region between station 2 and 3 can be derived:

$$-\left\{\int_0^{K_2} f(\eta_4)d\eta_4\right\}\left[\frac{d}{dx}\left\{U_e(U_e - U_w)(y_{2c} - \delta_3)\right\}\right]$$

$$+\left\{\int_0^{K_2} f^2(\eta_4)d\eta_4\right\}\left[\frac{d}{dx}\left\{(U_e - U_w)^2(y_{2c} - \delta_3)\right\}\right]$$

$$-\left\{\int_0^{K_2} f(\eta_4)d\eta_4\right\}\left[\frac{dU_e}{dx}(U_e - U_w)(y_{2c} - \delta_3)\right]$$

$$- (U_e - U_w)(U_m)\frac{d}{dx}(\delta_3 - \delta_5) - (U_e - U_w)(\delta_3 - \delta_5)\frac{dU_m}{dx} \qquad \text{(VIII-36)}$$

$$+\left\{\int_0^1 f(\eta_3)d\eta_3\right\}\left[(U_e - U_w)\frac{d}{dx}\left\{(U_m - U_w)(\delta_3 - \delta_5)\right\}\right]$$

$$- 2(U_e - U_w)\theta_5\frac{H_5(H_5 + 1)}{(H_5 - 1)^2}\frac{dU_m}{dx} + 4U_m(U_e - U_w)\frac{\tau_w}{\rho U_m^2}\frac{H_5^2}{(H_5 - 1)^2}$$

$$+ U_m(U_e - U_w)\left(\frac{5H_5 - 1}{H_5 - 1}\right)\frac{\tau_w}{\rho U_m^2}\frac{\tau(\delta_5)}{\tau_w} - 2(U_e - U_w)\frac{U_e}{U_m}\frac{dU_e}{dx}\theta_5\frac{H_5}{(H_5 - 1)^2}(2H_5^2 - 5H_5 + 1)$$

$$- U_m(U_e - U_w)\frac{(3H_5 - 1)^2}{(H_5 - 1)^2}\int_0^{\delta_5}\frac{\tau}{\rho U_m^2}\frac{\partial}{\partial y}\left(\frac{u}{U_m}\right)dy = -\frac{\tau(\delta_3)}{\rho}$$

The growth of wake layer $\delta_3 - \delta_4$ is expressed by the following equation:

$$\frac{d}{dx}(y_{2c} - \delta_3) = C_4\frac{(U_e - U_w)}{(U_e + U_w)} \qquad \text{(VIII-37)}$$

where C_4 is the empirical constant (≈ 0.185).

The solution to the six unknowns is to be found as a function of the independent variable X at discrete points in Main Region I. These unknowns are (1) wall layer momentum thickness, θ, (2) wall layer form factor, H, (3) velocity at the junction of wall layer and jet layer, $U_{m(x)}$, (4) velocity at the junction of jet and wake layer, $U_{w(x)}$, (5) outer edge of jet layer, $\delta_{3(x)}$,

and (6) outer edge of wake layer $\delta_{4(x)}$. These six unknowns are evaluated by simultaneous solution of the six differential equations (VIII-27), (VIII-28), (VIII-31), (VIII-32), (VIII-36) and (VIII-37).

The initial conditions required for the above equations are the values calculated at station 1 by the solution of the equations in the Initial Region. The initial conditions at station 1 are, (1) wall layer momentum thickness, θ_5, (2) wall layer form factor, H_s, (3) velocity at the edge of wall layer, U_c, (4) outer edge of jet layer, δ_3, (5) velocity at the junction of wake layer and jet layer, U_w, and (6) outer edge of wake layer, δ_4.

(I) <u>Equations in the Main Region II between stations 2 and 3, Figure VIII-2</u>

As seen in Figure VIII-2, the region between stations 2 and 3 differs from the previously considered one in that the wake layer does not exist. Thus the region between stations 2 and 3 consists of (i) wall layer and (ii) jet layer.

The number of unknowns in this case consists of θ_5, H_5, U_M and δ_6 which require four equations. The two wall layer equations namely (i) momentum integral equation and (ii) form factor or energy integral equation are essentially the same as the wall layer equations for region between stations 1 and 2. These are repeated here for the sake of continuity.

Wall-Layer Momentum Integral Equation, Stations 2-3.-

$$\frac{d\theta_5}{dx} = 2\frac{\theta_5}{H_5 - 1}\frac{1}{U_m}\frac{dU_m}{dx} - \theta_5 H_5 \frac{H_5 + 1}{H_5 - 1}\frac{U_e}{U_m^2}\frac{dU_e}{dx} + \frac{\tau_w}{\rho U_m^2} - \frac{\tau_{(\delta_5)}}{\tau_w}\frac{\tau_w}{\rho U_m^2} \qquad \text{(VIII-38)}$$

Wall-Layer Form Factor Equation, Stations 3-5. -

$$\frac{dH_5}{dx} = \frac{H_5}{\theta_5}(3H_5 - 1)\frac{\tau_w}{\rho U_m^2} + \frac{H_5 - 1}{2\theta_5}(3H_5 - 1)\frac{\tau_w}{\rho U_m^2}\frac{\tau_{(\delta_5)}}{\tau_w}$$

$$- \frac{U_e}{U_m^2}\frac{dU_e}{dx} H_5(H_5 - 1)(3H_5 - 1) - \frac{(3H_5 - 1)^2}{2\theta_5}\int_0^{\delta_5}\frac{\tau}{\rho U_m^2}\frac{\partial}{\partial y}\left(\frac{u}{U_m}\right)dy \qquad \text{(VIII-39)}$$

Jet-Layer Momentum Integral Equation, Stations 2-3. - Boundary conditions for the jet layer between stations 2-3 at $y = \delta_5$ are the same as for jet layer between station 1-2. At the other edge $y = \delta_6$, the jet layer under consideration is subjected to inviscid flow and hence the Euler equation can be used to advantage. In a manner similar to that previously described, the following momentum integral equation for the jet layer can be developed:

$$\left\{\int_0^1 \left(1 - f(\eta_5)\right)d\eta_5\right\}\left[\frac{d}{dx}\left\{U_m(U_m - U_e)(\delta_6 - \delta_5)\right\}\right]$$

$$-\left\{\int_0^1 f(\eta_5)d\eta_5\right\}\left[\frac{d}{dx}\left\{(U_m - U_e)^2(\delta_6 - \delta_5)\right\}\right]$$

$$+\left\{\int_0^1 f^2(\eta_5)d\eta_5\right\}\left[\frac{d}{dx}\left\{(U_m - U_e)^2(\delta_6 - \delta_5)\right\}\right]$$

$$+\left\{\int_0^1 \left(1 - f(\eta_5)\right)d\eta_5\right\}\left[(U_m - U_e)(\delta_6 - \delta_5)\right]\frac{dU_e}{dx}$$

$$- 4U_m(U_m - U_e)\frac{\tau_w}{\rho U_m^2}\frac{H_5^2}{(H_5 - 1)^2} - U_m(U_m - U_e)\frac{\tau_w}{\rho U_m^2}\frac{{}^\tau(\delta_5)}{\tau_w}\frac{5H_5 - 1}{H_5 - 1}$$

$$+ 2(U_m - U_e)\frac{U_e}{U_m}\frac{dU_e}{dx}\theta_5\frac{H_5}{(H_5 - 1)^2}(2H_5^2 - 5H_5 + 1)$$

$$+ U_m(U_m - U_e)\frac{(3H_5 - 1)^2}{(H_5 - 1)^2}\int_0^{\delta_5}\frac{\tau}{\rho U_m^2}\frac{\partial}{\partial y}\left(\frac{u}{U_m}\right)dy$$

$$+ 2(U_m - U_e)\theta_5\frac{H_5(H_5 + 1)}{(H_5 - 1)^2}\frac{dU_m}{dx} = \frac{\tau_w}{\rho}\frac{{}^\tau(\delta_5)}{\tau_w}$$

(VIII-40)

Growth Equation for Jet Layer Between Stations 2-3. - In the same manner as before, the growth equation can be written as;

$$\frac{d}{dx}(\delta_6 - \delta_5) = C_5\frac{(U_m - U_e)}{(U_m + U_e)}$$

where C_5 is an empirical constant (≈ 0.17)

(VIII-41)

Thus Equations (VIII-38), (VIII-39), (VIII-40) and (VIII-41) are four equations for the solutions for θ_5, H_5, U_M and δ_6 in the region between stations 2 and 3 in Figure VIII-2.

(J) Equations in the Main Region Downstream of Station 3

The viscous flow downstream of station 3 in Figure VIII-2, is found to be qualitatively similar to the ordinary turbulent boundary layer as revealed by measured experimental velocity profiles in the region downstream of Main Region II. The theory and equations used to calculate the boundary layer quantities in this region are those of Nash. This theory is described briefly in Section V. The initial conditions required for the start of the calculations, for example, momentum thickness and form factor at station 3, are supplied by Main Region II confluent boundary layer solution.

(K) **Auxiliary Equations.** - The equations presented in the previous paragraphs contain terms such as $\dfrac{\tau_w}{\rho U_m^2}$, $\int \dfrac{\tau}{\rho U_m^2}\dfrac{\partial}{\partial y}\left(\dfrac{U}{U_m}\right)dy$; $\dfrac{\tau_w - \tau_{\delta_5}}{\rho U_m^2}$, etc.

As the viscous flow under consideration is of a turbulent nature, theoretical expressions for the above quantities are not available as in the case of laminar boundary layers. Recourse is made to experimental measurements to obtain empirical expressions for these parameters as a function of those dependent variables which are calculated for the problem solution. The expressions for wall shear, wall layer shear dissipation integral and shear at the edge of the wall layer have been derived from measured velocity profiles and pressure distributions and, by solving the differential momentum integral equation by finite difference methods. The least-square curve-fit expressions for the above quantities are given by the following:

Wall Shear. -

$$\frac{\tau_w}{\rho U_m^2} = 1.964 \exp\left[1.819H + 35.68y - 1.365y^2\right]y^{-114.6} \times 10^{16}$$

(VIII-42)

where $\qquad y = \ln\left[\dfrac{U_m \theta}{\nu}\right]$

Wall Layer Shear Dissipation Integral. -

$$\frac{\tau}{\rho U_m^2}\frac{\partial}{\partial y}\left(\frac{U}{U_m}\right)dy = 1.616 \exp\left[-0.636H + 48.55y - 1.82y^2\right](y)^{-158.7} \times 10^{23}$$

where $\qquad y = \ln\left[\dfrac{U_m \theta}{\nu}\right]$

(VIII-43)

Difference Between Wall Shear and Shear at the Edge of Wall Layer. -

$$\frac{\tau_w - \tau_{\delta_5}}{\rho U_m^2} = 2.518 \exp\left[-0.918H + 17.21y - 0.743y^2\right](y)^{-45.79}$$

where $\qquad y = \ln\left[\dfrac{U_m \theta}{\nu}\right]$

(VIII-44)

The non-dimensional velocity profile for the jet layer in the Initial Region is given by:

$$f(\eta_1) = 0.992 + 0.478\eta_1 - 6.105\eta_1^2 + 6.796\eta_1^3 - 2.166\eta^4$$

Non-dimensional velocity profile for the wake layer in the Initial Region is as follows:

125

$$f(\eta_2) = 1.032 - 0.416(\eta_2) - 0.195(\eta_2)^2 + 0.12(\eta_2)^3 - 0.015(\eta_2)^4$$

The non-dimensional velocity profile for the jet layer in the Main Region from the least-square polynomial fit is:

$$f(\eta_3) = 1.002 - 0.164(\eta_3) - 1.967(\eta_3)^2 + 1.338(\eta_3)^3 - 0.209(\eta_3)^4$$

The non-dimensional velocity profile for the wake layer in the Main Region is expressed as:

$$f(\eta_4) = 1.0194 - 0.4506(\eta_4) - 0.2029(\eta_4)^2 + 0.1543(\eta_4)^3 - 0.024(\eta_4)^4$$

The definitions for the above functions have been given in the nomenclature list.

From experimental evidence, a one-parameter family of velocity profiles has been found to exist for the wall layer in the Initial and Main Regions similar to that characterizing an ordinary turbulent boundary-layer. However, the relation between parameters such as $H = \delta^*/\theta$ and $\widetilde{H} = \delta^{**}/\theta$ for the wall layers in the Initial and Main Regions, has been found to differ from the ordinary turbulent boundary layer flow. The corresponding relations are given by the following equations:

For Initial and Main Regions. -

$$H = 4.411 - \frac{23.9}{\widetilde{H}} + \frac{33.11}{\widetilde{H}^2} \tag{VIII-45}$$

and for the Ordinary Turbulent Boundary Layer region:

$$H = 16.133 - \frac{56.91}{\widetilde{H}} + \frac{54.54}{\widetilde{H}^2} \tag{VIII-46}$$

Correlation (Confluent Boundary Layer). - The various sets of differential equations for each region (i.e. Initial Region, Main Region I, etc.) derived in the previous sections were first reduced in the form of sets of difference equations which are amenable to simultaneous solutions for the physical quantities in each layer (e.g. wall layer, wake layer, etc). Thus, for example, referring to the Main Region I, the solution for the unknown variables θ, U_M, δ_3, H and δ_4 is obtained through the simultaneous solution of the six Equations (VIII-27), (VIII-28), (VIII-31), (VIII-32), (VIII-36) and (VIII-37). The unknown parameters in the above equations, such as τ_w, τ_{δ_5}, etc. may be substituted from the auxiliary Equations, (VIII-42) through (VIII-46). These set of equations were programmed on the RAX version of an IBM-360 computer and also as a confluent boundary layer subroutine on the UNIVAC 1108. The numerical method

used for the solution is a modified, one-step Euler method with a repeated iteration solution.

The input to the subroutine version of the confluent boundary layer program is the six boundary layer quantities at the slot exit, as shown in Figure VIII-2, and the velocity ratio, $U_c(o)/U_e(o)$. The pressure distribution at the edge of the viscous layer is also a necessary input quantity. The program computes the following parameters of primary interest. (i) The X-location for the beginning and end of each region, (ii) local skin friction, (iii) velocities U_M and U_W at the junction of layers, as well as the thickness of each layer, and (iv) "equivalent displacement thickness" to be added to the airfoil geometry for the viscous solution.

Figures VIII-3A, VIII-3B and VIII-3C show the comparison of experimental and predicted values of $\dfrac{U_M}{U_e}$, H, $\widetilde{H}$, δ^*, δ^{**}, δ_1, δ_2. The experimental data shown in Figures VIII-3A, 3B, and 3C have been obtained from the wall-jet test facility at Lockheed-Georgia Company. In the above figures, the comparison is shown for Main Region II. The initial velocity ratio at the slot exit, $\dfrac{U_c(o)}{U_e(o)}$ was approximately equal to 1.6 and the pressure distribution was adverse. Figures VIII-4A through VIII-4C show a comparison of the calculated and experimental data in the initial region. In this case also, the experimental data have been obtained from the previously-mentioned source. The initial velocity ratio at the slot exit was approximately equal to 1.12 and the pressure distribution was highly adverse.

It can be seen from the foregoing correlated cases, that the comparisons of the computed values are in satisfactory agreement with the experimentally-measured parameters. Thus, the agreement appears to validate both the theoretical model as well as the numerical techniques utilized for the solution of the differential equations involved. It should be noted, however, that the mathematical model has been developed from a relatively small quantity of experimental boundary layer data representing a specific configuration. These data and the resulting model, may not represent entirely all the conditions which prevail on two-to-four-piece airfoils.

Therefore, while the present computational methods appear adequate for the present program objectives, additional test data and a more comprehensive mathematical model representing the confluent boundary-layer should be considered. Of primary concern is the effect of the multi-vaned flap configuration on separation, reattachment and Cl_{max} prediction.

(See also Figure VIII-2)

C_P = Pressure coefficient = $\dfrac{P - P_\infty}{\frac{1}{2}\rho_\infty U_\infty^2}$

C_{P0} = Pressure coefficient at station 0 in Figure VIII-2

$\bar{C}_P$ = Constant pressure specific heat

$f(\eta_1)$ = $\dfrac{U_c - u}{U_c - U_w}$

$f(\eta_2)$ = $\dfrac{U_e - u}{U_e - U_w} = f(\eta_4)$

$f(\eta_3)$ = $\dfrac{U_m - u}{U_m - U_w}$

$f(\eta_5)$ = $\dfrac{U_m - u}{U_m - U_e}$

g = Earth's gravitational constant

H_1 = Wall layer form factor in the Initial Region = $\dfrac{\delta_1^*}{\theta_1}$

H_5 = Wall layer form factor in the Main Region between station 2 and 5 in Figure VIII-2 = $\dfrac{\delta_5^*}{\theta_5}$

H_7 = Form factor downstream of station 5 in Figure VIII-2 = $\dfrac{\delta_7^*}{\theta_7}$

$\tilde{H}_1$ = $\dfrac{\delta^{**}}{\theta_1}$

$\tilde{H}_5$ = $\dfrac{\delta^{**}}{\theta_5}$

$\tilde{H}_7$ = $\dfrac{\delta^{**}}{\theta_7}$

K_1 = Value of η_2 at $y = \delta_4$

K_2 = Value of η_4 at $y = \delta_4$

n = Exponent in the wall layer velocity profile assumption

P = Wall static pressure

P_∞ = Free stream static pressure

P_0 = Wall static pressure at station 0

P_1 = Constant in the equation $\dfrac{T - T_m}{T_{a_w} - T_m} = 1 - \left(\dfrac{y}{\delta_5}\right)^{P_1/n}$

P_r = Prandtl number

q = Turbulent heat transfer at any point in the viscous layer = $\rho g \, \overline{C}_p \, \overline{V'T'}$

$q(\Delta_1)$ = q at $y = \Delta_1$ in Initial Region

$q(\Delta_s)$ = q at $y = \Delta_5$ in Main Region

R_1 = $\dfrac{U_e}{U_c}$

R_o = $\dfrac{U_{e(o)}}{U_o}$

T = Temperature at a distance y above the wall in the viscous layer

T_{aw} = Adiabatic wall temperature, function of x

T_c = Temperature in the core of the Initial Region

T_e = $T_{e(x)}$ temperature at the edge of a viscous layer

T_m = Temperature at the edge of wall layer $y = \delta_5$ in the Main Region

T_S = Temperature of the air at the exit of slot

T_W = Wall temperature

T_∞ = Temperature of free stream

t_I = $T - T_c$ in the Initial Region

$t_{I_{aw}}$ = $T_{aw} - T_c$ in the Initial Region

U = X component of velocity in the viscous layer

U_C = Velocity in the core in the Initial Region

U_e = Velocity at the edge of viscous layer

$U_{e(o)}$ = Velocity at the edge of viscous layer at station 0

U_0 = Initial velocity at station 0 through the slot

U_W = Velocity at the junction of jet and wake layer

V = y component of velocity in the viscous layer

y_{1c} = Distance y above wall in the wake layer in the Initial Region where $u = \dfrac{U_e + U_W}{2}$

y_{2c} = Distance y above wall in the wake layer in the Main Region where $u = \dfrac{U_e + U_W}{2}$

δ_1 = Wall layer thickness in the Initial Region

δ_2 = Distance y above wall at the junction of potential core and jet layer in the Initial Region

δ_3 = Distance above wall at the junction of jet layer and wake layer in the Initial Region

δ_4 = Distance above wall where the flow can be considered as inviscid in the Initial Region

δ_5 = Wall layer thickness in the Main Region between stations 1 and 3 of Figure VIII-2

δ_6 = Edge of viscous layer in the Main Region between stations 1 and 3 of Figure VIII-2

δ_7 = Edge of viscous layer in the Main Region after station 3

δ_1^* = Wall layer displacement thickness in the Initial Region = $\displaystyle\int_0^{\delta_1}\left(1 - \frac{u}{U_c}\right)dy$

δ_5^* = Wall layer displacement thickness in the Main Region between stations 2 and 5 in Figure VIII-2 = $\displaystyle\int_0^{\delta_5}\left(1 - \frac{u}{U_m}\right)dy$

δ_7^* = Wall layer displacement thickness in the downstream of station 5 in

Figure VIII-2 = $\displaystyle\int_0^{\delta_7} \left(1 - \frac{u}{U_e}\right) dy$

δ_1^{**} = Wall layer dissipation energy thickness in the Initial Region

= $\displaystyle\int_0^{\delta_1} \frac{u}{U_c}\left\{1 - \left(\frac{u}{U_c}\right)^2\right\} dy$

δ_5^{**} = Wall layer dissipation energy thickness in the Main Region between

stations 2 and 5 in Figure VIII-2 = $\displaystyle\int_0^{\delta_5} \frac{u}{U_m}\left\{1 - \left(\frac{u}{U_m}\right)^2\right\} dy$

δ_7^{**} = Wall layer dissipation energy thickness in the Main Region downstream

of station 5 in Figure VIII-2 = $\displaystyle\int_0^{\delta_7} \frac{u}{U_m}\left\{1 - \left(\frac{u}{U_m}\right)^2\right\} dy$

Δ_1 = Wall layer thermal energy thickness in the Initial Region

Δ_5 = Wall layer thermal energy thickness in the Main Region

Δ_6 = Distance y above the wall in the outer layer in the Main Region
where $T = T_e$

η_1 = $\dfrac{\delta_3 - y}{\delta_3 - \delta_2}$

η_2 = $\dfrac{y - \delta_3}{y_{1c} - \delta_3}$

η_3 = $\dfrac{\delta_3 - y}{\delta_3 - \delta_5}$, $\eta_4 = \dfrac{y - \delta_3}{y_{2c} - \delta_3}$

η_5 = $\dfrac{\delta_6 - y}{\delta_6 - \delta_5}$

θ_1 = Wall layer momentum thickness in the Initial Region = $\displaystyle\int_0^{\delta_1} \frac{u}{U_c}\left(1 - \frac{u}{U_c}\right) dy$

θ_5 = Wall layer momentum thickness in the Main Region between stations

2 and 5 in Figure VIII-2 = $\displaystyle\int_0^{\delta_5} \frac{u}{U_m}\left(1 - \frac{u}{U_m}\right) dy$

θ_7 = Momentum thickness in the Main Region downstream of station 5 in

Figure VIII-2 = $\displaystyle\int_0^{\delta_7} \frac{u}{U_e}\left(1 - \frac{u}{U_e}\right) dy$

$$\theta(\eta_s) = \frac{T_m - T}{T_m - T_\infty} = \text{Similarity function for temperature profile in outer layer in Main Region}$$

ρ_e = Density at the edge of viscous layer

ρ_o = Density based on some characteristic temperature in Initial Region

ρ_∞ = Free stream density

τ = Shear stress at any distance y above wall

τ_w = Wall shear stress

Subscripts:

∞ = Free stream values

( )   = Functional dependence of the quantity in the bracket

VIII - REFERENCES

VIII-1   Seebohm, T., Boundary Layer, Transition, and Wake Measurements at
         Low Mach Number for an Aerofoil with Single-Slotted Flap, Report
         69-1, Mechanical Engineering Research Laboratories, McGill Univ.

VIII-2   Bradshaw, P., and Gee, M. T., Turbulent Wall Jets With and Without
         an External Stream, A.R.C. 22, 008, June 1960

VIII-3   Goradia, S. H., Turbulent Wall-Jet Flow Development in the Presence
         of an External Stream with Arbitrary Pressure Gradients and Possible
         Temperature Gradients. A proposed Doctoral Research program to the
         Graduate Committee, School of Mechanical Engineering, Georgia In-
         stitute of Technology

VIII-4   Goradia, S. H., Turbulent Wall-Jet Flow Development in the Presence
         of an External Stream with Arbitrary Pressure Gradients and Possible
         Temperature Gradients. Ph.D. Thesis, (to be published), Georgia
         Institute of Technology

BIBLIOGRAPHY

Harris, G. L., The Turbulent Wall Jet in a Moving Stream, Proceedings of
Specialists Meeting sponsored by AGARD Fluid Dynamic Panel, May 1965

Goradia, S. H., Collwell, G. T., A Parametric Study of the Turbulent Wall Jet
Flow in the Presence of Pressure Gradients, (to be published)

Graham, B. J., A Review of Theoretical Methods Related to Boundary Layer
Control by Blowing, Boeing Scientific Research Lab Tech. Memorandum No. 40,
April 1965

Myers, G. E., Schauer, J. J., and Eustis, R. H., Plane Turbulent Wall Jet
Flow Development and Friction Factor, Journal of Basic Engineering, March 1962

Myers, G. E., Schauer, J. J., and Eustis, R. H., Heat Transfer to Plane
Turbulent Wall Jets, Journal of Heat Transfer, August 1963

Kruka, V. and Eskinasi, S., The Wall Jets in a Moving Stream, Journal of Fluid
Mechanics, Volume 20, Part 4, 1964

Hartnett, J. P., Birkebak, R. C., and Eckert, E. R. G., Velocity Distributions,
Temperature Distributions, Effectiveness and Heat Transfer for Air Injected
Through a Tangential Slot Into a Turbulent Boundary Layer, Journal of Heat
Transfer, August 1961

Seban, R. A., Heat Transfer and Effectiveness for a Turbulent Boundary Layer with Tangential Fluid Injection, Journal of Heat Transfer, November 1960

Seban, R. A., and Back, L. H., Effectiveness and Heat Transfer for a Turbulent Boundary Layer with Tangential Injection and Variable Free Stream Velocity, Journal of Heat Transfer, August 1962

Kacker, S. C., and Whitelaw, J. H., Some Properties of the Two-Dimensional Turbulent Wall Jet in a Moving Stream, Journal of Applied Mechanics, Paper No. 68 - WA/APM 13

Sigulla, A., Measurements of Skin Friction in a Plane Turbulent Wall Jet, Journal of Royal Aeronautical Society, December 1958

MacMillan, F. A., Experiments on Pilot-Tubes in Shear Flow, A.R.C. Technical Report, R & M No. 3028, 1957

Glauert, M. B., The Wall Jet, Journal of Fluid Mechanics, Vol. 1, 1956

Escudier, M. P., and Nicoll, W. B., The Entrainment Function in Turbulent Boundary-Layer and Wall Jet Calculations, Journal of Fluid Mechanics, Vol. 25, Part 2, pp. 337-336

Parajpe, S. C., and Sridhar, K., Effects of Initial Gap on the Turbulent Jet Flow over Curved Wall, The Aeronautical Journal of the Royal Aeronautical Society, Vol. 72, January 1968

Clauser, F. H., The Turbulent Boundary Layer, Advances in Applied Mechanics, Vol. IV, Academic Press, New York, 1954

Townsend, A. A., The Structure of the Turbulent Shear Flow, Cambridge University Press, 1956

Mallonee, R. C., and Jacoby, S. L. S., Plane Turbulent Compressible Wall Jet With and Without Parallel Free Stream, ASME Paper No. 68-FE-40

Schwart, W. R. and Cosart, W. P., The Two-Dimensional Turbulent Wall Jet, Journal of Fluid Mechanics, Vol. 10, Part 4, June 1961

Schlicting, H., Boundary Layer Theory, Fourth Edition, McGraw Hill Book Company, Inc.

Nash, J. F., A Practical Calculation Method for Compressible Turbulent Boundary Layers in Two-Dimensional and Axisymmetric Flows, Lockheed-Georgia Research Memorandum ER-9428, August 1967

Seban, R. A., and Back, L. H., Velocity and Temperature Profiles in Turbulent Boundary Layers with Tangential Injection, Journal of Heat Transfer, February 1962

Zerbe, J., and Selna, J., An Empircal Equation for the Coefficient of Heat Transfer to a Fleet Surface from a Plane Heated-Air Jet Directed Tangentially to the Surface, NACA Technical Note No. 1070, June 1946

Abramovich, G. N., The Theory of Turbulent Jets, The M.I.T. Press, Cambridge, 1963

FIGURE VIII-1.- BOUNDARY LAYER DEVELOPMENT ON MULTIPLE AIRFOIL
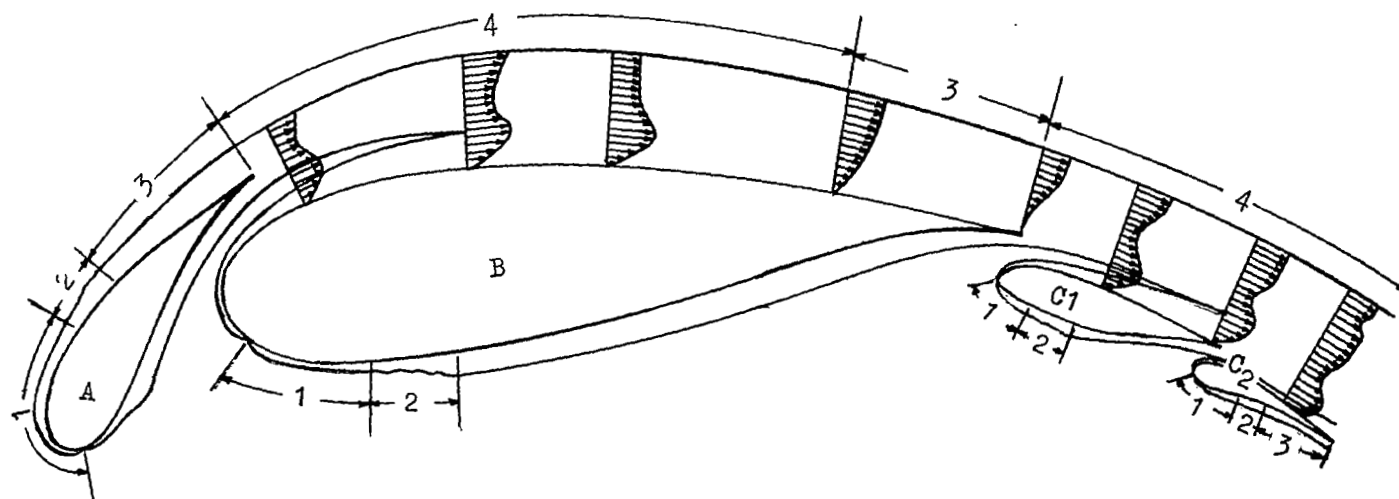
A   LEADING EDGE SLAT

B   MAIN COMPONENT

C1 }
C2 } DOUBLE SLOTTED FLAP

1 = LAMINAR B.L.

2 = TRANSITION REGION

3 = ORDINARY TURBULENT B.L.

4 = CONFLUENT BOUNDARY LAYER

FIGURE VIII-2
MATHEMATICAL MODEL FOR CONFLUENT BOUNDARY LAYER
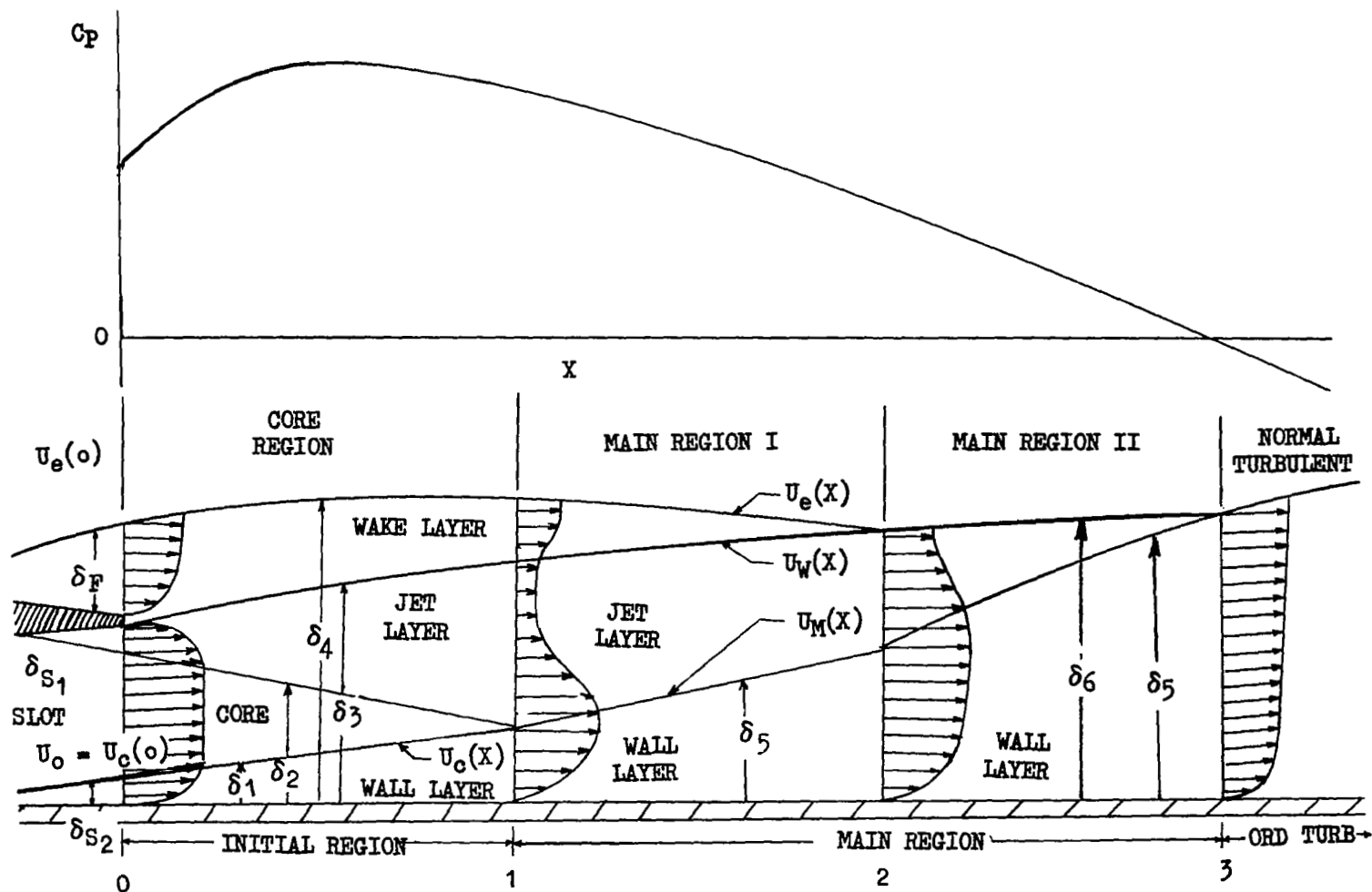
FIGURE VIII-3(a)
COMPARISON OF EXPERIMENTAL AND CALCULATED
CONFLUENT BOUNDARY LAYER PARAMETERS
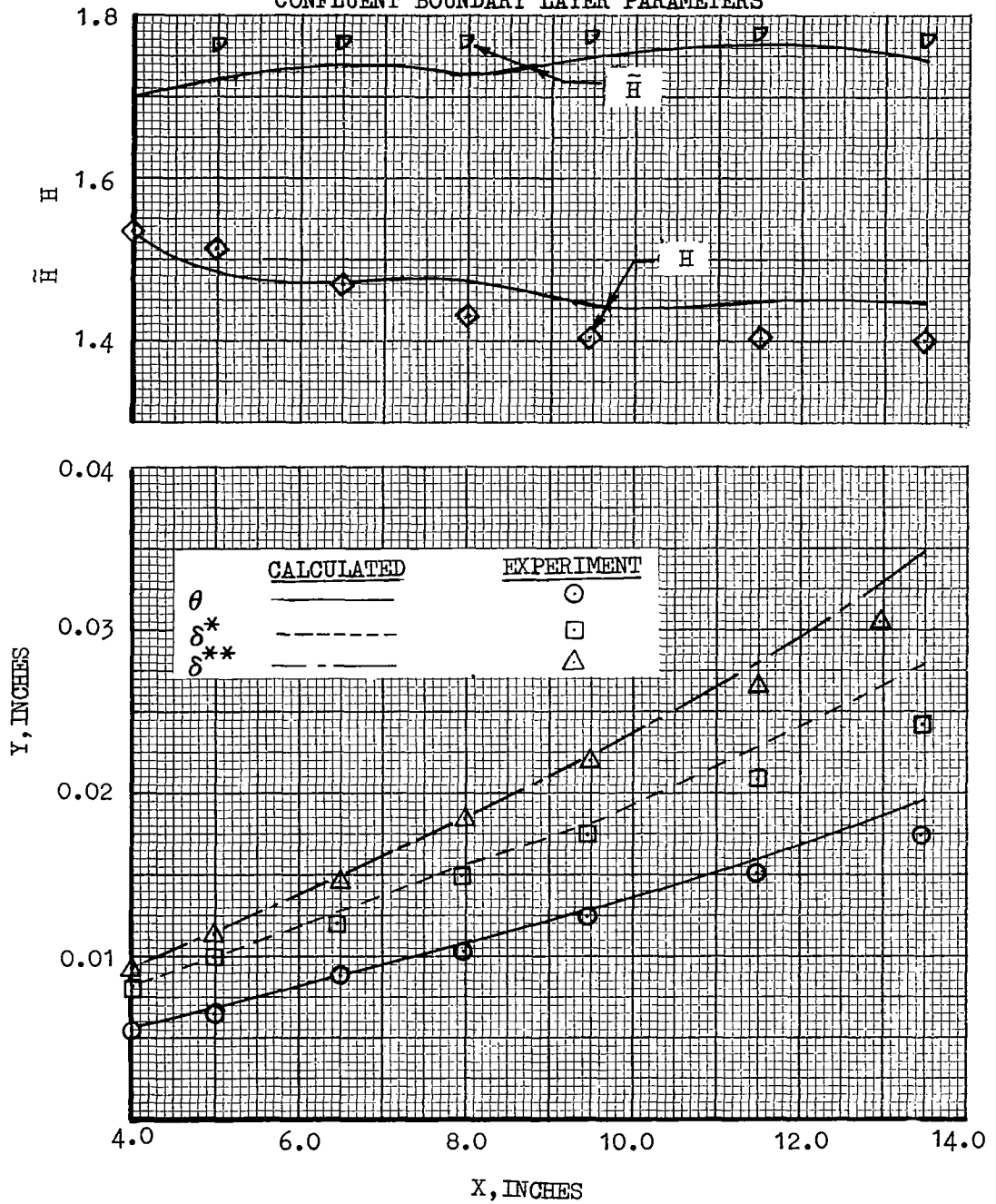
FIGURE VIII-3(b)
COMPARISON OF EXPERIMENTAL AND CALCULATED
CONFLUENT BOUNDARY LAYER PARAMETERS
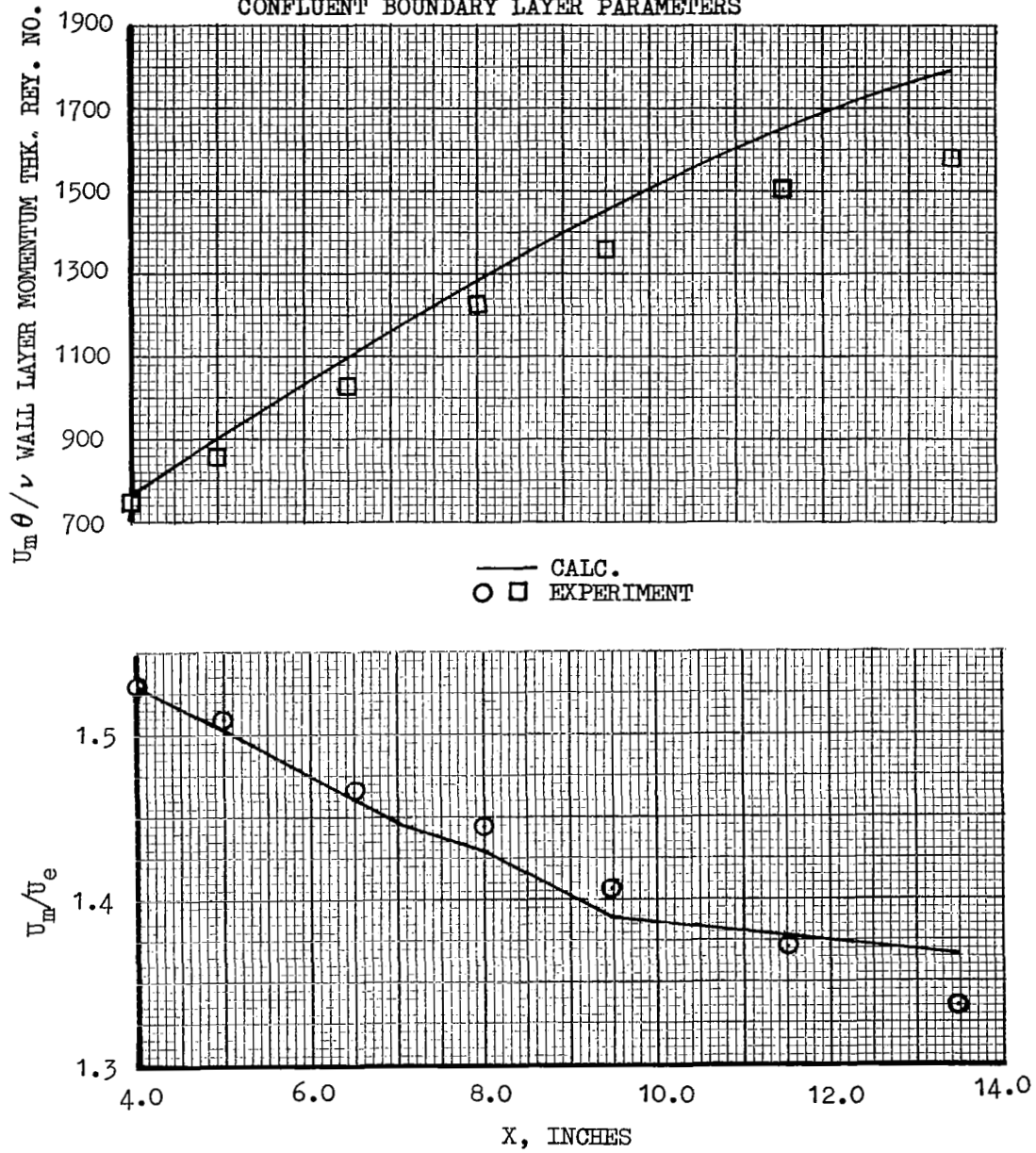
FIGURE VIII-3(c)
COMPARISON OF EXPERIMENTAL AND CALCULATED
CONFLUENT BOUNDARY LAYER PARAMETERS

δ_1 = COMPUTED WALL LAYER THICKNESS

δ_2 = COMPUTED EDGE OF JET LAYER

⊙ ———— EXPERIMENTAL WALL LAYER THICKNESS

◻ ———— EXPERIMENTAL JET LAYER EDGE, $U/U_e \cong 1.01$

△ ———— EXPERIMENTAL JET LAYER EDGE, $U/U_e \cong 1.00$
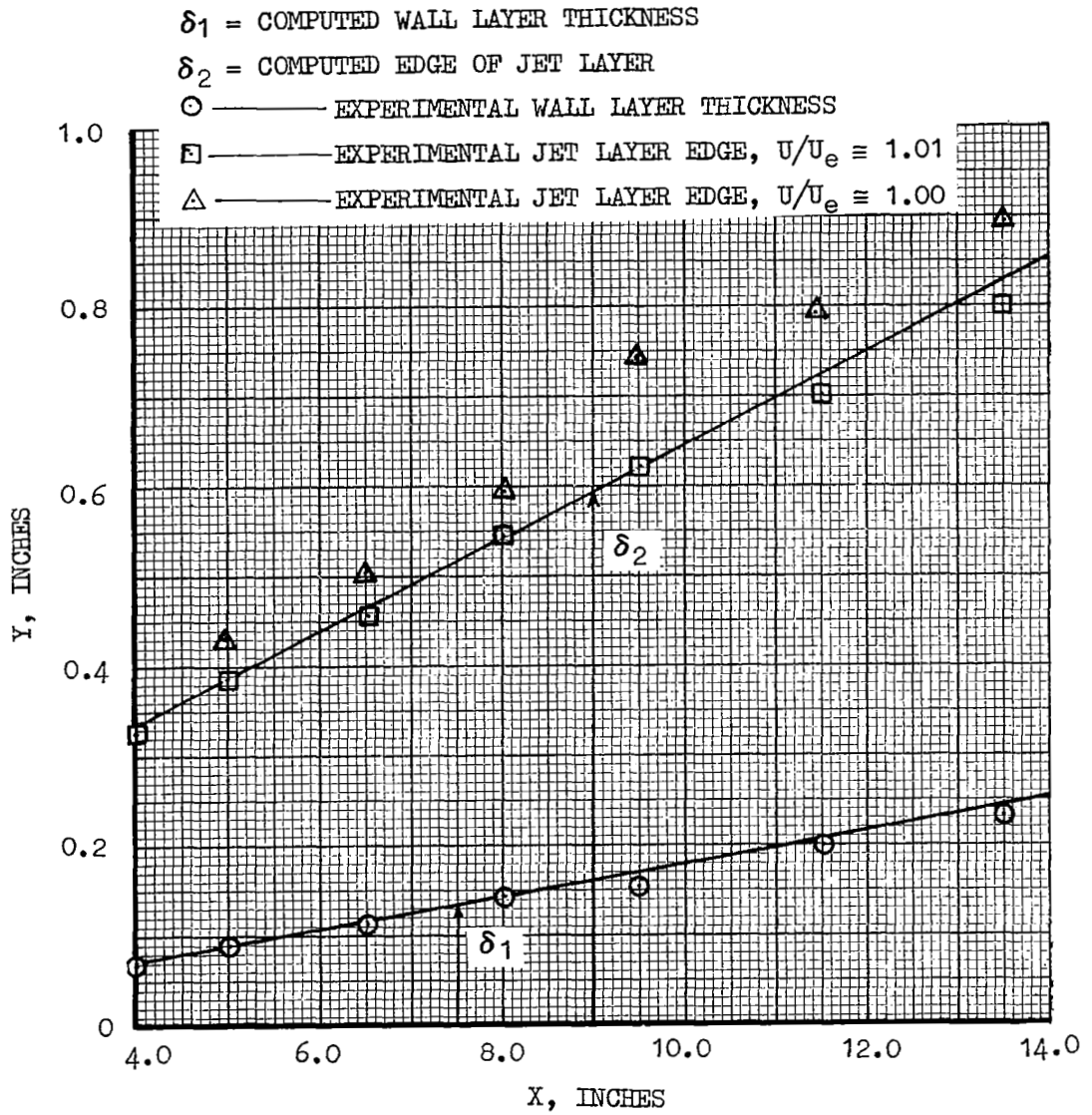
FIGURE VIII-4(a)

CORE REGION
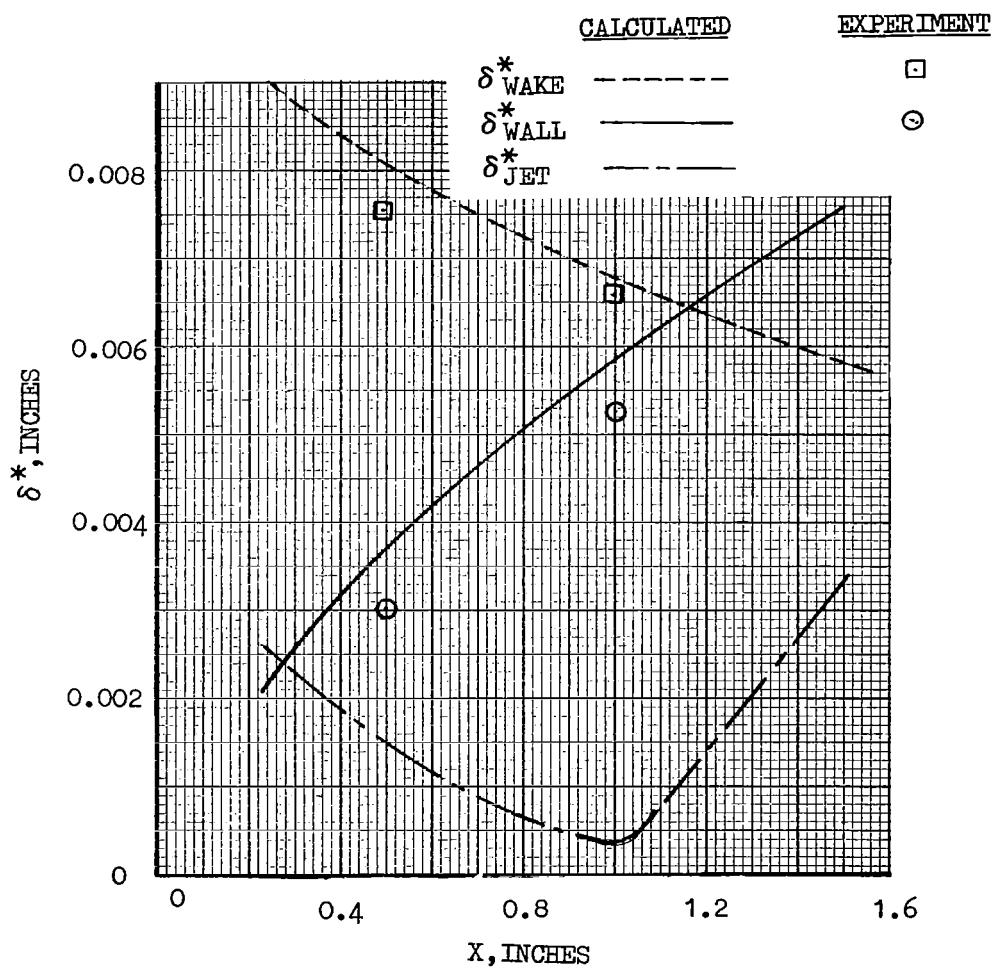
FIGURE VIII-4(b)
COMPARISON OF EXPERIMENTAL AND CALCULATED
CONFLUENT BOUNDARY LAYER PARAMETERS

Calculated	Experiment	Parameter
————————	⊙	δ_1
- - - - - -	▫	δ_2
—— · ——	△	δ_3
—— · · ——	◇	Y_{1c}
	◖	Y for $u/U_e = 0.99$
—— · · —	◖	Y for $u/U_e = 1.00$

142
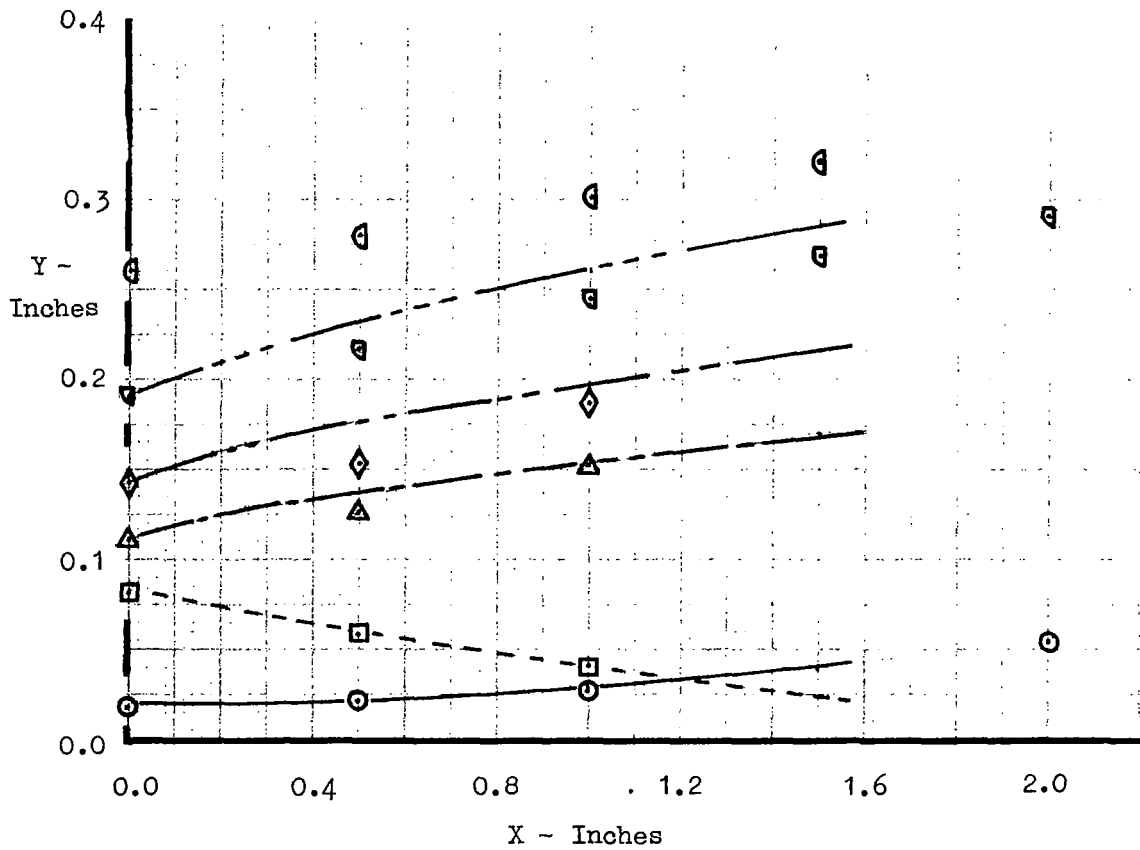
FIGURE VIII-4(c)
CORE REGION

VELOCITY IN CORE, FT/SEC.

—— CALC.
O EXPERIMENT

NON-DIMENSIONAL WAKE VELOCITY

WALL LAYER MOMENTUM THICKNESS

X, INCHES
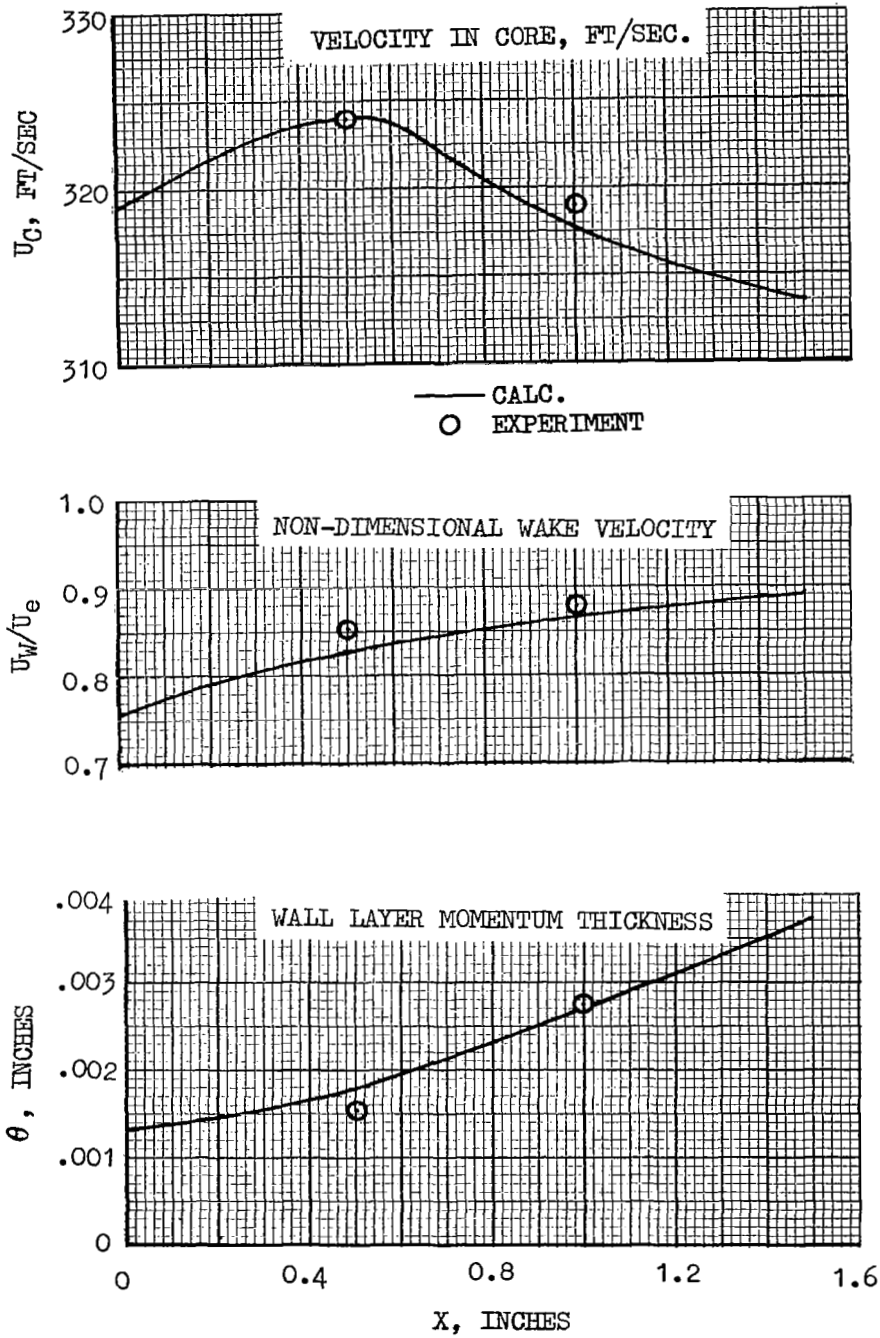
IX - EQUIVALENT AIRFOIL (MULTI-COMPONENT)

The present section discusses the manner in which the combined or viscous solution is obtained for the multi-element case and, provides comparisons between experimental and calculated data. The specific experimental cases used in the correlation have been selected, with approval of the NASA, on the basis of availability of both force and pressure measurements. In some instances, the best available high-lift data are from systematic NACA tests conducted about thirty years ago. The present study has found that considerable disparity can exist between the airfoil performance as originally documented and that shown for comparative purposes in later documents. Therefore, in some cases, several sets of data may be cited as representative of experimental results. Additionally, in those cases where difficulty was experienced in defining precise deflections or positions of the components from the available documentation, such instances will be noted in the discussions.

Airfoil Representation. - The treatment of the multiple component "equivalent" airfoil is very similar to the single component case discussed in Section VI. The camber and angle-of-attack shift, due to the boundary layer, is applied to each component of the multiple airfoil in the same manner as it is applied to the single airfoil case. The thickness relief effect is neglected since it is found to be small and the validity of this same procedure in the multiple-component case is open to question.

For the multi-element airfoil the velocity distribution near the trailing-edge of each component is artificially modified in the same manner as the single-element case. This modification is used to reduce the tendency for fluctuations in the intermediate solutions during the iterative process and thus improves the rapidity of the convergence. The extrapolation process employed on the single-element airfoils (see Section VI) for the displacement thickness ($\delta *$) parameter is not used in the case of the multi-component airfoils. The more powerful effect of the thick confluent boundary layer has a stabilizing influence on the intermediate calculations such that the extrapolation of $\delta *$ at the trailing-edges of each component has little effect. The smoothing function on $\delta *$ is used, however, for each component in the same manner as noted in Section VI for the single-element airfoils.

The convergence criteria used in the multiple airfoil case requires that the integrated normal force on each component does not change during successive iterations more than a predetermined amount. Again, this is the same procedure used in the single-element case.

Correlation. - The correlation analyses will be discussed in an order consistent with the number of components involved beginning with the two-element cases. The objective in these discussion will be to

- define the general degree of correlation provided by the viscous computer program for representing pressure and force measurements.

144

- note where known analytical model limitations are encountered and, where possible, define the influence of such limitations.

- define the range of operational or configurational variables (i.e. angle-of-attack, component deflections) over which program results are most valid to the aerodynamic definition of the multi-element cases.

- define those areas where program extensions would be of the greatest value for further improving the correlation.

The two-element cases selected for correlation with the multiple-airfoil program are

1. The modified NACA 4418 single-slotted configuration of Reference IX-1.

2. The NACA 23012 single-slotted configuration of Reference IX-2.

3. The NACA 23012 external airfoil flap configuration of Reference IX-3.

4. An NACA 64A010 slatted airfoil of Reference IX-5.

Figures IX-1 and IX-2 show a comparison between the calculated and experimental pressure distributions on the modified NACA 4418 single-slotted airfoil at several flap deflections. The experimental data is relatively unique in that measurements were made of the confluent boundary-layer velocity profiles along with associated pressure distributions. The geometric arrangement of the flap relative to the main element was not precisely defined, however. In both of the cases shown, the pressure distributions are in reasonable agreement with the test results. The computed lift coefficients, however, are less than those obtained by either force measurements or integration of test pressures, particularly at a flap deflection of 10 degrees. While it is believed that the required accuracy for defining flap deflection and a precise gap size may partially account for these differences, later correlations will show that at low flap deflections, the calculated data generally underpredict the lift coefficient.

Figure IX-3 compares some of the calculated confluent boundary layer parameters with measured values for the airfoil considered in Figure IX-2 (NACA 4418, MOD.) The experimental results were obtained by boundary layer traverses on the flap upper surface at 80 percent and 100 percent chord stations. The latter position, in actuality, corresponds to a position about $\frac{1}{4}$-inch downstream of the trailing-edge due to the deflection of the probes. It is also noted in Reference IX-1 that appreciable streamwise variations in the velocity profiles were observed near the trailing-edge with more gradual variations noted around the 80 percent point. The calculated quantities shown in Figure IX-3 correspond to four iterations of the main program in approaching a viscous solution for the airfoil. Thus, the initial conditions for the confluent boundary layer calculations represent the boundary layer conditions at the slot exit as combined with the upper surface flow on the forward element. Although the amount of experimental data is small, the comparison shown in the figure indicates that both

trends and magnitudes of the confluent boundary layer parameters are well represented.

Comparative data plots are provided for the NACA 23012 single-slotted flap in Figures IX-4 through IX-6. Pressure distributions are shown in Figures IX-4 and IX-5 for two flap deflections. Both the pressure data and the corresponding lift coefficients are in reasonable agreement with test results. Normal force coefficients, as a function of angle-of-attack, are given in Figure IX-6 for the same two flap deflections. The 20-degree deflection data is in excellent agreement with experimental results even near the stall angle-of-attack about 13 degrees. The fact that the normal force at 30 degrees flap deflection is higher than the experimental results is not unexpected. At this deflection, it could be anticipated that separation on the flap upper surface should be present in the experimental results. The confluent boundary layer model, in its present form, does not include separation criteria. This implies that for separation to be predicted on the flap upper surface, the boundary layer must return downstream to the ordinary turbulent-type for which separation criteria are available in the program. In the present case, the confluent boundary layer persists to the flap trailing-edge and therefore, the calculations would not reflect the onset of separation in this area nor the uncambering effect of the flow on the flap.

One of the notable features of the pressure comparisons of Figures IX-4 and IX-5 are the calculated pressure spikes near the trailing-edge of the main element. With the spacing of the experimental pressure taps in this area, the test data neither confirms nor denies the existence of such spikes. Since similar pressure variations are found in the correlation performed on other multi-element cases, this is an area where more definitive test data would be beneficial inasmuch as the pressure gradients associated with these spikes significantly influence the trailing-edge boundary layer properties.

At the lowest angle-of-attack for which calculations were made for the 20-degree flap deflection, one of the program limitations was encountered. The slot exit velocity ratio, X_{MG}, reached the limiting level of 0.90. This parameter represents the ratio of the velocity at the edge of the boundary layer (U_e) to the average efflux velocity from the slot and is limited to values between 0.90 and 1.0. As the angle-of-attack increases, the value of this parameter goes within these limits.

Additional correlations between calculated and experimental results are shown for the NACA 23012 external flap configuration in Figures IX- 7 (pressure data) and IX- 8 (force data). While the data shown in the latter figure are from Reference IX-3, additional data on these test results are provided in Reference IX-4. The later documentation shows a significant reduction in the performance of the airfoil (particularly at a flap deflection of 20 degrees) when compared to the data of Figure IX- 8. As seen in Figure IX- 8, however, the calculated results agree reasonably well with the data of Reference IX-3.

It should also be noted that in the calculations for the two lower angles-of-attack at 20 degrees deflection, the thickness of the boundary layer at the slot exit exceeded the slot-exit height (1.3 percent chord). The boundary-layer readjustment process, described in Section VII, does not appear to have significantly altered the trends of the data indicating that the effect of this limitation is not large.

To evaluate the degree of correlation available with a leading-edge slat, Figures IX-9 and IX-10 provide pressure distributions and force-data, respectively, for a slotted NACA 64A010 airfoil. While force data on this configuration is available at $M_\infty = 0.25$, the experimental pressure distribution data are for $M_\infty = 0.50$. For correlation purposes in Figure IX-9, the $M_\infty = 0.50$ pressure data have been corrected to an equivalent $M_\infty = 0.25$ freestream condition by the Prandtl-Glauert equation.

Additionally, the slat undersurface, as tested, is sharply convexed at the slot entry. Prior to performing the calculations, this area of the slat was locally faired to provide some insight into the sensitivity of this area to local recontouring. However, at all angles-of-attack, flow separation was predicted on the slat lower surface in the strong adverse gradient shown at $X/C \approx 0.05$. This agrees with the experimental pressure data shown. For the angle-of-attack indicated in Figure IX-9, some flow reattachment apparently occurs in the slot inasmuch as the main element pressure data are in good agreement with the attached flow calculations. Although pressure data are not shown, the calculations made at higher angles-of-attack showed an increasing disparity between the calculated and experimental pressures on the main element indicating an incomplete flow reattachment in the slot area. Additionally, calculations at the higher angles-of-attack indicated flow separation on the slat upper surface as well as the lower. These effects are reflected in the increasing differences in the force data comparison of Figure IX-10.

The data discussed in the previous paragraphs for the 64A010 airfoil with leading-edge slat are believed to be typical of the degree of correlation to be expected for such configurations. There appears to be only a small angle range in which either upper-surface or lower-surface separation is not evident someplace on the airfoil. This also emphasizes the strong need for incorporating turbulent reattachment criteria in the program to broaden the range of applicable configurations. Additionally, such data evidences the need for a separated flow model to permit a refined representation of such configurations, even under separated flow conditions. While $C_{l_{max}}$ predictions would be a natural fall-out with such a flow model, and this of course is a greatly needed capability, the added flexibility and efficiency that such a model would add to the utilization of the present program would be highly desirable.

Figure IX-11 shows typical variations of the lift coefficient during the iteration process for several two-element cases. As seen, the convergence to the viscous solution normally occurs within 4-5 iterations. The viscous corrections for these airfoils are from 20 to 25 percent of the potential lift level. While these data may be considered as typical examples, some airfoils used in the correlation analysis showed higher viscous corrections.

To evaluate the computer program for a three-element case, the NACA 23012 of Reference IX-12 with a leading-edge slot and single-slotted flap was selected for the correlation. Figure IX-12 shows a comparison of the pressure distributions for a flap angle of 20° and angle-of-attack of 8 degrees. As seen, the calculated pressure distribution is generally lower than experiment on all components. The reason for this difference is believed to be two-fold: the test documentation indicates that tunnel corrections were made to the force measurements in such a direction as to reduce the overall pressure levels; the pressure data were left uncorrected. Additionally, in performing the calculations for this airfoil on the multiple-airfoil program, the boundary layer data for the last (4th) iteration indicates turbulent flow separation on the slat upper and lower surface as well as the lower surface of the main element just ahead of the aft slot. A subsequent net thickening of the boundary-layer on the flap upper surface causes the equivalent airfoil to uncamber and thereby reduce the normal force coefficient below that of the experimental value.

Results from a program check-out on a four-element case is presented in Figure IX-13. Experimental data on four-element cases for which completely attached flow would be inferred are lacking in the literature. To provide a measure of comparison with experiment, the NACA 64A010 airfoil with leading-edge slat and double-slotted flap was selected from Reference IX-7. In the tests of this configuration, a slat angle of -26 degrees and flap angle of 55 degrees were utilized. To suppress flow separation tendencies, the calculations assumed a leading-edge slat angle of -3.3 degrees and a flap angle of 20 degrees. In reducing the flap angle, the flap and vane were rotated together to the appropriate angle and then lowered to maintain an exit gap of approximately 1.5 percent chord on the forward slot. Contrary to these precautions, the calculations indicate turbulent flow separation on the lower surfaces of the slat and main-element throughout four iterations. While the convergence to the final iterated lift coefficient was smooth and rapid, the true effects of the separated flow on the converged solution is unknown.

Figure IX-14 provides a breakdown of the calculated normal forces on each element of the four-component airfoil as a function of angle-of-attack. The potential flow solution and the experimental data are shown for comparison. In contrast to the potential flow solution, the lift-curve slope for the viscous solution approaches that of the experimental data. Additionally, the variation of the elemental loadings are as expected with increasing angle-of-attack.

In both the three- and four-element cases, it was noted that the confluent boundary layer persisted downstream of the forward slot to the trailing-edge of the main element. In the assumptions for the confluent boundary-layer model, it is assumed that conditions at the trailing-edge of the main element (upper surface) represent an ordinary turbulent boundary-layer. Thus, in the two cases cited, further assumption of an equivalent boundary layer profile at the trailing-edge becomes necessary to establish initial conditions for the second confluent boundary layer calculations. Such an equivalent condition was formulated for these cases as well as other configurations utilizing closely spaced slots. In the present correlation analysis, the complete generalization of the equivalent profile concept has not been verified.

IX - REFERENCES

IX-1 Seebohm, T.; Boundary Layer, Transition, and Wake Measurements at Low
      Mach Number for an Aerofoil with Single-Slotted Flap, Report 69-1,
      Mechanical Engineering Research Laboratories, McGill University

IX-2 Wenzinger, C. J. and Delano, J. B.; Pressure Distribution Over an NACA
      23012 Airfoil with Slotted and Plain Flap, NACA TR 633

IX-3 Wenzinger, C. J.; Pressure Distribution Over an NACA 23012 Airfoil with
      an NACA 23012 External-Airfoil Flap, NACA TR 614, 1937

IX-4 Wenzinger, C. J. and Rogallo, F. M.; Resume of Air-Load Data on Slats
      and Flaps, NACA Tech. Note 690

IX-5 Axelson, J. A. and Stevens, G. L.; Investigation of a Slat in Several
      Different Positions on an NACA 64A010 Airfoil for a Wide Range of
      Subsonic Mach Numbers; NACA TN 3129, 1954

IX-6 Harris, T. A. and Lowry, J. G.; Pressure Distribution Over an NACA 23012
      Airfoil with a Fixed Slot and a Slotted Flap, NACA TR 732, 1942

IX-7 Kelly, J. A. and Hayter, N. F.; Lift and Pitching Moment at Low Speeds
      of the NACA 64A010 Airfoil section Equipped with Various Combinations
      of a Leading-Edge Slat, Leading-Edge Flap, Split Flap and Double-Slotted
      Flap, NACA TN 3007, 1953

FIGURE IX-1 — COMPARISON OF EXPERIMENTAL AND
PREDICTED PRESSURE DISTRIBUTIONS
FOR NACA 4418(MOD.) WITH 35% C. SLOTTED FLAP
$M_\infty = 0.19$ $\alpha = 0°$ $\delta_F = 10°$ RN $= 2.5 \times 10^6$

CALCULATED, $C_l = 0.85$
⊙ ⊙ EXPERIMENTAL, $C_l = 1.107$ FORCE
$C_l = 1.084$ PRESSURE

C_p

-3.0

-2.0

-1.0

0

+1.0

0   0.2   0.4   0.6   0.8

X/C
(WING)

0.6   0.8   1.0

X/C
(FLAP)
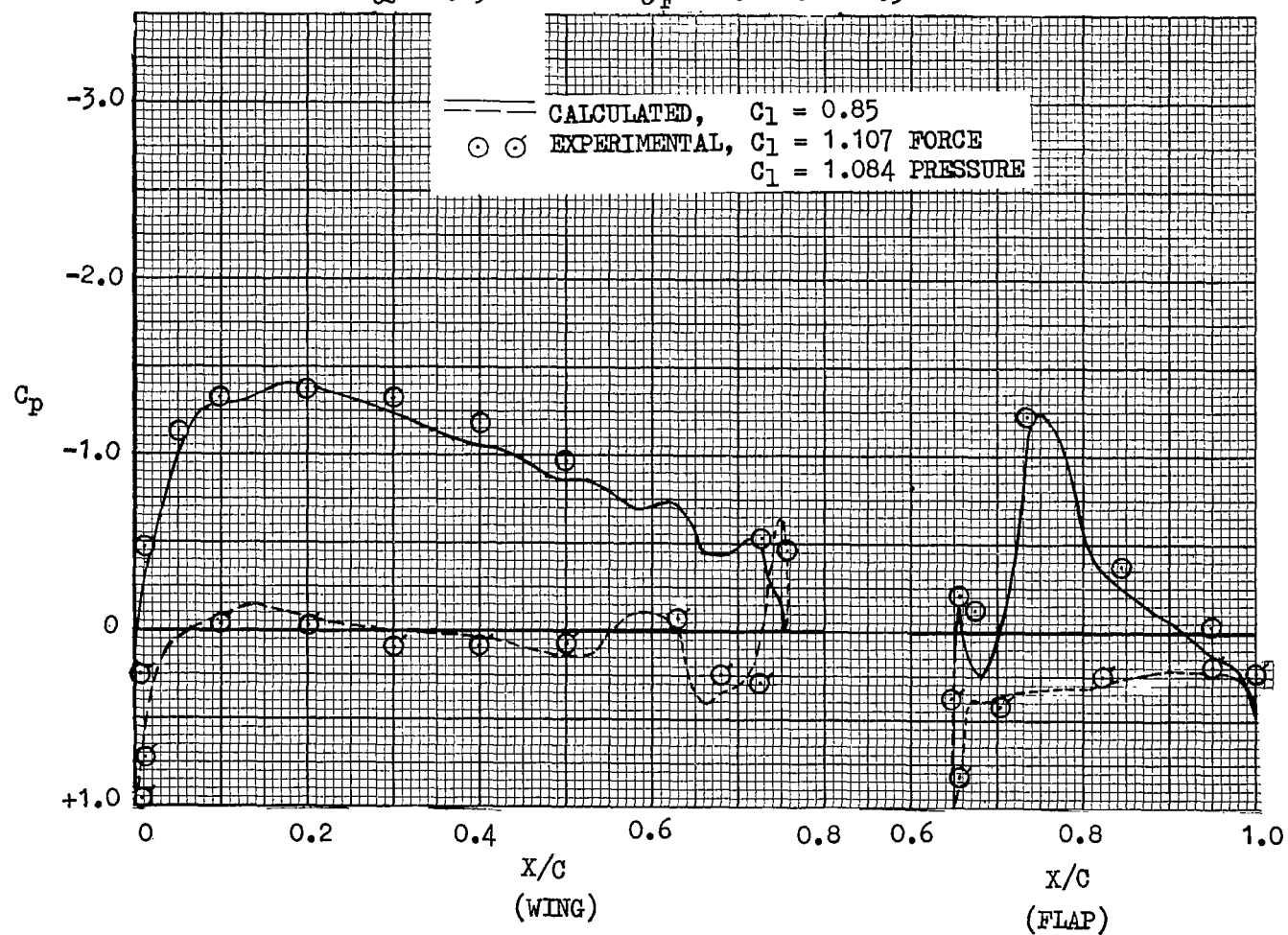
FIGURE IX-2 — COMPARISON OF EXPERIMENTAL AND
PREDICTED PRESSURE DISTRIBUTIONS
FOR NACA 4418(MOD.) WITH 35% C. SLOTTED FLAP
$M_\infty = 0.19$ $a \approx 0°$ $\delta_F = 20°$ RN $= 2.5 \times 10^6$
(REF. IX-1)

CALCULATED $C_l = 1.524$
EXPERIMENTAL $C_l = 1.760$ FORCE
$C_l = 1.656$ PRESSURE

C_p

X/C
(WING)

X/C
(FLAP)
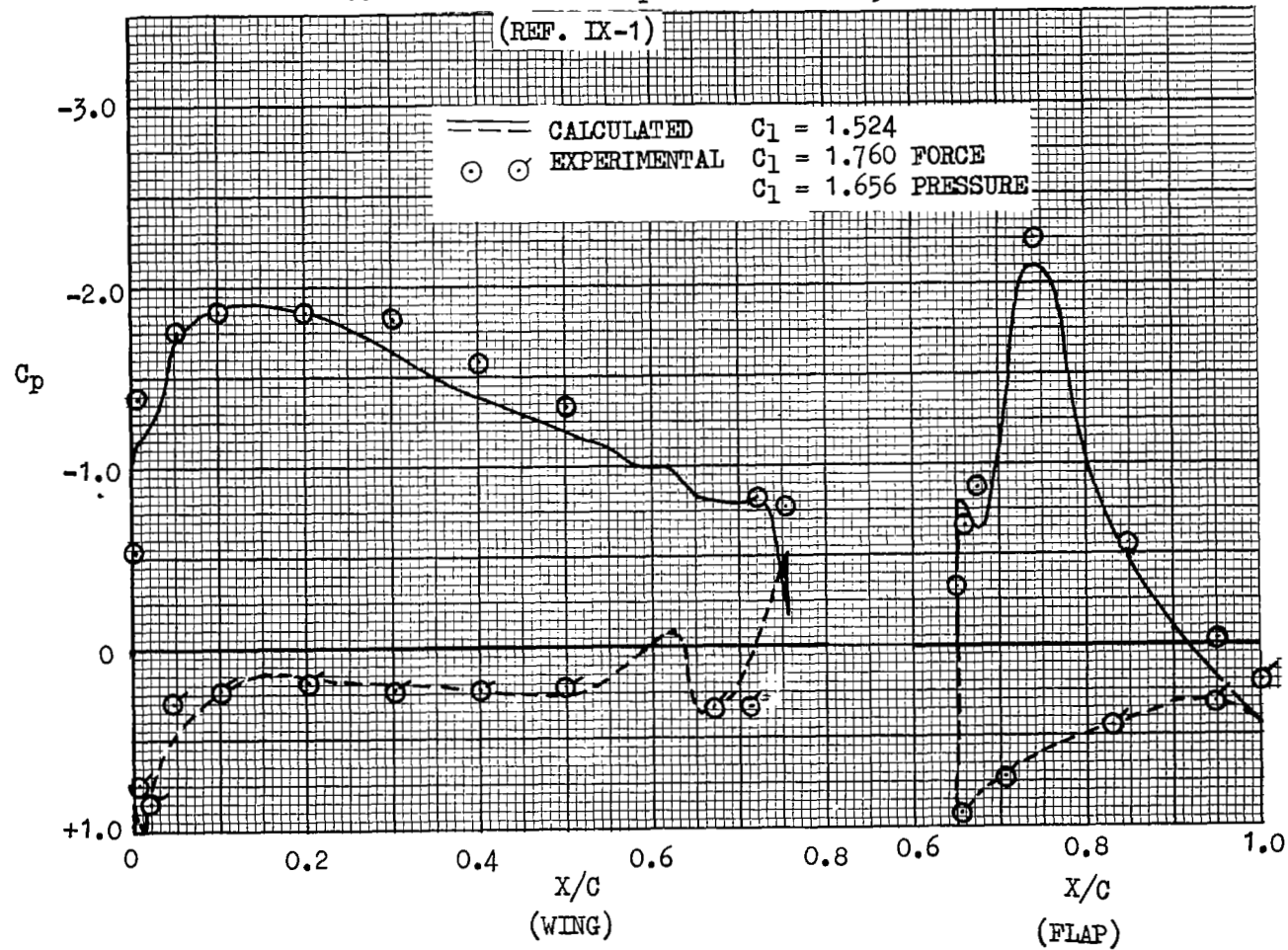
FIGURE IX-3
COMPARISON OF CONFLUENT BOUNDARY LAYER PARAMETERS
4418(MOD) SINGLE-SLOT AIRFOIL

$$\delta_F = 20° \qquad a = 0°$$

(REF. IX-1)
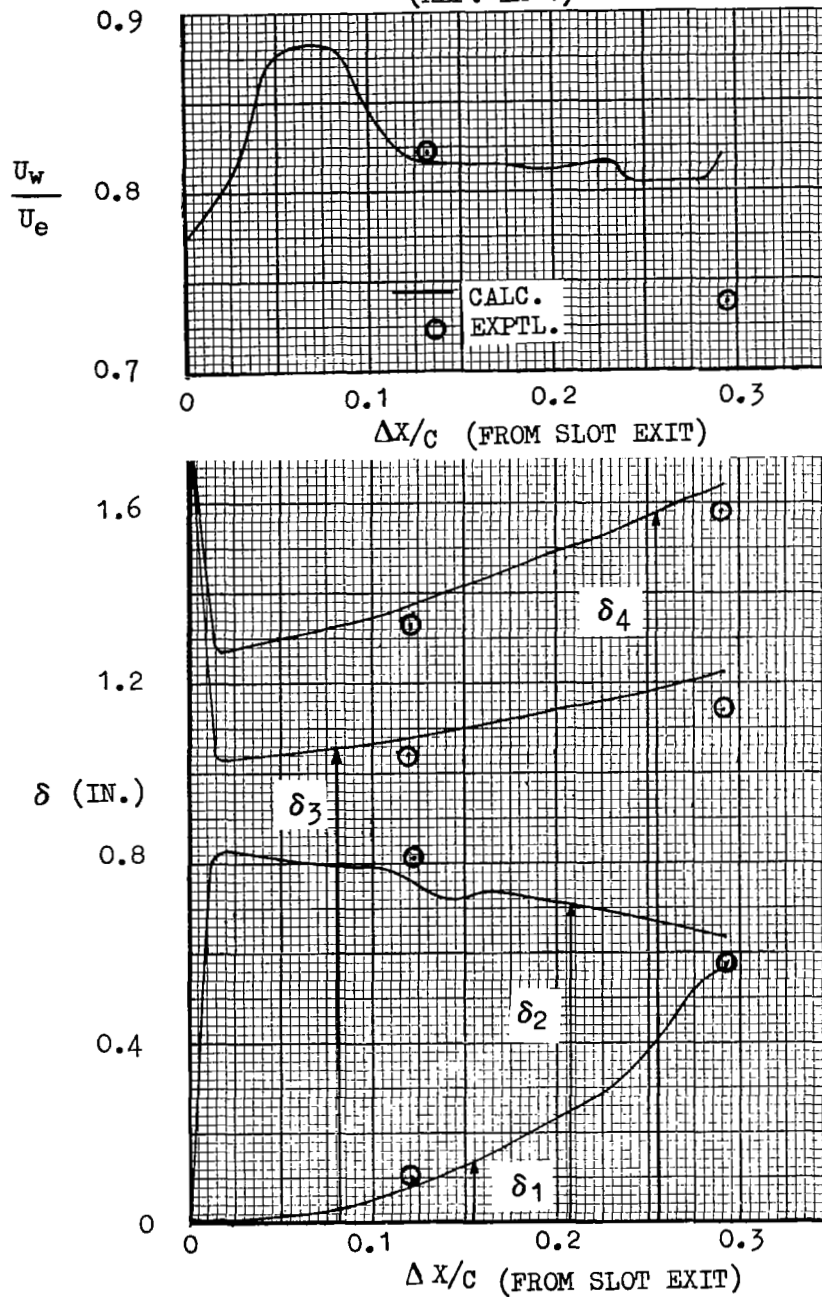
FIGURE IX-4 — COMPARISON OF EXPERIMENTAL AND
PREDICTED PRESSURE DISTRIBUTIONS
FOR NACA 23012 WITH 25% C. SLOTTED FLAP
$M_\infty = 0.105$ $R_N = 1.46 \times 10^6$
$a = 8.0°$ $\delta_F = 20°$
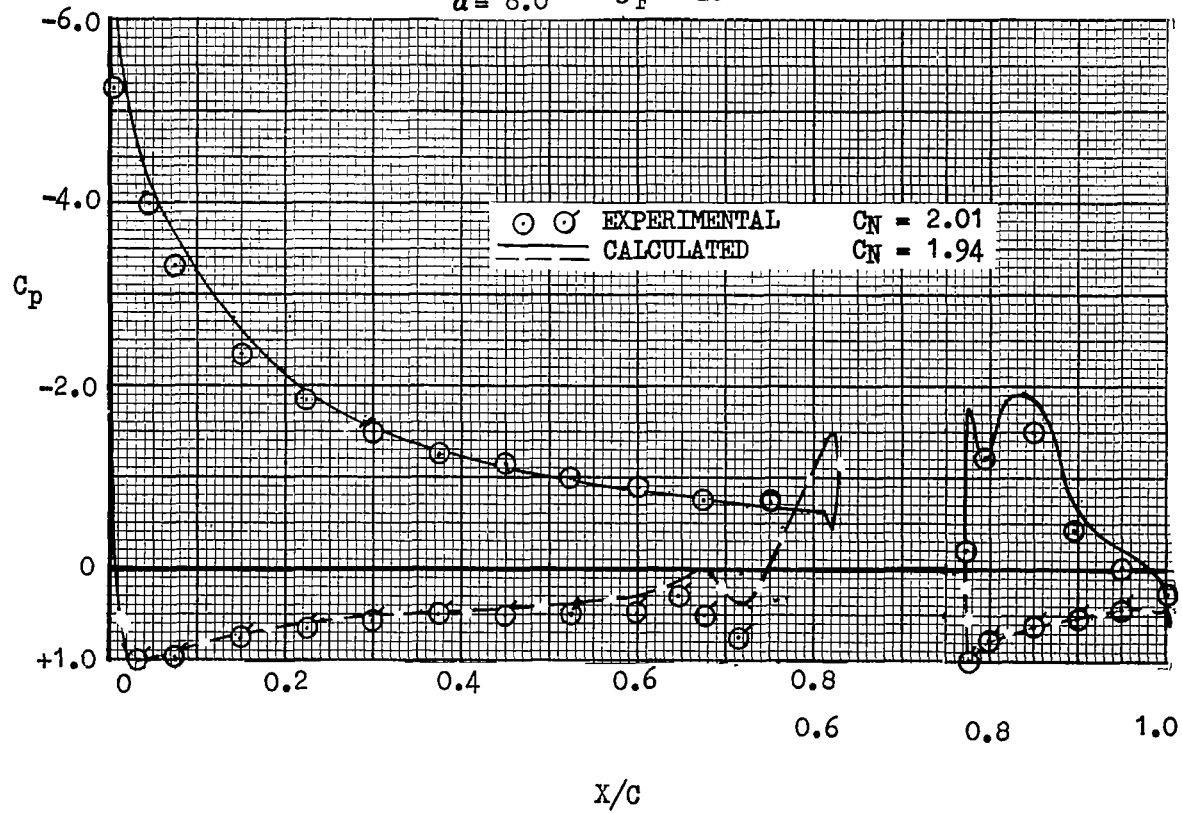
FIGURE IX-5 – COMPARISON OF EXPERIMENTAL
AND PREDICTED PRESSURE DISTRIBUTION
FOR NACA 23012 AIRFOIL
WITH 25% C. SLOTTED FLAP
$M_\infty = 0.105$ $RN = 2.19 \times 10^6$
$\alpha = 8°$ $\delta_F = 30°$

EXPERIMENTAL $C_N = 2.22$
CALCULATED $C_N = 2.62$
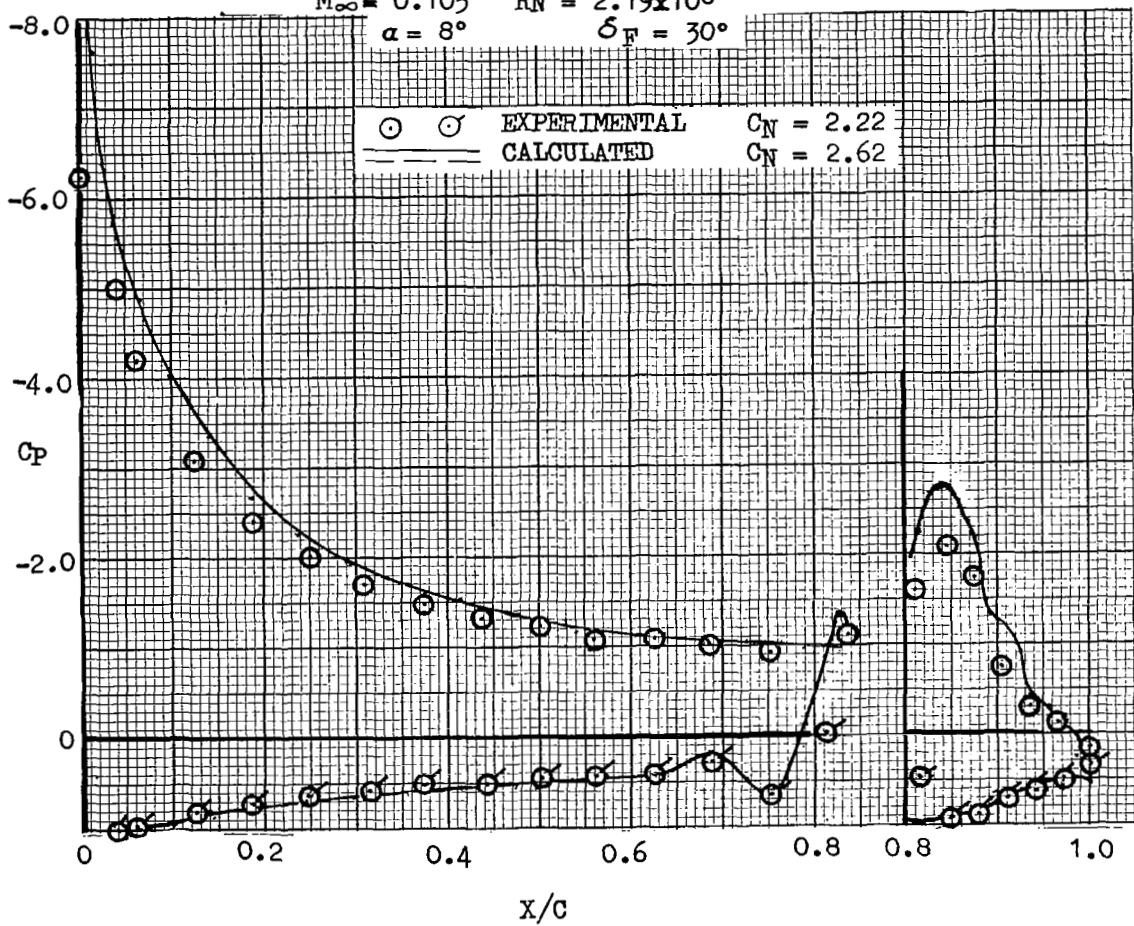
FIGURE IX-6.- COMPARISON OF EXPERIMENTAL
AND PREDICTED NORMAL FORCE AND
PITCHING MOMENT COEFFICIENTS FOR
NACA 23012 AIRFOIL WITH
25% CHORD SLOTTED FLAP

$M_\infty = 0.105$ $R_N = 2.19 \times 10^6$
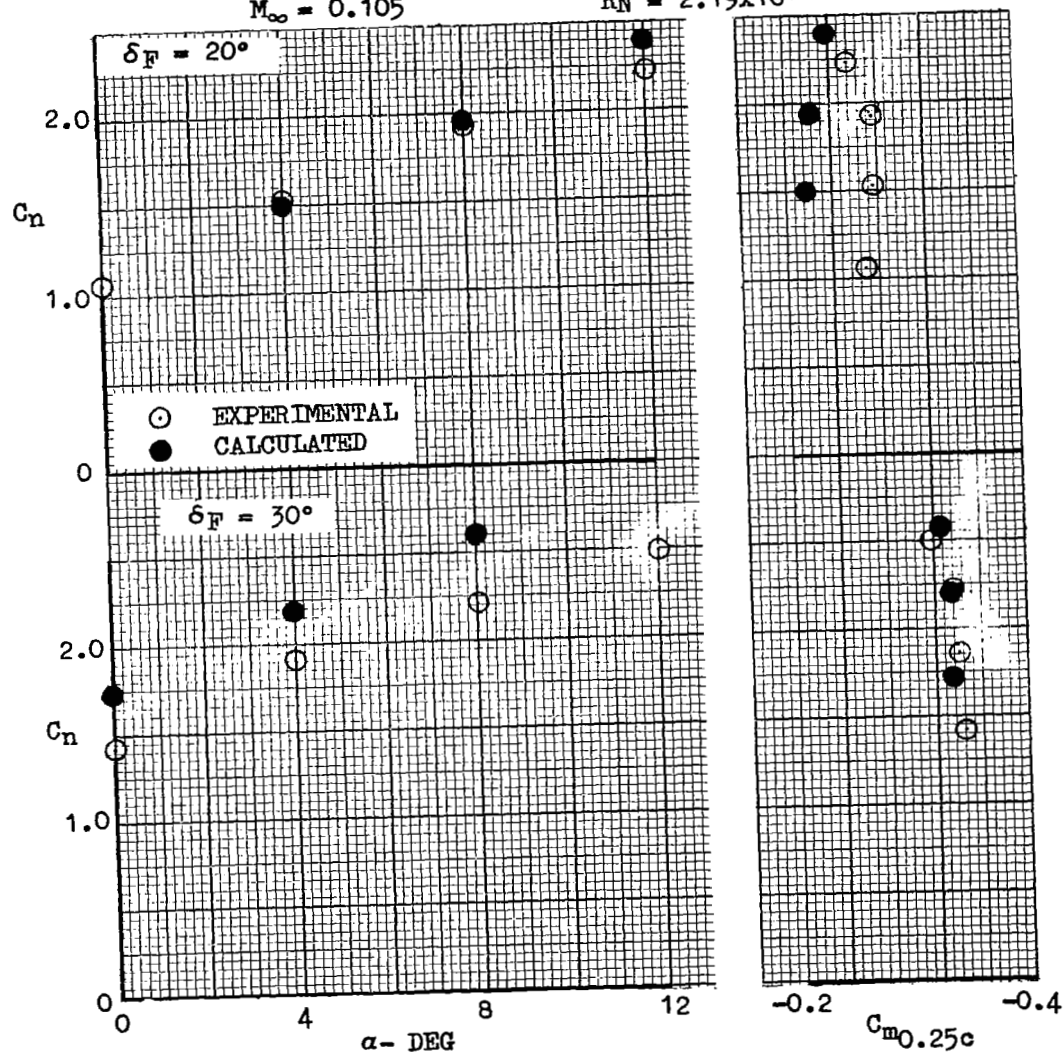
FIGURE IX-7 —COMPARISON OF EXPERIMENTAL AND
PREDICTED PRESSURE DISTRIBUTIONS
FOR NACA 23012 AIRFOIL WITH EXTERNAL-AIRFOIL FLAP
$M_\infty = 0.105$ $a = 5.85°$ $\delta_F = 20°$ $RN = 1.46 \times 10^6$
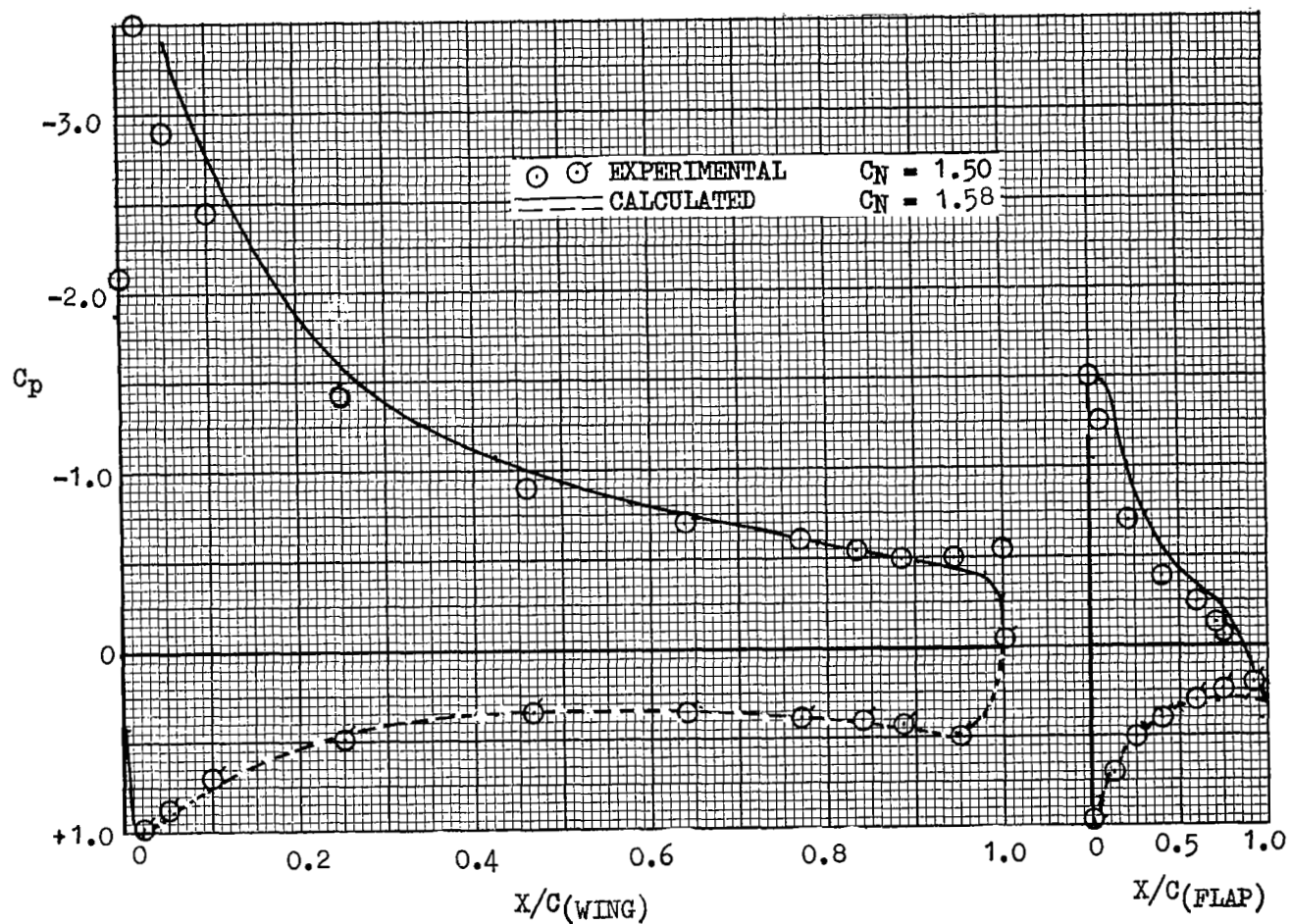
FIGURE IX-8 - COMPARISON OF EXPERIMENTAL
AND PREDICTED NORMAL FORCE AND
PITCHING MOMENT COEFFICIENTS FOR
NACA 23012 AIRFOIL
WITH EXTERNAL-AIRFOIL FLAP
$M_{\infty} = 0.105$ $R_N = 1.46 \times 10^6$
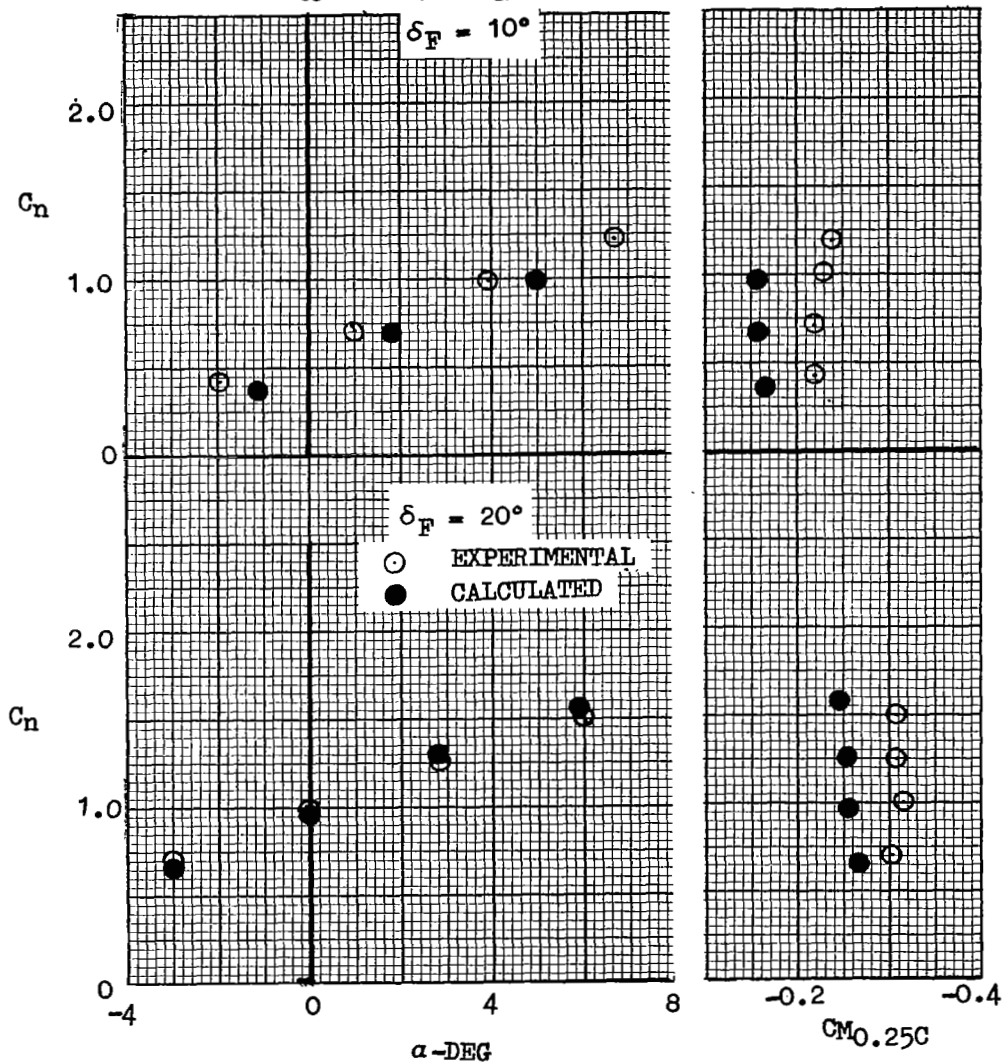
FIGURE IX-9—COMPARISON OF EXPERIMENTAL AND
PREDICTED PRESSURE DISTRIBUTIONS FOR
NACA 64A010 AIRFOIL WITH L.E. SLAT

$M_\infty = 0.25$ $\alpha = 6°$ $\delta_{SLAT} = -1.6°$ $RN = 6.25 \times 10^6$
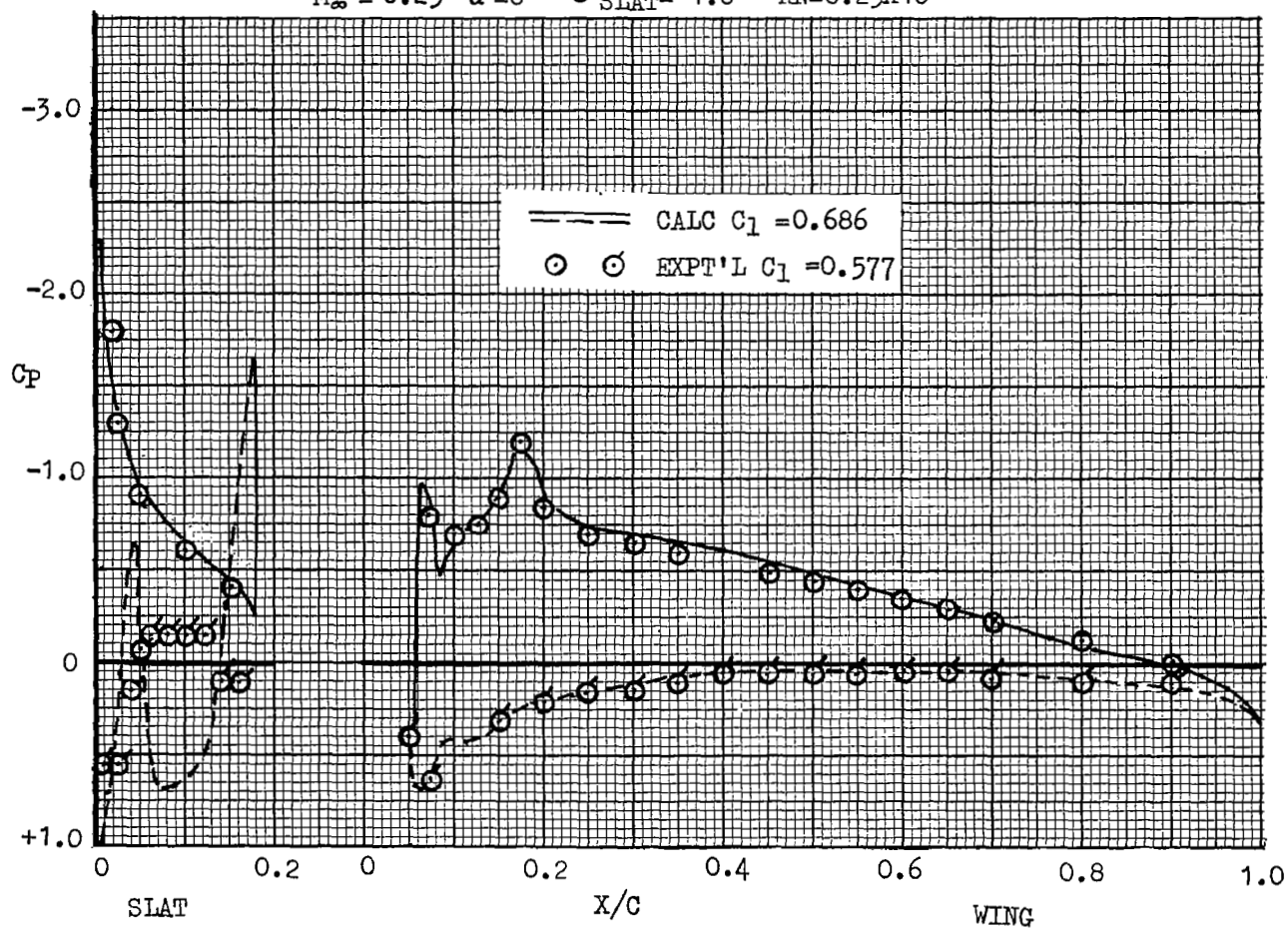
FIGURE IX-10—COMPARISON OF EXPERIMENTAL AND
PREDICTED NORMAL FORCE AND PITCHING MOMENT
FOR NACA 64A010 AIRFOIL WITH L.E. SLAT
$M = 0.25$ $\delta_{SLAT} = -1.6°$ $RN = 6.25 \times 10^6$
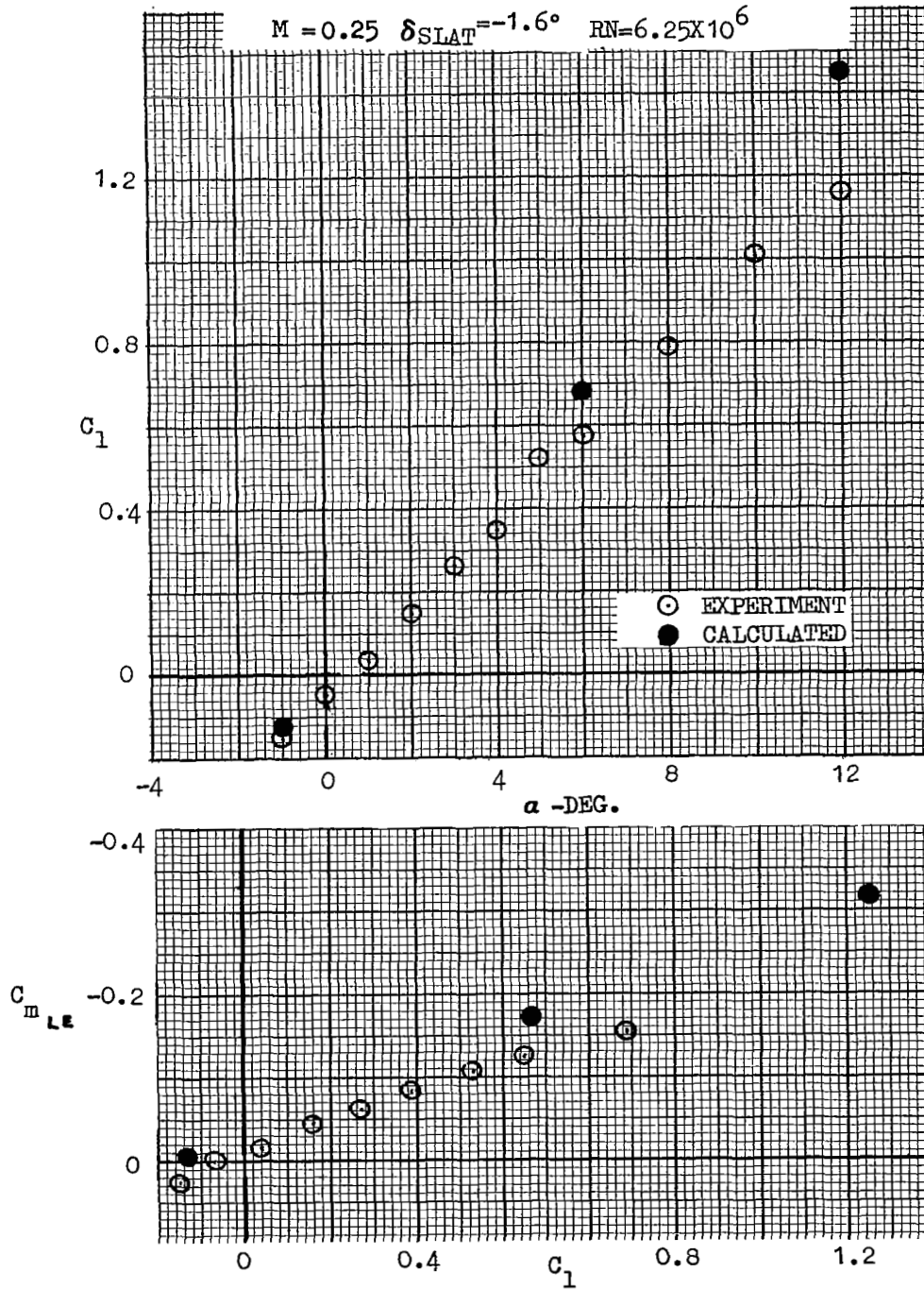
FIGURE IX-11 VARIATION OF LIFT COEFFICIENT
IN ITERATION PROCESS
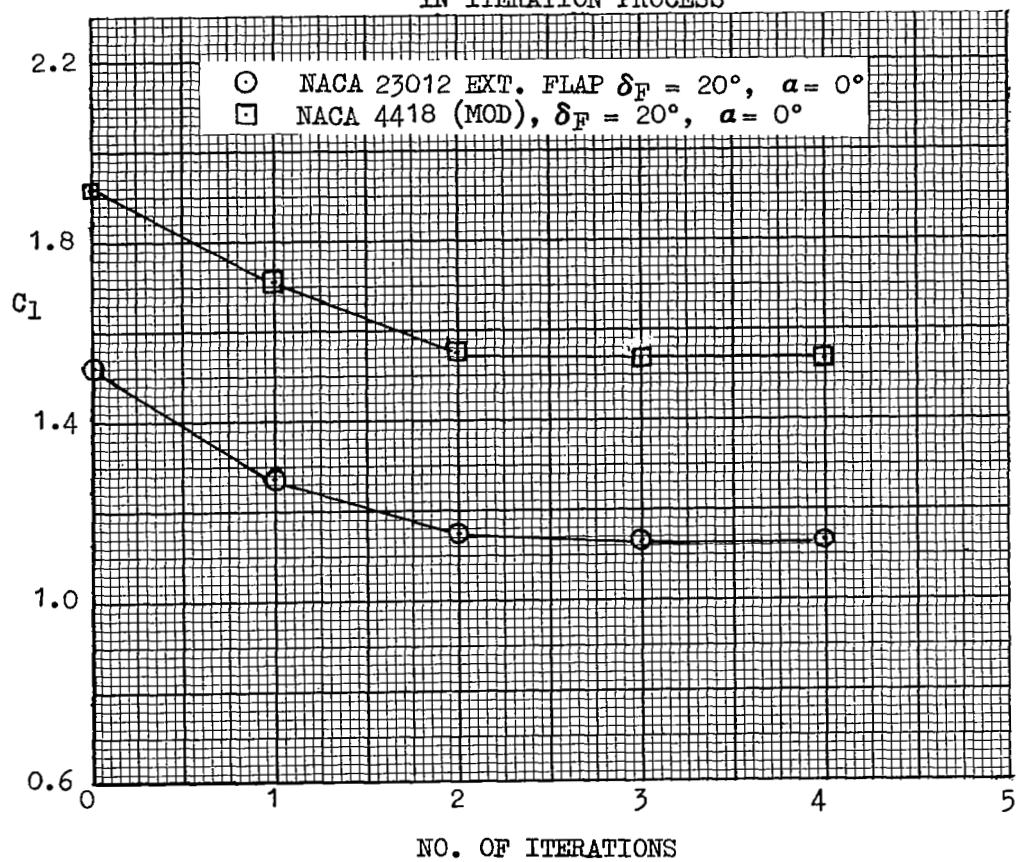
$\odot$ NACA 23012 EXT. FLAP $\delta_F = 20°$, $a = 0°$
$\square$ NACA 4418 (MOD), $\delta_F = 20°$, $a = 0°$

C_l

NO. OF ITERATIONS

$M_\infty = 0.1$ $a = 8°$ $\delta_{SLAT} = 0°$

$\delta_{FLAP} = 20°$ $RN = 2.2 \times 10^6$

(REF. IX-7)

⊙ ⚬ EXPERIMENTAL $\begin{cases} C_N = 1.88 \text{ (CORRECTED FORCE)} \\ C_N = 2.08 \text{ (UNCORR. PRESS.)} \end{cases}$

---- CALCULATED $C_N = 1.76$

C_p

X/C
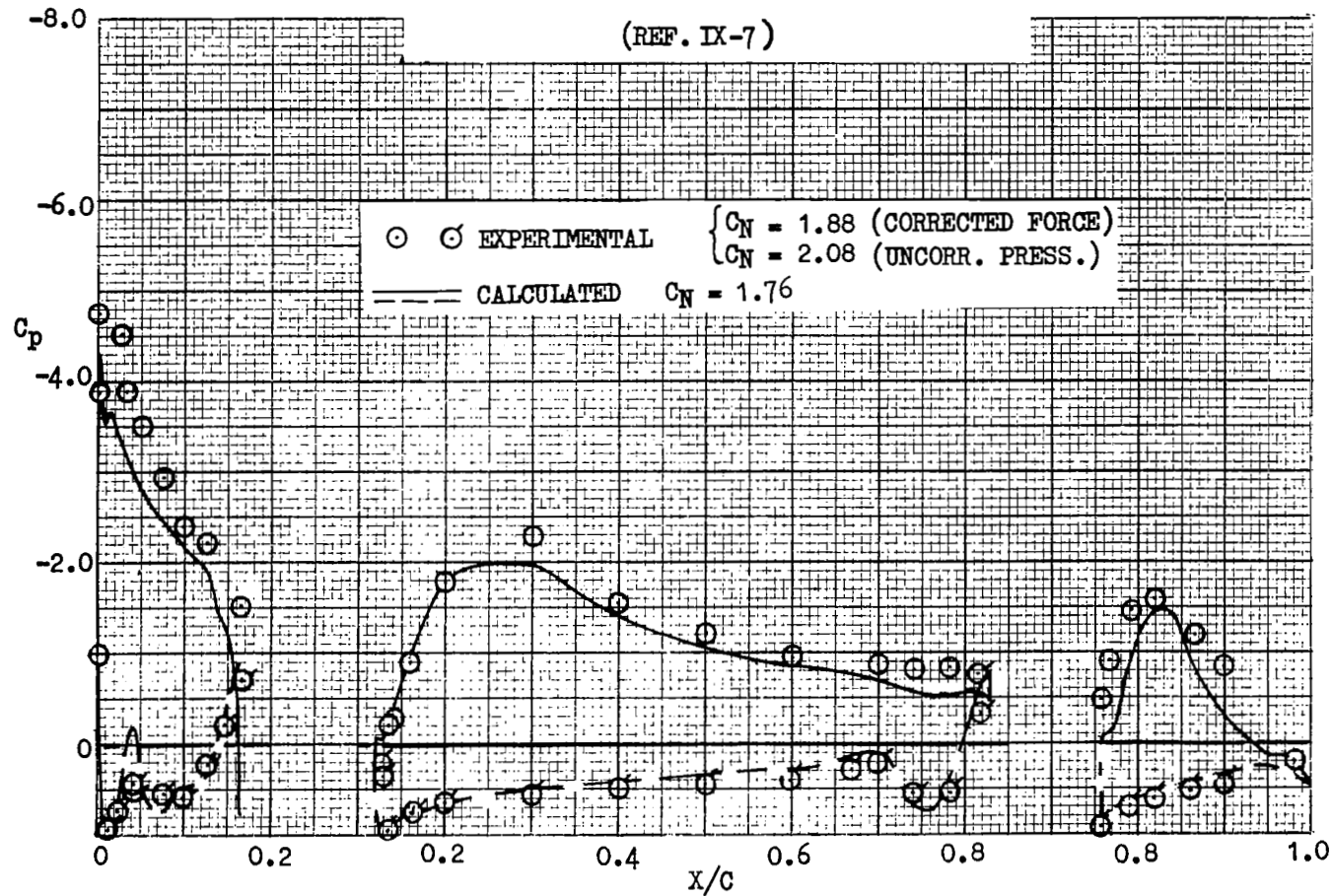
FIGURE IX-13   CALCULATED PRESSURE DISTRIBUTION ON NACA 64A010
AIRFOIL WITH SLAT AND DOUBLE SLOTTED FLAP

$M_\infty = 0.170$ $a = +4°$ $\delta_{SLAT} = -3.3°$

$\delta_{FLAP} = 20°$ $RN = 1.2 \times 10^6$
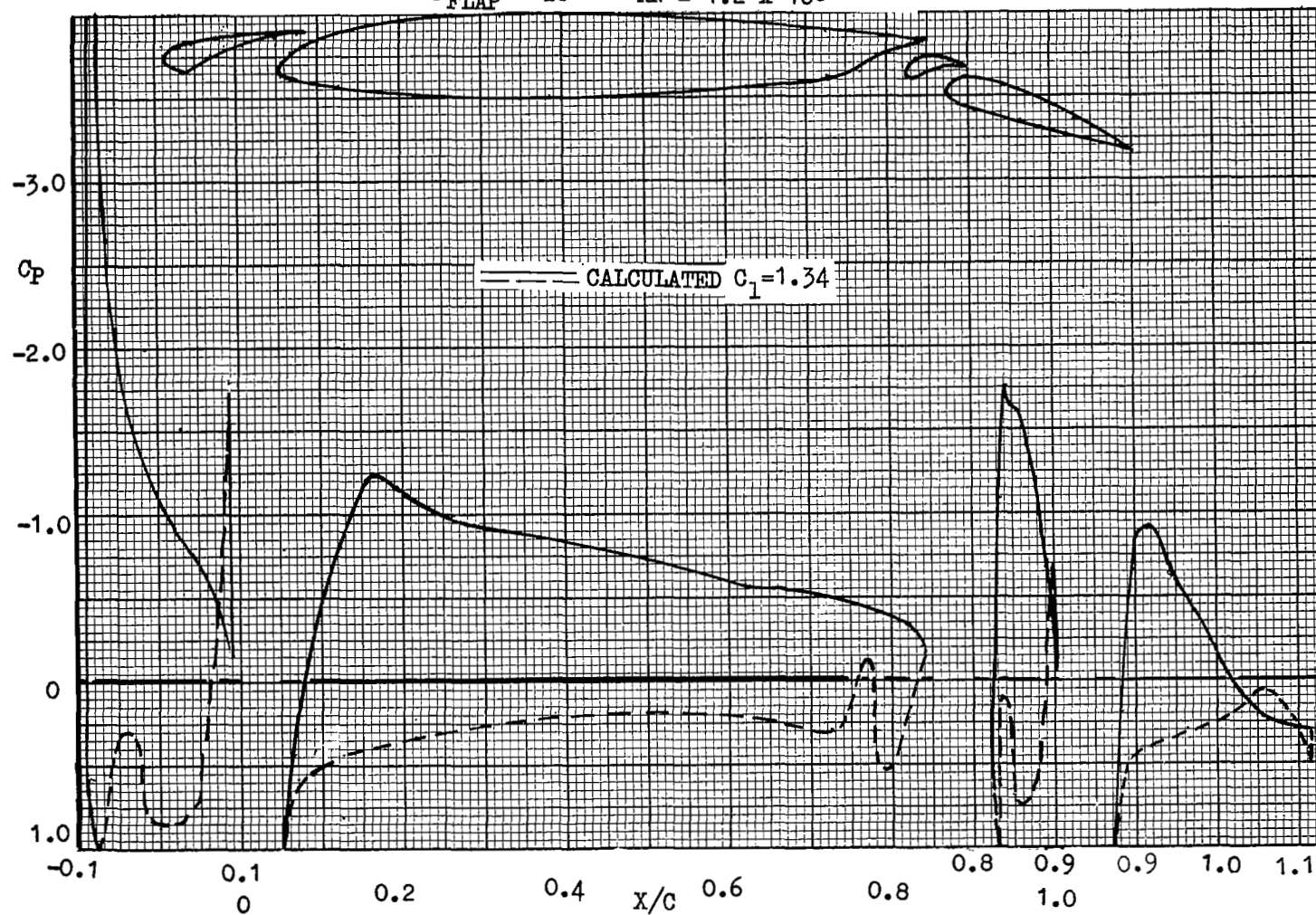
FIGURE IX-14 – TYPICAL NORMAL FORCE
PREDICTED VARIATION ON FOUR COMPONENT
64A010 AIRFOIL AT M = 0.17, R_N = 6x10^6

163
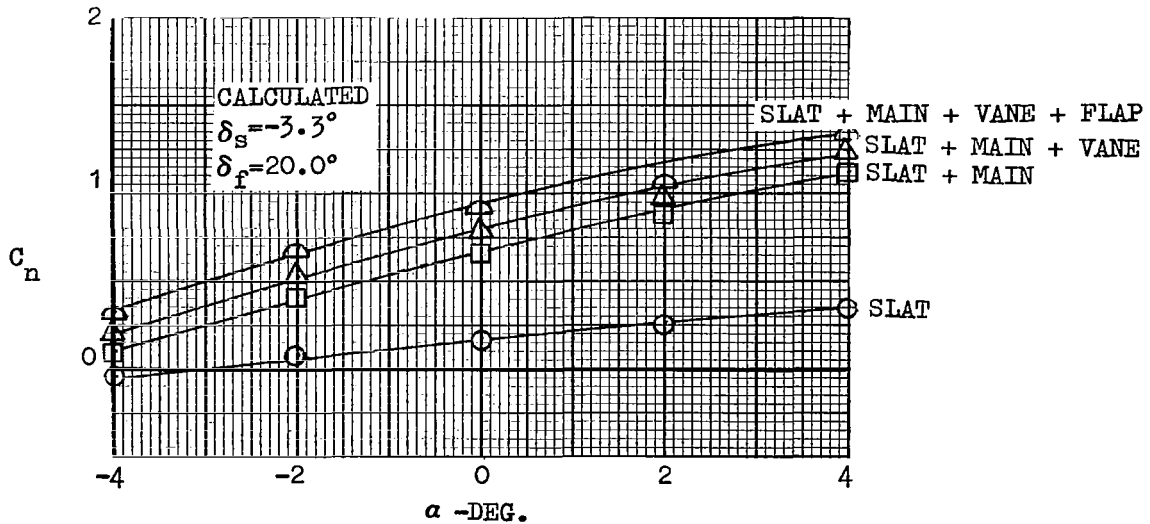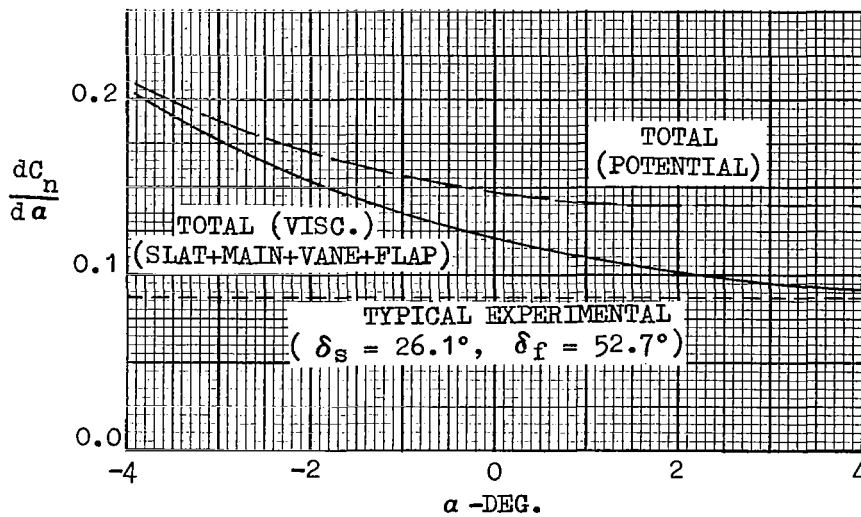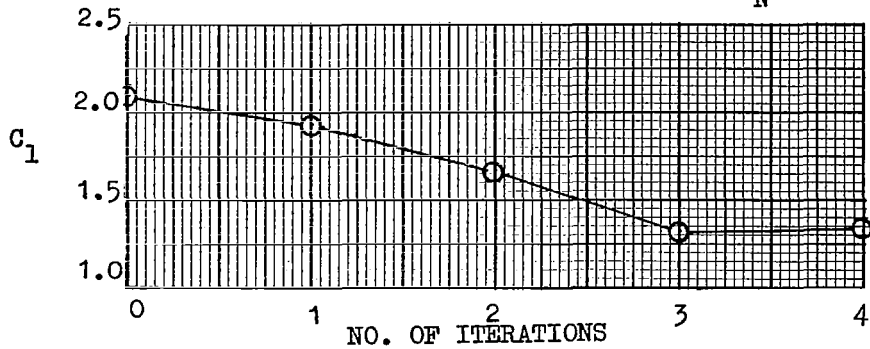
X - COMPUTER PROGRAM STRUCTURE

In describing the formulation of the multi-component program, there are two kinds of program structures to be considered, the algorithmic structure and the topographical structure. These two structural forms will be discussed in this same order since the first form is of primary interest to the engineer who is concerned with the logical make-up of the model. The second form is primarily for the programmer who has the responsibility for transferral of information between program elements and the computer efficiency of the total program package.

Figures X-1 through X-3 present the algorithmic structure of the computer model. The input and geometry functions, in addition to the iteration control, are governed by the main control program. "MAIN2" and "MAIN3" are secondary control programs which direct the potential flow and boundary layer models, respectively. The names in parenthesis are the names of the principal subroutines involved in the computation in question.

Figure X-4 depicts the core-overlay structure with "MAIN" being the zeroth level segment. This program is designed to fit into a 65K computer and hence the number of segments could be reduced in a larger machine. The individual segments are expanded in more detail in Figures X-5 through X-8 to show all the individual subroutines in the sequence in which they are referenced internal to the various routines.

The routines to perform the plotting of the airfoil geometry, pressure distribution, and basic boundary layer parameters on a CRT plotter are included as an integral part of the program deck. However, these programs are in higher level segments which are not called into core to be compiled unless the plot option is activated. Since the basic plot routines are non-standard with a wide variation between various installations, these routines are not considered further in this report. The FORTRAN listings of these plot routines are not included as the last five subroutines in the program listing (Appendix B in the Supplement to NASA CR-1843).

FIGURE X-1
ALGORITHMIC STRUCTURE OF THE COMPUTER PROGRAM

```
                                    ┌─────────────────┐
                                    │ INPUT GEOMETRY, │
                                    │    AMBIENT      │
  ( START )──────────────────────→ │   CONDITIONS    │───────────┐
                                    │    (READIT)     │           │
                                    └─────────────────┘           │
  ┌──────────────────────────────────────────────────────────────┘
  │ ┌─────────────┐      ┌──────────────────┐     ┌─────────────────┐
  │ │   OUTPUT    │      │ CONVERT GEOMETRY │     │ OUTPUT GAUSSIAN │
  └→│  THE INPUT  │─────→│   TO GAUSSIAN    │────→│   QUADRATURE    │
    │  GEOMETRY   │      │ QUADRATURE POINTS│     │     POINTS      │
    │  (ROTRAN)   │      │     (GEOM)       │     │    (ROTRAN)     │
    └─────────────┘      └──────────────────┘     └─────────────────┘
```

```
    ┌─────────────┐    ┌──────────────────┐                    ┌──────────────┐
    │ COMPUTE AND │    │   COMPUTE THE    │    ┌───┐  ┌───┐     │  INITIALIZE  │
    │ OUTPUT THE  │    │ BASIC THICKNESS  │    │FOR│  │FOR│     │  THE ARRAYS  │
    │SLOT GEOMETRY│───→│  VELOCITIES ON   │───→│EACH│→│EACH α│→│AND DETERMINE │
    │   (ASLOT)   │    │ EACH COMPONENT   │    │ M∞│  └───┘     │  THE NUMBER  │
    │             │    │    (VOVET)       │    └───┘            │OF INTERATIONS│
    └─────────────┘    └──────────────────┘                    └──────────────┘
```

```
                              ┌───┐  FOR EACH
                              │   │  INTERATION
                              └───┘
                        ┌──────────────────────────┐
                        │         MAIN 2           │
                        └──────────────────────────┘

                        ┌──────────────────────────┐
                        │         MAIN 3           │
                        └──────────────────────────┘
```

```
              ◇IS◇           ◇ HAVE ◇          ◇ HAVE ◇
  NO        ◇ THE ◇   YES  ◇ALL ANGLES◇  YES ◇ALL MACH NOS.◇  YES  ( STOP )
         ◇ SOLUTION ◇─────◇   BEEN   ◇─────◇    BEEN    ◇─────
          ◇CONVERGED◇      ◇  USED  ◇      ◇   USED   ◇
                              NO                NO
```

FIGURE X-2

FLOW DIAGRAM FOR SUBROUTINE MAIN 2

INPUT TO MAIN 2

```
SET UP EQUIVALENT          SET UP THE            SET UP INFLUENCE
    AIRFOIL                  CONTROL           COEFFICIENTS AND
   GEOMETRY                  POINTS           BOUNDARY CONDITIONS
   (EQUIV)                  (CONTPT)               (COEFF)


SOLVE FOR VORTEX            SHOULD          COMPUTE THICKNESS
   STRENGTH            B.L. THICKNESS  YES      VELOCITIES
  DISTRIBUTION           RELIEF BE        ON EACH COMPONENT
   (VORTEX)              COMPUTED              (VOVBT)

                            NO

COMPUTE THE          COMPUTE COMPRESSIBILITY
  SLOT FLOW            EFFECTS AND OUTPUT
 VELOCITIES          PRESSURE DISTRIBUTION
  (SLOTFL)                 (COMPR)


                       FIND THE
                   STAGNATION POINT
                  ON EACH COMPONENT
                       (STAG)
```

OUTPUT FROM MAIN 2

166

FIGURE X-3

FLOW DIAGRAM FOR SUBROUTINE MAIN 3

FIGURE X-4
PROGRAM CORE-OVERLAY STRUCTURE

| MAIN |

| SEGMENT 1 |

| SEGMENT 7 |

| SEGMENT 2 |

| SEGMENT 3 |

| SEGMENT 4 |

| SEGMENT 5 |

| SEGMENT 6 |

FIGURE X-5
INPUT AND GEOMETRY SEGMENT
SEGMENT 1

FIGURE X-6

POTENTIAL FLOW SEGMENTS

(A)
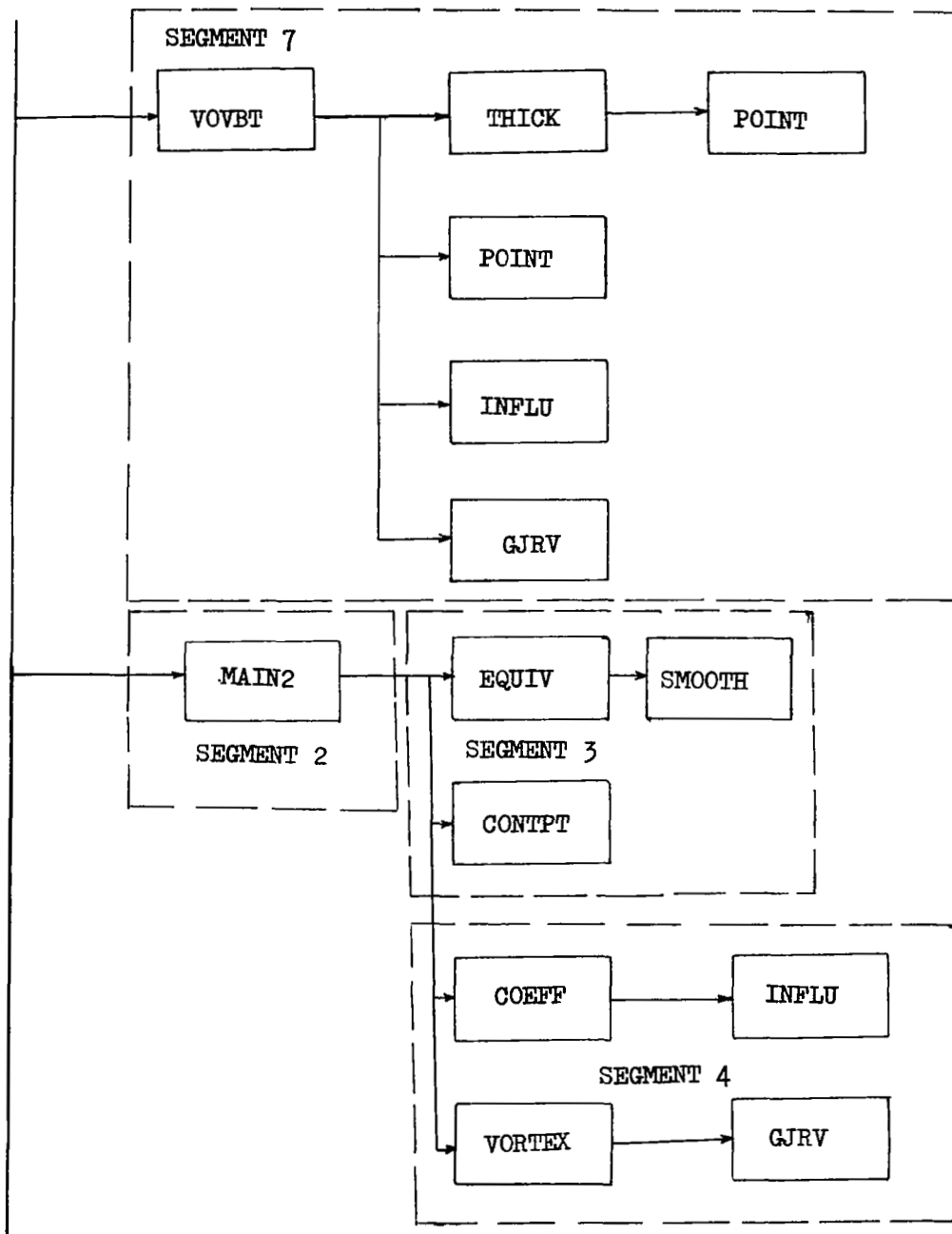
FIGURE X-7
POTENTIAL FLOW SEGMENT
(B)

FIGURE X-8
BOUNDARY LAYER SEGMENT
SEGMENT 6
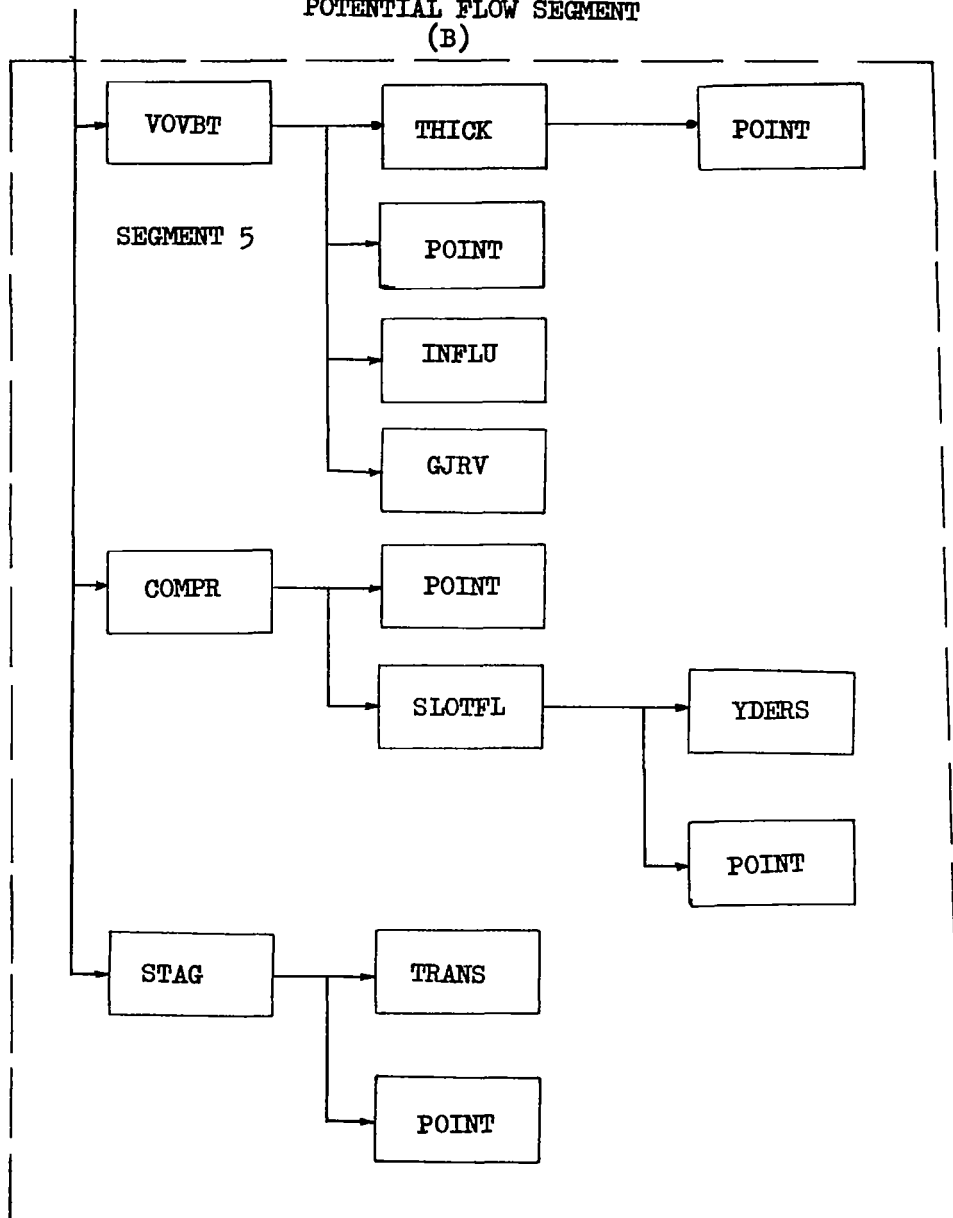
FIGURE X-8
BOUNDARY LAYER SEGMENT
SEGMENT 6
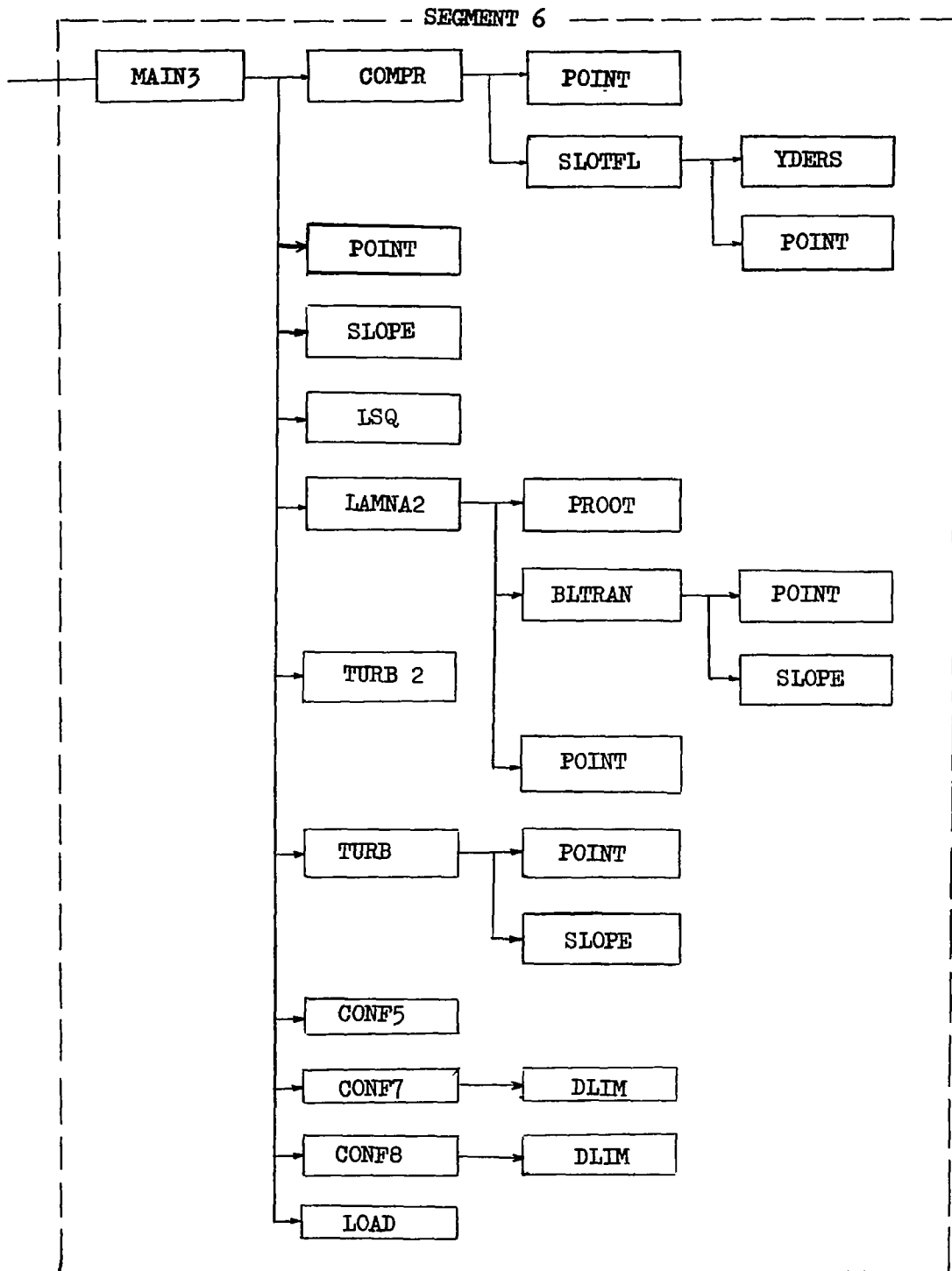
XI- CONCLUSIONS AND RECOMMENDATIONS

The computer program in its present state is an extremely useful working tool, which, by virtue of the variety of calculations available, provides state-of-the-art application to a broad range of airfoil design areas. The present study has served to validate the individual component conceptual approaches and to verify the feasibility of the methods for unifying the components into the combined solution. The present section summarizes those conclusions drawn in the course of the study concerning the individual subroutines as well as the combined solution. Recommendations are also offered in the areas of program utilization, program refinements and program extensions.

Geometry Subroutine. - The multiple-airfoil program can be used effectively to represent viscid and inviscid attached flow about smooth-contoured two-dimensional bodies exhibiting sharp trailing-edges. Where localized contour irregularities exist, such as slat lower surfaces or flap cove areas, a limited amount of correlation indicates that reasonable contour representation can be obtained by local re-fairing. It is recommended that additional correlation be performed to define the techniques and limitations of the re-fairing process.
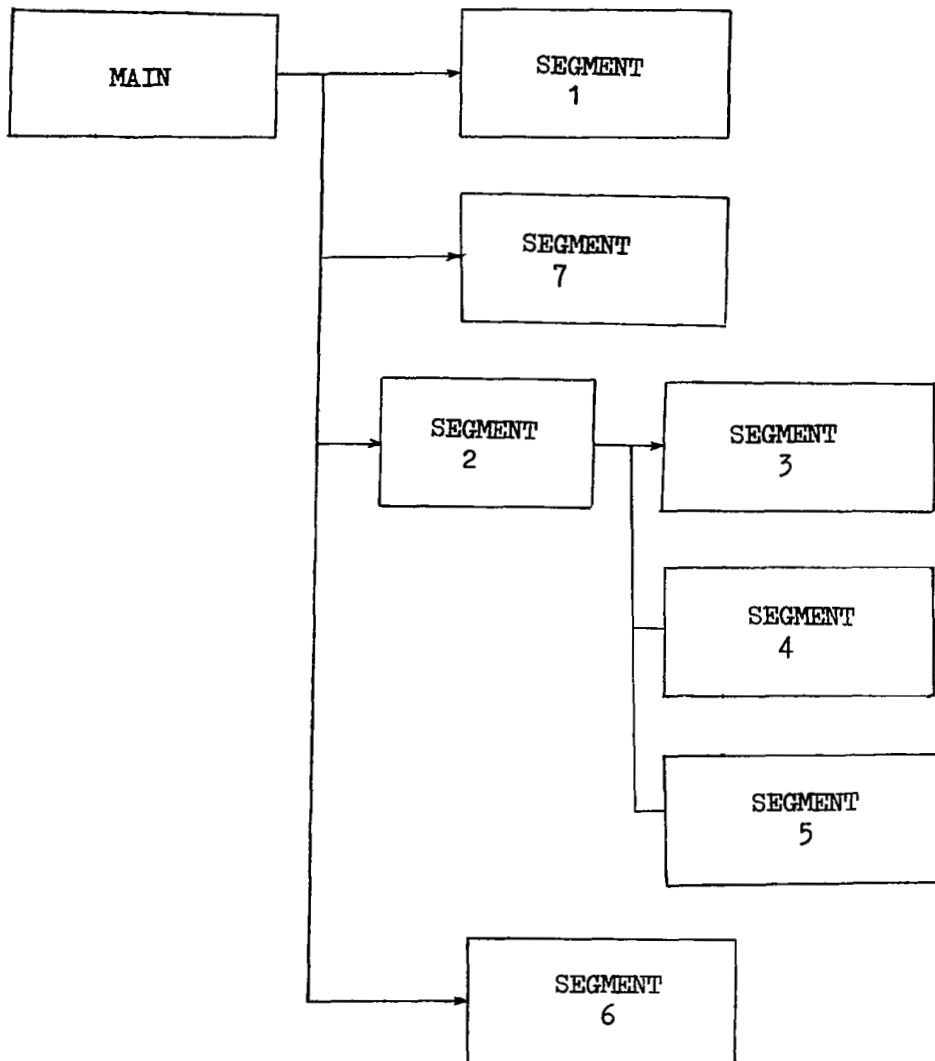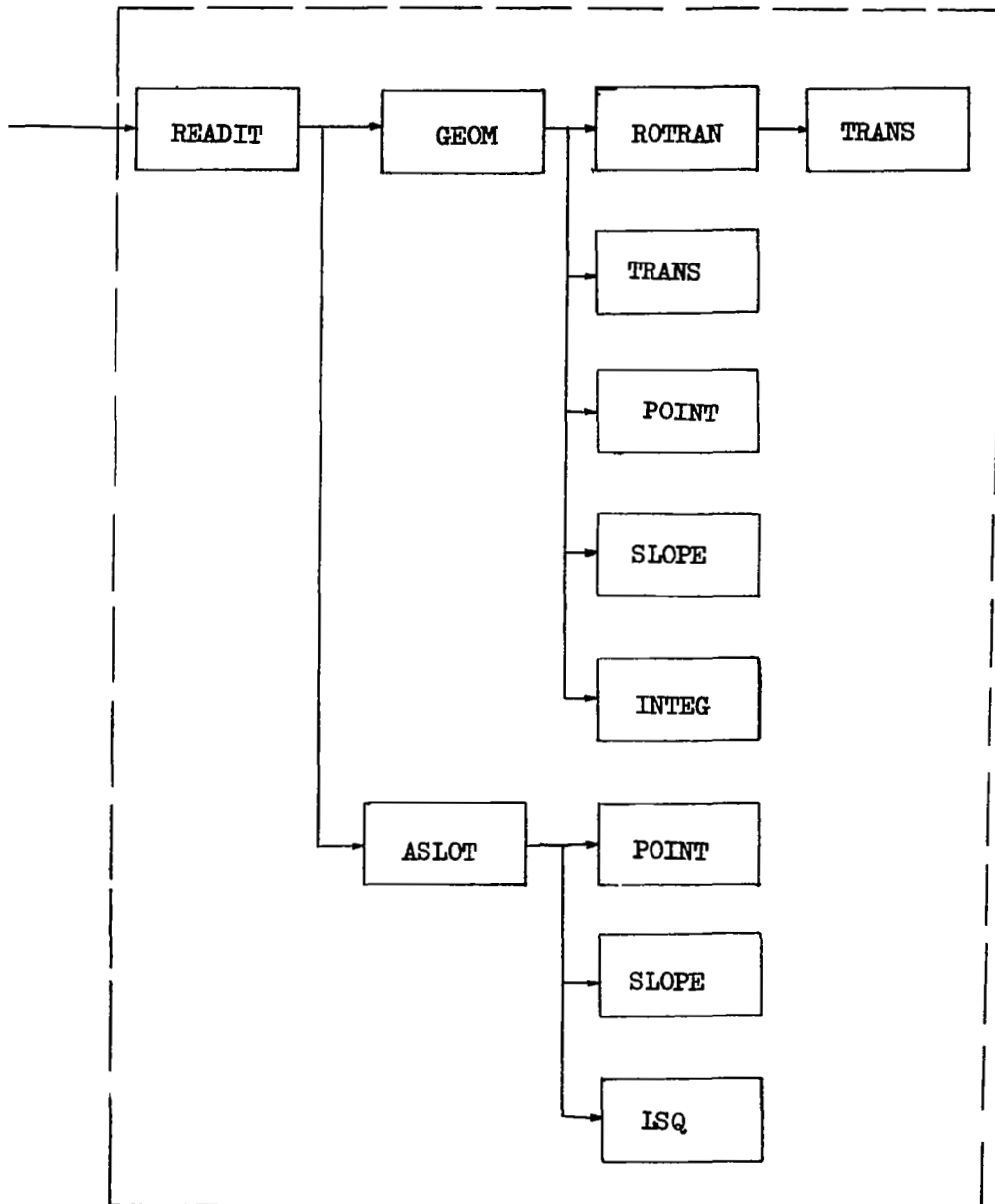
The scheme devised for geometrically orienting one component relative to another proved to be an efficient descriptive technique for computer utilization and has general application for representing a wide variety of configurations composed of any number of components. It is believed that a smoothing function on geometric input data, such as Hermite or Chebyshef polynomials, would be of value in smoothing local pressure gradients and thereby obtaining a smoother "equivalent airfoil".

Potential-Flow Subroutine. - The distributed-vortex method for obtaining the inviscid solution was found to be an accurate and stable approach. Limitations on this method appear to be governed more by computer facilities available than an inherent limitation in the concept itself.

For long, extremely thin trailing-edges the potential-flow solution tends to generate a singular matrix, possibly resulting in trailing-edge pressure irregularities. This was not found to be a severe problem for the range of airfoils considered since extremely thin trailing-edges are not normally found in practice.

Ordinary Boundary-Layer Subroutines. - Computer subroutines which evaluate the flat plate development of laminar, transition and turbulent boundary-layers provided reasonable agreement with available boundary layer measurements on airfoils up to separation.

Laminar stall criteria, specifically developed for the multi-component program provided an excellent technique, in the cases considered, for predicting leading-edge, short bubble breakdown. The application of these criteria to a few thin airfoils indicated that the angle-of-attack for maximum lift, as limited by laminar stall, was accurately determined.

Based upon potential-flow pressures, an area of incipient, turbulent separation was found on the majority of the multi-element cases considered at practically all angles-of-attack. To prevent program shutdown during the initial iterations, an approximately turbulent boundary-layer model was formulated which is insensitive to separation but provides reasonable approximations to the boundary layer parameters even under the influence of extreme gradients. This boundary layer model was found to interface well with the calculations performed by the more accurate model. Further use of the program should provide guidance in fully utilizing the flexibility of this scheme in terms of breakdown and number of iterations best suited for particular configurations or flow conditions. In the present study, it was found that the Nash turbulent boundary layer model accurately predicts the onset of turbulent separation where the initial separation point occurs over the last 5 percent of the airfoil chord. Where mid-chord turbulent separation is indicated, the present model is inadquate for defining the downstream flow characteristics.

It is recommended that the present laminar and turbulent boundary layer models be refined to include curvature effects providing more effective predictions of separation and reattachment phenomena. Similarly, the transition model should be extended to include roughness, and free-stream turbulence effects as well as compressibility terms. To provide a sound basis for these refinements, considerably more detailed, experimental data than is presently available, is needed throughout the Mach range.

Confluent Boundary-Layer Subroutines. - An incompressible mathematical model of a confluent boundary-layer, based on very limited experimental data, was found to be in reasonable agreement with test results. This model indicates a much more rapid boundary-layer growth downstream of the slot than is found in the case of ordinary boundary-layers. A correspondingly greater "uncambering" of the airfoil trailing-edge is obtained.

Refinements to the present model, representing an initial attempt at defining the behavior of highly complex boundary-layer phenomena, is essential to the realistic representation of multi-component airfoils. Comprehensive test data are crucial for extending this model to the compressible case and to provide valid refinements for representing high-deflection angles (Coanda effects).

Slot-Flow Subroutine. - A slot-flow model designed for and incorporated within the computer program has the capability of accounting for high frictional and curvature effects normally encountered in long, narrow slot regions. For the airfoils investigated, pressures within the relatively short slots, appeared to be governed primarily by the potential flow field. Additional correlation is required to refine the generalization of the methods as applied to either long or short slot geometries and to reduce the sensitivity of the flow calculations to aft-component orientation.

Combined Solution. - Calculated viscous solutions for single- and multi-element airfoils, at constant angle-of-attack were found to be in generally

good agreement with experimental pressure distributions where calculations indicated fully attached flow. It is difficult to assess the overall precision of the multiple-component airfoil program inasmuch as the multiple airfoils exhibit local areas of separated flow over most of the operating angle-of-attack range. Thus a need for turbulent flow reattachment criteria is indicated to fully evaluate the influence of local separation on downstream boundary layer development. The correlation study also indicated a definite need for accurate two-dimensional test data (force, pressure and boundary-layer measurements) on well-defined configurations. Such data is considered to be prerequisite to providing an overall evaluation of the program capabilities. In its present form, the correlation analysis shows that the program can be used as a valuable aid in both design and testing in providing consistent two-dimensional pressure and force data for the attached flow condition.

General Comments. - The present program is comprised of a number of component subroutines each in itself representing a complete computer program designed to explore the many facets of multiple-airfoil design. True limitations of the conceptual approaches utilized were not fully delineated in the brief correlation analysis described herein. It is believed that a continued and systematic use of the program in both the elemental and combined modes for purposes of design, analysis and test correlation is required to fully establish such limitations.

It is recognized that each sub-routine, representing a unique mathematical model, is limited to a specified range of geometric simulations, environmental parameters or local flow conditions. Figure XI-1 provides a summary of the major limitations governing each sub-routine as well as those specific to the combined viscous solution. For the most part, the limitations shown in the summary are concerned with limiting freestream conditions which could be expanded as required. Of particular importance are those limitations noted under the confluent boundary-layer sub-routine which represent limitations due to either the numerical scheme being utilized or in the formulation of the model itself. The more important of these are discussed below:

X_{MG} - This parameter represents the ratio of the velocity at the edge of the boundary layer (U_e) to the average efflux velocity from the slot. On the basis of available experimental evidence, the limitation placed on this parameter should not be severely restrictive to the generalized application of the program. The upper limit of the ratio (i.e. 1.0) reflects a constraint on the scope of the mathematical model while the lower limit (0.9) is due primarily to the particular numerical technique being utilized in the Initial Region of the confluent boundary layer. Further work in either of these two areas could remove this limitation.

$\dfrac{U_M}{U_e}$ - This ratio (see Figure VIII-2) represents the velocity in the Main Region to that at the edge of the boundary-layer. The limitation $(\dfrac{U_M}{U_e}) \geq 1.0)$ is imposed in the formulation of the confluent boundary layer model which reflects the best experimental data currently available. Additional test data, encompassing a broad spectrum of

values for this ratio, would permit the ready extension of the present analytical model. Such an extension would enhance those analytical studies concerned with skin friction optimization or off-design orientation of the airfoil elements.

$$\frac{d\left(\frac{U_M}{U_e}\right)}{d_x}, \frac{d\left(\frac{U_w}{U_e}\right)}{d_x}$$ — These two gradient parameters are currently limited to values between, and inclusive of, ± 0.8. The limitation is imposed to insure stability of the calculation procedures in Main Region I of the confluent boundary-layer. Again, this is not a severe restriction on program application inasmuch as gradients falling beyond these limits become unrealistic.

Program Extensions. — The multi-element airfoil program, as presently formulated provides a natural framework within which a number of extended capabilities, entailing both major and minor program modifications, may be developed. Figure XI-2 categorizes the specific refinements and modifications which could provide a greater range of applicability to the two-dimensional case and would ultimately lead to three-dimensional applications.

The category noted as "Refinements" is largely those items previously mentioned in the "Conclusions" section. The term "Modifications" implies that a greater degree of technical effort is required to achieve the desired results. Conceptually, however, it is believed that the modifications proposed are within the reach of current state-of-the-art. Specifically noteworthy are those refinements relating to the incorporation of a separated flow model. As evidenced by the present study, the efficient utilization of the present attached-flow program would be heavily augmented by a generalized, separated-flow boundary-layer representation.

FIGURE XI-1. MULTIPLE-AIRFOIL PROGRAM LIMITATIONS SUMMARY

Analytical Model	Limitation or Cautionary Areas
1. Potential Flow Solution	
° Geometry	one to four components
° Profiles	smooth, sharp trailing-edges, extremely long and thin trailing edges can generate pressure spikes.
° Orientation	limits not completely defined to date; correlation performed on conventional arrangements with coplanar segments separated by at least 1% C.
° Mach number	$0 \leq M_\infty < M_{crit.}$, as limited by Karman-Tsien correction
° Trailing-Edge Pressures	last several pressures extrapolated to suppress flow separation prior to viscous solution
2. Slot-Flow	
° Geometry	Smooth, continuous area distribution through slot; abrupt area changes not evaluated to date; limitations on sharp corner smoothing not completely defined.
° Mach number	Calculations sensitive to M_∞; correlations to date based on $0 \leq M \leq 0.25$; high Mach effects not evaluated
° Entry/Exit Conditions	Defined by program, reflects specific geometric definition of slot, additional correlation advisable to assure generalization
° General	Recommended for use with long narrow slots exhibiting high friction and curvature effects

FIGURE XI-1. (CONTINUED)

MULTIPLE-AIRFOIL PROGRAM, LIMITATIONS SUMMARY

<u>Analytical Model</u>	<u>Limitation or Cautionary Areas</u>
3. Ordinary Boundary Layer	
° Laminar	$0 \leq M \leq M_{crit}$, curvature effects not considered
° Laminar stall criteria	no compressibility or curvature effects, applicable to single element or leading-edge of multi-component. Reattachment criteria applicable to single element only.
° Transition model	$0 \leq M_{\infty} < M_{crit}$, curvature effects not considered, roughness, free-stream turbulence not considered
° Ordinary turbulent model	Nash - no curvature effects $0 \leq M_{\infty} < M_{crit}$ Goradia - $M_{\infty} = 0$, no curvature effects
° Turbulent separation criteria	$0 \leq M_{\infty} < M_{crit}$, no reattachment criteria
4. Confluent Boundary Layer	
° Core region	$0.9 \leq X_{MG} \leq 1.0$; arithmetical averaging of slot exit velocity
° Main Region I	$\dfrac{U_M}{U_e} \geq 1.0$ $-0.8 \leq \dfrac{d(U_M/U_E)}{dx} \leq +0.8$ $-0.8 \leq \dfrac{d(U_W/U_E)}{dx} \leq +0.8$
° Main Region II	Same as general limitations of confluent boundary layer model.
° General	Incompressible ($M_{\infty} = 0$); curvature or Coanda effects not considered; isoenergic flow assumes conversion to ordinary turbulent boundary layer prior to separation.

FIGURE XI-1. (CONTINUED)

MULTIPLE-AIRFOIL PROGRAM LIMITATIONS SUMMARY

Analytical Model	Limitation or Cautionary Areas
5. Combined Solution	limited by program objectives to attached flow conditions; primary limits governed by component subroutines; format of iterative scheme should be varied to determine optimum usage of flexibility provided.

FIGURE XI-2 MULTIPLE AIRFOIL PROGRAM
EXTENDED CAPABILITIES

PRESENT

GEOMETRY (POT'L FLOW)
- SMOOTH STREAMLINE PROFILES
- 1 TO 4 COMPONENTS
  (ARBITRARY CONFIG.)

REFINEMENTS

- SMOOTHING PROCESS
  (INPUT DATA)
- SWEEP EFFECTS
- PROTUBERANCES

MODIFICATIONS

- EFFECTS OF TAPER
- IRREGULAR SLOT PROFILES

CALC. DATA
- VISCOUS PRESS. DISTRIBUTION
- VISCOUS FORCE DATA (c_ℓ, c_m, c_f)
- SLOT-FLOW CHARACTERISTICS
- B.L. PARAMETERS
- SEPARATION TYPE, POSITION
- TRANSITION POSITION

- FREE-STREAM TURBULENCE
- ROUGHNESS EFFECTS
- CURVATURE EFFECTS

- $M_\infty \leq M_{critical}$
- SEPARATED FLOW MODEL

FLOW ENVIRONMENT
- LOCAL MACH < 0.5
- VARIABLE REYNOLDS NO.
- VARIABLE
- ATTACHED, VISCOUS FLOW

- IMPROVED
    SLOT FLOW ANALYSIS
    VISCOUS EFFECTS
    CONFL. B.L. MODEL
    SEPARATION/REATTACH. CRITERIA
- INVERSE SOL'N

- TOTAL PROFILE DRAG
- SEPARATED FLOW
    C_p, C_ℓ, C_m
    B.L. DATA
- FLOW-FIELD DEF.
- C_ℓ, C_m @ $M_\infty \leq M_{critical}$

APPLICATIONS
- EFFECTS OF AIRFOIL GEOMETRY
- EFFECTS OF FLOW ENVIRONMENT
- LEADING-EDGE STALL $c_{L_{MAX}}$
- SLOT DESIGN ANALYSIS
- B.L. ANALYSES

- SLOT-DESIGN EFFECTS
- "DESIGN-TO" CRITERIA
- OPTIMIZATION TECHNIQUES
- EFFECTS OF SWEEP ON
  OPTIMIZATION

- MULTI-ELEMENT CHARACT.
  TO $M_{critical}$
- EFFECTS OF TAPER ON OPT.
- $c_{L_{MAX}}$ (SUBSONIC)
  STORE/NAC. PLACEMENT
- PROTUBERANCE EFFECTS,
  CRITERIA
- VALIDATE 2-D TESTS

SYSTEMATIC AND
CONT'D REFINEMENT, &
MODIFICATIONS